

**Complex Hydrogen Bonded
Liquids with Different Poliarities
from Molecular Dynamics
Simulations**

Dissertation

zur Erlangung des

Doktorgrades der Naturwissenschaften (Dr. rer. nat.)

der

Naturwissenschaftlichen Fakultät II
Chemie, Physik und Mathematik
der Martin-Luther-Universität
Halle-Wittenberg

vorgelegt von

Tobias Watermann

geb. am 12. August 1984 in Berlin

1. Reviewer:

Prof. Dr. Daniel Sebastiani
MLU Halle-Wittenberg
Institut für Physikalische Chemie
Von-Danckelmann-Platz 4
06120 Halle (Saale)
Germany

2. Reviewer:

Prof. Dr. Michael Vogel
TU Darmstadt
Fachbereich Physik
Hochschulstraße 12
64289 Darmstadt
Germany

Day of public defense: 13.07.2020

Acknowledgements

I would like to acknowledge my supervisor Prof. Daniel Sebastiani for his support during my work and all the valuable discussions and hints. I would also like to thank the other members of the AG Sebastiani for the great work atmosphere and their support.

I would like to thank my parents and brother who supported and encouraged me throughout my education, my friends and especially my wife Elisabeth for giving me motivation and support, without which this work would have not been possible.

Contents

1	Introduction	1
2	Theory	5
2.1	Molecular Dynamics Simulations	5
2.1.1	Equations of Motion	5
2.1.2	Ensembles – Temperature and Pressure Coupling	7
2.1.3	Force Fields	9
2.1.4	Ab-Initio Molecular Dynamics	10
2.2	Electronic Structure Theory	11
2.2.1	Born-Oppenheimer Approximation	11
2.2.2	Hartree-Fock Method	12
2.2.3	Density Functional Theory	14
2.3	Response Calculations	18
2.3.1	NMR via DFPT	22
3	Overview of Papers	25
3.1	Effects of Different Polarity on the Properties of (Bio-) Solvents and Solute	25
3.1.1	Solvent Induced Conformational Switching in Phycocyanobilin	26
3.1.2	Solvents in Confinement	28
3.1.3	Polyphilic Molecules in Membranes	33
4	Publications	39
5	Conclusion	131
	References	133

CONTENTS

6 Academic Curriculum Vitæ	139
7 Eidesstattliche Erklärung / Declaration under oath	143

1

Introduction

Hydrogen bonded liquids show a range of interesting features due to the special properties of hydrogen bonds. They have a very high interaction energy, or bond strength, while also being directional, leading to rather rigid hydrogen bond networks. These effects are most well known and investigated in water, where this strength and directionality, in combination with the water's ability to form four hydrogen bonds in a tetrahedral geometry, leads to a range of anomalous thermodynamic and structural properties, many of which are integral to life itself.

Often, only hydrophilic and hydrophobic interactions are differentiated. Upon closer look, however, there is a wider variety of different 'philicities', such as the well known lipophilicity, as exhibited e.g. by alkyl chains or fluorophilicity, which manifests e.g. in perfluorinated alkyl chains.

As soon as multiple philicities are prevalent in a single system or even a single 'polyphilic' molecule, a variety of structural and dynamical effects can emerge, caused by the intricate interplay of competing attractive and repulsive forces. They can lead from demixing or phase separation in simple oil-water mixtures up to the formation of supermolecular structures in more complex systems. One example are membranes, which are prevalent in nature and an important structure in all living organisms. Here, amphiphilic molecules, i.e. molecules with two philicities on opposing ends build up a bilayer membrane in water. While the lipophilic sides point to each other, only the hydrophilic parts are exposed to water, leading to a significant energetic advantage.

Experimentally, these types of systems are often investigated by means of statistical averages e.g. in different spectroscopic methods. The investigated mechanisms,

1. INTRODUCTION

however, often take place on an atomistic or molecular level and are measured only indirectly. Complete analytical treatment of the system is also usually not possible, as already small molecular assemblies are already too complex. Here, molecular dynamics simulations can offer a valuable tool to elucidate the microscopic origin of the measured effects. Molecular dynamics simulations can be, depending on the investigated effects and complexity of the system, performed on different levels of theory ranging from ab-initio levels all the way to classical force fields and coarse grained methods. By computing ensemble averaged properties such as NMR or vibrational spectra, structure factors or similar observables, the simulations can be validated against experiments and can reveal the real atomistic picture underlying the investigated effects.

In this thesis, the structure and dynamics of different complex, hydrogen bonding systems is investigated. Molecular dynamics simulations with different levels of theory and supplementing calculations with spectroscopic and free energy methods have been applied. The nine publications that have been published during this doctorate(1, 2, 3, 4, 5, 6, 7, 8, 9) can be grouped in the following broader classes of systems:

- In a first project, we investigated the influence of solvents of different philicity – hydrophilic and neutral – on the conformation of a chromophore.
- In a second class of systems, we investigated solvents in confinement. Here, a – usually rigid – confining host material with pores with diameters of only some nanometers strongly modifies the behavior of guest molecules in this confinement. With softer confinements, also changes to the structure and dynamics of the host material can be observed.
- In the last system class, we investigated newly synthesized polyphilic molecules and their interaction with phospholipid bilayer membranes. To this end we calculated new force field parameters and used them to investigate systems ranging from simple perfluoroalkanes up to small clusters of polyphilic transmembrane molecules.

The thesis has been written in a cumulative way. During this thesis I co-authored nine peer reviewed publications and one book chapter – they can be found in chapter 4. In chapter 2, the theoretical background of the published papers is introduced, while in

chapter 3, the individual publications are summarized. In chapter 5, I briefly conclude the thesis and offer some outlook.

1. INTRODUCTION

2

Theory

2.1 Molecular Dynamics Simulations

Molecular dynamics simulations provide a way to simulate the temporal evolution of molecular systems of various complexities and sizes. Generally atomic positions are propagated by evaluating the forces acting on the individual atoms. These forces can be generated by a method of choice(10, 11), ranging from quantum mechanical calculations over parametrized classical potentials to coarse grained approaches featuring even more generalized potentials of averaged interactions. Depending on the approach, the used particles can be atoms, or groups of atoms in the case of coarse grained models.

They have become a widely used tool in physics, chemistry, biochemistry and even pharmacy. Especially in combination with experiments they can often validate results and offer insight into the molecular origin of observed effects as for example in spectroscopy(12, 13, 14, 15, 16, 17, 18).

2.1.1 Equations of Motion

In molecular dynamics simulations we want to numerically propagate the positions and velocities of the atoms of a system by means of Newtons laws. Generally, this means, we have to integrate Newtons equation of motion, where the forces can be derived from a potential V acting on the atoms considered in the simulation:

$$F = m a = -\nabla V(R_i) \tag{2.1}$$

2. THEORY

Realizing that the acceleration \mathbf{a} is the second derivative of the position \mathbf{r} , we could get the velocities and positions simply by integrating to the lower derivatives and propagating the two arising differential equations with finite time steps:

$$v(t) = a(t)t + v_0 , \quad (2.2)$$

$$r(t) = v(t)t + r_0 . \quad (2.3)$$

For efficient computation of the systems dynamics, a few constraints have to be met by the used algorithm. The dynamics should remain stable, i. e. it should conserve energy and momentum of the simulated system, ideally with a rather large time step. The algorithm should be computationally efficient, requiring as few calculations per time step as possible.

Most molecular dynamics programs use one of two variations of this scheme, the velocity verlet(19, 20) or the leap frog approach. In these schemes, the overall error is reduced, while the computational effort compared to other integration schemes is minimized.

Here we briefly discuss a frequently used algorithm – the velocity verlet algorithm:

$$\mathbf{r}(t + \Delta t) = \mathbf{r}(t) + \mathbf{v}(t)\Delta t + \frac{1}{2}\mathbf{a}(t)\Delta t^2 \quad (2.4)$$

$$\mathbf{v}(t + \Delta t) = \mathbf{v}(t) + \frac{1}{2}[\mathbf{a}(t) + \mathbf{a}(t + \Delta t)] \Delta t \quad (2.5)$$

In the standard implementation, the velocity is first calculated at half the step size $\mathbf{v}(t + \frac{1}{2}\Delta t)$, which is in turn used to calculate the new positions. In a next step, the acceleration is derived from the interaction potential at the new positions to finally compute the new velocities.

The one missing ingredient, however, are the forces acting on the atoms. Ideally they would be calculated by directly solving the Schrodinger Equation of the investigated system and using the obtained potential energy to calculate the forces. As this is not feasible, the potential has to be approximated by a method with the required accuracy and properties. That might be an ab-initio method, semi-classical approximations, classical force fields or even coarse grained models, that combine several atoms into one 'atomic' particle.

2.1.2 Ensembles – Temperature and Pressure Coupling

Canonical Velocity Rescaling

A very simple approach to reach a simulation with a constant temperature is to simply calculate the kinetic energy and, in every step of the simulation, scale all particles velocities to keep the kinetic energy constant. A similar approach is used in the canonical velocity rescaling(21), where, as suggested by the name, the velocities are rescaled in a manner that the resulting simulation will resemble a canonical NVT ensemble. To this end a velocity rescaling has been developed that reproduces a canonical NVT ensemble. The velocities are scaled by a rescaling factor to reach the target kinetic energy K_t and thus the associated target temperature. The target kinetic energy is chosen as a canonical distribution

$$\alpha = \sqrt{\frac{K_t}{K}} \quad (2.6)$$

Since the temperature response should smoothly converge to the desired state, a delayed dynamics is obtained by incrementing the kinetic energy over time by small increments

$$dK = (\bar{K} - K) \frac{dt}{\tau} + 2 \sqrt{\frac{K \bar{K}}{N_f}} \frac{dW}{\sqrt{\tau}} \quad (2.7)$$

The first term influences via the coupling constant τ and the difference from the target kinetic energy \bar{K} , how fast the systems kinetic energy equilibrates and thus how fast the target temperature is reached. This term is equivalent to the standard Berendsen thermostat. The second term with a Wiener noise dW and the degrees of freedom N_f becomes more important once equilibration is reached and introduces a stochastic noise to the energy so that a canonical distribution is achieved.

In the limit of $\tau = 0$ only the stochastic velocity-rescaling part remains retaining the microcanonical ensemble, while for $\tau \rightarrow \infty$ the system instantaneously thermalizes.

Nosé-Hoover Thermostat

In the Nosé-Hoover thermostat(22), the system is extended by a heat bath. The main idea is to treat the heat bath as an integral part of the system by adding a new variable η and their conjugate momentum p_η and their associated "mass" Q , describing

2. THEORY

a friction-like force. In the new system, the Hamiltonian is modified to conserve the energy of the original system and the new heat bath

$$H' = H + \frac{1}{2}Qp_\eta^2 + gkTs \quad (2.8)$$

After some reformulation(23), the Nosé-Hoover equations read as

$$\dot{q}_i = \frac{p_i}{m_i} \quad (2.9)$$

$$\dot{p}_i = -\frac{\partial V(\mathbf{q})}{\partial q_i} - p_i \frac{p_\eta}{Q} \quad (2.10)$$

$$\dot{p}_\eta = \sum_{i=1}^N \frac{p_i^2}{m_i} - NkT \quad (2.11)$$

$$\dot{\eta} = \frac{p_\eta}{Q} \quad (2.12)$$

with the coupling strength

$$Q = \frac{\tau^2 T_0}{4\pi^2} \quad (2.13)$$

In contrast to the CSVN thermostat, this formulation leads to an oscillatory relaxation towards the target temperature. Again, the strength of the coupling Q and thus relaxation time can be adjusted with the τ , which is typically chosen 5 times larger than in the case of the CSVN thermostat.

The original Nosé-Hoover formulation can lead to non-ergodic trajectories for certain - especially small and stiff - systems. The solution to always guarantee an ergodic trajectory is to couple each heat bath to another one, leading to an infinite chain of Nosé-Hoover baths. In most cases, however, already a chain length of up to 10 is sufficient to produce an ergodic trajectory.

Berendsen Barostat

In the Berendsen barostat, the system is weakly coupled to an external pressure bath. To this end, the equations of motion are extended by an additional term for the pressure change

$$\left(\frac{dp}{dt}\right)_{bath} = \frac{P_0 - P}{\tau_p} \quad (2.14)$$

with the instantaneous pressure P . Similar to the thermostats, τ_p is the time constant of the coupling. The equations of motion are extended by a term that scales the volume by modifying both, coordinates and box dimensions, minimizing the local disturbances. Assuming an isotropic system in a cubic box, the rescaling factor can be simplified to

$$\mu = 1 - \frac{\beta \partial t}{\tau} (P_0 - P) \quad (2.15)$$

$$P = \frac{1}{V} \left[\frac{1}{3} \sum_i^N \left(\sum_{j>i}^N F_{ij} r_{ij} + \frac{|\mathbf{p}_i|^2}{m_i} \right) \right] \quad (2.16)$$

2.1.3 Force Fields

One way to compute the potential to calculate the inter-atomic or inter-molecular forces on is, as mentioned before, the classical force field approach. In this type of approach, interactions are modeled as classical equation, while either all atoms are considered in all-atom force fields, hydrogens are merged into their neighboring atoms in united atoms force field or even multiple (non-hydrogen) atoms are unified in coarse grained force fields. While the empirical modeling by classic equations allows for an easy and fast calculation of the forces acting on the atoms, this also leads to some restrictions. The breaking and formation of bonds is generally not possible (even though there are some implementations that allow for a distance based breaking and creation of bonds). Electric polarization is only considered in polarizable force fields and van der Waals forces are also generally only poorly accounted for.

In the following example showcasing the CHARMM22 all-atom force field(24, 25), we can see the general structure and most-often used potentials for the different classical interactions that need to be modeled:

2. THEORY

$$V = \sum_{bonds} k_b(b - b_0)^2 + \sum_{angles} k_\theta(\theta - \theta_0)^2 + \sum_{dihedrals} k_\phi[1 + \cos(n\phi - \delta)] \quad (2.17)$$

$$+ \sum_{impropers} k_\omega(\omega - \omega_0)^2 + \sum_{urey-bradley} k_u(u - u_0)^2 \quad (2.18)$$

$$+ \sum_{nonbonded} \epsilon \left[\left(\frac{R_{min_{ij}}}{r_{ij}} \right)^{12} - \left(\frac{R_{min_{ij}}}{r_{ij}} \right)^6 + \frac{q_i q_j}{\epsilon r_{ij}} \right] \quad (2.19)$$

The bonded interactions are modeled as classical springs with a quadratic energy function with force constants k_b and distances to the equilibrium $b - b_0$. Angles utilize force constants k_θ and the angle from equilibrium between each 3 bonded atoms. The dihedrals or torsion angles ϕ with force constants k_ϕ are modeled by cosine functions with the multiplicity n and phase shifts δ . Improper dihedral angles or out of plane bending is again modeled by harmonic potentials with force constants k_ω and the out of plane angles $\omega - \omega_0$. The Urey-Bradley term describes angle bending using 1,3 non-bonded interactions and is again modeled with harmonic potentials with force constants k_u and distances from equilibrium $u - u_0$. Non-bonded interactions are modeled using a standard 12-6 Lennard-Jones potential for the van der Waals interactions and a coulombic potential for the electrostatic interactions.

All of the described parameters have to be generated in a way that results in a realistic behavior of the system. Depending on the force field and parametrization procedure, this can be achieved by comparison to higher levels of theory, e.g. ab-initio calculations or by direct comparison with experimentally derived properties.

2.1.4 Ab-Initio Molecular Dynamics

In ab-initio molecular dynamics simulations, or Born-Oppenheimer molecular dynamics simulations, the movement of the nuclei and the forces stemming from the electronic structure are handled separately, assuming that the coupling can be neglected due to the different time scales of the movements (see sec. 2.2.1). The movement of the nuclei is handled by the classical equations described in section 2.1.1, while the forces are calculated on every time-step from the chosen ab-initio level of theory.

2.2 Electronic Structure Theory

The properties of matter can, in principle, be calculated just from the interactions of electrons with the different possible atomic nuclei. I.e. from the quantum mechanical attraction between electrons and nuclei, and the pairwise repulsion of two nuclei and two electrons. Solving the full Schroedinger Equation

$$H\psi(\mathbf{x}_i, \mathbf{R}_j) = E\psi(\mathbf{x}_i, \mathbf{R}_j) \quad , \quad (2.20)$$

of all interacting electrons at \mathbf{x}_i and nuclei at \mathbf{R}_j would yield the exact solution to this problem. Since this, however, is not feasible for more than a few particles, over the time several methods have been developed to tackle this problem by employing various simplifications and approximations.

These approximations include the purely classical description, where the electronic structure is simplified to classical electrostatic interactions, often combined with (semi-) empirical van der Waals corrections.

Going towards a more realistic description of the quantum nature, there are semi-empirical methods, wave function based theories as well as approaches based on the local electronic density.

One of the earliest approaches, where the electron density was used to calculate properties was the semi-empirical Thomas-Fermi Model.

One very popular and commonly used approach to calculate ground state properties is through density functional theory (DFT), that has also been used in this thesis and is introduced on page 14.

2.2.1 Born-Oppenheimer Approximation

In the time dependent Schroedinger Equation, electrons and nuclei possess masses differing in orders of magnitude. Generally, this leads to velocities and kinetic energies with a similar discrepancy, thus motivating a separation of the electronic movements from that of the nuclei by reformulating the electronic problem (with positions \vec{r}_i) for fixed nuclei with only a parametric dependence on the position of the nuclei \vec{R}_I :

$$\mathcal{H}_{el}(\vec{r}_i, \vec{R}_I)|\Psi_k(\vec{r}_i, \vec{R}_I)\rangle = E_k(\vec{R}_I)|\Psi_k(\vec{r}_i, \vec{R}_I)\rangle \quad (2.21)$$

2. THEORY

with orthonormal eigenfunctions $\Psi_k(\vec{r}_i, \vec{R}_I)$ and eigenvalues E_k .

Expanding the wave function in the basis of the eigenstates with time-dependent expansion coefficients yields

$$|\phi_0(\vec{r}_i, \vec{R}_I, t)\rangle = \sum_l |\Psi_l(\vec{r}_i, \vec{R}_I)\rangle \chi_l(\vec{R}_I, t) \quad (2.22)$$

Inserting into the time-dependent Schroedinger Equation and multiplying with $\langle \Psi_k |$ leads to

$$\left[T_n(\vec{R}_I) + V_n(\vec{R}_I) + E_k(\vec{R}_I) \right] \chi_k + \sum_l C_{kl} \chi_l \quad (2.23)$$

with the adiabatic coupling operator

$$C_{kl} = \langle \Psi_k | T_n | \Psi_l \rangle + \sum_I \frac{-i \nabla_I}{M_I} \langle \Psi_k | -i \hbar \nabla_I | \Psi_l \rangle \quad (2.24)$$

Within the nondiabatic approximation, all non-diagonal terms are neglected, i.e. coupling between the different electronic states is ignored. In the "Born-Oppenheimer approximation", the diagonal coupling terms are neglected as well.

2.2.2 Hartree-Fock Method

While the exact solution of the Schrödinger equation can in theory from the variational principle by minimizing the energy function with respect to test-N-electron wave functions, the exact solution would only be found if the correct wave function is tested(26). A more straight forward approach is used in the Hartree-Fock approximation. Here, the N-electron wave function is approximated by an anti-symmetrized product of N one-electron wave functions, a Slater determinant(27)

$$\Psi(\mathbf{x}_1, \mathbf{x}_2, \dots, \mathbf{x}_N) = \frac{1}{\sqrt{N!}} \begin{vmatrix} \chi_a(\mathbf{x}_1) & \chi_b(\mathbf{x}_1) & \dots & \chi_k(\mathbf{x}_1) \\ \chi_a(\mathbf{x}_2) & \chi_b(\mathbf{x}_2) & \dots & \chi_k(\mathbf{x}_2) \\ \vdots & \vdots & \dots & \vdots \\ \chi_a(\mathbf{x}_N) & \chi_b(\mathbf{x}_N) & \dots & \chi_k(\mathbf{x}_N) \end{vmatrix} = |\chi_a \chi_b \dots \chi_k\rangle \quad (2.25)$$

The energy is made up from the kinetic energy, nucleus-electron and electron-electron interaction

$$\mathcal{H}_{el} = -\frac{1}{2} \sum_i^N \nabla_i^2 - \sum_i^N \sum_A^M \frac{Z_A}{|\vec{r}_i - \vec{R}_A|} + \frac{1}{2} \sum_{i,j \neq i}^N \frac{e^2}{|\vec{r}_i - \vec{r}_j|}$$

and needs to be minimized to find the ground state energy

$$E_0 \leq \langle \Psi_{SD} | \mathcal{H}_{el} | \Psi_{SD} \rangle \quad (2.26)$$

Using the variational principle under the constraint of orthonormal wave functions $\langle \psi_i | \psi_j \rangle = \delta_{ij}$, we get the equation for the Hartree-Fock energy

$$E_{HF} = \sum_a^N \epsilon_a = \sum_a^{N/2} \langle a | h | a \rangle + 2 \sum_a^{N/2} \sum_b^{N/2} [2abab - abba] \quad (2.27)$$

The Fock equation can then be derived as

$$f | \psi_a \rangle = \epsilon_a | \psi_a \rangle \quad (2.28)$$

with the Fock-operator

$$f = h_1 + \sum_b^{N/2} 2\mathcal{J}_b - \sum_b^{N/2} 2\mathcal{K}_b \quad (2.29)$$

and the coulomb

$$\sum_b^{N/2} \int \psi_b^*(\vec{r}_2) \frac{1}{r_{12}} \psi_b(\vec{r}_2) d\vec{r}_2 \psi_a(\vec{r}_1) = \mathcal{J}_b \psi_a(\vec{r}_1) \quad (2.30)$$

and exchange operators

$$\sum_b^{N/2} \int \psi_b^*(\vec{r}_2) \frac{1}{r_{12}} \psi_b(\vec{r}_1) d\vec{r}_2 \psi_a(\vec{r}_2) = \mathcal{K}_b \psi_a(\vec{r}_1) \quad (2.31)$$

Developing orbitals of the Fock equation into p basis functions

$$\psi_i = \sum_{\mu=1}^p c_{\mu i} \phi_{\mu} \quad (2.32)$$

and some reformulation leads to the Roothan-Hall equation

$$FC = SCE \quad (2.33)$$

2. THEORY

with the Fock matrix $F = H^{core} + G$ consisting of the single particle matrix H and two-particle matrix G , overlap matrix S and coefficient matrix C .

This equation can now be solved in the so called self consistent field method. Here, first some atomic orbitals are chosen as initial guess, from where the Fock matrix is calculated and then diagonalized to yield new orbitals. This procedure is repeated until the orbitals remain (nearly) constant and thus self-consistency is reached.

2.2.3 Density Functional Theory

The foundation of the density functional theory (DFT) is built by the Hohenberg-Kohn theorems (28), tracing the ground state properties to only the systems electronic density.

Hohenberg-Kohn theorem I:

For any system of interacting particles in an external potential $V_{ext}(\vec{r})$, the electron density is uniquely determined.

Hohenberg-Kohn theorem II:

A universal functional for the energy $E[n]$ can be defined in terms of the density. The exact ground state is the global minimum value of this functional.

Kohn-Sham Approach

The central idea in the Kohn-Sham (29) approach is the realization, that the kinetic energy can not be determined through an exact functional, but instead try to calculate as much of the kinetic energy exactly and finding an approximation for everything else. Kohn and Sham proposed a way to calculate the functional by first starting with a set of non-interacting electrons in a local potential $V_s(\vec{r})$:

$$T_S = -\frac{1}{2} \sum_{i=1}^N \langle \varphi_i | \nabla^2 | \varphi_i \rangle \quad (2.34)$$

This non-interaction energy differs from the real kinetic energy even for systems of the same density. The ground state wave function of the Hamilton operator of the non-

interacting system is a Slater determinant as in the Hartree-Fock case. The analogue Kohn-Sham equations read as

$$f^{KS} \varphi_i = \epsilon_i \varphi_i \quad (2.35)$$

with the Kohn-Sham operator

$$f^{KS} = -\frac{1}{2} \nabla^2 + V_s(\vec{r}) \quad (2.36)$$

The potential V_s must now be chosen in a way that the density calculated from the Kohn-Sham orbitals results in the correct ground state density of the interacting system:

$$\rho_s(\vec{r}) = \sum_{i=1}^N \sum_s |\varphi_i(\vec{r}, s)|^2 = \rho_0(\vec{r}) \quad (2.37)$$

We can now rewrite the energy

$$E_0[\rho] = T_S[\rho] + J[\rho] + E_{XC}[\rho] + E_{Ne}[\rho] \quad (2.38)$$

with the known parts in the terms for the non-interacting kinetic energy T_S , the classical electron-electron interaction J :

$$J[\rho] = \frac{1}{2} \int \int \frac{\rho(\vec{r}_1) \rho(\vec{r}_2)}{r_{12}} d\vec{r}_1 d\vec{r}_2 \quad (2.39)$$

the electron-nuclei interaction E_{Ne}

$$E_{Ne}[\rho] = - \sum_{I=1}^M Z_I \int \frac{\rho(\vec{r})}{|\vec{r} - \vec{R}_I|} d\vec{r} = \int v_{ext}(\vec{r}) \rho(\vec{r}) d\vec{r} \quad (2.40)$$

and the exchange-correlation energy E_{XC} , that incorporates all unknown contributions. Formally, the exchange energy is made up from the difference of the classical electronic energy to the full electron electron interaction energy and the difference between non-interacting and interacting kinetic energy:

$$E_{XC}[\rho] = (T[\rho] - T_S[\rho]) + (E_{ee}[\rho] - J[\rho]) \quad (2.41)$$

Rewriting the energy in Kohn-Sham orbitals and minimizing under the constraint of orthonormal orbitals yields (30)

2. THEORY

$$\left(-\frac{1}{2}\nabla^2 \left[\int \frac{\rho(\vec{r}_2)}{r_{12}} + V_{XC}(\vec{r}_1) - \sum_{I=1}^M \frac{Z_I}{r_{1I}} \right] \right) \varphi_i \quad (2.42)$$

$$= \left(-\frac{1}{2}\nabla^2 + V_{eff}(\vec{r}_1) \right) \varphi_i = \epsilon_i \varphi_i \quad (2.43)$$

By comparing with the reformulation at the beginning of this chapter, we can see that V_{eff} is equivalent to V_S :

$$V_S(\vec{r}) = V_{eff}(\vec{r}) = \int \frac{\rho(\vec{r}_2)}{r_{12}} + V_{XC}(\vec{r}_1) - \sum_{I=1}^M \frac{Z_I}{r_{1I}} \quad (2.44)$$

If we know the contributions in V_S , we can insert into the one-particle equations and calculate the orbitals and ground state density and energy. Since V_S also depends on the density, the equations must be solved in an iterative approach.

Exchange-Correlation Functionals

While DFT is an exact theory, as long as an exact exchange-correlation functional is computed, the popularity of DFT also stems from the fact that efficient, yet accurate approximations for the exchange-correlation functional have been developed.

Local Density Approximation (LDA)

Functionals of the local density approximation type generally only depend on the local electron density $\rho(\vec{r})$ and assume a uniform electron gas. While this uniform distribution is on the first look very far from the reality of a distribution in a realistic system, this approximation provides good results for a multitude of properties.

$$E_{XC}^{LDA}[\rho] = \int \rho(\vec{r}) \epsilon_{XC}^{unif}(\rho(\vec{r})) d\vec{r} \quad (2.45)$$

with the elemental exchange-correlation energy $\epsilon_{XC}^{unif}(\rho(\vec{r}))$ of an uniform electron gas. Dividing the exchange-correlation energy into their exchange and correlation parts $\epsilon_{XC}^{unif}(\rho(\vec{r})) = \epsilon_X^{unif}(\rho(\vec{r})) + \epsilon_C^{unif}(\rho(\vec{r}))$, the exchange part of the energy can be exactly calculated as

$$\epsilon_X^{unif}(\rho(\vec{r})) = -\frac{3}{4} \left(\frac{3\rho(\vec{r})}{\pi} \right)^{3/2} \quad (2.46)$$

For the correlation energy there is no exact solution. It can, however, be estimated with high accuracy by other methods.

Generalized Gradient Approximation (GGA)

GGA functionals also take the gradient of the electronic charge distribution into account. Compared to local density functionals, the generalized gradient approximation takes better into account density inhomogeneities. This leads to an improvement in calculated total energies, atomization energies, energy barriers and structural energy differences.

They can generally be written as

$$E_{XC}^{GGA} = \int f(\rho(\vec{r}), \nabla\rho(\vec{r}))d\vec{r} \quad (2.47)$$

For the function f many different approaches exist, some of them are derived from some physical model, while others are purely empirical. The energy function can again be split into a separate exchange and correlation part. These two parts are often derived and parametrized separately and even mixed from different approaches. They are usually named by combining the abbreviations of the exchange and the correlation functional: some of the most popular GGA functionals are the BLYP(31, 32) (Becke88 exchange and Lee-Yang-Parr correlation), PW91(33) (exchange and correlation from Perdew and Wang), BP86 (Becke88 exchange and Perdew correlation) and , PBE(34) (exchange and correlation from Perdew, Burke and Ernzerhof) functionals.

Hybrid Functionals

Another class of functionals are hybrid functionals. In this type of functional the density distributions purely local contribution in the LDA and GGA exchange-correlation functionals is enhanced by an additional non-local exchange contribution. This contribution is chosen in form of the exact Hartree-Fock exchange. Similar to the GGA functionals, many different combinations of various exchange and correlations have been proposed with again different ratios of HF-exchange mixed in. Some often used functionals include the PBE0(34), B3LYP(35) and IGLO(36) functionals.

2. THEORY

2.3 Response Calculations

Density functional theory (DFT) presented on page 14 has proven itself to be a powerful tool which has been widely used to investigate systems of physical, chemical and biological importance with the structure ranging from single atoms and molecules to condensed phase systems and from crystalline to amorphous structures. Many experimentally observable properties, however, do not depend on the ground state of the system alone, but correspond to a reaction of the system to external influences, resulting in an excitation of the system. The direct computation of excited state properties within the framework of DFT can be achieved using time-dependent DFT. For many spectroscopic observables however, it is possible to use an alternative route for the calculation. These properties then are related to second or third derivatives of the total energy of the system, which can be calculated in a finite-differences approach. This is achieved by minimally modifying, e.g., the atomic positions or external field to retrieve the changes in energy. This method has the advantage of a straightforward implementation, but its results often strongly depend on the chosen parameters of the finite variation.

Another possibility to calculate these spectroscopic properties is the direct perturbative calculation of the systems response to an infinitesimally small external perturbation. In DFT this is achieved within the framework of density functional perturbation theory.

Vibrational properties for example depend on the second derivate of the total energy with respect to the atomic coordinates

$$\mathcal{H} \quad , \quad (2.48)$$

which build the components of the Hessian matrix, whose eigenvalues and eigenvectors are directly connected to the frequencies and modes of the harmonic vibration.

The static polarizability, on the other hand, is the second derivate with respect to an external electric field:

$$\frac{\partial^2 \mathcal{E}_{\text{KS}}}{\partial E_a \partial E_b} \quad . \quad (2.49)$$

For an explicitly time-dependent electric field, such as the field of a laser beam, the polarizability becomes frequency dependent. This frequency dependent polarizability is a necessary input to obtain the van der Waals interaction, which is missing in conventional DFT approaches.

The NMR shielding tensor is related to the energy derivative with respect to the magnetic moment and an external magnetic field:

$$\frac{\partial^2 \mathcal{E}_{\text{KS}}}{\partial m_a \partial B_b} \quad (2.50)$$

In the NMR section 2.3.1, the specific implementation details of this formulation are discussed in detail.

The theoretical concept of DFPT is based on the variational principle applied to a perturbed system. In case of an unperturbed system in its electronic ground state, the variational principle states that the ground state KS-orbitals are those which minimize the KS-energy. In presence of a perturbation, the electronic structure will adjust in such a way that the perturbed energy is again minimized. This property is used to calculate the perturbed states by a variational approach (37, 38, 39).

In the unperturbed ground state, the standard Kohn-Sham functional is given by

$$\mathcal{E}_{\text{KS}}[\{\phi_o\}] = \sum_o f_o \langle \phi_o | -\frac{1}{2} \nabla^2 | \phi_o \rangle + \int (V_{\text{ext}} + V_H)(\mathbf{r}) n(\mathbf{r}) d^3r + \mathcal{E}_{\text{xc}}[n] \quad (2.51)$$

where the sum is over the N doubly ($f_o = 2$) occupied states with $o \in \{1, \dots, N\}$ and the electronic density is given by

$$n(\mathbf{r}) = \sum_o f_o |\phi_o(\mathbf{r})|^2. \quad (2.52)$$

In presence of a small perturbation, the response of any property represented by an observable X can be obtained in general arbitrary order by a perturbative expansion around its unperturbed value $X^{(0)}$ according to

$$X = \sum_n \lambda^n X^{(n)}, \quad (2.53)$$

with

$$X^{(n)} = \frac{1}{n!} \frac{d^n X}{d\lambda^n}. \quad (2.54)$$

Common quantities for X are the energy E , the KS-orbitals $|\phi_o\rangle$, or the density n . The perturbation parameter λ is an infinitesimally small auxiliary variable which helps to

2. THEORY

separate different orders of the response with respect to the perturbation and do not occur in the final expressions.

The presence of the perturbation is represented by an additional linearized energy term in the total energy functional

$$\mathcal{E}^{tot}[\{\phi_o\}] = \mathcal{E}^{KS}[\{\phi_o\}] + \lambda \mathcal{E}^{pert}[\{\phi_o\}] \quad , \quad (2.55)$$

with the ensemble of occupied KS orbitals $\{\phi_o\}$ which represent a single-determinant wave function.

In principle, this equation can be solved for a finite perturbation strength λ with the standard ground state variational approach. The results of this finite-difference approach, however, show dependencies on the choice of the perturbation strength, and possibly induced symmetry breaking increase the computational costs.

Instead, the more common alternative route is an analytical separation of the different orders of the perturbation and their explicit calculation via DFPT. In case of a variational approach (40), the total energy in presence of the perturbation is minimized by varying the electronic states. Its explicit expansion is given as

$$\mathcal{E}^{tot} = \mathcal{E}^{tot}[\{\phi_o^{(0)} + \lambda \phi_o^{(1)} + \dots\}] \quad (2.56)$$

$$= \mathcal{E}^{(0)} + \lambda \mathcal{E}^{(1)} + \lambda^2 \mathcal{E}^{(2)} + \mathcal{O}(\lambda^3) \quad (2.57)$$

Due to the variational property of the ground state energy, the true ground state orbitals minimize the unperturbed functional. By stationarity the linear order energy always vanishes. The first non-vanishing term is thus the second order energy. At the extremal point, this gives the following stationarity condition

$$\frac{\delta \mathcal{E}^{tot}}{\delta \phi_o^{(1)}} = 0 \quad (2.58)$$

The variation of the electronic states is supplemented by additional constraints in order to maintain the orthonormality of the total states. A particular convenient choice is the orthogonalization of the $\{\phi^{(1)}\}$ manifold with respect to the $\{\phi^{(0)}\}$ manifold by using the parallel-transport gauge

$$\langle \phi_o^{(1)} | \phi_{o'}^{(0)} \rangle = 0 \quad , \quad \forall o, o'. \quad (2.59)$$

In this parallel-transport gauge (38, 40), the second order term in the functional expansion of the total energy is given by

$$\begin{aligned} \mathcal{E}^{(2)} &= \sum_o f_o \left[\langle \phi_o^{(1)} | \mathcal{H}_{KS}^{(0)} - \epsilon_o^{(0)} | \phi_o^{(1)} \rangle \right] + \frac{1}{2} \iint d^3r d^3r' K(\mathbf{r}, \mathbf{r}') n^{(1)}(\mathbf{r}) n^{(1)}(\mathbf{r}') \\ &+ \sum_o f_o \left[\langle \phi_o^{(1)} | \frac{\delta \mathcal{E}^{pert}}{\delta \langle \phi_o^{(0)} |} + \frac{\delta \mathcal{E}^{pert}}{\delta | \phi_o^{(0)} \rangle} | \phi_o^{(1)} \rangle \right], \end{aligned} \quad (2.60)$$

with the Hartree-exchange-correlation kernel, the KS-Hamiltonian and its eigenvalues given by

$$K(\mathbf{r}, \mathbf{r}') = \frac{\delta(\mathcal{E}_H + \mathcal{E}_{xc})}{\delta n(\mathbf{r}) \delta n(\mathbf{r}')} \quad (2.61)$$

$$\mathcal{H}_{KS}^{(0)} = -\frac{1}{2} \nabla^2 + V_{ext} + V_H + V_{xc} \quad (2.62)$$

$$\epsilon_o^{(0)} = \langle \phi_o^{(0)} | \mathcal{H}_{KS}^{(0)} | \phi_o^{(0)} \rangle \quad (2.63)$$

The corresponding Lagrangian for the minimization then is

$$\mathcal{L}^{(2)} = -\mathcal{E}^{(2)} + \sum_{oo'} \langle \phi_o^{(1)} | \phi_{o'}^{(0)} \rangle \Lambda_{o'o}^{(1)}. \quad (2.64)$$

The Lagrange multipliers $\Lambda_{o'o}^{(1)}$ ensure that the orthogonality according to eq. (2.59) is actually imposed during the minimization cycles. Their explicit values can be derived analytically and are related to the mixed expectation values of $\mathcal{H}_{KS}^{(0)}$ between the unperturbed and the perturbed orbitals. For details see the original papers (40).

The resulting Sternheimer equation is an inhomogeneous system of equations

$$-P_e (\mathcal{H}_{KS}^{(0)} - \epsilon_o^{(0)}) P_e | \phi_o^{(1)} \rangle = P_e \left[\int d^3r' K(\mathbf{r}, \mathbf{r}') n^{(1)}(\mathbf{r}') | \phi_o^{(0)} \rangle + \frac{\delta \mathcal{E}_{KS}^{pert}}{\delta \langle \phi_o^{(0)} |} \right]. \quad (2.65)$$

where $P_e = \sum_o 1 - | \phi_o \rangle \langle \phi_o |$ is a projection operator on the empty orbitals. This equation is usually solved self-consistently by linear algebra algorithms as, e.g., the conjugated-gradient minimization.

With this result it is possible to calculate the response properties for various perturbations such as nuclear displacements or electronic and magnetic fields. In the following it will be applied to the calculation of NMR chemical shifts, which requires the calculation with a perturbation due to an external magnetic field.

2. THEORY

2.3.1 NMR via DFPT

Nuclear magnetic resonance spectroscopy (NMR) is a widely used experimental tool to analyze various structural and dynamic properties of molecular, as well as, solid state systems, ranging from simple liquids, amorphous and crystalline solids to complex macromolecules of biological relevance. (41, 42)

The NMR chemical shifts depend on the local chemical environment of the nuclei and are therefore intrinsically connected to the local electronic structure. Formally, the nuclear spin $\boldsymbol{\mu}_I$ interacts with the external magnetic field via

$$E = -\boldsymbol{\mu}_I \cdot \mathbf{B}^{tot} = -\gamma m \hbar B^{tot} \quad , \quad (2.66)$$

with the gyromagnetic ratio γ . This leads to an energy splitting of degenerate spin $m = \pm \frac{1}{2}$ energies of

$$\Delta E = -\gamma \hbar B^{tot} \quad . \quad (2.67)$$

The total magnetic field is given by

$$\mathbf{B}^{tot}(\mathbf{r}) = \mathbf{B}^{ext} + \mathbf{B}^{ind}(\mathbf{r}) \quad , \quad (2.68)$$

where \mathbf{B}^{ext} is the applied external field and $\mathbf{B}^{ind}(\mathbf{r})$ the induced field modifying the total field acting on the nucleus.

In the linear regime, the induced field $\mathbf{B}^{ind}(\mathbf{r})$ is proportional to the external field; the negative proportionality coefficient is called nuclear shielding:

$$\sigma_{\alpha\beta}(\mathbf{r}) = -\frac{\partial B_{\alpha}^{ind}(\mathbf{r})}{\partial B_{\beta}^{ext}} \quad . \quad (2.69)$$

The external magnetic field does not directly enter the electronic Hamiltonian. Instead, the underlying vector potential $\mathbf{A}(\mathbf{r})$ is used. These are related via

$$\mathbf{B}^{ext}(\mathbf{r}) = \nabla \times \mathbf{A}(\mathbf{r}) \quad . \quad (2.70)$$

The presence of an infinitesimally small external magnetic field \mathbf{B}^{ext} is then included in the electronic Hamiltonian by replacing the kinetic momentum by its canonical equivalent $\mathbf{p} \rightarrow \boldsymbol{\pi}$,

$$\boldsymbol{\pi} = \mathbf{p}^{kin} - e\mathbf{A} \quad . \quad (2.71)$$

This gives rise to the following first-order perturbation Hamiltonian (in atomic units)

$$\mathcal{H}^{(1)} = -\mathbf{p} \cdot \mathbf{A}(\mathbf{r}) = -\mathbf{A}(\mathbf{r}) \cdot \mathbf{p} \quad , \quad (2.72)$$

since in the Coulomb gauge, the vector potential of a homogeneous magnetic field is then given by

$$\mathbf{A}(\mathbf{r}) = -\frac{1}{2}\mathbf{r} \times \mathbf{B}^{ext} \quad , \quad (2.73)$$

and thus commutes with \mathbf{p} . The choice of the gauge origin should in general not affect the physical observables of a system. This gauge invariance, however, is not trivially guaranteed in numerical computations. The effects of finite basis sets or non-local pseudopotentials introduce origin dependencies which require further corrections. To address these issues, a variety of methods have been developed, as to mention the IGLO (36, 43), GIAO (44) and CSGT gauge.

In periodic systems it is not possible to define the vector potential of a homogeneous magnetic field \mathbf{B} . This is due to the ill-definition of the position operator. Also here, various methods have been developed for the calculation of NMR-shifts in extended systems (45, 46, 47, 48, 49, 50, 51).

For finite closed-shell systems, the above definition can be applied and the corresponding first order perturbation functional is then given as

$$\lambda \mathcal{E}^{pert} = \sum_o f_o \langle \phi_o | \mathbf{p} \cdot \mathbf{A}(\mathbf{r}) | \phi_o \rangle \quad (2.74)$$

$$= - \sum_o f_o \langle \phi_o | \mathbf{p} \cdot \frac{1}{2} \mathbf{r} \times \mathbf{B}^{ext} | \phi_o \rangle \quad (2.75)$$

$$= + \sum_o f_o \langle \phi_o | \frac{1}{2} \mathbf{r} \times \mathbf{p} | \phi_o \rangle \cdot \mathbf{B}^{ext}. \quad (2.76)$$

In the last step, a cyclic permutation of the triple product has been used which is possible since $p_i r_j$ commute for $i \neq j$.

The remaining dependence of the perturbation on the magnetic field strength is compensated by the λ on the left side of the equation, i.e., the magnetic field plays the role of the perturbation parameter. Therefore, effectively three different perturbations for each component are necessary.

The nature of this particular perturbation simplifies the calculation of the perturbed states. Since $\mathbf{r} \times \mathbf{p}$ is Hermitian and purely imaginary in the position representation,

2. THEORY

the perturbation KS-Hamiltonian and the linear order KS-orbitals are purely imaginary (45)

$$\langle \mathbf{r} | \mathcal{H}^{(1)} | \mathbf{r}' \rangle = \frac{i}{2} \delta(\mathbf{r} - \mathbf{r}') (\mathbf{r} - \mathbf{R}) \times \mathbf{B} \cdot \nabla \quad (2.77)$$

Therefore, the linear order density response vanishes analytically

$$n^{(1)}(\mathbf{r}) = \sum_o f_o \left[\phi_o^{(0)*}(\mathbf{r}) \phi_o^{(1)}(\mathbf{r}) + \phi_o^{(1)*}(\mathbf{r}) \phi_o^{(0)}(\mathbf{r}) \right] = 0 \quad \forall \mathbf{r}. \quad (2.78)$$

This is the expected behavior, since magnetic fields should not change the density related physical observables.

In the Sternheimer equation for this perturbation, the dependency on the perturbed density therefore vanishes and no self-consistent solution is required

$$-P_e (\mathcal{H}_{KS}^{(0)} - \epsilon_o^{(0)}) P_e |\phi_o^{\mathbf{B}}\rangle = P_e \mathbf{r} \times \mathbf{p} |\phi_o^{(0)}\rangle. \quad (2.79)$$

The \mathbf{B} superscript is a useful shorthand notation for a partial derivative with respect to the \mathbf{B} field and indicates the vector nature of the response

$$|\phi_o^{\mathbf{B}}\rangle = \frac{\partial |\phi_o\rangle}{\partial \mathbf{B}} \quad (2.80)$$

$$|\phi_o^{(1)}\rangle = |\phi_o^{\mathbf{B}}\rangle \cdot \mathbf{B} \quad (2.81)$$

For each of the three perturbation components it is possible to calculate the induced electronic flow

$$\mathbf{j}(\mathbf{r}) = \frac{1}{2} \sum_o f_o [\phi_o^{(1)*} \nabla \phi_o^{(0)} + \phi_o^{(0)*} \nabla \phi_o^{(1)}](\mathbf{r}) + n(\mathbf{r}) \mathbf{A}(\mathbf{r}) \quad (2.82)$$

The induced magnetic field then is readily obtained by applying the law of Biot-Savart

$$\mathbf{B}^{ind}(\mathbf{r}) = \int d^3 r' \frac{\mathbf{r}' - \mathbf{r}}{|\mathbf{r}' - \mathbf{r}|^3} \times \mathbf{j}(\mathbf{r}') \quad (2.83)$$

The shielding tensor then is given by analytically taking the derivative with respect to the external magnetic field \mathbf{B}^{ext} .

$$\sigma_{\alpha\beta}(\mathbf{r}) = -\frac{\partial B_{\alpha}^{ind}(\mathbf{r})}{\partial B_{\beta}^{ext}} \quad (2.84)$$

This final derivative is necessary in order to obtain a result which is independent of the perturbation parameter.

3

Overview of Papers

3.1 Effects of Different Philicity on the Properties of (Bio-) Solvents and Solutes

Solvent effects and interactions of molecules with different philicity play a crucial role not only in biological systems but also technological and medical applications. In biological systems they are the forces that lead e.g. to membrane formation, where the lipophilic phospholipid tail builds the inner part, avoiding the energetically less favorable interaction with water, while exposing the hydrophilic head groups.

Systems with molecule-specific attractive interactions could be used for steered demixing of solvents, e.g. for purification or de-salting. In pharmacological and medical fields, applications reach from the design of drugs with their interactions tailored to e.g. fit and block active centers to the design of transport mechanisms for drug delivery.

In nanoporous systems surface effects influence solvents at the host material interface get even more strongly, in an effect called 'confinement', as with pore diameters of only a few nanometers the solvent 'feels' the surface effects more strongly, leading to changes in the guest molecules properties, influencing the microstructure, folding characteristics in proteins, mixing behavior in mixtures and many other effects.

In this thesis, a solvated chromophore of the biliprotein phycocyanin and its interactions with its surroundings has been investigated. This is on the one hand the simplest system considered here, with only a single molecule in a pure (i.e. no mixture) solution. The flexibility and size of the solute, however presents a challenge in both, simulation size and needed sampling. In a project focusing more on the fundamental

3. OVERVIEW OF PAPERS

understanding of the effect of confinement on the confined substances, solvents confined in different matrices on the nanometer scale have been investigated. The model systems included water and water - alcohol mixtures confined in rigid silica pores, water in a more flexible, biologically relevant cellulose confinement as well as aromatic carbon confinements. An even stronger focus on the influence of different and counter-acting philicities existed in the last project, the integration of specifically synthesized polyphilic transmembrane molecules into DPPC membranes.

In the following the published papers are briefly summarized. The papers themselves can be found in Chapter 4.

3.1.1 Solvent Induced Conformational Switching in Phycocyanobilin

The chromophore phycocyanobilin (PCB) can be found in various photoproteins in plants, fungi and bacteria. The properties of these and other chromophores crucially depend on the interaction with the immediate surrounding, e.g. by hydrogen bonds. Previous studies(52, 53, 54, 55, 56, 57, 58) showed e.g. a strong dependence of the quantum yield during excitation on the shape of the binding pocket. Similarly, the color can be tuned by the protein surrounding, enabling e.g. bacteria to absorb light over a wide range of the sunlights spectrum.

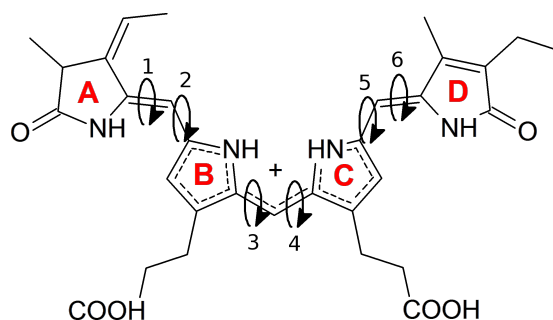


Figure 3.1: The structure of the chromophore phycocyanobilin with its four pyrrole rings and the six screened dihedral angles

In a protein binding pocket, the conformational freedom of the PCB is highly limited. When looking at the isolated chromophore, however, the four pyrrole rings can rotate freely. In experiments by Roben et al.(59), the isolated chromophore has been investigated by means of 2D NMR spectra (1H ^{15}N NOESY) of each pyrrole rings amino

3.1 Effects of Different Philicity on the Properties of (Bio-) Solvents and Solutes

group. The spectra show a strong shift upon changing the solvent from methanol to HMPT, hinting at a conformational change in the chromophore.

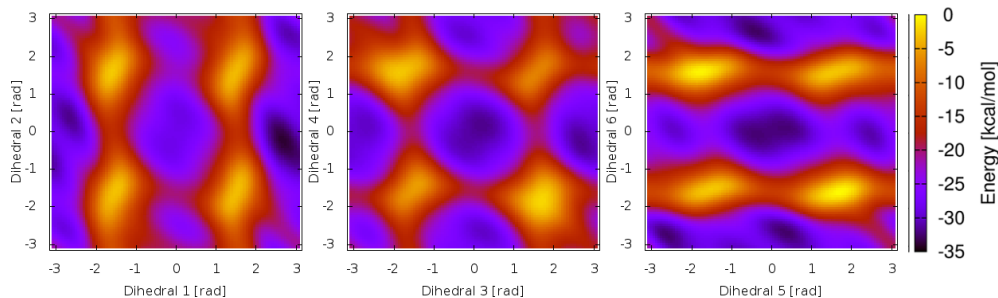


Figure 3.2: Energy surface for the three dihedral pairs. Minima for the planar conformations are clearly visible.

Since we assume a changed geometry of the chromophore to be the main reason for the change in the observed NMR fingerprints, we needed to sample the conformational degrees of freedom of the PCB molecule. The system can then be described in terms of the 3 dihedral angle pairs connecting the rings A to D. Since the computational effort to sample this six-dimensional conformational space with either a straight molecular dynamics approach or a full screening of all dihedral angles with single-point NMR calculations would be unreasonably high due to the high energy barriers or the number of calculations needed, we first performed two-dimensional metadynamics(60, 61) simulations of the dihedral pairs.

The free energy surface obtained by the metadynamics simulations show a (local) minimization of the energy for the different planar conformations. While for the dihedral angles to the outer rings A and D differences between the minimal energies can be seen, almost identical energies are found for the central dihedral angles. Due to this similarity in energy, small changes in the surrounding of the molecule can lead to a new preferred conformation and thus induce a flip around the central bonds.

In combination with ensemble averaged NMR chemical shift calculations(31, 32, 62, 63, 64) and experimental input, we could now identify the main conformations that occur in the two solvents HMPT and methanol. They belong to very different conformations, one with both amino groups of the rings B and C pointing towards each other resembling a helical shape. Opposed to that, in methanol, either of the two central dihedrals is changed by 180 degree, changing the overall shape to a linear one.

3. OVERVIEW OF PAPERS

This effect can be traced back to the different philicity of the solvents: Methanol is hydrophilic, providing hydrogen bonding partners for the amide and carboxyle groups. HMPT on the other hand offers no such interaction, resulting in an energy penalty, if the hydrogen bonds are not saturated. The chromophore can compensate this by changing to a conformation of similar energy, that in turn enables the formation of intramolecular hydrogen bonds.

Concluding, in this chromophore, small changes in the philicity of the surrounding can trigger a strong structural response, that can be observed indirectly via the chromophores NMR fingerprints.

3.1.2 Solvents in Confinement

In confinement, a solvent is confined on length scales in the nanometer range. This confinement leads to very strong modifications of the solvents by both the geometric confinement as well as the interactions with the confining material. Geometric constraints can lower the dimensionality of the system, by confining it in one (slab), two (pore) or three (dot) dimensions.

The investigations have been performed under the scope of the research group FOR 1583; here, confinements have been synthesized and the behavior of solvents in different confinements has been investigated experimentally and theoretically. The publications in this section focus on systems using one and two dimensional confinement in mesoporous amorphous silica, aromatic carbon materials and cellulose. The solvents include water and water-alcohol mixtures.

We investigated a small model system using ab-initio molecular dynamics simulations and computed the confined waters H_2 NMR fingerprint, showing a characteristic shift in proximity of the silica wall.

Larger classical molecular dynamics simulations were performed to assess the structural and dynamical characteristics of a water-ethanol mixture confined in silica slabs, as well as water confined in a "softer" cellulose confinement.

Water in Silica Confinement

In hydrophilic, mesoporous silica pores, the properties of water are strongly modified. Experimentally, a strongly lowered freezing point is observed, the diffusion properties

3.1 Effects of Different Philicity on the Properties of (Bio-) Solvents and Solutes

as well as spectroscopic fingerprints are modified by the interaction with the confining material as well as the geometric confinement.

1H NMR experiments show only a small change in the proton NMR chemical shifts for completely filled silica nanopores. When investigating partially filled pores, however, a strong change can be observed, hinting to a strongly perturbed hydrogen bonding next to the wall.

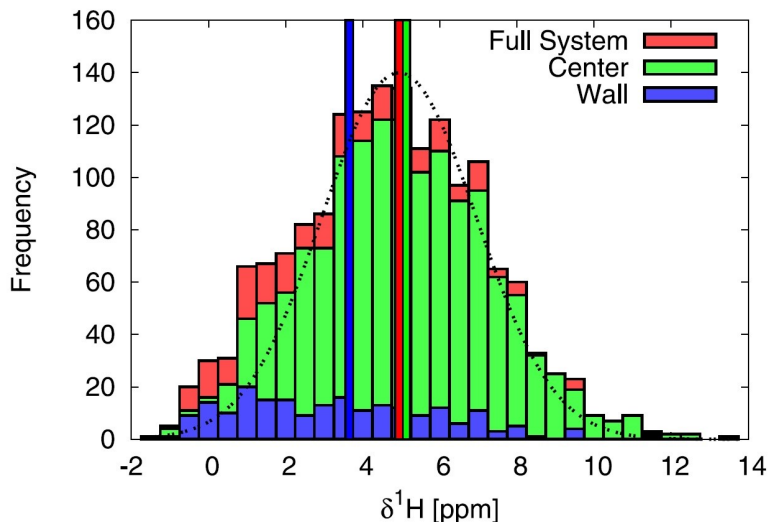


Figure 3.3: Calculated 1H NMR chemical shift values of water within a 3 Å distance to the walls (blue), center of the confinement (green) and the whole system (red)

We performed ab-initio molecular dynamics simulations of a simplified silica confinement. The surface contained of silicid acid groups with a density tuned to match the hydroxy group density in MCM-41 nano-pores. The amorphous silica walls have been modeled by a repelling potential acting on the confined water molecules.

The density profile of the confined water shows three pronounced solvation layers at the walls, until the density approaches bulk behavior towards the center. The influence of the confinement also shows in a visible reduction of the diffusion by a factor of 3.

Our 1H NMR chemical shift calculations show a structure inverse to that of the water density: in the three solvation layers a decreased chemical shift is found at zones of increased water density and vice versa. In the center, higher shifts than in bulk water can be observed, while within 2 Å of the wall, the shift starts to quickly drop towards zero.

3. OVERVIEW OF PAPERS

Our results nicely explain the experimental results on filled as well as partially filled pores. Our minimalistic model covers both the structural and dynamical changes the confined water experiences. This sets the stage to investigate larger confinements as well as more complex solvents such as mixtures and bio-molecules.

Water-Alcohol Mixtures – Demixing

After understanding the behavior of a single solvent in a hydrophilic confinement, the next logical step is to move to more complex solvent mixtures. In the following simulation we chose to use a binary mixture of two different hydrophilic solvents: Ethanol and water.

When we analyze the properties of the mixture without differentiating between the two solvent molecule types we see the typical behavior of a hydrophilic solvent in a hydrophilic confinement: the density profile shows solvation layers at the surface, while further away from the walls bulk-like behavior can be observed.

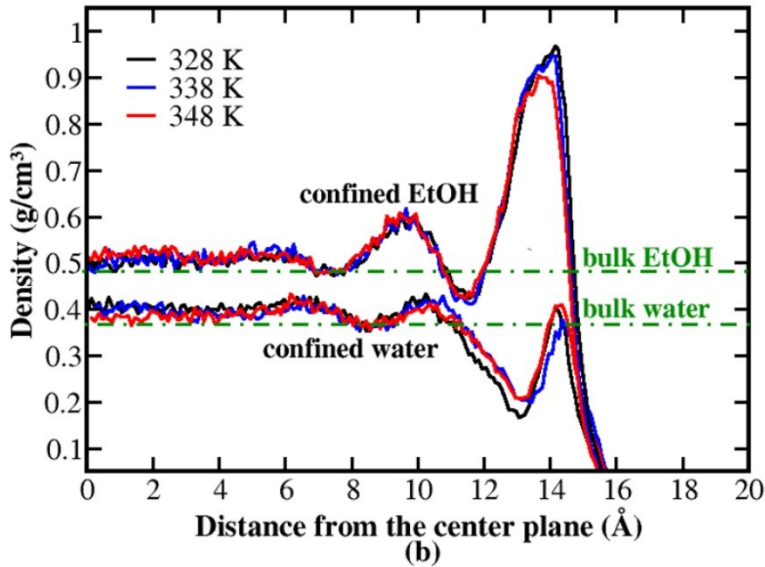


Figure 3.4: Profile of the partial densities of ethanol and water in the confinement with the wall located at 16 Å

This picture gets more interesting, once we examine the partial densities of the two solvents. For each individual solvent we again see a modulation of the density next to the wall resembling the different solvation layers of the wall. In close proximity to

3.1 Effects of Different Polarity on the Properties of (Bio-) Solvents and Solutes

the wall, however, a strongly reduced peak can be observed for the water molecules, leading to a partial demixing at the silanol surface.

The confinement also has a crucial effect on the solvent hydrogen bond network, leading to a strong influence on the orientation of OH groups of ethanol. In proximity to the silanol surface, they point toward the wall, while at the center region no such preference can be found.

Yet another effect can be found in the mixture, that has already been found experimentally in non-confined mixtures: also in the bulk region clustering of the water molecules can be seen through the radial distribution functions. This leads to an enhanced hydrogen bond network among the water molecules when compared to an even distribution of the two types of molecules, leading to an energetic advantage.

Water in Amorphous Carbon

In the scope of our investigations on confined water, we also investigated mesoporous amorphous carbon. This class of material possesses a wide range of morphologies and is used in the industry for adsorption, separation and catalysis. Here the material was synthesized employing polymers and silica gels as structure directing templates. The microscopic structure of this material also depends strongly on the carbonization temperature when creating the different systems. Our collaborators Buntkowsky et al. synthesized carbon materials C600 and C800 at different carbonization temperatures(65) of 600 and 800 degrees Celsius respectively. They performed 1H NMR chemical shift measurements on water confined in the nano-pores at different filling percentages. The resulting chemical shifts indicate a high aromaticity of the amorphous carbon especially in the C800 material.

To gain insight into the cause of change in chemical shifts, we performed ab-initio NMR calculations, more specifically we calculated NICS maps(66), i.e. nucleus independent chemical shift maps. While NMR experiments require probe molecules (e.g. 1H), calculations can obtain the chemical shielding at every point in space and calculate the chemical shift by referencing that value to a known one. As a result, we can easily visualize the spacial distribution in two dimensional slices of the investigated system.

Our calculations support the effects of different carbonization temperatures on the aromaticity of the resulting porous structure. The C600 material is slightly aromatic, showing slightly changed chemical shieldings for water at the surface, while the C800

3. OVERVIEW OF PAPERS

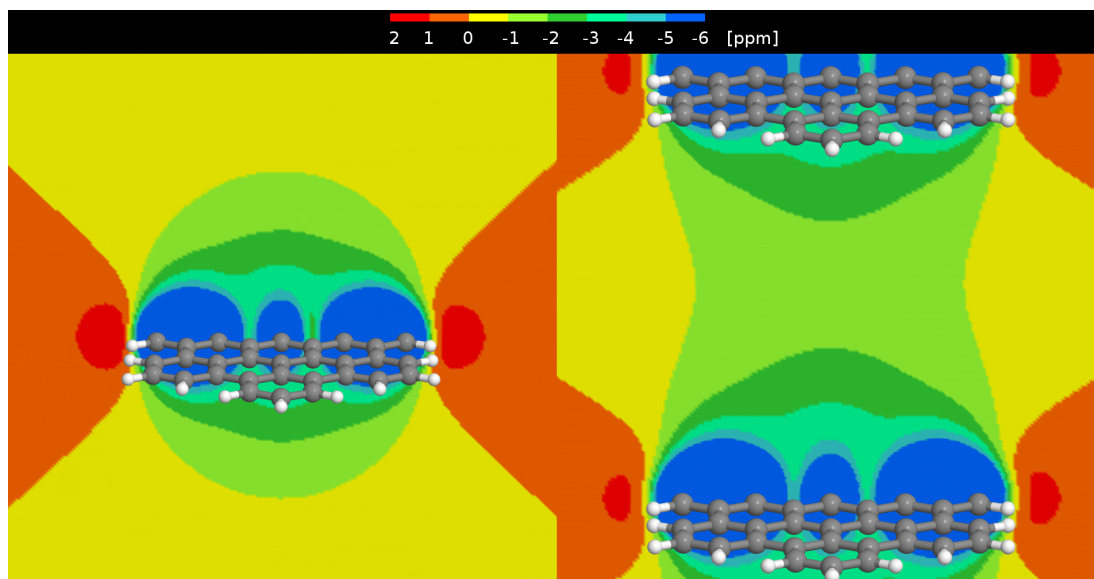


Figure 3.5: ^1H NICS maps in the proximity of hexabenzocoronene. Left: a single molecule. Right: a periodic stack with an intermolecular distance of 15 Å

material shows a much stronger change in chemical shieldings that can only be explained by a strongly aromatic guest material with strong π - π -stacking.

Water in a Soft Cellulose Confinement

Crystalline cellulose(67), a crystal made from infinite chains of cellobiose, i.e. 1-4 β -linked D-glucose monomers, makes for another interesting candidate for a confinement material(68, 69). We use cellulose as a confinement for water slabs. We created two different hydrophilic confinement structures built from slabs of a cellulose I β crystal. The hydrophilic surfaces are created by cutting the cellulose crystal along different symmetry axes. In one system, the zigzag-shaped 111 surface is exposed to the solvent, while in the other one the smoother 110 surface is used.

In contrast to the extremely rigid silica and carbon confinements, the cellulose surface is a "softer" confinement. The surface layers of the crystalline cellulose structure offer a higher mobility, while they can also be partially penetrated by water molecules.

The two different surface structures influence the confined water very differently. While the smooth 110 surface shows only a weak interaction through hydrogen bonds, the 111 surface exhibits a stronger hydrogen bonding network with the interface water.

3.1 Effects of Different Philicity on the Properties of (Bio-) Solvents and Solutes

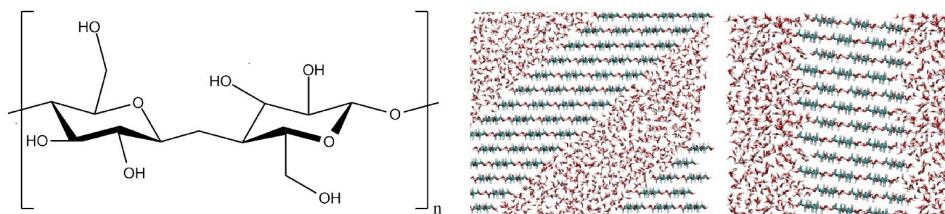


Figure 3.6: Left: Structure of the cellulose polymer. Right: Two confinements built from cutting a cellulose crystal along different axes.

This leads to the structuring of the surface water we already observed in the hydrophilic silica confinements. Similarly, the rotational freedom of the water is reduced and the diffusion is slowed down considerably.

3.1.3 Polyphilic Molecules in Membranes

We investigate the interplay of newly synthesized transmembrane molecules(70, 71, 72) with membranes. Membranes are an extremely important and highly complex building block of all living organisms. Finding new ways of modifying their structure(73, 74) or passing through them may enable the development of new approaches e.g. for targeted drug delivery(75).

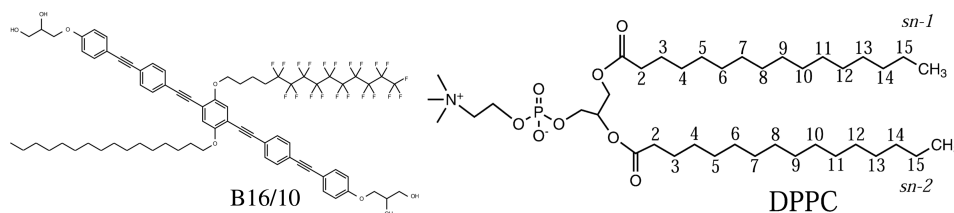


Figure 3.7: Left: The molecular structure of the polyphilic trans-membrane molecule B16/10. Right: Molecular structure of a dipalmitoylphosphatidylcholin (DPPC) molecule.

These transmembrane molecules are so-called polyphilic molecules(76, 77, 78, 79, 80): They combine an aromatic core and two hydrophilic headgroups with two side-chains at the center of the core. Here, lipophilic alkyl chains and fluorophilic perfluoroalkanes can be attached. The structure is built in such a way, that the headgroups are in contact with the water outside the membrane, and the side-chains interact with the inner part of the membrane. This provides an exciting new way of modifying the

3. OVERVIEW OF PAPERS

properties of the membrane directly at its core.

Parametrization of Fluorocarbon Compounds

As our goal is to simulate newly synthesized polyphilic molecules in a membrane environment by means of classical molecular dynamics simulations, new parameters needed to be derived. We chose the widely used CHARMM force field to perform simulations of our model membrane systems(81) with. Since there were no previous parameters for fluorinated compounds, a natural starting point was the parametrization of fluoroalkanes with arbitrary length. In our investigations, we followed parametrization procedures described for the CGenFF(82), that is also applicable to the CHARMM force field, as it used the same energy functional.

In this parametrization procedure all parameters for bond lengths, angles and torsional profiles are optimized in comparison to MP2/6-32G(d)S calculations. The partial charges are found by placing water molecules at the interaction sites and optimizing the interaction energies.

Finally, the Lennard-Jones parameters are optimized against liquid densities of the pure compounds. This optimization cycle is repeated until self-consistency of the parameters is reached.

The newly derived parameters were then tested by performing a broad range of simulations comparing the miscibility with alkanes, and thermodynamic properties (heat of vaporization, heat capacity, thermal expansion coefficient, static dielectric constant, and viscosity) with experimental results.

(Semi-)Perfluoroalkanes in a DPPC Model Membrane

With our previously derived and tested parameters for fluorinated alkanes, we now were able to perform simulations of membrane systems with additive molecules.

We investigated a model DPPC bilayer membrane with an added non-, semi- and perfluorinated alkanes as well as a fluorotelomer by means of molecular dynamics simulations. In the temporal evolution of the system, two different behaviors can immediately be seen for the fluorinated and non- and semi-fluorinated alkanes. For the non-fluorinated alkanes, the area per lipid stays roughly constant, while for the perfluorinated alkanes and the fluorotelomer, the area per lipid drops to a lower value

3.1 Effects of Different Philicity on the Properties of (Bio-) Solvents and Solutes

in the course of the simulation. This behavior is caused by a phase transition in the DPPC bilayer from the liquid crystalline phase into the gel phase.

Other observables calculated from the simulation confirm the changed structure and dynamics caused by the phase transition to the gel phase: The self-diffusion coefficients are reduced for both, DPPC and the additives. The S_{CD} order parameter changes to significantly lower values and the DPPC tails dihedral angles change to values corresponding a more straightened chain and finally, the typical tilting of the DPPC tails in the gel phase can also be observed in the tail vector projections.

The non- and semi-flourinated alkanes, however, show no signs of an induced phase transition. Here, the diffusivity of the DPPC molecules slightly increases with respect to that of a pure bilayer, while the diffusion constant of the additive molecules displays very high values, hinting towards only weak interaction with the membrane.

Further analysis shows the cause of the induced phase transition into gel phase: the non- and semi-flourinated alkanes reside mostly in the center between the leaflets, where they have only a minimal interaction with the membrane molecules. The perflourinated alkane and fluorotelomer, on the other hand, integrate into the membrane leaflets in between the DPPC tails. Due to the stiffness of the flourinated compounds, this can also change the average conformation of the DPPC tails, leading to a straighter orientation and therefore inducing the transition to the gel phase.

A Polyphilic Molecule in a DPPC Model Membrane

Moving to more complex polyphilic molecules, we investigated the previously described, recently synthesized(70, 71, 72) x-shaped polyphilic molecule. While the domain-building properties of the molecule in membranes has been investigated experimentally, not much is known about the behavior of the individual molecules and their sidechains of different philicity. In a first study we placed a single molecule in a DPPC bilayer in transmembrane orientation. We performed four individual molecular dynamics simulations of two different initial conformations in two initial transmembrane orientations each to analyze the structural and dynamical properties.

The polyphilic molecule remains in stable transmembrane orientation throughout the simulations. The molecules phenyl backbone takes a slightly bent shape, with angles to the membrane normal of roughly 15 to 30 (in exceptions 50) degree.

3. OVERVIEW OF PAPERS

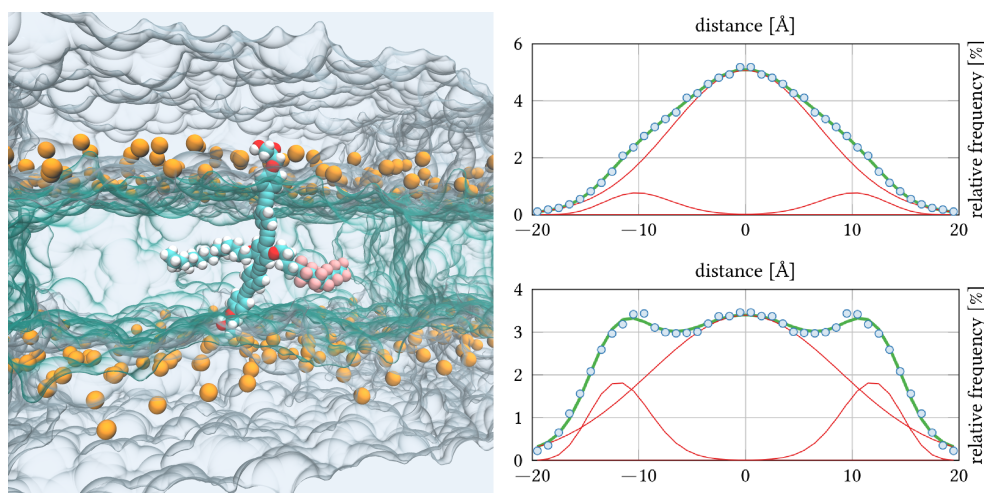


Figure 3.8: Left: The polyphilic trans-membrane molecule embedded in a DPPC bilayer with surrounding water. Right: Probability distribution of the side-chains terminal groups for the non-flourinated (upper graph) and flourinated chain (lower graph).

The two sidechains of different philicity show the most interesting behavior. Both chains tend to be mostly integrated into the leaflets, while for less than one third of the time, the sidechains are located in between the membrane leaflets. The two different types of sidechain behave differently: The perflourinated chain exhibits fewer changes between the two leaflets and has a slightly higher probability to be found integrated into a leaflet than the alkyl sidechain.

The self-diffusion for the lipids is in good agreement with experimental data. Compared to the diffusion coefficient of the lipids, that of the polyphilic molecule is smaller by a factor of about 2. This illustrates that the polyphile is almost as mobile as a regular lipid, despite its twofold anchoring at both lipid-water interfaces and its additional side chains within the membrane.

Small Cluster of Polyphilic Molecules in a DPPC Model Membrane

In fluorescence spectroscopy experiments of the polyphilic transmembrane molecules in membranes domains of polyphile rich and DPPC rich membrane parts can be seen. In a next step towards understanding the formation process of these domains, we performed 1 μ s long molecular dynamics simulations of a DPPC membrane with six x-shaped polyphilic molecules (B16/10) integrated into the bilayer.

3.1 Effects of Different Philicity on the Properties of (Bio-) Solvents and Solutes

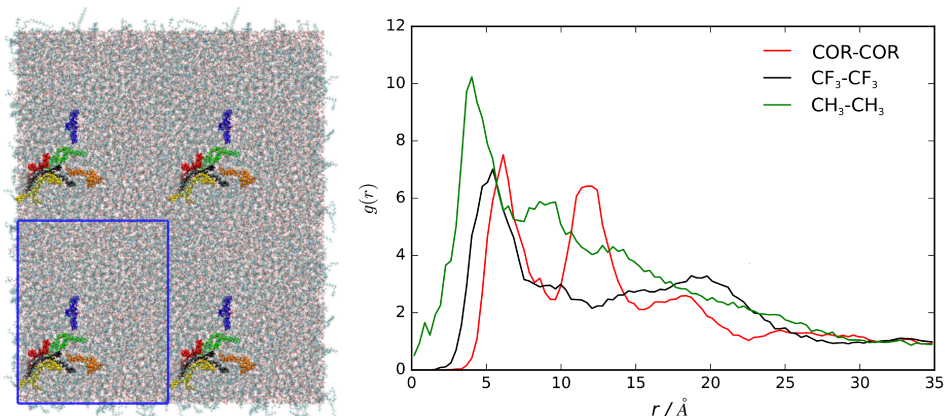


Figure 3.9: Left: A snapshot taken from the simulation. Right: Radial distribution functions for different parts (core, flourinated end group, non-flourinated end group) of the transmembrane molecules.

As a starting point we chose a circular arrangement in a transmembrane configuration. In the course of the simulation, movement of the B16/10 molecules through the membrane can be observed - with phases of separation as well as clustering of the molecules. We can observe a repeated formation of a trimer of polyphiles on a timescale of 100 ns. This clustering can be seen clearly in the core-core radial distribution functions, where two pronounced peaks at 6–7 \AA and 12–13 \AA can be seen. This distance equals roughly the diameter of a single DPPC molecule,

The internal properties of the single transmembrane molecules such as bending angles and side chain integration remains similar to the isolated molecule in a membrane.

The transmembrane molecules exhibit a diffusivity roughly half of the diffusion constant of DPPC molecules in a pure membrane, while the DPPC molecules themselves show a slightly accelerated diffusion constant in the mixed system.

3. OVERVIEW OF PAPERS

4

Publications

First Principles Calculations of NMR Chemical Shifts of Liquid Water at an Amorphous Silica Interface

Xiang Yang Guo, Tobias Watermann, Shane Keane, Christoph Allolio and Daniel Sebastiani

Zeitschrift für Physikalische Chemie International journal of research in physical chemistry and chemical physics, 2012

For this publication I performed parts of the NMR and density calculations and evaluation, contributed to the corresponding sections in the manuscript and was involved in the redaction of the manuscript.

Phycocyanobilin in solution—a solvent triggered molecular switch

Tobias Watermann, Hossam Elgabarty and Daniel Sebastiani

Physical Chemistry Chemical Physics, 2014

In this project I performed the calculations and evaluations of the publication and wrote the manuscript. Hossam Elgabarty performed initial test calculations, contributed to the design of the study and was involved in the redaction of the manuscript.

Water and small organic molecules as probes for geometric confinement in well-ordered mesoporous carbon materials

Yeping Xu, Tobias Watermann, Hans-Heinrich Limbach, Torsten Gutmann, Daniel Sebastiani and Gerd Buntkowsky

Physical Chemistry Chemical Physics, 2014

In this combined experimental and theoretical paper, I prepared, performed and evaluated the calculations and wrote the manuscript sections of the theoretical parts of the paper.

4. PUBLICATIONS

Local Microphase Separation of a Binary Liquid under Nanoscale Confinement

Xiang-Yang Guo, Tobias Watermann and Daniel Sebastiani

The Journal of Physical Chemistry B, **2014**

In this publication I was involved in the system preparation and contributed to the evaluation and the redaction of the manuscript.

Perfluoroalkane Force Field for Lipid Membrane Environments

Guido F. von Rudorff, Tobias Watermann and Daniel Sebastiani

The Journal of Physical Chemistry B, **2014**

I supervised this project and was involved in the project planning and redaction of the manuscript.

Linear Response Methods in Quantum Chemistry

Tobias Watermann, Arne Scherrer and Daniel Sebastiani

Many-Electron Approaches in Physics, Chemistry and Mathematics, **2014**

In this book chapter, I wrote the sections for the van der Waals interactions and applications.

Influence of Small Fluorophilic and Lipophilic Organic Molecules on Dipalmitoylphosphatidylcholine Bilayers

Martin Brehm, Ghulam Saddiq, Tobias Watermann and Daniel Sebastiani

The Journal of Physical Chemistry B, **2017**

I supervised the beginning project and was involved in the project planning and redaction of the first manuscript.

Conformational Space of a Polyphilic Molecule with a Fluorophilic Side Chain Integrated in a DPPC Bilayer

Guido F. von Rudorff, Tobias Watermann, Xiang-Yang Guo and Daniel Sebastiani

Journal of Computational Chemistry, **2017**

I supervised this project and was involved in the project planning and redaction of the initial manuscript as well as the modifications for the resubmission of the manuscript.

Cluster Formation of Polyphilic Molecules Solvated in a DPPC Bilayer

Xiang-Yang Guo, Christopher Peschel, Tobias Watermann, Guido F. von Rudorff and Daniel Sebastiani

Polymers, **2017**

In this project I created the initial system setup and simulation and was involved in the evaluation as well as the redaction of early stages of the manuscript./

Liquid Water Confined in Cellulose with Variable Interfacial Hydrophilicity

Tobias Watermann and Daniel Sebastiani

Zeitschrift für Physikalische Chemie, **2018**

In this project, I performed the system setup, simulations evaluation and wrote the manuscript.



PCCP

PAPER

View Article Online
View Journal | View Issue

Phycocyanobilin in solution – a solvent triggered molecular switch

Tobias Watermann,^a Hossam Elgabarty^b and Daniel Sebastiani^{*a}Cite this: *Phys. Chem. Chem. Phys.*,
2014, 16, 6146Received 11th October 2013,
Accepted 5th February 2014

DOI: 10.1039/c3cp54307b

www.rsc.org/pccp

We present a computational investigation of the conformational response of phycocyanobilin (PCB) to the ability of solvents to form hydrogen bonds. PCB is the chromophore of several proteins in light harvesting complexes. We determine the conformational distributions in different solvents (methanol and hexamethylphosphoramide HMPT) by means of *ab initio* molecular dynamics simulations and characterize them *via ab initio* calculations of NMR chemical shift patterns. The computed trajectories and spectroscopic fingerprints illustrate that the energy landscape is very complex and exhibits various conformations of similar energy. We elucidate the strong influence of the solvent characteristics on the structural and spectroscopic parameters. Specifically, we predict a *cis-trans* isomerization of phycocyanobilin upon switching from the aprotic to the protic solvent, which explains an experimentally observed change in the NMR patterns. In the context of technological molecular recognition, solvent induced conformational switching can be considered a precursor mechanism to the recognition of single molecules.

1 Introduction

Phycocyanobilin (PCB) is an open chain tetrapyrrole chromophore that can be found in the biliproteins allophycocyanin and phycocyanin. Similar open tetrapyrroles can be found in a vast variety of phytochrome photoreceptors as well as in phyco-biliproteins that are found in various plants as well as in different bacteria and fungi. The general function of those photoreceptors is the reaction to light with the goal of collecting energy or triggering further processes in larger biological systems. The process is initialized by isomerization of the chromophore, which then starts the propagation of the absorbed energy toward the photocenter or triggers the systems' structural response to the excitation. While the exact microscopic processes of the latter two steps are still under discussion, the structure of the phytochromes as well as the isomerization process is well documented by different experimental and theoretical investigations. On the experimental side, structural analysis has been performed based on X-ray spectroscopy and neutron scattering experiments. Spectroscopic properties as well as the dynamics during the photocycle have been investigated using various techniques, among them ultrafast mid infrared spectroscopy^{1–3} as well as Raman and NMR^{4–6} spectroscopy. Theoretical investigations have been performed on a wide range of aspects employing various theoretical

approaches ranging from classical molecular dynamics simulations, as well as QM/MM hybrid approaches. Additionally, various theoretical spectroscopic approaches have been used, including Raman,⁷ UV/VIS *via* TDDFT^{8–11} as well as NMR simulations,¹² *i.e.* giving insights into the different chromophore conformations of the single states during the photocycle. In many cases, only the isolated chromophore has been considered, modeling the missing protein structure either by PCM models or ignoring it completely.

In addition to the investigations on the whole protein or photo-system, both experimental and theoretical investigations have also been performed on the isolated chromophore. Naturally, the conformational distribution of the chromophore alone is difficult to assess using diffraction techniques. However, magnetic resonance methods, in particular NMR, are highly sensitive to small changes in structural parameters such as dihedral angles.

The conformational space of a chromophore embedded in the binding pocket of a protein framework is highly restricted. In contrast to that, an isolated chromophore in solution can adopt any configuration, which often leads to an extended distribution of structures. Here, a computational analysis provides a thermodynamically weighted ensemble of geometries from the molecular phase space; this ensemble can subsequently be validated by calculations of spectroscopic observables which can be compared to experimental data.^{13–19}

Previous theoretical investigations on the conformational behavior of isolated similar chromophores have been performed employing Monte Carlo conformational sampling methods²⁰ as well as direct dihedral scanning.²¹

In a recent experimental NMR study on the isolated chromophore, performed by M. Röben *et al.*,²² two fully assigned spectra

^a Institute of Chemistry, Martin Luther University Halle-Wittenberg, Von-Danckelmann-Platz 4, 06120 Halle (Saale), Germany.
E-mail: daniel.sebastiani@chemie.uni-halle.de

^b Institute of Physical Chemistry, Johannes Gutenberg University Mainz, Staudingerweg 9, 55128 Mainz, Germany



of the isolated PCB in two different solvents have been obtained. In both 2D ^1H - ^{15}N spectra, we can observe typical patterns. The B and C rings chemical shifts are in close proximity in both chemical shift directions, while the A and D ring shifts maintain their relative distances of around 1 ppm in the hydrogen and 30 ppm in the nitrogen direction. When changing the solvent from the aprotic HMPT to the protic methanol, a general small downfield shift for the hydrogen chemical shifts can be observed. Additionally, the B and C ring nitrogen chemical shifts are strongly shifted downfield. At the first look, the hydrogen chemical shifts seem to indicate stronger hydrogen bonding for the HMPT solvent, while actually stronger hydrogen bonding can be anticipated for methanol. The nitrogen chemical shifts suggest specific conformational changes, which at the first look also cannot be predicted from a solvent change.

The possible conformational changes as a response to the presence of specific molecules in the direct environment are specific forms of molecular recognition. In our case, it is not a specific key-lock mechanism, but rather a modification of the average hydrogen bonding patterns. Nevertheless, this mechanism can be considered a special variant of molecular recognition.^{23–26}

We investigate the said system by a combination of free energy, molecular dynamics simulations and *ab initio* NMR chemical shift calculations to gain insight into the microscopic origin of these at the first look contradictory findings.

Since the nature of the system allows for a huge variety of different conformations and possible hydrogen bonding patterns, in the first step the underlying energy surface in regard to the characteristic geometric variables of the system has to be explored. In the next step, we will perform molecular dynamics simulations based on the previously identified most important conformations to finally compute ensemble averaged NMR chemical shifts of the chromophore. Using experimental data as the benchmark, we will identify the preferred conformations, molecular structure and hydrogen bonding networks depending on the local surroundings of the chromophore.

2 Computational details

Well tempered 2D metadynamics simulations^{27,28} have been employed using the 3 dihedral pairs (1,2), (3,4) and (5,6). The simulation was based on a DFTB²⁹ approach including dispersion correction. The timestep was set to 0.5 fs. A canonical ensemble has been used, utilizing the canonical velocity rescaling (CSVR) thermostat.³⁰ Gaussian hills with a width of 20 degrees and an initial height of 0.001 Ha have been spawned every 200 timesteps. The temperature of the tempering algorithm was set to 3000 K.

The metadynamics algorithm allows the scanning of collective variables, which is performed by modifying the underlying potential energy while running a molecular dynamics simulation. This modification is achieved by depositing Gaussian hills at regular time intervals. By this, frequently visited regions of the collective variable energy surface are less likely to be visited again in the simulation, energy basins are slowly filled, enabling the molecular dynamics simulation to escape minima and explore

regions of the energy surface that could otherwise not be reached in the limited simulation time and temperature. The energy surface can then be reconstructed from the deposited Gaussians.

For the additional sampling of the various minima found, 75 ps DFTB molecular dynamics simulations with dispersion correction³¹ have been performed with a timestep of 0.5 fs and employing a canonical ensemble using the Nosé–Hoover³² thermostat. The same settings have been used for the calculations including the explicit solvent molecules. Here 212 methanol molecules have been added in a fully periodic system with a box size of 25 Å.

We employed a combined gaussian plane wave method (GPW)³³ using the BLYP functional^{34,35} with additional van der Waals dispersion³⁶ for performing the *ab initio* molecular dynamics simulations, in order to incorporate hydrogen bonding effects as accurately as possible. We used a time step of 0.4 fs for the integration of the equations of motion, in combination with a Nosé–Hoover thermostat. All MD and metadynamics simulations have been performed using the CP2K program package.

QM/MM molecular dynamics simulations have been performed on two selected conformations, based on a BLYP/ForceField mixed approach. The coupling of the two regions has been done within the gaussian expansion of the electrostatic potential (GEEP).³⁷

NMR chemical shift averages have been calculated based on regular snapshots (50 snapshots per trajectory) from the molecular dynamics simulations. All calculations have been performed using the ORCA program³⁸ within the IGLO approach.³⁹ The PBE0⁴⁰ functional as well as the optimized IGLO-III⁴¹ basis set have been used. For the explicit solvent calculations, solvent molecules residing within 3 Å of the chromophore have been considered.

3 Results and discussion

3.1 Free energy surface and preferred conformations

The overall structure of phycocyanobilin can be described by means of the dihedral pairs connecting the four pyrrole rings A to D (see Fig. 1). The determination of the equilibrium conformation for a given surrounding solvent thus requires a careful sampling of this conformational space. Since the energy barriers of the partly double bonded and possibly conjugated electronic

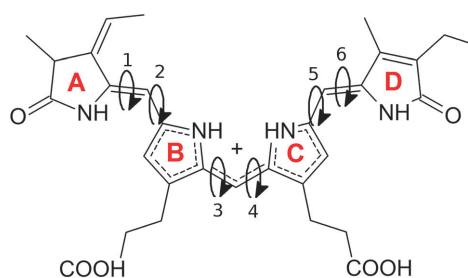


Fig. 1 Structure of the fully protonated (charge +1) phycocyanobilin with the 4 pyrrole rings labeled A to D, connected by 6 dihedrals labeled 1 to 6. The conformation is described by the three double (*cis/trans*) and three single (*syn/anti*) bonds between the pyrrole rings.



systems are considerable, the molecule will cross them only rarely. Hence, the application of straight molecular dynamics simulations would result in an insufficient sampling or even in stable conformations for the entire simulation. A wealth of methods has been developed to overcome such sampling problems, and have proven to effectively escape local minima. Among them are the parallel tempering algorithm,⁴² transition path sampling,^{43,44} various basin hopping methods,^{45–47} minima hopping^{48,49} and different tabu search based strategies.^{50,51} Other algorithms have been inspired from selective mechanisms found in nature, such as artificial bee colony algorithms,^{52–54} evolutionary algorithms⁵⁵ and genetic algorithms.⁵⁶

Recent studies on a different hydrogenation state of the PCB used Monte Carlo sampling,²⁰ while others generated conformations by changing all degrees of the molecule dihedral angles²¹ to tackle this problem. In this work, we used the technique of metadynamics simulations, which is an alternative approach that allows the explicit representation of the free energy hypersurface with regards to selected collective variables. This in turn enables us to detect local minima and the corresponding energy barriers between physically meaningful conformations.

We first performed three independent 2D metadynamics simulations of the chromophore *in vacuo*, each using one of the three pairs of dihedral angles connecting the rings A/B, B/C and C/D as collective variables. For all three calculations, a linear (ZESS) conformation has been used to initialize the simulation. During the simulations for each dihedral pair, all doubly bonded dihedral angles not driven by the metadynamics remained stable throughout the simulation. Thus, the resulting energy landscape is only valid for the given conformation of the unbiased dihedral angles. However, the perturbation of the energy landscape by changes in the electronic structure in distant parts of the chromophore will only have a minor influence.

The resulting free energy surfaces are illustrated in Fig. 2 for the three metadynamics simulations sampling the dihedral angles between A/B, B/C and C/D. In the resulting energy surfaces, four minima for each dihedral pair are located at $(0,0)$, $(0,\pi)$, $(\pi,0)$ and (π,π) . All four minima appear twofold degenerate; this effect can be traced back to steric hindering of the amide hydrogen atoms and the pyrrole ring sidegroups.

The actual depth of the energy minima however cannot be explained as easily and delicately depending on possible steric repulsion, hydrogen bonding and dihedral energies.

Examining the energy hypersurface of the dihedral pair (1,2) connecting rings A and B, the previously described twofold degenerate minima can be observed at all four conformations leading to planar arrangement of the rings. The minima are separated by two clearly distinguishable energy barriers, a small barrier of approximately 10 kcal mol^{-1} in the direction of 2 located at $\pm\frac{\pi}{2}$ and a larger barrier of 30 kcal mol^{-1} in the direction of dihedral 1 at a similar position. This result clearly shows the different bond characteristics, resembling a double bond character for the central bond of dihedral 1 and single bond characteristics for dihedral 2.

For the two central dihedral angles 3 and 4 connecting the rings B and C, again we can see four distinctive minimum energy conformations that again correspond to the planar conformations. Again, the local maxima within the energy basins are caused by the proximity of different groups and sidechains of the B and C rings. Compared to the previous dihedral pair, however, a clear distinction in the bond character and rotational energy barriers for the two dimerals cannot be made. The height of the energy barriers lies in-between those of the rigid dihedral 1 and the rotatable dihedral 2. With a height of approximately 12 kcal mol^{-1} , the barrier is small enough to be overcome in the time-limit of actual experiments, resulting in a delicate equilibrium for the two lowest minima of similar energy $((0,0)$ and $(0,\pi))$ with the actual population ratio critically depending on the exact energy difference and external influences.

The remaining two dihedral angles behave similar to the dimerals connecting rings A and B. The dihedral 5 can rotate easily, while in the direction of dihedral 6 a high rotational barrier can be seen. However, here the energy barrier is even higher than in the first case. Also we see a clear energetic preference for a value of 0 deg for dihedral 6, with the lowest possible energy being found at $(0,0)$.

As a main result from our metadynamics simulations, we see similar energetic properties for the different configurations of the (3,4) dihedral pair. The (π,π) and $(-\pi,-\pi)$ states however are

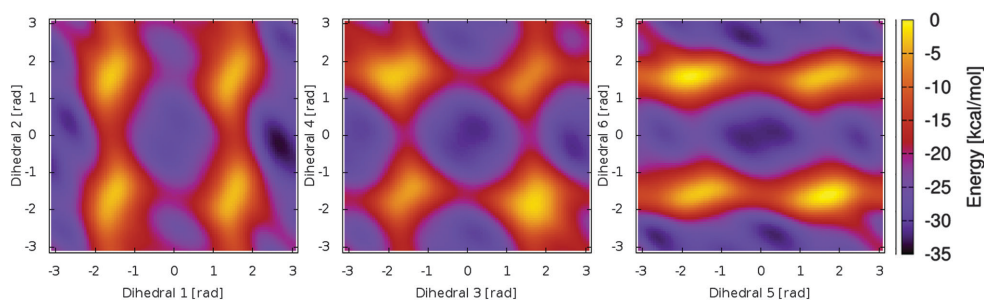


Fig. 2 Energy surface for the three dihedral pairs (1,2) to (5,6) connecting the pyrrole rings A to D. Twofold degenerate minima are visible for planar conformations, while the overall depth of the minima and height of the energy barriers vary to a great extent.

less favorable due to strong steric hindering. For the dihedral pair (1,2), a preference for the $(\pi,0)$ conformation can be seen, while for the (5,6) pair the (0,0) state is energetically favorable. This information already heavily reduces the number of needed conformations for a sufficient sampling of the conformational space using molecular dynamics simulations. Additionally, induced by the delicate equilibrium between the two lowest energy minima, the central dihedral pair (3,4) can be expected to react strongly to small changes in the chromophore and its surroundings.

3.2 Unbiased molecular dynamics simulations

Based on the energy surfaces of our metadynamics simulations, unbiased molecular dynamics simulations of the PCB have been employed to allow for a sampling of the unperturbed system. Based on the same DFTB level of theory, we performed simulations for a broad selection of energetically favorable conformations. In 75 ps of simulation time, a good sampling of the relevant regions in the energy surface can be achieved, *i.e.* positions in both sides twofold degenerate minima are visited, while the general conformation does not change during the simulation. This behavior can be observed for all other conformations and dihedral pairs. As a result, a multitude of differently initialized molecular dynamics simulations is needed to calculate the properties of the system. When evaluating the dihedral distributions during the simulation, the bond characteristics found in the metadynamics simulations can be confirmed (cp. Fig. 3). While the outer dihedral angles 1 and 6 show a narrow double bond like distribution, the neighboring bonds 2 and 5 exhibit a broad distribution indicating a single bond like behavior. The width of the central dihedrals 3 and 4 lies in between the previous ones, pointing towards a conjugated electronic system. While the semi-empirical level of theory allows for the needed sampling, intramolecular hydrogen bonding however is underestimated; the rarely emerging hydrogen bonds remain stable only for parts of picoseconds.

In the next step, a proper description of the hydrogen bonds needs to be achieved. Here a BLYP with the VdW correction level of theory has been used, which strongly improves the description of the intramolecular hydrogen bonds. Maximally hydrogen bonded conformers can be found in the ZZZsas and ZEZsss conformations, enabling the formation of 6 stable hydrogen bonds (cp. Fig. 4)

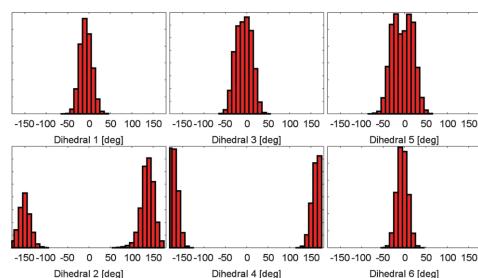


Fig. 3 Dihedral angle distributions during a molecular dynamics simulation. All dihedral angles remain stable at the simulation time of 75 ps. The different bond characteristics are clearly visible.

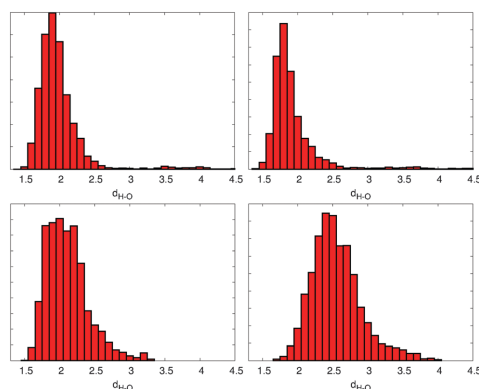


Fig. 4 Distribution of the four possible hydrogen bonds between the NH groups and the carboxylic group lone oxygens, taken from a 10 ps BLYP-D trajectory of the ZEZsss conformation. Top left: ring A, right: ring B; bottom left: ring C, right: ring D.

between the B and C rings carboxyl groups and the C and D or A and B ring NH and oxygens.

3.3 Explicit solvent calculations

For the conformational distribution of a solute in an aprotic solvent with only weak specific intermolecular interactions, the gas phase can usually be considered a very good first approximation. For other solvents, in particular hydrogen-bonding liquids such as water or alcohols, an explicit representation of the solvent molecules is normally the method of choice in order to reproduce the sensitive equilibrium of intra- and intermolecular interactions. Hence, we have considered the solvent molecules explicitly in our unbiased molecular dynamics simulations.

The higher complexity of explicit solvent models would result in considerably higher computational costs for metadynamics simulations which require several nanoseconds of simulation time even for an approximate convergence. An additional side effect is caused by the inertia of the explicitly moving solvent, which slows down the effective response time of conformational changes in the solute. This in turn requires a more conservative choice of specific metadynamics parameters (in particular either the amplitude and width of the spawned potential energy hills or the deposition rate). Again, this issue would result in longer simulation times.

When looking at the overall dynamical behavior of the chromophore, again no conformational change can be observed on the computationally accessible timescales. Judging from the dihedral angle distribution, there are no strong changes in the structure of the energy surface. Also the bond lengths suggest no strong changes in the electronic structure.

When analyzing the overall potential energy, however, we see a clear change in lower energies for the closed compared to the open conformation. This behavior can be explained by the formation of intermolecular hydrogen bonds between the chromophore and the surrounding solvent molecules. While the closed



conformations *in vacuo* showed no intramolecular hydrogen bonds during the 75 ps simulation time, we now observe an average of two to four intermolecular bonds to the solvent for the different conformations. In contrast, the open conformation was able to form two to six intramolecular hydrogen bonds in the *in vacuo* simulation, while in methanol the possible hydrogen bonding sites are blocked by intermolecular hydrogen bonding partners. Thus, in a solvent that forms strong hydrogen bonds, the energetic advantage of the open conformation vanishes.

In a conclusion we can assume a different probability for the open and closed classes of conformations, depending on the polarity of the surrounding solvent molecules. The higher the polarity of the solvent, the more intermolecular hydrogen bonds will counter the energy advantage of intramolecular hydrogen bonds.

3.4 NMR chemical shifts

In comparison to the recent NMR chemical shift measurements mentioned in the introduction, we perform ensemble averaged NMR chemical shift calculations on the different low energy conformations obtained from the metadynamics simulations.

In the experiment, a full assignment of PCB NMR chemical shifts in the HMPT solvent has been achieved.²² Additionally, a 2D NMR spectrum of the PCB in methanol has been provided by the group of P. Schmieder. While the spectra show a similar shape and ordering, at the first look contradictory changes can be identified. When taking the actual values of the changes between the two different solvents (see Fig. 5) into account, we see that the A and D rings δN change by 2 ppm, the δH by 0.6 ppm. For the B and C rings, we see changes of δN by 10 ppm and δH by 1.2 ppm. Assuming that the change is mainly induced by hydrogen bonds and exhibits a linear behavior, *i.e.* upon change in hydrogen bond strength the chemical shift values move on a straight line in the 2D spectrum, an additional change in the δN by around 6 ppm has to be explained.

Based again on the most promising conformations taken from our metadynamics calculations, we perform ensemble averaged ^{15}N as well as ^1H NMR chemical shift calculations (see Table 1). When looking at the ^{15}N chemical shifts of the

Table 1 ^1H and ^{15}N NMR chemical shift values for a series of characteristic conformations. ^1H referenced to benchmark calculations of TMS, ^{15}N referenced to match the PCB D ring in methanol

Conformation	N_A	N_B	N_C	N_D	H_A	H_B	H_C	H_D
EZZaas	163.8	151.8	160.6	131.1	8.2	10.5	9.6	7.0
EEZsss	163.2	155.8	161.4	131.5	8.1	12.7	9.7	7.6
ZEZass	163.0	150.0	159.7	131.7	8.2	10.1	9.9	7.5
ZZZass	164.1	145.4	149.9	130.4	8.4	9.4	10.6	7.7
EZZsss	164.1	144.4	145.4	129.2	8.0	11.8	10.5	7.6
ZZZasa	162.4	142.9	148.4	139.4	8.4	8.9	9.3	7.7

outer rings A and D, we can see that the shifts vary only within a range of 5 ppm for all energetically favorable conformations, indicating only a minor distortion in the local electronic structure upon conformational changes. Generally, the chemical shift of ring D is the lowest, A the highest, while those of rings B and C are always within a range of 5–10 ppm to each other. This overall behavior already is in good agreement with experiments not only in solvent but also with previous experiments on the whole protein. Since the experimental nitrogen shifts are similar even for hugely different systems or more specifically different surrounding hydrogen bonding networks, one can suspect the main influence on the nitrogen shifts to be the conformation of the system, while the hydrogens on the other hand are well known to be strongly influenced by hydrogen bonds.

When changing the conformation by moving between the two lowest energy basins of the dihedrals 3 and 4, we see a change in the rings B and C ^{15}N chemical shifts by approximately 10 ppm. When we look at changes in the chemical shifts induced by rotation around the outer double and single bonds, we observe a number of small changes in the range of 5 ppm in different directions for the chemical shifts of the central rings B and C (Fig. 6).

By a combination of all these possible permutations, a multitude of different within the sampling accuracy not clearly distinguishable distributions of chemical shifts arises. This quite ambiguous result however can be refined by using the previously attained information about the underlying energy surface and considering only the spectra of the energetically most probable conformations, as well as by comparing the large influence of the central dihedrals on the experimental data.

When considering explicit methanol solvent molecules on the same level of theory, we again see the pattern and changes upon change in the conformation known from the *in vacuo* calculations. The B and C ring nitrogen chemical shifts are in close proximity and move by approximately 10 ppm upon change in the central dihedrals, while the A and D ring positions remain stable. As a result from the hydrogen bonding to the solvent, the hydrogen chemical shifts slightly move downfield. However, on the DFTB level of theory combined with the range cutoff in the NMR calculations, these interactions are weakened, resulting in a lower hydrogen chemical shift than expected. As the main result we notice that the influence of the surrounding explicit solvent can mainly be seen in the hydrogen chemical shifts, while the nitrogen shifts stay close to the *in vacuo* results, however, within their usual broad distribution and thus higher possible error from low sampling rates. In no case an influence of the same

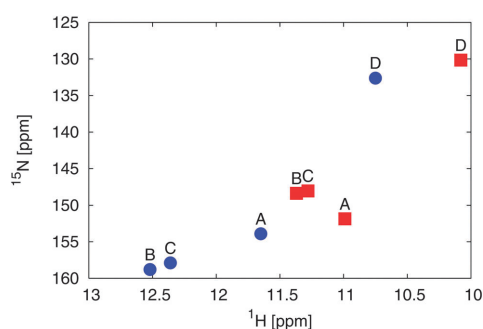


Fig. 5 Experimental 2D ^1H and ^{15}N NMR spectra different solvents: HMPT²² (blue dots) and methanol⁵⁷ (red squares) of the amine groups of rings A to D.

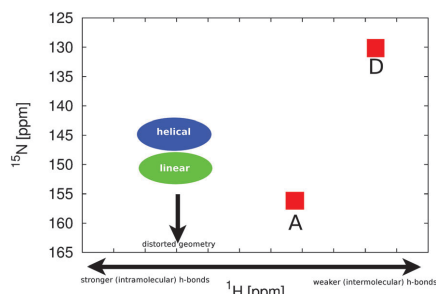


Fig. 6 Overview of the different influences on the ^1H and ^{15}N chemical shifts of PCB. A conformational change in the central dihedral pair of rings B and C causes a change in the positions of the signals of ring B and C as indicated by the green and blue areas. The remaining signals A and D remain stable. Changes in hydrogen bonding strength mainly cause the hydrogen chemical shifts to change.

strength as that of the change in the central dihedral angles on the nitrogen chemical shifts can be observed.

3.5 Effect of hydrogen bonding

To properly include hydrogen bonding effects in the suspected main conformations for the HMPT case, BLYP calculations with VdW correction have been performed. In each of those simulations the system has been prepared in a maximally hydrogen bonded state. Here, the hydrogen bonds of the carboxylic groups of the ring B to the C and D rings and C to the A and B rings remained stable during the simulation. While the experimentally observed spectrum cannot be reproduced by one of those conformations, the influences of the single conformations can be attributed to different parts of the spectrum. Combining all of them finally gives an explanation of the experimentally observed chemical shifts.

A “sufficient” sampling of the dihedral energy surface would require long trajectories in the range of 50 to 100 ps which is not unfeasible with present-day computational resources, but appears unnecessary in view of the required computational cost. On the other hand, examining short trajectories of different hydrogen bonding patterns can also give insights into the resulting spectra and possible origins of the different characteristics for the two solvents.

One low energy conformation is the EEss configuration. Here however, for geometric reasons only one stable intramolecular hydrogen bond can be observed. The resulting 2D NMR spectrum shows NH positions similar to the non-hydrogen bonded case with exception of the C ring, that is strongly hydrogen bonded to the B ring carboxylic group. The appearance of a hydrogen bond increases the hydrogen chemical shift to around 13 ppm, while the nitrogen chemical shift moves to approximately 158 ppm.

For the maximally hydrogen bonded ZEZss conformation, we see a strong change in almost all ring positions in the spectrum. However, with exception of the only weakly hydrogen bonded B ring, the alignment of the chemical shifts is similar

to the non-hydrogen bonded case with only the hydrogen chemical shifts moving downfield by approx. 2 ppm. Most importantly, the non- or weakly hydrogen bonded B ring nitrogen chemical shift is strongly shifted downfield. This shows clearly that the position of the nitrogen chemical shift is not induced by the hydrogen bonding, but has instead to be caused by conformational effects and deviation from the energy minima of the dihedral distributions found in the metadynamics simulations.

4 Conclusions

We have quantified the dependence of the conformation of a tetrapyrrole chromophore (phycocyanobilin) on the character of its chemical environment, specifically the solvent type. By means of semiempirical metadynamics simulations, we have sampled the free energy hypersurface of the chromophore, resulting in the identification of the geometric equilibrium structures at ambient temperatures as a function of the solvent. In particular, our simulations show a delicate equilibrium between helical and linear conformations that reacts very sensitively on the solvent characteristics. Based on *ab initio* molecular dynamics simulations, we have computed the two-dimensional NMR pattern of ^{15}N and ^1H NMR chemical shifts at the *ab initio* level of theory.

The experimentally observed solvent shifts exhibit a counter-intuitive trend (towards higher ^1H NMR chemical shifts for HMPT which is expected to form fewer hydrogen bonds than methanol). Our *ab initio* molecular dynamics simulations have resolved this puzzling situation, which could be traced back to stronger *intramolecular* hydrogen bonding of the chromophore. These hydrogen bonds are broken in methanol due to the better electrostatic screening and the stronger intermolecular interactions with the solvent.

A striking secondary effect of the change in hydrogen bonding pattern is the isomerization of the chromophore which is equally visible in experimental as well as computed chemical shift pattern. This solvent-induced structural transition represents a mechanical switching function on the molecular scale. With a suitable chemical functionalization, this transition might be exploited for applications in the field of molecular sensors, molecular recognition or even externally triggered drug delivery.

Acknowledgements

We would like to gratefully acknowledge financial support from the Deutsche Forschungsgemeinschaft (DFG) within the SFB/TRR 102, as well as computing time provided by the HLRS.

References

- J. J. V. Thor, K. L. Ronayne and M. Towrie, *J. Am. Chem. Soc.*, 2007, **129**, 126–132.
- K. C. Toh, E. A. Stojkovi, A. B. Rupenyana, I. H. M. V. Stokkum, M. Salumbides, M.-L. Groot, K. Moffat and J. T. M. Kennis, *J. Phys. Chem. A*, 2010, **115**, 3778–3786.



4. PUBLICATIONS

View Article Online

PCCP

Paper

- 3 L. J. G. W. V. Wilderen, I. P. Clark, M. Towrie and J. J. V. Thor, *J. Phys. Chem. B*, 2009, **113**, 16354–16364.
- 4 J. J. V. Thor, M. Mackeen, I. Kuprov, R. A. Dwek and M. R. Wormald, *Biophys. J.*, 2006, **91**, 1811–1822.
- 5 S. Kaminski and M. A. Mroginski, *J. Phys. Chem. B*, 2010, **114**, 16677–16686.
- 6 T. Rohmer, H. Strauss, J. Hughes, H. de Groot, W. Gärtner, P. Schmieder and J. Matsysik, *J. Phys. Chem. B*, 2006, **110**, 20580–20585.
- 7 M. A. Mroginski, F. Mark, W. Thiel and P. Hildebrandt, *Biophys. J.*, 2007, **93**, 1885–1894.
- 8 R. A. Matute, R. Contreras and L. Gonzalez, *J. Phys. Chem. B*, 2008, **112**, 16253–16256.
- 9 R. A. Matute, R. Contreras and L. Gonzalez, *J. Phys. Chem. Lett.*, 2010, **1**, 796–801.
- 10 J. Wan, X. Xu, Y. Ren and G. Yang, *J. Phys. Chem. B*, 2005, **109**, 11088–11090.
- 11 C. Zazza, N. Sanna and M. Aschi, *J. Phys. Chem. B*, 2007, **111**, 5596–5601.
- 12 H. Elgabarty, P. Schmieder and D. Sebastiani, *Chem. Sci.*, 2013, **4**, 755.
- 13 U. F. Rohrig and D. Sebastiani, *J. Phys. Chem. B*, 2008, **112**, 1267–1274.
- 14 J. Schmidt, A. Hoffmann, H. W. Spiess and D. Sebastiani, *J. Phys. Chem. B*, 2006, **110**, 23204–23210.
- 15 C. Allolio and D. Sebastiani, *Phys. Chem. Chem. Phys.*, 2011, **13**, 16395–16403.
- 16 D. Banyai, T. Murakhtina and D. Sebastiani, *Magn. Reson. Chem.*, 2010, **48**, S56–S60.
- 17 C. Schiffmann and D. Sebastiani, *Phys. Status Solidi B*, 2012, **249**, 368–375.
- 18 D. Sebastiani and M. Parrinello, *ChemPhysChem*, 2002, **3**, 675.
- 19 C. Allolio, M. Sajadi, N. P. Ernsting and D. Sebastiani, *Angew. Chem., Int. Ed.*, 2013, **52**, 1813–1816.
- 20 P.-h. Tu, Y.-h. Yao, Y.-l. Li and B. Liu, *THEOCHEM*, 2009, **894**, 9–13.
- 21 A. H. Göller, D. Strehlow and G. Hermann, *ChemPhysChem*, 2001, **2**, 665–671.
- 22 M. Röben and P. Schmieder, *Magn. Reson. Chem.*, 2011, **49**, 543–548.
- 23 M. M. Boyle, R. A. Smaldone, A. C. Whalley, M. W. Ambrogio, Y. Y. Botros and J. F. Stoddart, *Chem. Sci.*, 2011, **2**, 204–210.
- 24 C. A. Bortolotti, L. Paltrinieri, S. Monari, A. Ranieri, M. Borsari, G. Battistuzzi and M. Sola, *Chem. Sci.*, 2012, **3**, 807–810.
- 25 J. M. Spruell and C. J. Hawker, *Chem. Sci.*, 2011, **2**, 18–26.
- 26 K. Xu, M. Qiang, W. Gao, R. Su, N. Li, Y. Gao, Y. Xie, F. Kong and B. Tang, *Chem. Sci.*, 2013, **4**, 1079–1086.
- 27 A. Laio and M. Parrinello, *Proc. Natl. Acad. Sci. U. S. A.*, 2002, **99**, 12562–12566.
- 28 A. Barducci, G. Bussi and M. Parrinello, *Phys. Rev. Lett.*, 2008, **100**, 1–4.
- 29 G. Seifert, *J. Phys. Chem. A*, 2007, **111**, 5609–5613.
- 30 G. Bussi, D. Donadio and M. Parrinello, *J. Chem. Phys.*, 2007, **126**, 014101.
- 31 M. Elstner, D. Porezag, G. Jungnickel, J. Elsner, M. Haugk, T. Frauenheim, S. Suhai and G. Seifert, *Phys. Rev. B: Condens. Matter Mater. Phys.*, 1998, **58**, 7260–7268.
- 32 S. Nosé, *Mol. Phys.*, 1984, **5**, 255.
- 33 J. V. Vondele, M. Krack, F. Mohamed, M. Parrinello, T. Chassaing and J. Hutter, *Comput. Phys. Commun.*, 2005, **167**, 103–128.
- 34 A. D. Becke, *Phys. Rev. A: At., Mol., Opt. Phys.*, 1988, **38**, 3098.
- 35 C. Lee, W. Yang and R. G. Parr, *Phys. Rev. B: Condens. Matter Mater. Phys.*, 1988, **37**, 785–789.
- 36 S. Grimme and M. Parac, *ChemPhysChem*, 2003, **3**, 292–295.
- 37 T. Laino, F. Mohamed, A. Laio and M. Parrinello, *J. Chem. Theory Comput.*, 2005, **1**, 1176–1184.
- 38 F. Neese, *ORCA – an ab initio, Density Functional and Semiempirical program package version 2.7.0*, University of Bonn, 2009.
- 39 W. Kutzelnigg, *Isr. J. Chem.*, 1980, **19**, 193.
- 40 J. Perdew, K. Burke and M. Ernzerhof, *J. Phys. Chem.*, 1996, **105**, 9982–9985.
- 41 W. Kutzelnigg, U. Fleischer and M. Schindler, *NMR: Basic Princ. Prog.*, 1990, **23**, 165.
- 42 U. H. Hansmann, *Chem. Phys. Lett.*, 1997, **281**, 140–150.
- 43 P. G. Bolhuis, D. Chandler, C. Dellago and P. L. Geissler, *Annu. Rev. Phys. Chem.*, 2002, **53**, 291–318.
- 44 M. Christen and W. F. van Gunsteren, *J. Comput. Chem.*, 2008, **29**, 157–166.
- 45 R. Gehrke and K. Reuter, *Phys. Rev. B: Condens. Matter Mater. Phys.*, 2009, **79**, 085412(10).
- 46 C. Grebner, J. Becker, S. Stepanenko and B. Engels, *J. Comput. Chem.*, 2011, **32**, 2245–2253.
- 47 D. J. Wales and H. A. Scheraga, *Science*, 1999, **285**, 1368–1372.
- 48 S. Goedecker, *J. Chem. Phys.*, 2004, **120**, 9911–9917.
- 49 M. Sicher, S. Mohr and S. Goedecker, *J. Chem. Phys.*, 2011, **134**, 044106.
- 50 S. Stepanenko and B. Engels, *J. Comput. Chem.*, 2008, **29**, 768–780.
- 51 S. Stepanenko and B. Engels, *J. Phys. Chem. A*, 2009, **113**, 11699–11705.
- 52 D. Karaboga, B. Gorkemli, C. Ozturk and N. Karaboga, *Artif. Intell. Rev.*, 2012, **1**–37.
- 53 W. Gao and S. Liu, *Comput. Oper. Res.*, 2012, **39**, 687–697.
- 54 C. Schiffmann and D. Sebastiani, *J. Chem. Theory Comput.*, 2011, **7**, 1307–1315.
- 55 S. E. Schönborn, S. Goedecker, S. Roy and A. R. Oganov, *J. Chem. Phys.*, 2009, **130**, 144108.
- 56 Z. E. Brain and M. A. Addicoat, *J. Chem. Phys.*, 2011, **135**, 174106.
- 57 M. Röben, *NMR-spektroskopische Untersuchungen des an Cph1-, Agp1-gebundenen und des freien Chromophors zur Aufklärung des Phytochrom Photozyklus*, PhD thesis, 2011.

Open Access Article. Published on 06 February 2014. Downloaded on 04/03/2015 12:33:52.
This article is licensed under a Creative Commons Attribution 3.0 Unported Licence.



First Principles Calculations of NMR Chemical Shifts of Liquid Water at an Amorphous Silica Interface

By Xiang Yang Guo¹, Tobias Watermann¹, Shane Keane¹, Christoph Allolio¹, and Daniel Sebastiani^{1,2,*}

¹ Physics Department, Freie Universität Berlin, Arnimalle 14, 14195 Germany

² Institute of Chemistry, Martin-Luther-Universität Halle Wittenberg, Kurt-Mothes-Strasse 2, 06120 Halle, Germany

Dedicated to Professor Hans Wolfgang Spiess on the occasion of his 70th birthday

(Received June 4, 2012; accepted in revised form September 21, 2012)

(Published online October 29, 2012)

Car-Parrinello Molecular Dynamics Simulations / DFT / NMR Chemical Shift Calculations / MCM-41 / Liquid Water Structure / Confinement

We investigate the anomalous structure and hydrogen bond network of water molecules confined inside a silica nanopore (MCM-41 type). In addition to geometric data, we use proton NMR chemical shifts as a measure for the strength of the H-bonding network. We compute the ¹H NMR shifts of confined water based on a first principle approach in the framework of density functional perturbation theory under periodic boundary conditions. The hydrophilic character of the silica is well manifested in the water density profile. Our calculations illustrate both the modifications of the ¹H NMR chemical shifts of the water with respect to bulk water and a considerable slowing down of water diffusion. In the vicinity of silanols, weakly hydrogen bonded liquid water is observed, while at the center region of the pore, the hydrogen bonding network is enhanced with respect to bulk water.

1. Introduction

Periodically structured porous materials have evoked wide interest for various applications in recent years. Their micro-structure is observed to be composed of orderly arranged pores with uniform size [1]. MCM-41, as one of the most studied type, is characterized by pores less than 40 Å in diameter, within which liquids can be confined. Experimental studies regarding MCM-41 and the properties of liquids confined within it have been performed at length. Techniques such as quasi-elastic and deep elastic neutron scattering [2–4], neutron diffraction with isotopic substitution [5], x-ray spectroscopy [6], sum frequency vibration spectroscopy [7], adsorption calorimetry [8],

* Corresponding author. E-mail: daniel.sebastiani@fu-berlin.de

and NMR spectroscopy [9–11] have provided a lot of experimental data which may be compared to simulation data.

The silanol groups on the silica surface play a special role for its ability of supplying hydrogen bonding sites for the confined solvent [14]. With respect to their density on the MCM-41 silica surface [9,10,13], the consensus seems to be about 2 to 3 nm⁻², meaning these groups cannot form hydrogen bonds with each other as they are too far apart. Since the average distance between them is about 5.8 Å, one water molecule cannot be simultaneously hydrogen bonded to two silanol groups [1]. Up to three water molecules, however, may be hydrogen bonded to a single silanol group [14]. The nature of water differed from bulk water when it is hydrogen bonded to the hydroxyl groups on the silica surface. Recent neutron scattering evidence suggests that the hydrogen bond formed between a water molecule and a silanol in mesoporous silica is stronger than the hydrogen bonds between water molecules [4].

Many simulations have been conducted focusing on the water silica interface. Since the structure of MCM-41 is not fully known, many varying models have been proposed to simulate its surface. For example, Shirono *et al.* [15] and Kleestorfer *et al.* [16] used a block of alpha-quartz out of which they cut circular pores of various sizes. In cases where there remained oxygens attached to only one silicon atom, hydrogen atoms were added to create the silanol groups characteristic of the surface of MCM-41. Gallo *et al.* [12] used beta-cristobalite which was melted and equilibrated at 1000 K. It was then quenched and a cylindrical pore 15 Å in diameter was carved into it. Again, oxygens left attached to only one silicon atom were capped with hydrogen atoms. Sherendovich *et al.* [9] use different experimentally derived criteria to recommend a model of MCM-41 based on the structure of tridymite. The model they proposed was not in fact tridymite, but a fictitious structure created from pieces of it stuck together in different configurations. With respect to the silica-water interface, Sulpizi *et al.* [29] conducted *ab initio* Molecular Dynamics (AIMD) on the hydroxylated (0001) α -quartz surface system. Two types of silanol groups were addressed in their results, so called out-of-plane silanols with a strong acidic character and in-plane silanols with weaker acidity.

In this work, a simplified surface model is constructed which has the virtue of containing the same density of silanol groups as MCM-41. We obtain the density and translational mobility profiles of water confined in this model by applying first principle density functional theory based molecular dynamics (AIMD) simulation. Then we compute ensemble averages of Nuclear Magnetic Resonance (NMR) calculations on the confined water molecules and compare the results with bulk water. Furthermore we analyze the distribution of the water NMR shifts along the pore axis and the impact of the geometric confinement on the bound water NMR shifts so as to increase our understanding of the influence of spatial confinement on the structure and dynamics of water.

2. Computational details

The water-silica interface is represented by a simplified yet realistic surface model which demonstrates the experimentally known structure of the MCM-41 pore. Figure 1

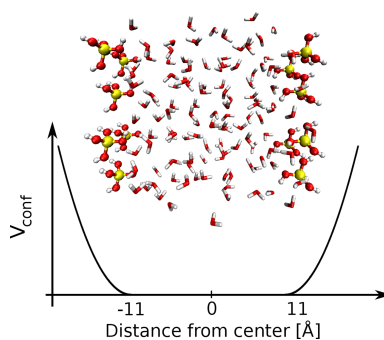


Fig. 1. Two silica-water unit cells from a snapshot of the MD simulation (xz side view). The three-dimensional periodic cell contains six silicic acid groups at the walls and 59 water molecules in between. Si, O and H atoms are represented in yellow, red and white respectively. The silica surface is represented by three isolated $\text{Si}(\text{OH})_4$ tetrahedrons.

shows a snapshot of the model. Silicic acid $\text{Si}(\text{OH})_4$ is used to model the silanol groups with the three outer hydroxy groups fixed.

Following the experimental results from the NMR spectroscopy [9,10] on the structure of MCM-41, the density of the silanol groups is taken to be 3 nm^{-2} . The possible hydrogen bonding between Si-O-Si bridge and water is missing in this model. We assume it is only of minor influence since the highly concentrated silanol groups on the surface hamper sterically the formation of this type of hydrogen bonds. In the next more sophisticated model, the actual amorphous pore will be considered.

The diffusion of water into the surface is prevented by a harmonic potential (Fig. 1). The potential only acts on the water molecules to allow free Si-OH vibrations. The simulation is carried out in a fully periodic box with a size of $28 \times 10 \times 10 \text{ \AA}$, two flat silanol walls are placed 22 \AA apart, 6 \AA space is left at either end of the potential to reduce periodic effects in the x direction. 59 water molecules are placed between the two walls. In order to employ a timestep of 1 fs, we choose heavy water instead of H_2O to double the calculation speed.

We run DFT based molecular dynamics simulations in the CP2K package [30]. The BLYP [31] exchange-correlation functional was used, as well as the TZVP basis sets and GTH pseudopotentials [32]. The DFT-D2 Grimme [33] dispersion correction was also used. In total, the simulation ran for over 45 ps.

The system was first equilibrated for 10 ps using the canonical ensemble, employing a Nosé-Hoover thermostat. The temperature was set to be 320 K. The simulation was then switched to the microcanonical ensemble for the remaining time.

The NMR chemical shifts are computed as ensemble averages from ab initio nuclear shielding calculations within the CP2K package [30]. A random set of 15 snapshots from the NVE trajectory was sampled, and chemical shifts of all atoms were calculated. For the referencing of the nuclear shielding tensors to chemical shifts, we utilized the method applied in Ref. [23] The NMR simulation used a Gaussian aug-

mented plane wave approach with GAPW plane wave cutoff 320 Ry, the BLYP-DFT exchange-correlation functional and the TZV2PX-MOLOPT-GTH basis set were employed [34].

It should be noted that we do not compute the quantum propagation of the nuclear spin state which occurs on a timescale of millisecond in a typical NMR experiment, but instead we compute directly the energy difference of the 2 states. Hence the simulation duration on a picosecond level is adequate to achieve the necessary sampling for the averaged instantaneous chemical shifts [35–40].

3. Results and discussion

3.1 Translational dynamical properties

One of the most salient properties of water confined in MCM-41, discovered by experiments and MD simulations [12,15,17,18] is a slower translational dynamics with respect to bulk water. The translational dynamics of our system were measured by calculating the diffusion coefficient of the system. The ratio of the diffusion coefficient of water confined in MCM-41 to that of bulk water

$$q = \frac{D_{\text{D}_2\text{O}}^{\text{Confined}}}{D_{\text{D}_2\text{O}}^{\text{Bulk}}}$$

has been ascertained experimentally and *via* simulation. Values of q range quite widely from 0.23 to 0.64 [15,17,18,24], with the consensus showing a much slower diffusion of water within MCM-41 pores. In this work, the reference self diffusion coefficient value for bulk heavy water is taken to be $0.187 \text{ \AA}^2/\text{ps}$ from Ref. [28]. In order to obtain the value of q for our system, we calculated the diffusion coefficient D for our confined water according to Einstein's relation

$$D = \frac{\text{MSD}}{2dt} = \left\langle \frac{(R_{\text{D}_2\text{O}}(t) - R_{\text{D}_2\text{O}}(0))^2}{2dt} \right\rangle_{\text{D}_2\text{O}}$$

with the numerator representing the mean-square displacement (MSD), t the time, and d the number of dimensions in which the quantity is measured. For the simulation of confined water, only diffusion in the two periodic directions (in our case the y and z dimensions) is taken into account in order to reduce possible distortion due to the presence of the walls [18].

The mean-square displacement (MSD) of water molecules over time in the confined cases is presented in Fig. 2. From this graph, the diffusion coefficient for confined water is calculated to be $0.05 \text{ \AA}^2/\text{ps}$. As $0.187 \text{ \AA}^2/\text{ps}$ for bulk water, the resulting ratio q is about 0.27 which falls into the range we obtained from literature.

As pointed out in several studies [11,12], however, taking the diffusion coefficient of the whole system all at once fails to take adequate consideration of different effects of the confinement at different position within the pore.

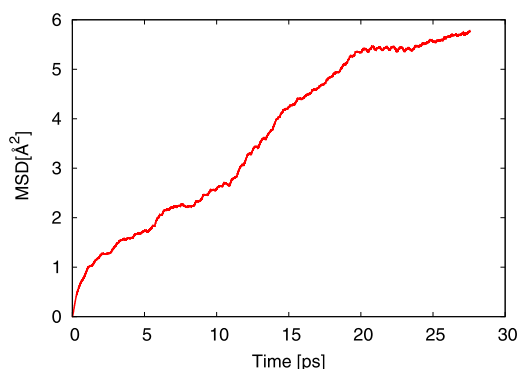


Fig. 2. Global MSD of the oxygen atoms of confined water at $T = 320$ K.

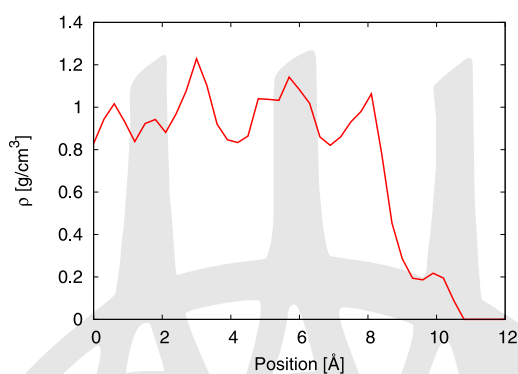


Fig. 3. Density Profile of Water confined between two silica slabs. The origin $x = 0$ Å corresponds to the center of the pore.

3.2 Density profile

The water density profile can demonstrate the configuration of confined water and the hydrophilic character of the silica surfaces. In the earlier empirical structure refinement simulations by R. Mancinelli *et al.* [5,27], the density of confined water in a MCM-41 pore is found to be higher in the vicinity of the silanol walls; at 300 K in the interfacial region the density was observed to be about 3 times as large as the density in the middle. This phenomenon stems from a so-called cohesive failure between water molecules. *I.e.* when water is confined between hydrophilic surfaces, voids occur in the middle of the water layer which leads to cohesive failure [26]. As to the present experimental results, Kocherbitov *et al.* [8] measured the apparent density of water in the MCM-41 pores at 298 K to be 0.88 g/cm^3 using H_2O and N_2 sorption method.

In our simulation, the density profile of water was constructed by creating a histogram of the spatial locations of all atoms across the pore with bins 0.3 Å wide and averaging over the entire NVE trajectory, as shown in Fig. 3. The position represents

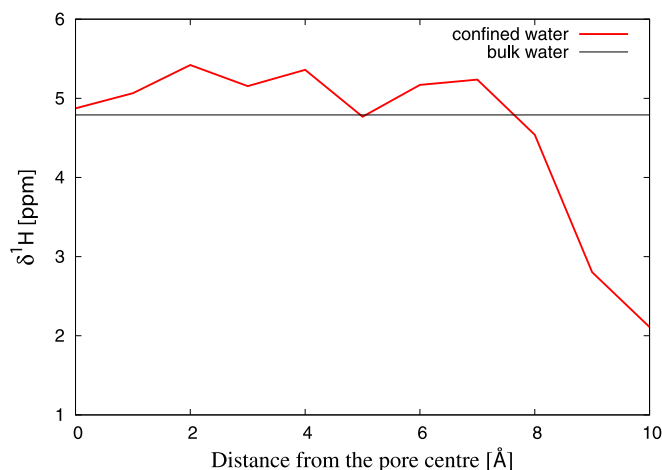


Fig. 4. Calculated ^1H NMR chemical shifts of water confined between silica slabs compared with bulk water, the distribution has been symmetrized with respect to the center ($x = 0 \text{ \AA}$), the value of ^1H NMR shifts are averaged in the x direction over the length of the model and the NVE trajectory of the system. The graph is drawn up to where the atoms in $\text{Si}(\text{OH})_4$ start to appear.

the distance of the oxygen atoms from the center along the pore axis perpendicular to the silica surface. At the core region of the cell (0 \AA to 2 \AA) a lower density appears in our result, and at the outer edge (7 \AA to 9 \AA) as well, then it gradually decays to zero at the silica wall. Notable density oscillations are observed from Fig. 3, which reveals that the spatial layering occurred in confined water due to the hydrophilic character of the substrate [21]. For example, we see 2 density peaks near the silica substrate, which indicates that there are 2 separate layers of water in this region. However in several other simulations, the produced density profile showed either one [5,18] or two [12,24,25] peaks in the interfacial region and lower density in the core region. The small bump in the density profile near the very edge of the pore is also present in other results [12,18]. One possible reason for the minimum appearing here is the presence of the silanol groups oxygen atoms in that area taking up space.

3.3 ^1H NMR chemical shift calculations

Lately the *ab initio* calculation of nuclear chemical shifts has become one of the most powerful methods for structure determination on the molecular level. Not merely can the calculation interpret the spectra returned by the experiments [23], but also it can produce instantaneous results that are beyond experimental capability. Particularly the instantaneous ^1H NMR shifts can provide significant probe for the hydrogen bonding network of specific chemical environments [41,42].

The NMR shifts profile we obtained, as shown in Fig. 4, substantially indicates the configuration of water confined between the 2 silica slabs. The experimental ^1H NMR chemical shift $\delta = 4.79 \text{ ppm}$ for bulk water is taken from the value given in Ref. [22]. Figure 4 displays that in the major part of the cell, within 7.6 \AA away from the center,

stronger H-bonded water appears with δ varying from 4.7 ppm to 5.4 ppm. The largest $\delta = 5.4$ ppm is reached at $x = 2$ Å. At the core of the pore ($x = 0$ Å), $\delta = 4.86$ ppm. Due to the confining effects of silica slabs, the NMR shifts are greater than those of bulk water. But at the core of the pore, the calculated shift approximates that of the bulk water, reflecting the hydrogen bonding in this region resembles bulk water H-bond network. While the shifts drop to upper-field as approaching the wall, in the vicinity of silanol walls (from $x = 7.6$ Å to $x = 10$ Å), water molecules are found to form weaker hydrogen bonds with each other or with silanols, the minimum value 2.1 ppm is found at $x = 10$ Å. As discussed before, the density profile shows layering effect took place in our cell. According to Gallo *et al.* [21], the interactions of the substrate atoms and thin water layers causes a strong distortion of the H-bond network. This explains why we see a decline of the shifts near the wall, even though it has been experimentally proven that the single silanol-water H-bond is stronger than the water-water H-bond [4].

We analogize the water filling process inside the pore by calculating the running average of ^1H chemical shifts up to a certain distance from the wall using equation

$$\delta_{\text{Avg}}^1\text{H}(x) = \frac{1}{N_{\text{H}}} \sum_{x'=x_{\text{wall}}}^x \delta^1\text{H}(x')$$

$\delta_{\text{Avg}}^1\text{H}(x)$ represents the average δ value of a fictitious water film with thickness x . For each value of $\delta_{\text{Avg}}^1\text{H}(x)$, we sampled from the wall to the plane at corresponding distance and calculated all the shifts of water between the 2 planes. Taking the limitation of sampling into account, we leave out the first averaged value from $x = 0$ Å to 0.5 Å. The range of averaged NMR shifts along the x direction over the length of the cell covers from 2 to 4.9 ppm which is in good agreement with the experimental value from 1.74 to 4.7 ppm achieved in Buntkowsky's group [1]. Grünberg *et al.* obtained the chemical shift spectra of confined water at varying hydration level using ^1H solid-state NMR. In their results for the fully hydrated pore, one single signal appears at 4.7 ppm, and with very small water content ($\leq 2.7\%$), one dominating peak locates at 1.74 ppm which is ascribed to the shift of silanol groups.

Figure 5 shows that the behavior of water in our model resembles the water filling process described in Ref. [1]. Comparing our data with the experimental findings, we observe the same varying tendency in the chemical shifts. The minimum value of δ in Fig. 5 was obtained by computing the shifts of water locating within 0.5 Å to the silica substrate, so as to correspond the very low water filling factor in the experiments. In the interfacial region, the experimental NMR shift is an approximation to the shift of silanol groups. Therefore, it is believed that all water molecules at this region were hydrogen bonded to the silanols. With increased water content, additional water molecules start to form hydrogen bonds with each other which gives rise to ascending chemical shifts. This phenomenon is also reflected in Fig. 5, but increasing distance from the wall plays the role instead of increasing water filling factor. When the water content goes up to 3.2%, a notable peak at 2.5 ppm arises beside a weakened line at 1.74 ppm, which indicates the coexistence of 2 different types of hydrogen bonds. The NMR peak shifts consistently towards down-field upon further increasing hydration level. When there is 23% of water, the line at 2.5 ppm is broadened and shifts to 3.4 ppm. When the pore is completely filled, a single shift appears at 4.7 ppm.

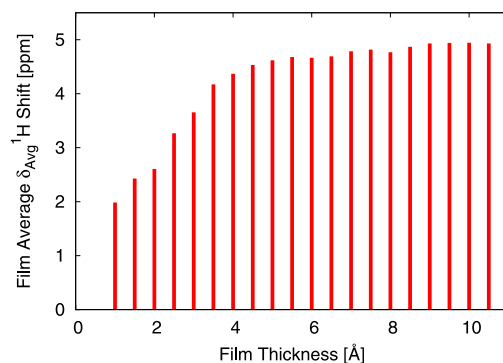


Fig. 5. Average of the ^1H NMR chemical shift values of those water molecules residing within a film of given thickness from the wall. The film thickness axis 0 Å and 11 Å are corresponding to the wall and the cell center respectively.

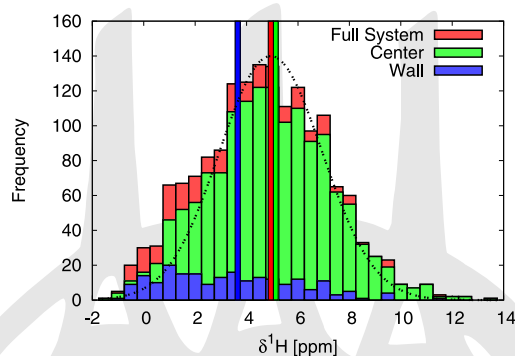


Fig. 6. Calculated ^1H NMR shift distribution of confined water. The ordinate is the occurrence of the shifts for various δ values. $\delta = 3.65$ ppm is the averaged value for the water within 3 Å proximity to the walls (blue), $\delta = 4.94$ ppm is the global average of the whole system (red), and $\delta = 5.13$ ppm is the average shift of the water at the center of the pore (green). The dashed curve represents a gaussian centered at $\delta = 4.94$ ppm (black).

Our averaged NMR shifts imitate this process (as shown in Fig. 5) in such a way that the δ value continually goes up from 2 ppm to 5.5 ppm as increasing thickness of the film which starts from the wall (0 Å). This denotes that the bonding between water and the silanols becomes less and less dominating which leads to the growing of the shifts until $x = 5.5$ Å. A plateau arises at $5.5 \text{ Å} < x < 11 \text{ Å}$ reflecting the water molecules at the center region are mostly bounded to each other and not influenced by the walls.

Figure 6 illustrates the spacial distribution of the ^1H NMR shifts inside the cell. Those water molecules situated within 3 Å proximity to the silica wall are denoted as wall water, and the rest are considered to be center water. In this way, the confined water is divided into 3 layers, silanol-water interface (wall water), water-water (center

water) and water-silanol interface (wall water). The computed global average value of the ^1H chemical shift for all the water inside this cell is 4.94 ppm, the averaged water shift in the close region of walls is 3.65 ppm, and that for the water in the core area is 5.13 ppm. Comparing the whole distribution with a Gaussian centered at the global average δ value 4.94 ppm, we can easily see that more water molecules fall into the up field in the proximity of silanols. Most wall water resides at the left half of the graph with $\delta \leq 4.94$ ppm. The overall average shift of the system moves towards lower δ (upper field) under the effects of silica walls. This gives further evidence that the silanol groups play a twisting role for the water-water hydrogen bonding network in the interfacial region [21].

4. Conclusion

In this paper, DFT based molecular dynamics simulations and first principles NMR chemical shift calculations are applied on a simplified surface model based on the structural properties of the MCM-41 pore. Our calculations demonstrate the strong influence of spatial confinement on the structure and dynamical properties of water.

On the structural level, we see a strong influence on the ^1H chemical shifts of the confined water. While at the center of the pore a 0.5 ppm increased chemical shift compared to bulk water is found, the chemical shift gradually decreases when approaching the wall, until it reaches a value 3 ppm below bulk water reference. This implies an enhanced hydrogen bonding network for the water at the center, and a strongly weakened network close to the silica-water interface. In the density profile, distinctive peaks appear next to the wall, indicating a structuring of the water by the wall geometry. By calculating average chemical shifts for fictitious water films at the wall, we can see a change from low chemical shifts for thin films towards bulk water like chemical shifts for a film thickness above 4 Å. This is in good agreement with a previous experimental model on the gradual filling of nanopores.

With respect to the dynamical behavior, we see a decrease in the diffusion rate by a factor of 4 when comparing to bulk water values.

Acknowledgement

This work has been supported by the German Research Foundation (DFG) under grants SE 1008/5 and 1008/8. Computing infrastructure was provided by the Northern German Supercomputing Alliance (HLRN) under grant HLRN/bec00073 and ZEDAT high-performance cluster in Freie Universität Berlin. We thank the German academic exchange service (DAAD) for a RISE internship.

References

1. B. Grünberg, T. Emmler, E. Gedat, I. Shenderovich, G. H. Findenegg, H. H. Limbach, and G. Buntkowsky, *Chem. Eur. J.* **10** (2004) 5689.
2. A. Faraone, L. Liu, C. Mou, P. Shih, J. Copley, and S. Chen, *J. Chem. Phys.* **7** (2003) 3963.
3. F. Mansour, R. M. Dimeo, and H. Peemoeller, *Phys. Rev. E* **66** (2002) 041307.

4. PUBLICATIONS

1424

X. Y. Guo *et al.*

4. C. Pantalei, R. Senesi, C. Andreani, P. Sozzani, A. Comotti, S. Bracco, M. Beretta, Mario, P. Sokol, and G. Reiter, *Phys. Chem. Chem. Phys.* **13** (2011) 6022.
5. R. Mancinelli, S. Imberti, A. K. Soper, K. H. Liu, C. Y. Mou, F. Bruni, and M. A. Ricci, *J. Phys. Chem. B* **113** (2009) 16169.
6. P. Smirnov, T. Yamaguchi, S. Kittaka, S. Takahara, and Y. Kuroda, *J. Phys. Chem. B* **104** (2000) 5498.
7. V. Ostroverkhov, G. A. Waychunas, and Y. R. Shen, *Phys. Rev. Lett.* **94** (2005) 046102.
8. V. Kocherbitov and V. Alfreðsson, *J. Phys. Chem. B* **112** (2007) 12906.
9. I. G. Shenderovich, D. Mauder, D. Akcakayiran, G. Buntkowsky, H. H. Limbach, and G. Findenegg, *J. Chem. Phys. B* **111** (2007) 12088.
10. X. S. Zhao, G. Q. Lu, A. K. Whittaker, G. J. Millar, H. Y. Zhu, *J. Chem. Phys. B* **101** (1997) 6525.
11. D. W. Hwang, A. K. Sinha, C. Y. Cheng, T. Y. Yu, and L. P. Hwang, *J. Phys. Chem. B* **105** (2001) 5713.
12. P. Gallo, M. Rovere, and S. H. Chen, *J. Phys.: Condens. Matter* **24** (2012) 064109.
13. S. Pizzanelli, S. Kababya, V. Frydman, M. Landau, and S. Vega, *J. Phys. Chem. B* **109** (2005) 8029.
14. E. P. Ng and S. Mintova, *Micropor. Mesopor. Mat.* **14** (2008) 1.
15. K. Shirono and H. Daiguji, *J. Phys. Chem. B* **111** (2007) 7938.
16. K. Kleestorfer, H. Vinek, and A. Jentys, *J. Mol. Catal. A: Chem.* **166** (2001) 53.
17. S. Takahara, N. Sumiyama, S. Kittaka, T. Yamaguchi, B. Funel, and M. Claire, *Adsorption* **109** (2005) 5814.
18. A. Lerbret, G. Lelong, P. Mason, M. L. Saboungi, and J. Brady, *Food Biophys.* **6** (2011) 233.
19. M. E. Tuckerman, *Statistical Mechanics: Theory and Molecular Simulation*, Oxford Graduate Texts, Oxford University Press Inc., New York (2010).
20. A. R. Bizzarri and S. Cannistraro, *J. Phys. Chem. B* **106** (2002) 6617.
21. P. Gallo, M. Rapinesi, and M. Rovere, *J. Chem. Phys.* **117** (2002) 7.
22. H. E. Gottlieb, V. Kotlyar, and N. Abraham, *J. Org. Chem.* **62** (1997) 7512.
23. D. R. Banyai, T. Murakhtina, and D. Sebastiani, *Magn. Reson. Chem.* **48** (2010) S56.
24. P. A. Bonnaud, B. Coasne, and R. J.-M. Pellenq, *J. Phys.-Condens. Mat.* **22** (2010) 284110.
25. A. A. Milischuk and B. M. Ladanyi, *J. Chem. Phys.* **135** (2011) 174709.
26. T. G. Lombardo, N. Giovambattista, and P. G. Debenedetti, *Faraday Discuss.* **141** (2009) 359.
27. R. Mancinelli, F. Bruni, and M. A. Ricci, *J. Phys. Chem. Lett.* **1** (2010) 1277.
28. R. Mills, *J. Phys. Chem.* **77** (1973) 685.
29. M. Sulpizi, M. Gaigeot, and M. Sprik, *J. Chem. Theory* **8** (2012) 1037.
30. Computer code CP2K, available from www.cp2k.org/.
31. A. D. Becke, *Phys. Rev. A* **38** (1988) 3098.
32. S. Goedecker, M. Teter, and J. Hutter, *Phys. Rev. B* **54** (1996) 1703.
33. S. Grimme, *J. Comput. Chem.* **27** (2006) 1787.
34. J. VandeVondele and J. Hutter, *J. Chem. Phys.* **127** (2007) 114105.
35. D. Sebastiani and M. Parrinello, *Chem. Phys. Chem.* **3** (2002) 675.
36. J. Schmidt, J. VandeVondele, I. F. Kuo, D. Sebastiani, J. I. Siepmann, J. Hutter, and C. J. Mundy, *J. Phys. Chem. B* **113** (2009) 11959.
37. J. Schmidt, A. Hoffmann, H. W. Spiess, and D. Sebastiani, *J. Phys. Chem. B* **110** (2006) 23204.
38. T. Murakhtina, J. Heuft, J. E. Meijer, and D. Sebastiani, *Chem. Phys. Chem.* **7** (2006) 2578.
39. Y. J. Lee, T. Murakhtina, D. Sebastiani, and H. W. Spiess, *J. Am. Chem. Soc.* **129** (2007) 12406.
40. A. Hoffmann, D. Sebastiani, E. Sugiono, K. S. Kim, H. W. Spiess, and I. Schnell, *Chin. Phys. Lett.* **388** (2004) 164.
41. K. Münnemann and H. W. Spiess, *Nature Phys.* **7** (2011) 522.
42. T. Metzroth, A. Hoffmann, R. Martín-Rapún, M. M. J. Smulders, K. Pieterse, A. R. A. Palmans, J. A. J. M. Vekemans, E. W. Meijer, H. W. Spiess, and J. Gauss, *Chem. Sci.* **2** (2011) 69.

This article is protected by German copyright law. You may copy and distribute this article for your personal use only. Other use is only allowed with written permission by the copyright holder.

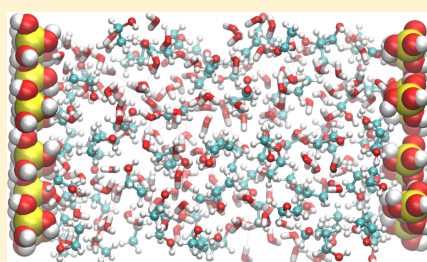
Local Microphase Separation of a Binary Liquid under Nanoscale Confinement

Xiang-Yang Guo, Tobias Watermann, and Daniel Sebastiani*

Institut für Chemie, Martin-Luther-Universität Halle-Wittenberg, 06120 Halle (Saale), Germany

ABSTRACT: The structural and diffusive properties of an ethanol–water mixture under hydrophilic nanoscale confinement are investigated by means of molecular dynamics simulations based on the CHARMM force field. The resulting density profiles illustrate that demixing of solvents occurs at the pore wall region, which is composed of silanol molecules in our case. Ethanol molecules are more likely to attach to the wall via hydrogen bonds than water molecules. A noticeable O–H bond orientation is observed for the ethanol molecules in this region, which can be explained by the formation of two specific hydrogen bonds between ethanol and silanol. Water, in contrast, resides mostly outside the interfacial region and is in favor of forming small hydrogen bonded strings and clusters with other water molecules.

This phenomenon is corroborated by both the orientation of ethanol hydroxyl groups and the radial distribution functions of the solvent oxygen atom to the silanol hydrogen atom. Ethanol selectively attaches to the wall and forms a layer close to the wall. The hydrophobic headgroups of these ethanol molecules lead to an internal hydrophobic interface layer, which in turn yields cluster structures in the adjacent water. The self-diffusion of water in the confined ethanol–water mixture at the center of the pore is faster than that of water in the bulk ethanol–water mixture; ethanol, on the other hand, diffuses slower when it is confined.



INTRODUCTION

Ethanol (EtOH) as one of the simplest alcohols has a lot of applications in laboratories and industrial processes. Considerable research into the nature of ethanol–water solutions at the molecular level gives us some insight into their properties. Already in the bulk phase, an ethanol–water mixture as a highly polar hydrogen-bonding liquid offers a great richness of structural diversity and physical–chemical phenomena.^{1–3} Also, it has been discovered that, when ethanol is mixed with water, the entropy of the solution increases far less than expected. Experimental evidence indicates that the hydrophobic part of alcohol molecules gives rise to the existence of heterogeneous structure at the molecular level in aqueous solutions.^{4–10}

Understanding the properties of ethanol–water at interfaces on the molecular level is very important for many chemical and physical processes.^{11–14} It has been proved by many studies that surface-directed phase separation appears in confined binary mixtures while one component is preferentially attracted to the walls.^{15–18} However, with regard to the interaction of ethanol–water mixtures with silica surfaces, our atomistic understanding is far from satisfactory. Water molecules can interact with the surface through hydrophobic or hydrophilic interactions and hydrogen bonding. This leads to the partial ordering of water molecules in the vicinity of the confining surface.¹⁹ To date, numerous studies focusing on water confined in porous frameworks have been carried out via simulations and experiments.^{20–27}

Previously, we have reported an ab initio study of pure water under silica confinement by using a surface model that resembles the pore structural feature of MCM-41.²⁸ We concluded that the presence of the silica walls has a strong effect on the structure and dynamical properties of pure water. At the center of the pore, the calculated ¹H chemical shifts of the confined water are found to be higher than bulk water, which implies an enhanced hydrogen bonding network in this region. In the vicinity of the wall, a strongly weakened hydrogen bonding and distinctive layering of the water density appeared. Furthermore, a decrease in the diffusion coefficient of the confined water rate by a factor of 4 was observed when comparing to bulk water values. The recognition of the confinement effect stimulated us to carry on the investigation to a new aspect, namely, the simulations of liquid mixtures under silica confinement.

Rodríguez et al.²⁹ studied equimolar mixtures of water and acetonitrile confined between two silica walls using MD simulations. Their result on the hydrophilic confinement shows a net increment of water in the interplate region with a highly inhomogeneous local distribution. This stable water layer is found to be fully coordinated to the silanol groups due to the optimal geometrical arrangement of the wall surfaces. B. Ratajska-Gadomska and W. Gadomski³⁰ reported the solvation of ethanol in water confined by gelatin gel studied by Raman

Received: May 27, 2014

Revised: August 7, 2014

Published: August 8, 2014

spectroscopy. Their work indicates that, when an ethanol-rich solution is confined in gelatin gel, so-called ethanol sandwich clusters exist with a layer of water molecules inside. In order to provide further atomistic insight into alcohol solutions under confinement, we present here a study of ethanol–water mixtures confined within silica surfaces. The silanol groups on the silica surface have a hydrophilic character. This yields a certain competition of hydrogen bonds between silanol–solvent and solvent–solvent. Therefore, the conformation and the donor–acceptor preferences in the ethanol–water mixture are even more complicated than water–silica and ethanol–water bulk mixtures. In this work, we perform classical MD simulations on ethanol–water mixtures at the presence of two silanol walls. We compute the density profiles and self-diffusion coefficients for both ethanol and water, and the results are compared with bulk solvents. The radial distribution functions and orientations of ethanol molecules are calculated as well. Furthermore, we analyze the hydrogen bonding in the ethanol + water/silanol system so as to increase our understanding of the influence of spatial confinement on the structure and dynamics of alcohol mixtures.

COMPUTATIONAL DETAILS

The NAMD software package³¹ was used throughout this work to perform the molecular dynamic simulations. The CHARMM force field parameter files^{32–34} were applied for both solvent molecules and silanol groups. The TIP3P water model was used. The particle-mesh Ewald (PME) algorithm was used for long-range electrostatics interactions, and a switching function with a cutoff of 12 Å and a switchdist of 10 Å was employed for the Lennard-Jones interactions. Diffusion simulations were carried out at six different temperatures from 298 to 348 K. A microcanonical (NVT) ensemble and canonical (NVE) ensemble were used, and the Langevin dynamics has been employed to keep the system at the desired temperature during NVT simulations. The simulation outcomes were analyzed through our own programs and VMD plugins.^{35–37}

A snapshot of the unit cell during one simulation is presented in Figure 1. Two flat silanol walls consisting of 24 Si(OH)₄ are

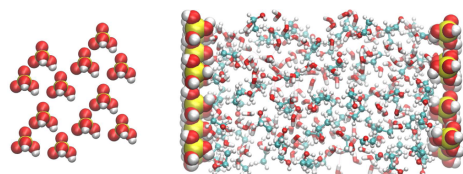


Figure 1. Picture of the silanol wall model normal to the wall surface (left) and a snapshot of an equilibrated ethanol–water/silanol system during a simulation at 338 K (right). Two silanol walls contain 24 Si(OH)₄, with 87 ethanol molecules and 148 water molecules confined in between.

placed along the *x* direction on both sides of an ethanol–water solution box with a size of 30 × 20 × 20 Å³. The unit cell contains 148 water, 87 ethanol, and 24 silicic acids. The total number of atoms is 1443. This corresponds to a molar composition of *x*_{H₂O} = 0.63 and *x*_{EtOH} = 0.37. Three hydroxyl groups facing outside the unit cell are fixed in space. In case molecules enter the vacuum region between the periodic boxes,

a force is applied on both sides of the wall to keep them in the solvent region.

To permit full electrostatic calculations via PME summation, the systems were made periodic in all directions with the elementary cell extended to accommodate a vacuum outside the silica surfaces along the *x* direction. The introduction of a vacuum gap between the unit cells is sufficiently large that adjacent images of the surface do not interact across the vacuum, which enables a surface to be modeled within the constraints of 3-D periodic boundary conditions. The resulting dimension of a simulation cell is 65 × 20 × 20 Å³. In order to better manifest the effect of confinement, simulations of bulk water, bulk ethanol, and bulk ethanol–water mixture under the same conditions were carried out to enable comparisons with a confined system. The periodic unit cell of the bulk ethanol–water mixture is the same as the solution box between the slabs, also with a size of 30 × 20 × 20 Å³.

RESULTS AND DISCUSSION

Diffusion. Self-diffusion is the simplest yet most fundamental form of transport at the molecular level which describes the translational motion of the individual component in a mixture.³⁸ The self-diffusion motion of molecules is characterized by a self-diffusion coefficient *D*_s. At 298.15 K, the *D*_s of bulk water and bulk ethanol has been experimentally determined to be 2.299 × 10⁹ s⁻¹ and 1.09 × 10⁹ m² s⁻¹, respectively.⁴⁰ The mobility of pure water in silica confinement is known to be slower than that in the pure bulk state due to the interactions with the hydrophilic pore walls. Experimental and computational reports indicate that *D*_s of confined water ranges from 23 to 64% of the value of bulk water.^{22,28,41–43} Nevertheless, in our system, water interacts not only with the silanol wall but also with ethanol, and the mutual diffusion of the two components leads to altering of individual self-diffusion. Figure 2 displays the values of *D*_s for water and

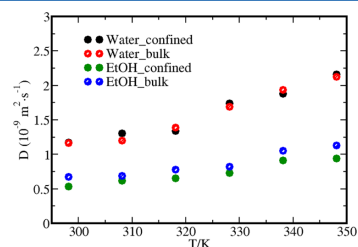


Figure 2. Self-diffusion coefficients of water and ethanol in confined alcohol solution at different temperatures compared with the corresponding bulk mixture.

ethanol confined in our hydrophilic slabs, along with the values of the corresponding unconfined (bulk) mixture under the same conditions. The temperature of the simulations varies from 298 to 348 K. All the diffusion coefficients *D*_s are determined from the time dependence of the mean squared displacement (MSD) via the Einstein relationship

$$D_s = \frac{\text{MSD}}{2dt} = \left\langle \frac{(R(t) - R(0))^2}{2dt} \right\rangle \quad (1)$$

with t representing the time and d the number of dimensions in which the diffusion is measured. For the simulations of confined water and ethanol, only diffusion in the two directions parallel to the surface is taken into account.⁴²

Our simulations show (Figure 2) that ethanol has a slower diffusion under confinement than in the bulk mixture at all temperatures. At 298 K, ethanol in the confined and bulk mixture exhibits diffusion constants of $D_{s,\text{EtOH mix}} = 0.53 \times 10^9$ and $0.67 \times 10^9 \text{ m}^2 \text{ s}^{-1}$, respectively. In both cases, the self-diffusion of ethanol is slower than that in pure liquid, which corresponds to $D_{s,\text{EtOH pure}} = 1.08 \times 10^9 \text{ m}^2 \text{ s}^{-1}$ obtained by our simulation. Water in the confined mixture, on the other hand, behaves differently. Surprisingly, the self-diffusion of confined water in the alcohol water mixture has almost the same rate as in the bulk mixture. At some temperatures, we see a slightly accelerated diffusion for water in the confined state. This anomalous dynamics of water under confinement is closely related to the solvent structure between slabs, as described in the following sections.

Intraliquid Layer Formation. The mixture density (Figure 3a) illustrates the overall spatial distribution of the water–ethanol solution inside the cell, which is similar to that in other hydrophilic confinement reported in the literature.^{20,24,44} The average density of the confined mixture is about $\rho_{\text{mix}} = 0.84 \text{ g/cm}^3$. Inspection of Figure 3a reveals the presence of a well-defined adsorption layer from $x = 12.5 \text{ \AA}$ to the wall. The highest density of the mixture is reached right next to the wall

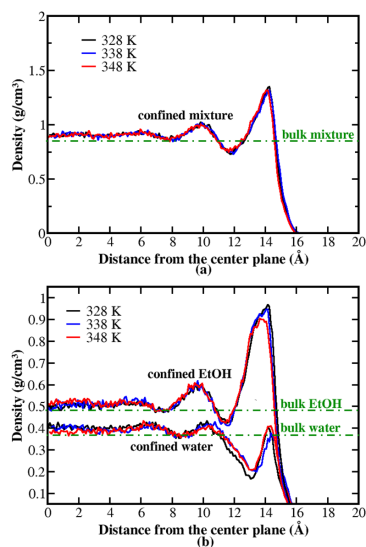


Figure 3. Density of the water/ethanol mixture (a) and partial densities of ethanol and water (b), all between silanol slabs at various T as a function of the perpendicular distance to the center (yz) plane at $x = 0$; the silica wall starts from 15 \AA . All densities are averaged over the NVT trajectory and symmetrized to the center plane. The densities are compared to the corresponding densities for the bulk mixture, which is 0.48 g/cm^3 for EtOH, 0.37 g/cm^3 for water, and 0.85 g/cm^3 for the mixture.

with an amplitude of around 1.30 g/cm^3 . The intermediate layer ($8\text{--}12.5 \text{ \AA}$) represents the boundary between the structured interfacial liquid and the ordinary bulk liquid, since no further structuring is evident beyond this layer. The density reaches a constant value around 0.92 g/cm^3 at the center ($x \leq 6.0 \text{ \AA}$).

The partial densities (Figure 3b) illustrate, in more detail, the contributions of the individual solvents to the total density profile. In the interfacial region, a surge in EtOH density is observed starting from 12.0 \AA , which also reaches its maximum in close vicinity to the wall at 14.0 \AA . The amplitude for the highest peak at 328 K is $\rho_{\text{EtOH}} = 0.96 \text{ g/cm}^3$, which is around twice as high as the EtOH density at the center region. The high density at the first peak indicates strong hydrogen bonding between ethanol molecules and silanol groups. Then, a diffuse layer from 7.7 to 10.7 \AA follows with amplitude around 0.6 g/cm^3 . For $0 \leq x \leq 7.0 \text{ \AA}$, the density approaches a plateau with a value of the cell average of 0.5 g/cm^3 . In contrast to ethanol, the water density is found to exhibit a rapid decrease in the proximity of the wall. After a narrow adsorption layer at 14.0 \AA , the water density falls rapidly under the bulk value and reaches a minimum at 13.0 \AA . Another layer of water is found located at $8\text{--}11 \text{ \AA}$. At the center of the cell ($0 \leq x \leq 7$), the water density is distinctively higher than in the interfacial region with a value around 0.4 g/cm^3 , which is also higher than the water density in the bulk mixture. Comparing the two graphs, we note that, in the proximity of the wall, we observe a surprisingly pronounced demixing: ethanol is concentrated at the wall, while water disseminates to the cell center.

The increased partial density of ethanol at the confinement silanol groups gives rise to the formation of a hydrophobic layer inside the liquid. This very interesting phenomenon results in an apparent competition of the hydrophilicity of the pore walls from the point of view of the water phase. Hence, the water which is located toward the center of the pore effectively sees a hydrophobic interface.

Regarding the temperature dependence of the density profile, we observe only a small variation in position and amplitude of the peaks. The highest EtOH density is obtained at the lowest temperature 328 K where the lowest water density is reached. This indicates that the demixing of ethanol and water tends to increase upon lowering the temperature, illustrating the reduction of entropic effects in favor of enthalpic aspects.

Internal Liquid Structure. The radial distribution functions (RDFs) between silanol hydrogen atoms and solvent oxygen atoms are presented in Figure 4 for water and ethanol confined in the silica slabs. The RDF in Figure 4 gives the probability of finding a solvent oxygen atom at distance r from a hydrogen atom of the silanols. Only those hydrogen atoms from the silanol hydroxyl group facing toward the center are included. The position of the first peak on both graphs is located at 1.97 \AA , which is very close to the value of a typical H–O hydrogen bond length.⁴⁵ This means that both water and ethanol molecules are acting as hydrogen bond acceptors for the silanols. On the other hand, the area under the first peak in both graphs (Figure 4) shows that the probability of finding an ethanol oxygen is much higher than finding a water oxygen. Besides, most of the curve for ethanol is above 1, which corresponds to the partial demixing phenomenon observed in the vicinity of the wall. The oxygen atoms of the ethanol are much more likely to form hydrogen bonds with silanol. Integrating the RDF over r , we find that, at the wall region, the numbers of water and ethanol are almost the same, despite the

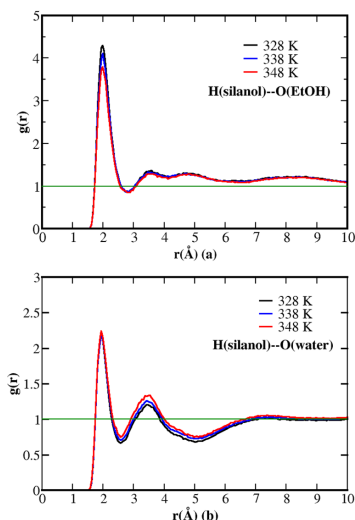


Figure 4. RDFs of silanol hydrogen atoms to solvent oxygen atoms: (a) H(si)–O(EtOH) and (b) H(si)–O(water) at three different temperatures.

fact that in the system there are many more water molecules. However, the numbers of two components start to differ from each other with increasing r from the wall; the number of water molecules goes up much faster when $r \geq 6$ Å.

As mentioned before, the solution becomes more structured as T decreases, and the change in temperature only affects the amplitudes of the peaks, not the positions. By comparing graphs in Figure 4a and b, the different impact of temperature on ethanol and water is demonstrated. In graph a, the growth of the height of the first peak with decreasing temperature corresponds to the fact that more ethanols are hydrogen bonded by the silanols at lower temperature. In comparison, the first peak in graph b for water does not vary much with temperature, but the height of the second peak goes up with the rising of temperature, whereas the second peak for $g(r)$ of H–O (EtOH) is not influenced by T . These results indicate the number of ethanol molecules at the wall region increases as the temperature decreases, but this influence becomes weaker with increasing distance from the wall. The number of water molecules at the adsorption layer, on the other hand, is not affected by the temperature, when the distance to the silanol oxygen is larger than 3.5 Å, the number of water molecules grows when temperature increases.

It is worth mentioning that, even without the presence of silanol walls, molecular segregation can still be observed in the bulk ethanol–water mixture. From the O–O RDF obtained from our simulation on bulk liquids at 298 K (Figure 5), the intrawater (Ow–Ow) RDF in pure water is compared with the Ow–Ow RDF in the bulk ethanol–water mixture. The first peak amplitude of the Ow–Ow RDF for the ethanol–water solution is obviously larger than that of the corresponding peak for pure water, but their shapes and positions are very similar. The second peaks of both Ow–Ow RDFs have close values in height and position. The Oe–Ow RDF has a different shape

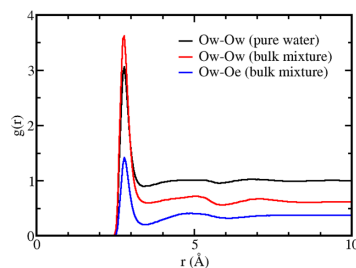


Figure 5. Oxygen–oxygen RDFs of bulk pure water compared with the bulk ethanol–water mixture. The RDFs are referenced to the molar fraction of water.

compared with the Ow–Ow RDF; especially its second peak at 5 Å is more apparent than that of the Ow–Ow RDFs. On the other hand, the first peak of the Oe–Oe RDF (Figure 6) for the

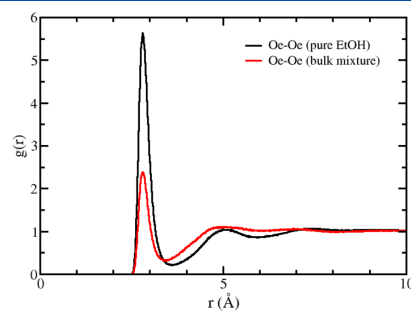


Figure 6. Oxygen–oxygen RDFs of bulk pure ethanol (black) compared with the bulk ethanol–water mixture (red).

mixture shrinks in size compared to pure ethanol and the second peak has a larger amplitude and radius. This is in very good agreement with the experimental results reported by Dixit et al.⁴ on methanol–water solutions using the neutron diffraction method. Their research suggests that the methanol hydroxyl group enhances tetrahedral structure in the surrounding water; most water molecules form small clusters and serve as a bridge between hydroxyl groups of methanol molecules. Upon addition of water, the methanol hydroxyl groups were pushing apart while the methyl headgroups were getting closer. In conclusion, the partial microphase separation which is detectable already in unconfined water–alcohol mixtures is amplified under hydrophilic geometric confinement. In our system, ethanol as the less hydrophilic species has a higher possibility to form hydrogen bonds with silanol groups compared to water. Hence, the water clustering is significantly enhanced at the center of the cell when the ethanol hydroxyl group attaches to the wall and the hydrophobic alkyl parts face toward the center. Also, we notice that the decrease of temperature strengthens this demixing behavior of confined solvents.

Angular Distribution of Ethanol Molecules. The results discussed above suggest that the ethanol molecules form a layer in the wall region. It is also interesting to probe the orientation

of these ethanol molecules and the influence of the wall on this orientation. Conversely, the arrangement of ethanol at the interface also reflects the dynamically fluctuating H-bonding network between ethanol and silanol. We define α , γ , and θ as the angles between the normal vector of the wall surface pointing toward the cell center, i.e., surface vector $(1, 0, 0)$ and O–H, $\text{CH}_3\text{--CH}_2$, and $\text{CH}_2\text{--OH}$ bonds of the ethanol molecule.

We computed the occurrence of all possible angles over the whole trajectory. The ethanol angular distribution recorded in the simulation at 328 K is illustrated by Figures 7 and 8. The

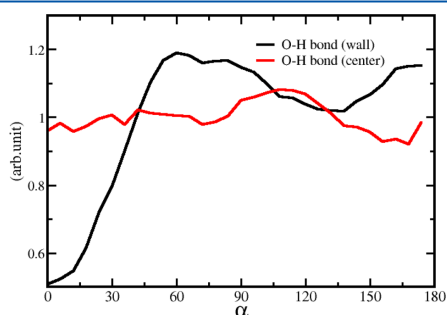


Figure 7. Angular distribution of the ethanol O–H bonds relative to the wall surface normal at the wall region (black) and at the cell center (red).

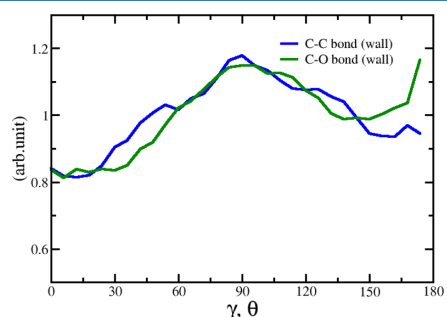


Figure 8. Angular distribution of ethanol $\text{CH}_3\text{--CH}_2$ bonds (blue) and $\text{CH}_2\text{--OH}$ bonds (green) at the wall region.

“wall” and “center” denote the ethanol located within 5 Å to the silica wall or 5 Å cell center, respectively. The angle α is normalized by $1/\sin(\alpha)$; the same normalization was applied to γ and θ .

Figure 7 shows that the occurrence of ethanol at the wall region is generally much higher than that at the center region. Notably, there is no apparent orientation for the ethanol at the cell center and the OH bonds are evenly distributed in all possible angles from 0 to 180°. In contrast, at the interfacial region, the ethanol O–H bond is more likely to be found pointing to the wall with α ranging from 60 to 180°. Two maximal values are visible at around 60 and 180°, respectively, which suggests two forms of hydrogen bonding between silanol

and ethanol, namely, $\text{O}(\text{EtOH})\text{--H}(\text{Si})$ and $\text{O}(\text{Si})\text{--H}(\text{EtOH})$. The $\text{CH}_3\text{--CH}_2$ and $\text{CH}_2\text{--OH}$ bonds of the ethanol molecule at the wall region tend to have a broad distribution over all possible angles (Figure 8). A peak at 90° is observed, which corresponds to an orientation of the bonds parallel to the silica surfaces. This information confirms the qualitative observations from the simulation that more ethanol can be found hydrogen bonded to silanol groups.

Hydrogen Bonding Network. There are in total five possible hydrogen bond (H-bond) species inside the system, namely, ethanol–ethanol (e–e), ethanol–water (w–e), water–water (w–w), silanol–ethanol (e–si), and silanol–water (w–si) hydrogen bonds. The competitive interplay between those hydrogen bonds and the combination of hydrogen bonds with van der Waals interactions between the ethanol alkyl chains with silanol groups are responsible for the peculiar behavior of the confined solution.

We calculated the average hydrogen bond numbers of ethanol and water confined between the slabs for the trajectory at 328 and 338 K (Table 1). In a H-bond, an electropositive

Table 1. Average Numbers of Hydrogen Bonds in Our Geometrically Confined Water–Ethanol Mixtures

	Solvent–Silanol		
	w-si	e-si	
328 K	9.5	9.2	
338 K	9.2	8.9	
	Solvent–Solvent at 328 K		
	w-w	w-e	e-e
total number ^a	110	92.4	18.1
wall region ^b	14.7	17.5	4.5
intermediate ^b	36.2	27.8	5.1
center region ^b	36.0	27.0	4.4
	Solvent–Solvent at 338 K		
	w-w	w-e	e-e
total number ^a	106	89.2	18.5
wall region ^b	14.3	16.6	4.8
intermediate ^b	34.4	26.6	5.2
center region ^b	35.9	26.5	4.4

^a“Total number” denotes the average overall number of H-bonds inside the unit cell. ^bThe solvent molecules located within 5 Å to the silanol walls and the center of the confinement are denoted as “wall region” and “center region”, respectively, while the remaining solvent molecules are denoted by “intermediate”.

hydrogen atom is shared between two electronegative atoms, e.g., the oxygens in ethanol, water, and silanol molecules. A H-bond is announced when the distance between a donor and an acceptor is less than 3.5 Å and when the angle between the bond vector and the O–O vector is less than a threshold angle 30°.

First, we notice that the number of water–silanol H-bonds is close to that of ethanol–silanol H-bonds. This reflects the fact that the number of ethanol and water molecules at the wall region is similar even though there are many more water molecules in the mixture. We can also see that the walls have a significant effect on the spatial distribution of all three solvent hydrogen bond species in the mixture. Solvent molecules are more structured in the intermediate region. At the wall region, the solvent–solvent H-bond number reaches the smallest value due to the hydrogen bonding capability of silanols. The number

of e–e hydrogen bonds is significantly smaller compared with w–w and w–e hydrogen bonds. This indicates that ethanol molecules were not clustering together like water; hence, their conformation can be distorted easier by silanol groups. This in turn is directly responsible for the high ethanol density at the wall region. We also note that this tendency does not change with temperature.

CONCLUSION

In this work, a binary mixture (water–ethanol) confined between silanol slabs was investigated by MD simulations based on the CHARMM force field. Our analysis of the trajectories revealed that, in the vicinity of silanols, a partial demixing of ethanol and water occurs. Water is more likely to form stable clusters, while ethanol is in contrast more flexible and therefore has a higher possibility to hydrogen bond with a silanol group. This, in return, enhances the water clustering structure; thus, demixing is most pronounced at the wall region. The molecular separation occurs due to the phenomenon of adsorption preference of silanol between water and ethanol. The results could also be important for better understanding the behavior of fluids in subsurface environments. Moreover, the self-diffusion coefficients of water and ethanol with and without confinement were calculated; the enhancement of the self-diffusion coefficients of water and the reduction of that of ethanol and the cause of this phenomenon are well manifested.

Special attention is paid to hydrogen bonding network and its influence on the anomalous diffusion behavior and molecular structure. Our simulations indicate that a significant restructuring of the hydrogen bond network between water and ethanol occurs as well as changes in the water–water hydrogen bonds due to the presence of the silanol walls. The hydrophobic environment generated by a layer structure of the ethanol alkyl groups further supports the stabilization of these water clusters as compared to the unconfined case.

AUTHOR INFORMATION

Corresponding Author

*E-mail: daniel.sebastiani@chemie.uni-halle.de.

Notes

The authors declare no competing financial interest.

ACKNOWLEDGMENTS

This work has been supported by the German Research Foundation (DFG) within the DFG-Forschergruppe 1583 (TP8). The computing infrastructure was provided by the ZEDAT high-performance cluster in Freie Universität Berlin. The authors thank the China Scholarship Council (CSC) for providing a scholarship.

REFERENCES

- (1) Onori, G. Adiabatic Compressibility and Structure of Aqueous Solutions of Ethyl Alcohol. *J. Chem. Phys.* **1988**, *89*, 4325–4332.
- (2) Wakisaka, A.; Matsuura, K.; Uranaga, M.; Sekimoto, T.; Takahashi, M. Azeotropy of Alcohol–water Mixtures from the Viewpoint of Cluster-level Structures. *J. Mol. Liq.* **2011**, *160*, 103–108.
- (3) Wakisaka, A.; Komatsu, S.; Usui, Y. Solute–solvent and Solvent–solvent Interactions Evaluated through Clusters Isolated from Solutions: Preferential Solvation in Water–Alcohol Mixtures. *J. Mol. Liq.* **2001**, *90*, 175–184.
- (4) Dixit, S.; Crain, J.; Poon, W. C. K.; Finney, J. L.; Soper, A. K. Molecular Segregation Observed in a Concentrated Alcohol–water Solution. *Nature* **2002**, *416*, 829–832.
- (5) Harris, K. R.; Newitt, P. J.; Derlacki, Z. J. Alcohol Tracer Diffusion, Density, NMR and FTIR Studies of Aqueous Ethanol and 2,2,2-trifluoroethanol Solutions. *J. Chem. Soc., Faraday Trans.* **1998**, *94*, 1963–1970.
- (6) Price, W. S.; Ide, H.; Arata, Y. Solution Dynamics in Aqueous Monohydric Alcohol Systems. *J. Phys. Chem. A* **2003**, *107*, 4784–4789.
- (7) Guo, J. H.; Luo, Y.; Augustsson, A.; Kashtanov, S.; Rubensson, J. E.; Shuh, D. K.; Ågren, H.; Nordgren, J. Molecular Structure of Alcohol–Water Mixtures. *Phys. Rev. Lett.* **2003**, *91*, 157401–157402.
- (8) Lin, K.; Hu, N.; Zhou, X.; Liu, S.; Luo, Y. Reorientation Dynamics in Liquid Alcohols from Raman Spectroscopy. *J. Raman Spectrosc.* **2012**, *43*, 82–88.
- (9) Asenbaum, A.; Pruner, C.; Wilhelm, E.; Mijakovic, M.; Zoranic, L.; Sokolic, F.; Kezic, B.; Perera, A. Structural Changes in Ethanol–water Mixtures: Ultrasonics, Brillouin Scattering and Molecular Dynamics Studies. *Vib. Spectrosc.* **2012**, *60*, 102–106.
- (10) Corsaro, C.; Maisano, R.; Mallamace, D.; Dugo, G. 1H NMR Study of Water/methanol Solutions as a Function of Temperature and Concentration. *Physica A* **2013**, *392*, 596–601.
- (11) Sung, J.; Waychunas, G. A.; Shen, Y. R. Surface-Induced Anisotropic Orientations of Interfacial Ethanol Molecules at Air/Sapphire(1102) and Ethanol/Sapphire(1102) Interfaces. *J. Phys. Chem. Lett.* **2011**, *2*, 1831–1835.
- (12) Tereshchuk, P.; Da Silva, J. L. F. Ethanol and Water Adsorption on Close-Packed 3d, 4d, and 5d Transition-Metal Surfaces: A Density Functional Theory Investigation with van der Waals Correction. *J. Phys. Chem. C* **2012**, *116*, 24695–24705.
- (13) Cooke, D. J.; Gray, R. J.; Sand, K. K.; Stipp, S. L. S.; Elliott, J. A. Interaction of Ethanol and Water with the {1014} Surface of Calcite. *Langmuir* **2010**, *26*, 14520–14529.
- (14) Andoh, Y.; Kurahashi, K.; Sakuma, H.; Yasuoka, K.; Kurihara, K. Anisotropic Molecular Clustering in Liquid Ethanol Induced by a Charged Fully Hydroxylated Silicon Dioxide (SiO₂) Surface. *Chem. Phys. Lett.* **2007**, *448*, 253–257.
- (15) Yabunaka, S.; Okamoto, R.; Onuki, A. Phase Separation in a Binary Mixture Confined between Symmetric Parallel Plates: Capillary Condensation Transition near the Bulk Critical Point. *Phys. Rev. E* **2013**, *87*, 32405.
- (16) Tanaka, H.; Araki, T. Surface Effects on Spinodal Decomposition of Incompressible Binary Fluid Mixtures. *Europhys. Lett.* **2000**, *51*, 154–160.
- (17) Chen, W. Phase Separation of Binary Nonadditive Hard Sphere Fluid Mixture Confined in Random Porous Media. *J. Chem. Phys.* **2013**, *139*, 154712.
- (18) Sharma, B. R.; Singh, R. N. Separation of Species of a Binary Fluid Mixture Confined between two Concentric Rotating Circular Cylinders in Presence of a Strong Radial Magnetic Field. *Heat Mass Transfer* **2010**, *46*, 769–777.
- (19) Grünberg, B.; Emmler, T.; Gedat, E.; Shenderovich, I.; Findenegg, G. H.; Limbach, H.; Buntkowsky, G. Hydrogen Bonding of Water Confined in Mesoporous Silica MCM-41 and SBA-15 Studied by 1H Solid-state NMR. *Chem.—Eur. J.* **2004**, *10*, 5689–5696.
- (20) Hwang, D. W.; Sinha, A. K.; Cheng, C. Y.; Yu, T. Y.; Hwang, L. P. Water Dynamics on the Surface of MCM-41 via 2H Double Quantum Filtered NMR and Relaxation Measurements. *J. Phys. Chem. B* **2001**, *105*, 5713–5720.
- (21) Faraone, A.; Liu, L.; Mou, C. Y.; Shih, P. C.; Copley, J. R. D.; Chen, S. H. Translational and Rotational Dynamics of Water in Mesoporous Silica Materials: MCM-41-S and MCM-48-S. *J. Chem. Phys.* **2003**, *119*, 3963–3971.
- (22) Shirono, K.; Daiguji, H. Molecular Simulation of the Phase Behavior of Water Confined in Silica Nanopores. *J. Phys. Chem. C* **2007**, *111*, 7938–7946.
- (23) Kleestorfer, K.; Vinek, H.; Jentys, A. Structure Simulation of MCM-41 Type Materials. *J. Mol. Catal. A: Chem.* **2001**, *166*, 53–57.
- (24) Gallo, P.; Rovere, M.; Chen, S. H. Water Confined in MCM-41: a Mode Coupling Theory Analysis. *J. Phys.: Condens. Matter* **2012**, *24*, 064109.

- (25) Shenderovich, I. G.; Mauder, D.; Akcakayiran, D.; Buntkowsky, G.; Limbach, H. H.; Findenege, G. H. NMR Provides Checklist of Generic Properties for Atomic-scale Models of Periodic Mesoporous Silicas. *J. Phys. Chem. B* **2007**, *111*, 12088–12096.
- (26) Sulpizi, M.; Gaigeot, M.; Sprik, M. The Silica–Water Interface: How the Silanols Determine the Surface Acidity and Modulate the Water Properties. *J. Chem. Theory Comput.* **2012**, *8*, 1037–1047.
- (27) Thompson, H.; Soper, A. K.; Ricci, M. A.; Bruni, F.; Skipper, N. T. The Three-dimensional Structure of Water Confined in Nanoporous Vycor Glass. *J. Phys. Chem. B* **2007**, *111*, 5610–5620.
- (28) Guo, X. Y.; Watermann, T.; Keane, S.; Allolio, C.; Sebastiani, D. First Principles Calculations of NMR Chemical Shifts of Liquid Water at an Amorphous Silica Interface. *Z. Phys. Chem.* **2012**, *226*, 1415–1424.
- (29) Rodriguez, J.; Elola, M. D.; Laria, D. Polar Mixtures under Nanoconfinement. *J. Phys. Chem. B* **2009**, *113*, 12744–12749.
- (30) Ratajska-Gadomska, B.; Gadomski, W. Influence of Confinement on Solvation of Ethanol in Water Studied by Raman Spectroscopy. *J. Chem. Phys.* **2010**, *133*, 2345051–2345057.
- (31) Phillips, J. C.; Braun, R.; Wang, W.; Gumbart, J.; Tajkhorshid, E.; Villa, E.; Chipot, C.; Skeel, R. D.; Kalé, L.; Schulten, K. Scalable Molecular Dynamics with NAMD. *J. Comput. Chem.* **2005**, *26*, 1781.
- (32) Klauda, J. B.; Venable, R. M.; Freites, J. A.; O'Connor, J. W.; Tobias, D. J.; Mondragon-Ramirez, C.; Vorobyov, I.; MacKerell, A. D.; Pastor, R. W. Update of the CHARMM All-atom Additive Force Field for Lipids: Validation on Six Lipid Types. *J. Phys. Chem. B* **2010**, *114*, 7830–7843.
- (33) Cruz-Chu, E. R.; Aksimentiev, A.; Schulten, K. Water-silica Force Field for Simulating Nanodevices. *J. Phys. Chem. B* **2006**, *110*, 21497–21508.
- (34) Lopes, P. E. M.; Murashov, V.; Tazi, M.; Demchuk, E.; Mackerell, A. D. Development of an Empirical Force Field for Silica. Application to the Quartz-water Interface. *J. Phys. Chem. B* **2006**, *110*, 2782–2792.
- (35) Humphrey, W.; Dalke, A.; Schulten, K. VMD: Visual molecular dynamics. *J. Mol. Graphics* **1996**, *14*, 33.
- (36) Giorgino, T. Computing 1-D Atomic Densities in Macromolecular Simulations: The Density Profile Tool for VMD. *Comput. Phys. Commun.* **2014**, *185*, 317–322.
- (37) Levine, B. G.; Stone, J. E.; Kohlmeyer, A. Fast Analysis of Molecular Dynamics Trajectories with Graphics Processing Units-Radial Distribution Function Histogramming. *J. Comput. Phys.* **2011**, *230*, 3556–3569.
- (38) Vergeles, M.; Szamel, G. A Theory for Dynamic Friction on a Molecular Bond. *J. Chem. Phys.* **1999**, *110*, 6827–6835.
- (39) Holz, M.; Heil, S. R.; Sacco, A. Temperature-dependent Self-diffusion Coefficients of Water and Six Selected Molecular Liquids for Calibration in Accurate ¹H NMR PFG Measurements. *Phys. Chem. Chem. Phys.* **2000**, *2*, 4740–4742.
- (40) Meckl, S.; Zeidler, M. D. Self-diffusion Measurements of Ethanol and Propanol. *Mol. Phys.* **1988**, *63*, 85–95.
- (41) Takahara, S.; Nakano, M.; Kittaka, S. Neutron Scattering Study on Dynamics of Water Molecules Confined in MCM-41. *J. Phys. Chem. B* **1999**, *103*, 5814–5819.
- (42) Lerbret, A.; Lelong, G.; Mason, P. E.; Saboungi, M. L.; Brady, J. W. Water Confined in Cylindrical Pores: A Molecular Dynamics Study. *Food Biophys.* **2011**, *6*, 233–240.
- (43) Bonnaud, P. A.; Coasne, B.; Pellenq, R. J. M. Molecular Simulation of Water Confined in Nanoporous Silica. *J. Phys.: Condens. Matter* **2010**, *22*, 284110.
- (44) Ng, E. P.; Mintova, S. Nanoporous Materials with Enhanced Hydrophilicity and High Water Sorption Capacity. *Microporous Mesoporous Mater.* **2008**, *114*, 1.
- (45) Dougherty, R. C. Temperature and Pressure Dependence of Hydrogen Bond Strength: A Perturbation Molecular Orbital Approach. *J. Chem. Phys.* **1998**, *109*, 7372–7378.



PCCP

PAPER

View Article Online
View Journal | View Issue

Water and small organic molecules as probes for geometric confinement in well-ordered mesoporous carbon materials

Yeping Xu,^a Tobias Watermann,^b Hans-Heinrich Limbach,^c Torsten Gutmann,^a Daniel Sebastiani^b and Gerd Buntkowsky^{*a}

Cite this: *Phys. Chem. Chem. Phys.*, 2014, 16, 9327

Received 24th February 2014,
Accepted 24th March 2014

DOI: 10.1039/c4cp00808a

www.rsc.org/pccp

Mesoporous carbon materials were synthesized employing polymers and silica gels as structure directing templates. The basic physico-chemical properties of the synthetic mesoporous materials were characterized by ¹H and ¹³C MAS solid-state NMR, X-ray diffraction, transmission electron microscopy (TEM) and nitrogen adsorption measurements. The confinement effects on small guest molecules such as water, benzene and pyridine and their interactions with the pore surface were probed by a combination of variable temperature ¹H-MAS NMR and quantum chemical calculations of the magnetic shielding effect of the surface on the solvent molecules. The interactions of the guest molecules depend strongly on the carbonization temperature and the pathway of the synthesis. All the guest-molecules, water, benzene and pyridine, exhibited high-field shifts by the interaction with the surface of carbon materials. The geometric confinement imposed by the surface causes a strong depression of the melting point of the surface phase of water and benzene. The theoretical calculation of ¹H NICS maps shows that the observed proton chemical shifts towards high-field values can be explained as the result of electronic ring currents localized in aromatic groups on the surface. The dependence on the distance between the proton and the aromatic surface can be exploited to estimate the average diameter of the confinement structures.

Introduction

Porous carbon materials are widely used in industry for adsorption, separation and catalysis.^{1,2} Due to the binding versatility of the carbon atom, these materials exhibit an unprecedented wealth of morphologies. They depend not only on the starting material but also on the conditions of preparation, such as the carbonization temperature which strongly influences the amount of oxygen-containing surface functional groups. Activated carbon is a material with high porosity, broad pore size range and localized microcrystalline structure.³ The broad pore size distribution^{4–8} results in a fairly large number of different local structures and thus different microenvironments for the molecules adsorbed on the surface. This difficult to control nature of activated carbon gave rise to develop well-ordered mesoporous carbon materials with regular properties. The well-ordered mesoporous carbon (CMK-1) was firstly synthesized by using ordered silica as a

template in 1999.⁹ It has a narrow distribution of pore sizes and an ordered pore structure which simplify the surface and pore conditions.

In the last two decades, several systems of activated carbon,^{10–14} carbon nanotubes^{15–18} and graphite^{19–21} have been studied by X-ray^{11,17,18,22–24} and neutron diffraction²⁵ as well as thermal analysis.^{26,27} Most of these studies focused on activated carbon^{28–30} and carbon black³¹ which lack a regular pore structure, and detailed solid-state NMR studies have been very rare up to now.^{30,32,33} This fact motivates us to investigate well-ordered carbon materials employing a combination of solid-state NMR, quantum chemical calculations and thermodynamic methods.

Quantum chemical calculations of the chemical shifts are indispensable for the structural interpretation of NMR-data. Within electronic structure theory, NMR chemical shifts arise from quantum-mechanically induced electronic ring currents. There are two main contributors to a given NMR chemical shift: the intramolecular electrons and the electrons from other molecules. The intramolecular contribution depends on the molecular geometry (bond lengths and angles), whereas the intermolecular part is a function of the relative position and orientation of the considered nuclear spin relative to the molecular fragment or the other molecule which creates these ring currents. This second contribution can be modeled

^a Eduard-Zintl-Institut für Anorganische und Physikalische Chemie, Technische Universität Darmstadt, Alarich-Weiss-Str. 8, D-64287 Darmstadt, Germany.
E-mail: gerd.buntkowsky@chemie.tu-darmstadt.de

^b Institut für Chemie, Martin-Luther-Universität Halle-Wittenberg, von-Danckelmann-Platz 4, 06120 Halle, Germany

^c Institut für Physikalische und Theoretische Chemie, Freie Universität Berlin, Takustr. 3, D-14195 Berlin, Germany



quantum-chemically by means of the so-called nucleus independent chemical shift (NICS) maps.^{34–43}

In the present work we are studying hexagonally ordered mesoporous carbon with a narrow pore size distribution, both experimentally and theoretically, employing guest molecules with characteristic interactions. In the first step, three types of carbon materials are synthesized and their basic properties are characterized by TEM, BET and solid-state NMR. In the second step, small molecules such as water, benzene and pyridine are employed as probes for the surface properties. These systems are characterized employing solid-state NMR experiments at variable temperature. Finally, the interpretation of experimental results is approved by employing theoretical calculations of NICS maps.

Theoretical section

NICS fields

The values of NICS fields at a particular coordinate quantify the relative offset in terms of the NMR chemical shift that a given nuclear spin would experience if it is located at this coordinate. It can be seen as an additive displacement of the actual NMR chemical shift value, which is independent of the species of the nucleus. In other words, the NMR resonance of a proton (or carbon) atom with a NMR chemical shift of X ppm, located in a region with a NICS value of -2 ppm, will appear in the spectrum at $X - 2$ ppm. It should be noted that these NICS fields are computed in all points of space, and not only at the coordinates of actual atoms/spins.

Formally, the induced magnetic field B^{ind} is well defined at any given point R in space without the need for the actual nucleus at that position. $B^{\text{ind}}(R)$ is obtained from a DFT response calculation. The chemical shielding $\sigma(R)$ is then calculated by

$$\sigma(R) = -\frac{\partial B^{\text{ind}}(R)}{\partial B^{\text{ext}}} \quad (1)$$

where B^{ext} is the strength of the external magnetic field. The isotropic chemical shift can be calculated from the trace of this tensor according to

$$\delta(R) = -\frac{1}{3}\text{Tr}[\sigma(R)] \quad (2)$$

Unlike in the case of regular NMR chemical shifts, there is no need for a reference atom per molecule for converting the nuclear shielding into chemical shift values (e.g. TMS). The value of the NICS maps gives the change in the chemical shift for arbitrary protons, e.g. two protons with chemical shifts of 5 and 6 ppm in a NICS map region with -2 ppm will be modified to 3 and 4 ppm, respectively.

Computational details

Calculations of the optimized geometries and nucleus independent chemical shift (NICS) maps have been performed using the CPMD program package. The response calculations were performed using the density functional perturbation (DFPT)^{44,45} module. The BLYP exchange and correlation functional^{46,47} with

additional van der Waals correction and pseudopotentials of Martins–Trouiller type were used employing a plane-wave cutoff of 100 Ry.^{48,49} The visualizations of the NICS maps have been performed using the JMOL program as well as the GIMP image manipulation package for post-processing purposes.

Experimental section

Synthesis of mesoporous carbon

Three different types of mesoporous carbon materials were synthesized for this study. The first two mesoporous carbon materials with ordered pore sizes were directly prepared using Pluronic F-127 as the template, employing a method derived from the procedure described in ref. 50. In a 200 ml polypropylene bottle (PP bottle), 6.61 g of resorcinol was added to a solution composed of 17.4 g of distilled water, 23 g of ethanol and 0.6 ml of hydrochloric acid (5.0 mol l⁻¹). 3.78 g of Pluronic F-127 was added. After stirring for one hour, 10 g of formaldehyde was added to the pellucid solution and continued to stir for 2 hours at 333 K in the sealed PP bottle. To stabilize the gel, the entire system was warmed at 363 K and opened to air for 5 h. The resulting gel was heated under N₂ gas in a home-built tubular oven starting at a carbonization temperature of 300 °C. This temperature was raised in steps of 100 °C every 30 minutes until the final carbonization temperatures of 600 °C or 800 °C were reached. At these temperatures the materials were tempered for 4 hours. According to the final carbonization temperature the materials are denoted as C600 and C800.

The third porous carbon material was synthesized in replica from silica gel and carbonized at 800 °C similar to the description in ref. 51. In this preparation, 1.8 g of sucrose was added into a silica solution containing 4.2 g of tetraethyl orthosilicate (TEOS) in the ratio TEOS:H₂O:EtOH:HCl = 1:6:6:0.01 at 60 °C to form a carbon/silica gel. The composite was carbonized at 800 °C under argon for 4 hours. The silica was removed from the composite by HF solution. This porous carbon material is denoted as C₂SiO₂.

Characterization of ordered carbon materials

The pore textures were investigated through physical adsorption of nitrogen at 77 K on an automatic volumetric sorption analyzer, Quantachrome Nova 1200. The surface area was calculated by the Brunauer–Emmett–Teller (BET)⁵² method in the relative pressure range from 0.05 to 0.2. The pore size distributions were calculated by the Barrett–Joyner–Halenda (BJH) method^{53,54} from desorption branch.

TEM was carried out using a Tecnai F20 (FEI Company, Oregon, USA) equipped with a field emission gun. Images were taken at an accelerating voltage of 160 kV.

All NMR experiments were performed on a 14 T Varian Infinity plus solid state NMR spectrometer equipped with 4 mm and 3.2 mm probes, respectively, corresponding to a frequency of 600.0 MHz for ¹H and 150.9 MHz for ¹³C. All ¹H MAS spectra were recorded at 10 kHz spinning with the spin-echo pulse sequence with a repetition delay of 3 s. 16 scans



were performed for the proton spectra of host materials, and 4 scans for the spectra when guest molecules were added.

^1H and ^{13}C signals were referenced employing the proton, respectively carbon, signals of the trimethylsilyl group of TSP (trimethylsilyl-propionate) set as 0 ppm.

Adsorption of small molecules

To investigate the behavior of small guest molecules in these ordered carbon materials, water as well as benzene and pyridine were chosen as probes. In these adsorption studies, defined amounts of the liquid guest compounds were directly added to the NMR rotor containing weighted amounts of the carbon materials.

To determine the adsorption state of the guest molecules (monolayer or multilayer), the total area of the adsorbate $S_{\text{total area}}$ is needed, which is calculated from:

$$S_{\text{total area}} = S_{\text{cross-section area}} \times \frac{V \times \rho}{M} \times N_A, \quad (3)$$

where $S_{\text{cross-section area}}$ is the cross-section of a single adsorbate molecule, V the volume of the adsorbate, ρ the density of the adsorbate, M the molar mass and N_A the Avogadro constant. The total area of 2 μl of monolayered benzene (the area of a single benzene molecule is 108 \AA^2)⁵⁵ is ca. 14.5 m^2 . If the cross-sectional area of the benzene molecule (42.3 \AA^2)⁵⁶ is employed, the total area of 2 μl of monolayered benzene is estimated to be 5.7 m^2 . In the same way, the total area of 1 μl of pyridine is estimated to be 1.9 m^2 (cross-sectional area of pyridine is 26 \AA^2).⁵⁷

Results and discussion

N_2 isotherms and pore size distributions of the carbon materials

The N_2 isotherms and pore size distributions are shown in Fig. 1. Structural information on the mesoporous materials is collected in Table 1. According to the IUPAC convention,⁵⁸ both

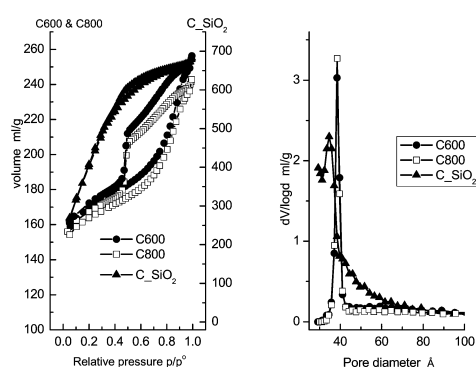


Fig. 1 N_2 isotherms (left) and pore size distributions (right) of the mesoporous carbon materials, C600, C800 and C-SiO_2 .

Table 1 Pore properties of mesoporous carbon materials

	S_{BET} ($\text{m}^2 \text{ g}^{-1}$)	Total pore volume (ml g^{-1})	Pore size (BJH) (nm)
C600	526	0.39	3.85
C800	507	0.37	3.85
C-SiO_2	1556	1.05	3.57

the C600 and C800 materials possess type IV isotherms with type H2 hysteresis loops. Their pore size distribution plots calculated from the desorption branch using the BJH method practically coincide. The similar pore structure characteristics of these two materials show that the difference in carbonization temperature has no influence on the textural structures or pore morphologies.

In contrast, the C-SiO_2 material possesses a type I isotherm according to the IUPAC convention.⁵⁸ Moreover, the pore size distribution is broader compared to the C600 and C800 materials, which is attributed to the absence of the surfactant as a structural template during preparation.

Both the C600 and C800 materials have similar specific surface areas and pore volumes as well as the same narrowly centered pore diameter of 3.85 nm. The C-SiO_2 material has nearly three times larger specific surface area above $1500 \text{ m}^2 \text{ g}^{-1}$, owing to the large number of micropores. Finally, a wider pore size distribution with a slightly smaller median of 3.57 nm is found.

TEM of mesoporous carbon

High resolution TEM images and the corresponding hexagonal diffraction pattern of C600 (Fig. 2) reveal the highly ordered

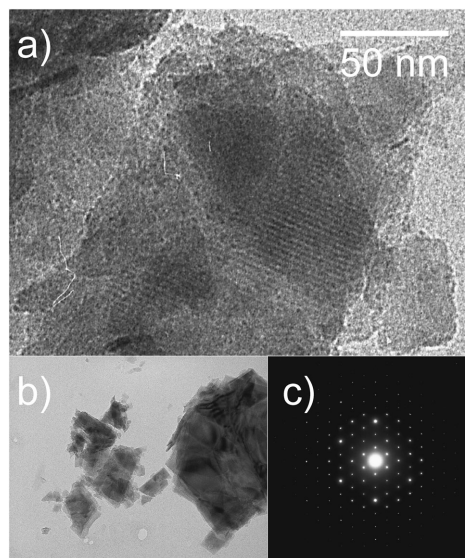


Fig. 2 TEM images (a, b) and electron diffraction pattern (c) of mesoporous carbon C600.



structure of the material. The hexagonal structure of the material is confirmed by the electron diffraction image.

The TEM image of C800 (not shown) shows similarity compared to that of C600 which corroborates the results of the adsorption measurements shown above. In contrast, TEM images of C₂SiO₂ related carbon materials (see ref. 51) showed an amorphous structure with a worm-like pore system. Thus, for C₂SiO₂ in this work, for which no TEM data were available, similar pore structure properties are expected.

NMR experiments of bulk materials

The ¹H spin-echo MAS and the single-pulse ¹³C MAS NMR spectra of the three samples are shown in Fig. 3. All proton spectra showed a very low signal to noise ratio, which indicates that the three materials are all proton-poor. In all spectra a broad signal in the region at 7 ppm is visible indicating the aromatic character of these protons. This hypothesis is also corroborated by the ¹³C MAS NMR spectra which display weak signals in the range of sp² carbons.

Next to these aromatic signals in the ¹H spin-echo MAS a second high-field shifted signal is visible which dominates in the spectrum of C800 at -7 ppm. For organic compounds this unusual chemical shift value is a clear indication of the presence of interactions with the inside of aromatic rings (see the discussion below).

No signal could be obtained by CPMAS from the two samples carbonized at 800 °C (C800 and C₂SiO₂). This is a clear indication of the low concentration of protons in these systems, which prevents cross polarization. In contrast, a CP-MAS signal is found for the C600 sample after 20k scans, which shows that the concentration of protons in C600 is higher than those in the other two samples. A comparison of this signal to the signal of the single pulse spectrum (Fig. 3, right panel) shows that both experiments reveal the same line shape. This is a clear indication that no local areas containing only carbon are present in the sample and thus the material is well ordered.

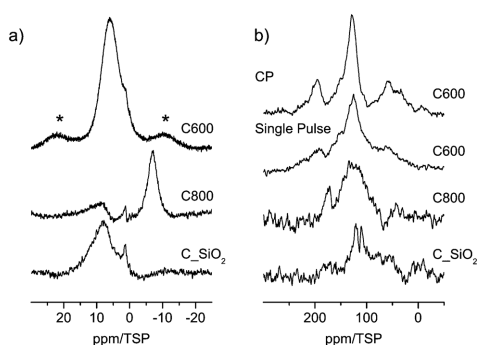


Fig. 3 (a) ¹H MAS NMR spectra (asterisks mark spinning sidebands) and (b) ¹³C (right) MAS NMR spectra of carbon materials (see discussion in the text).

Water adsorption in neat carbon materials

Fig. 4 displays the ¹H MAS-NMR spectra of water adsorbed on the surface of C600 as a function of various amounts of water. The sample containing no water displays only a very weak broad proton background signal centered on the aromatic region. This signal is clearly separated from the signal of the adsorbed water. With 1 μl of water loading, three high-field shifted signals appear at 1.1, 0.8 and 0.4 ppm. The absence of a bulk-water peak at ca. 5 ppm shows that all water molecules are in contact with the carbon surface. The high-field shifts are attributed to the aromatic structure of the carbon material surface where ring currents from the surface shield the external magnetic field. This situation is similar to results found for monomeric water molecules dissolved in deuterated benzene, where a chemical shift of 0.4 ppm was observed.⁵⁹

Since the pore size distribution is narrowly centered at 3.8 nm, as shown above, a pore size effect as the origin of the three different signals can be ruled out. Thus, one can conclude that all water molecules are adsorbed at primary and secondary sites^{60,61} and the three signals are an indication of the diversity of the surface functional group.

Upon increasing the water content to 3 μl, the signal becomes strongly broadened and now consists mainly of two broad lines centered at ca. 1.5 ppm and 4 ppm. The line at 1.5 ppm has a shoulder at 1 ppm. While the high-field shift of the first line is again indicative of surface water, the more low-field shifted line at 4 ppm for small water clusters (H₂O)_n, n = 2 to 4, exhibiting a similar number of free and hydrogen bonded OH groups.⁶² The strong line broadening is a clear indication of dynamic processes inside these water clusters or phases, e.g. hydrogen bonding and proton exchange. The strong line broadening is a clear indication of dynamic processes inside these water phases which cause the exchange of proton or water molecules.

As shown in Fig. 5 the line shape of the spectra changes as a function of time. Shortly (3 min) after water is injected into the pores the low-field phase contains a strong contribution

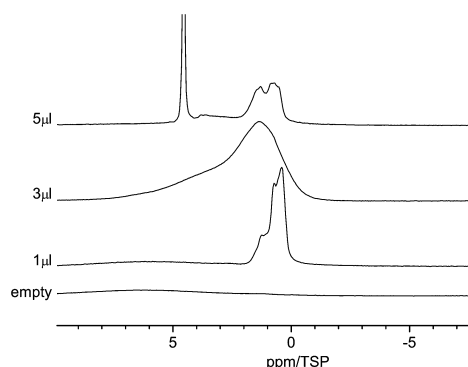


Fig. 4 Room temperature ¹H MAS NMR spectra of water in C600 for various amounts of water between 1 μl and 5 μl.



4. PUBLICATIONS

View Article Online

Paper

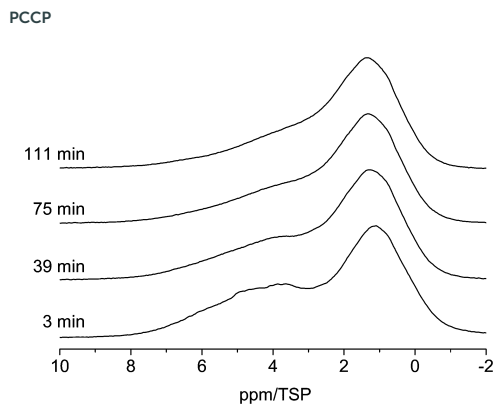


Fig. 5 Evolution of the ^1H MAS NMR spectra of the C600 sample containing $3\ \mu\text{l}$ of water (room temperature, spin-echo spectrum, 10 kHz spinning speed).

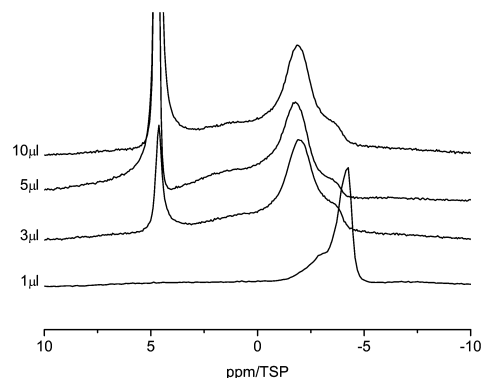


Fig. 6 ^1H MAS NMR spectra of water in C800 sample (room temperature, spin-echo spectrum, 10 kHz spinning speed).

centered at *ca.* 5 ppm. 39 min after the injection the relative intensity of this component decreased and the line shifted towards a slightly higher field. This development of the line shape continues until the final line shape is obtained in the spectrum at 111 min. Since the chemical shift of *ca.* 5 ppm is indicative of bulk water one can conclude that after 3 min part of the water is still in the form of small droplets, and not the whole surface is wetted completely with hydrogen bonded water molecules. The water from these small droplets then continues to wet the surface, which causes the shift to a higher field and the intensity changes.

With $5\ \mu\text{l}$ of water content, the spectrum changes considerably. It now shows a strong narrow peak at 4.8 ppm, two additional and relatively narrow peaks at 1 ppm and 1.5 ppm, and a weaker broad peak between 2 ppm and 4 ppm. The peak at 4.8 ppm can be attributed to the confined bulk water phase. The value is similar to the one of 5.2 ppm found for larger water clusters in benzene.⁵⁹ The broad peak is typical again for small water clusters (H_2O)_{*n*}, *n* = 2 to 4, which are located in different slowly exchanging environments.⁶² The two relatively narrow lines at 1 ppm and 1.5 ppm are from water molecules which are not hydrogen bonded to other water molecules. Since the preparation time of the sample was long enough to ensure an equilibrium distribution of water inside the pores, this is indicative of the presence of special water adsorption sites in micropores or similarly separated positions.

Fig. 6 shows the ^1H MAS NMR spectra of the C800 sample as a function of water loading. There are clear differences compared to the C600 material. With $1\ \mu\text{l}$ of water loading, the water signal is strongly shifted to high field and two lines centered at $-3\ \text{ppm}$ and $-4\ \text{ppm}$ are observable. This shift is a clear indication of the surface effect of the aromatic rings. Similar high-field shifts were calculated by Marques⁶³ and some of us⁴³ for carbon nanotubes. Increasing the water content to $3\ \mu\text{l}$ causes a shift of the high-field signal at $-4\ \text{ppm}$ to $-2\ \text{ppm}$. In addition a new line at 5 ppm appears. This is an indication of the presence of large water clusters in the sample, which

exhibit a bulk-like chemical shift. Upon further increase of the water content the high-field shifted part of the spectrum remains constant and only the intensity of the bulk-like water in the sample increases. In particular both lines stay well separated, which means that there is no exchange between bulk-like water and the strong surface interacting water.

Fig. 7 compares the evolution of the spectra when water is entering the pores of the carbon materials, C600 and C800. For both samples the first spectrum was recorded 3 minutes after injection of water into the carbon material. While the bulk water peak disappears very fast in the case of the C600 sample (in less than 3 minutes), showing a fast intake of the water into the pores, there is a much slower dynamics in the case of the C800 sample, where it takes more than two hours to adsorb the major amount of water onto the pores.

This result is again a clear indication of the strong hydrophobicity of the C800 sample, where the low density of

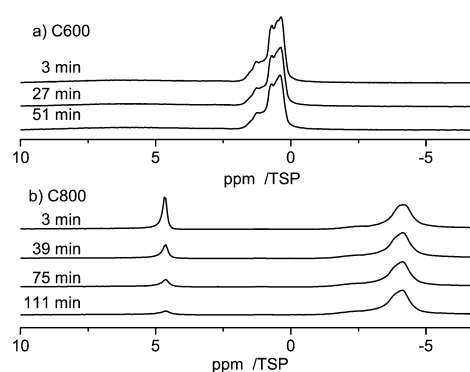


Fig. 7 (a) Evolution of $1\ \mu\text{l}$ of water in C600, and (b) evolution of $1\ \mu\text{l}$ of water in C800 at RT.

Open Access Article. Published on 25 March 2014. Downloaded on 04/03/2015 12:33:57. This article is licensed under a Creative Commons Attribution-NonCommercial 3.0 Unported Licence.



terminal oxygen containing groups causes a stronger aromaticity of the material.

The difference in the NMR chemical shift value of monomeric water in C600 (0.4 ppm) and in C800 (−4 ppm) can be explained by a lower degree of aromaticity in the C600 pore walls, which results in the absence of magnetic shielding effects with respect to water molecules confined inside. This would yield proton NMR resonances of about the value of a monomeric water molecule *in vacuo* (of precisely +0.4 ppm).⁶⁴ In turn, a stronger aromatic character of the C800 sample can shift the proton NMR signal by several ppm further down to −4 ppm, in good agreement with our quantum-chemical calculations (see below, Fig. 12).

Water adsorption in C₂SiO₂

The RT ¹H MAS NMR spectra of the C₂SiO₂ sample containing 1 μl of water are shown at the top of Fig. 8 (marked as “Fresh”). Directly after filling the pores the signal has its main intensity at 3.3 ppm. After 40 minutes the main intensity is shifted to 2.9 ppm. This shift is accompanied by a line narrowing. The line-shape after two hours coincides with the one after 40 minutes.

Cooling the sample to −15 °C causes a low field shift of the signal to 3.6 ppm and a further cooling to −40 °C increases the low-field shift of the signal to 3.8 ppm. This temperature dependent shift is most probably the result of a complex interplay of the relatively broad distribution of pore-diameters of the C₂SiO₂ sample, which was already visible in the BJH-results (Fig. 1) and in different silanol group densities on the pore surfaces: (i) porous media in general cause a strong reduction of the melting, respectively glass-transition temperatures, of fluids inside the pores; (ii) the surface induced chemical shifts of the carbon part of the pore surfaces are also expected to depend on the pore diameter; (iii) the density of silanol-groups and thus the number of possible water–silanol hydrogen bonds changes the observed chemical shift. Since all three effects can influence

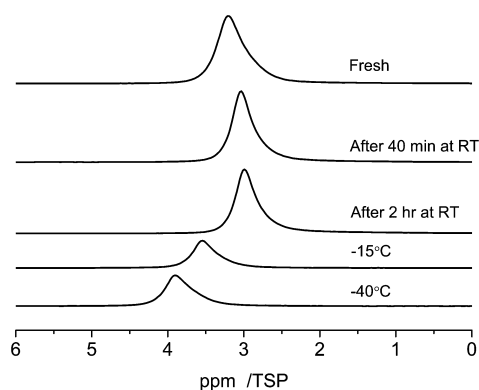


Fig. 8 Temperature dependent ¹H MAS-NMR spectra at 10 kHz spinning speed of 1 μl of water in C₂SiO₂ depending on the evolution time at room temperature and on the sample temperature.

the chemical shift of the water inside the pores a detailed theoretical modeling of the pore surfaces and the water inside the pores is necessary to model the experiments in Fig. 8.

The freezing process of water and non-freezable water

Due to the capillary effect⁶⁵ the freezing process and the melting process can exhibit a temperature hysteresis, which is visible in DSC.⁶⁶ Moreover the interaction with the surface can lead to the formation of non-freezable water phases, similar to the situation found in silica pores⁶⁷ or water–protein solutions.⁶⁸

To search for such a hysteresis or the presence of non-freezable water we recorded the ¹H MAS NMR spectra for decreasing and increasing temperatures. Upon lowering the temperature a disappearance of the signal from bulk water is observed in the temperature range of −14.5 to −15.8 °C (Fig. 9a). This disappearance is caused by the formation of ice inside the pores, which has a very broad NMR-line, which disappears in the baseline of the spectrum.⁶⁹

Upon further lowering the temperature (not shown) the peak at −3.8 ppm almost remains constant during the entire temperature range down to −50 °C. The latter is a clear indication that the interactions with the surface cause the formation of a phase of non-freezable surface water. Moreover, also a strong temperature hysteresis is observed. Upon increasing the temperature the reappearance of the signal from bulk water occurs at a temperature close to 0 °C, as shown in Fig. 9b.

Benzene in C600

The interaction of guest molecules with pore surfaces depends strongly on the type of the guest molecules.⁷⁰ As shown in the previous paragraphs, in the case of water as the guest, the molecule can act both as a donor or an acceptor of a hydrogen bond. Thus, the interactions among the molecules and of the molecules and the surface are dominated by hydrogen bonding interactions, in particular with silanol groups in the case of silica supports. In the case of an aromatic guest molecule like benzene, however, the main intermolecular interaction is the

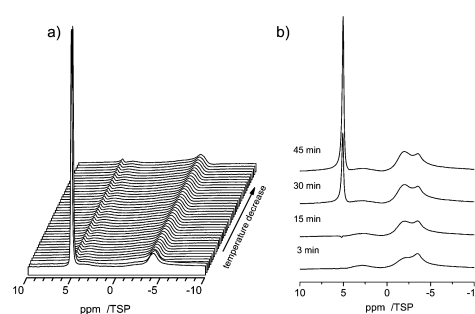


Fig. 9 Variable temperature ¹H MAS spectra of 3 μl of water in C800 measured at 10 kHz spinning speed. (a) The process of temperature decrease between −14.5 and −15.8 °C is displayed. Spectra were recorded every 3 minutes for two hours. (b) Evolution during temperature increase between −16 °C and room temperature.



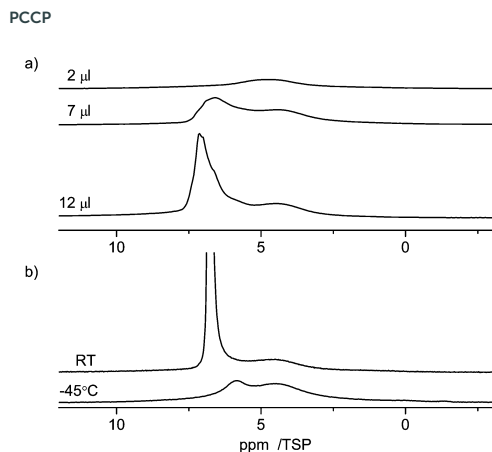


Fig. 10 ^1H MAS NMR spectra at 10 kHz spinning speed of benzene in C600 (a) at room temperature (RT) with different loadings between 2 and 12 μl , and (b) at variable temperature.

π - π stacking interaction.^{28,71} Owing to these various types of possible interactions, different guest molecules can probe the properties of the material surfaces. For benzene in C600 one can assume that the main interaction is with the graphitic parts of the carbon surface, which also has an aromatic structure. In addition, there may also be weak hydrogen bonding like interactions of the silanol groups with the ring center of the benzene molecules.

Fig. 10 shows the ^1H NMR spectra of various amounts of benzene (2 μl , 7 μl , 12 μl) adsorbed on C600. As the lowest filling volume, a value of 2 μl was chosen. Comparing the total area of 2 μl of monolayered benzene (5.7 m^2 , respectively 14.5 m^2 , depending on the cross-sectional area used for the benzene) with the specific area of 24 mg of C600 (12.6 m^2) calculated from BET it can be considered that just a monolayer is formed by this adsorption. At this filling level a relatively broad signal in the range from 6 ppm to 3 ppm is visible in the spectrum. Compared to the standard value for bulk benzene (7.3 ppm), this corresponds to a high-field shift of 1–4 ppm of the benzene molecules inside the pores. This observation clearly shows that the benzene molecule experiences a similar ring current effect from the carbon surface as the water molecules discussed above. To explain the equivalence of the ring current for all protons a rotation of the benzene molecules parallel to the graphite layer is assumed. Such rotation is well known for bulk benzene⁷² and benzene in other porous media,⁷³ and was discussed by Ueno *et al.*³⁰ who calculated the motion of benzene molecules over the microporous activated carbon.

The large line width of the signal may result from two different effects: (i) inhomogeneities of the carbon surface which yield a distribution of chemical shifts and (ii) interactions of the benzene with the surface which lead to a partial anisotropy of the motion of the benzene molecules that creates intramolecular residual dipolar couplings among the protons of the benzene molecule.

When the amount of benzene is increased to 7 μl or 12 μl a strong asymmetric signal of bulk benzene at *ca.* 7 ppm is observed in addition to the broad monolayer signal at 1–4 ppm. Both signals are broad, which indicates an exchange effect with an intermediate rate between bulk and surface species.

At $-45\text{ }^\circ\text{C}$ (note: melting point of bulk benzene is $5\text{ }^\circ\text{C}$), the intensity of the signal from surface benzene molecules is kept the same and the intensity of bulk benzene large-scale dropped and shifted to a higher field as seen in Fig. 10. This spectrum also shows a broad signal at 4.4 ppm indicating the presence of non-freezable species on the surface. The mechanism of the freezing process of benzene in carbon pores seems to be similar to the freezing-melting process of benzene inside the silica material as measured by ^2H NMR.⁷³ The benzene molecules were almost divided into two groups during the freezing-melting process: the ordered molecules on the surface and the amorphous ones in the pore center. Herein, the interaction of benzene with the carbon surface is stronger than that of benzene with silica since silica materials are strongly hydrophilic. Therefore, it is reasonable that the surface layer of benzene molecules is better ordered on the carbon surface according to the surface properties.

Pyridine in C600

Pyridine, which is similar in structure to benzene, has two different possibilities to interact with the surface. On the one hand, owing to its aromatic character it can form π - π stacking interactions with the surface, which cause it to lie flat on the aromatic carbon surfaces. On the other hand, pyridine is an acceptor for hydrogen bonding and can form hydrogen bonds with surface hydrogen donors.^{74,75}

Fig. 11 shows the ^1H NMR spectra of various amounts of pyridine (1 μl , 3 μl , 6 μl and 10 μl) adsorbed on C600. As the lowest filling volume, a value of 1 μl was chosen. Comparing the total area of 1 μl of monolayered pyridine (1.9 m^2 , mentioned above) with the specific area of 27 mg of C600 (14 m^2) calculated

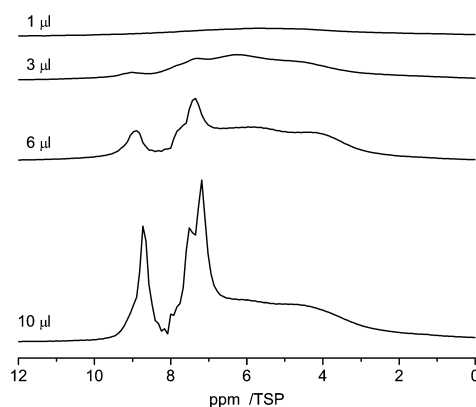


Fig. 11 ^1H NMR spectra recorded at 10 kHz spinning speed of pyridine in C600 for different loadings between 1 μl and 10 μl .





from BET it can be assumed that just a monolayer is formed by this adsorption.

With 1 μl of loading, the spectrum of pyridine adsorbed on C600 (Fig. 11) shows one broad signal including the signals from all non-equivalent protons. This observation is very similar to the former one where benzene was adsorbed. This behavior is also supported by previous simulations.²⁸ In addition the reduced motion of the pyridine caused by hydrogen bonding interactions contributes to the large chemical shift distribution of the protons from 10 ppm to 2 ppm.

With increasing loading of the sample two signal groups in the aromatic region between 7 and 9 ppm appear which are assigned to bulk pyridine which is present next to the adsorbed pyridine.

Aromaticity of carbon materials

To characterize the aromaticity of the mesoporous carbon surface, the chemical shift difference $\Delta\delta$ between the molecule in the bulk phase δ_{bulk} and the molecule adsorbed on the carbon material δ_{C} can be used as an indication as shown in ref. 10.

The results regarding water and benzene are summarized in Table 2. The largest $\Delta\delta$ value is found for water molecules in the C800 sample. This observation refers to the large graphitic surface unit and a low concentration of surface functional groups in the C800 sample. Both of them result in stronger ring current effects which increase the aromaticity.

In the C600 material, the protons in benzene had a less high-field shift, 2.1 ppm, compared to that of the proton in the surface water molecule (3.9 ppm). This could be caused by the difference in the distance of the protons in the two molecules, which means that the water molecule is closer to the surface than the benzene molecule. A detailed analysis of this result would necessitate molecular dynamics simulations, which are beyond the scope of the present paper.

Computational results

We calculated ^1H Nucleus Independent Chemical Shift (NICS) maps for hexabenzocoronene, an aromatic graphene like structure, as an example of structures that might be found in an aromatic amorphous carbon. One calculation (Fig. 12, left) has been performed in a large cell to avoid artifacts stemming from the periodic boundary conditions that are employed during the calculations. This situation resembles an isolated structure.

Table 2 $\Delta\delta$ of ^1H of water and benzene in carbon materials^a

Sample	Guest molecule	δ_{bulk}	δ_{C}	$\Delta\delta$	Average
C600	Water	4.7	1.1	3.6	3.9
			0.8	3.9	
C800	Water	4.7	-2.8	7.5	8.1
			-4.0	8.7	
			3.0	1.7	
C-SiO ₂	Water	4.7	3.0	1.7	
C600	Benzene	6.9	4.4	2.1	2.1

^a $\Delta\delta = \delta_{\text{bulk}} - \delta_{\text{C}}$ is an indication of aromaticity of the mesoporous carbon surface.¹⁰ δ_{bulk} is the proton chemical shift of the guest molecule in the bulk phase. δ_{C} is the proton chemical shift of the guest molecule in carbon materials.

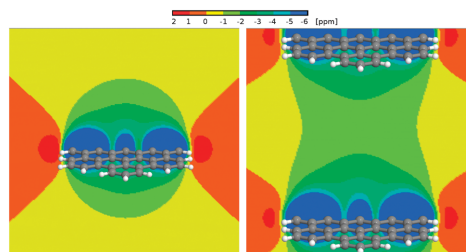


Fig. 12 Left panel: ^1H NICS maps of a hexabenzocoronene molecule. Right panel: ^1H NICS maps of a periodic stack of hexabenzocoronene molecules with an intermolecular distance of 15 Å.

The second calculation (Fig. 12, right) used a smaller periodicity of 1.5 nm perpendicular to the surface, resembling an infinite stack of molecules. This situation would be closer to the structures found in an aromatic confinement, resulting in an increased high-field shift between the molecules compared to the isolated case. The NICS maps show a strong influence of the aromatic structure, namely a high-field shift of > -1 ppm between the stacked molecules and up to -4 ppm in 2 Å distance to the molecule.

Bulk water exhibits a ^1H chemical shift of 4.8 ppm. It was shown before that this value strongly decreases in the proximity of the surface of, e.g., a silica confinement.^{76,77} For the extreme case of an isolated water molecule, water vapor, experiments show proton chemical shifts of ca. 1.0 ppm.⁷⁸ In the proximity of the aromatic surface this would then, depending on the actual distance to the surface, be high-field shifted by 2–4 ppm. Even in the center between the periodic surfaces, a shift by more than -1 ppm can be observed. This results in (isolated) water proton chemical shifts of -0.5 (center) to -2.5 ppm (2 Å to the wall) depending on the distance to the surface, and $\delta < 0.5$ ppm even in the center between two aromatic molecules.

Summary and conclusion

Mesoporous carbon materials were synthesized employing polymers and silica gels as structure directing templates. Their basic properties were probed by electron microscopy, nitrogen adsorption, and ^1H and ^{13}C MAS solid-state NMR spectroscopy. They were used as host-materials for the investigation of carbon–guest molecule interactions. For this, small guest molecules, such as water, benzene and pyridine, were adsorbed inside the pores and their properties monitored by solid state MAS NMR spectroscopy. The interactions of the guest molecules were found to be strongly dependent on the carbonization temperature and the pathway of the synthesis. In particular the interaction of water with the inner pore surface was very interesting. At low water concentrations a layer of non-freezable water was formed. All water molecules in this layer exhibited relatively high chemical shift values, indicating that basically all water molecules are bound at the primary and secondary

adsorption sites^{60,61} of the carbon materials. Similar results were found for the proton shifts of benzene and pyridine molecules, which revealed that they are adsorbed on the carbon surface mainly via π - π -stacking interactions, which cause them to lay flat on the surface. The pore structure strongly influences the surface properties of carbon materials when the materials were carbonized at the same temperature by comparison of the adsorption properties of water in the C800 and C-SiO₂ samples. For the carbon materials prepared by the same method, the surface properties depend on the carbonization temperature, although they have the same pore size distributions. The theoretical calculation shows that the high-field shift of the proton over the aromatic surface depends on the distance between the proton and the surface.

Acknowledgements

We thank Dr Christoph Boettcher from the Forschungszentrum für Elektronenmikroskopie, FU Berlin, for the TEM-measurements. Financial support from the Deutsche Forschungsgemeinschaft in the research group FOR 1583 contracts Bu-911/18-1 and Se-1008/8-1 is gratefully acknowledged.

References

- J. Lee, J. Kim and T. Hyeon, *Adv. Mater.*, 2006, **18**, 2073–2094.
- R. Ryoo, S. H. Joo, M. Kruk and M. Jaroniec, *Adv. Mater.*, 2001, **13**, 677–681.
- A. Dandekar, R. T. K. Baker and M. A. Vannice, *Carbon*, 1998, **36**, 1821–1831.
- V. M. Gun'ko, V. V. Turov, O. P. Kozynchenko, D. Palijczuk, R. Szmigielski, S. V. Kerus, M. V. Borysenko, E. M. Pakhlov and P. P. Gorbik, *Appl. Surf. Sci.*, 2008, **254**, 3220–3231.
- R. Lebeda, V. V. Turov, W. Tomaszewski, V. M. Gun'ko and J. Skubiszewska-Zieba, *Carbon*, 2002, **40**, 389–396.
- V. V. Turov, V. M. Gun'ko, R. Lebeda, T. J. Bandoz, J. Skubiszewska-Zieba, D. Palijczuk, W. Tomaszewski and S. Zietek, *J. Colloid Interface Sci.*, 2002, **253**, 23–34.
- N. S. Polyakov, M. M. Dubinin, L. I. Kataeva and G. A. Petuhova, *Pure Appl. Chem.*, 1993, **65**, 2189–2192.
- V. M. Gun'ko, O. P. Kozynchenko, V. V. Turov, S. R. Tennison, V. I. Zarko, Y. M. Nychiporuk, T. V. Kulik, B. B. Palyanytsya, V. D. Osovskii, Y. Ptushinskii and A. V. Turov, *Colloids Surf., A*, 2008, **317**, 377–387.
- R. Ryoo, S. H. Joo and S. Jun, *J. Phys. Chem. B*, 1999, **103**, 7743–7746.
- V. V. Turov and R. Lebeda, *Adsorpt. Sci. Technol.*, 1998, **16**, 837–855.
- R. K. Harris, T. V. Thompson, P. Forshaw, N. Foley, K. M. Thomas, P. R. Norman and C. Pottage, *Carbon*, 1996, **34**, 1275–1279.
- R. S. Vartapetyan, A. M. Voloshchuk, M. M. Dubinin, J. Karger and H. Pfeifer, *Bull. Acad. Sci. USSR, Div. Chem. Sci. (Engl. Transl.)*, 1985, **34**, 2241–2245.
- R. K. Harris, T. V. Thompson, P. R. Norman and C. Pottage, *J. Chem. Soc., Faraday Trans.*, 1996, **92**, 2615–2618.
- F. Cosnier, A. Celzard, G. Furdin, D. Begin, J. F. Mareche and O. Barres, *Carbon*, 2005, **43**, 2554–2563.
- P. Kim and S. Agnihotri, *J. Colloid Interface Sci.*, 2008, **325**, 64–73.
- M. Sliwinska-Bartkowiak, M. Jazdzewska, L. L. Huang and K. E. Gubbins, *Phys. Chem. Chem. Phys.*, 2008, **10**, 4909–4919.
- S. H. Mao, A. Kleinhammes and Y. Wu, *Chem. Phys. Lett.*, 2006, **421**, 513–517.
- S. Ghosh, K. V. Ramanathan and A. K. Sood, *Europhys. Lett.*, 2004, **65**, 678–684.
- P. Cabrera-Sanfelix and G. R. Darling, *J. Phys. Chem. C*, 2007, **111**, 18258–18263.
- B. Collignon, P. N. M. Hoang, S. Picaud and J. C. Rayez, *Chem. Phys. Lett.*, 2005, **406**, 430–435.
- S. Picaud, B. Collignon, P. N. M. Hoang and J. C. Rayez, *Phys. Chem. Chem. Phys.*, 2008, **10**, 6998–7009.
- E. V. Khozina, R. S. Vartapetyan and D. S. Idiyatullin, *Russ. Chem. Bull.*, 2002, **51**, 2036–2043.
- R. K. Harris, T. V. Thompson, P. R. Norman, C. Pottage and A. N. Trethewey, *J. Chem. Soc., Faraday Trans.*, 1995, **91**, 1795–1799.
- L. M. Dickinson, R. K. Harris, J. A. Shaw, M. Chinn and P. R. Norman, *Magn. Reson. Chem.*, 2000, **38**, 918–924.
- M. C. Bellissent-Funel, *J. Phys.: Condens. Matter*, 2001, **13**, 9165–9177.
- M. R. Smith, S. W. Hedges, R. LaCount, D. Kern, N. Shah, G. P. Huffman and B. Bockrath, *Carbon*, 2003, **41**, 1221–1230.
- B. B. Marosfoi, A. Szabo, G. Marosi, D. Tabuani, G. Camino and S. Pagliari, *J. Therm. Anal. Calorim.*, 2006, **86**, 669–673.
- Y. Ueno, Y. Muramatsu, M. M. Grush and R. C. C. Perera, *J. Phys. Chem. B*, 2000, **104**, 7154–7162.
- P. Kowalczyk, E. A. Ustinov, A. P. Terzyk, P. A. Gauden, K. Kaneko and G. Rychlicki, *Carbon*, 2004, **42**, 851–864.
- Y. Ueno and Y. Muramatsu, *Carbon*, 2000, **38**, 1939–1942.
- G. R. Birkett and D. D. Do, *J. Phys. Chem. C*, 2007, **111**, 5735–5742.
- T. Yamaguchi, H. Hashi and S. Kittaka, *J. Mol. Liq.*, 2006, **129**, 57–62.
- C. B. Minella, I. Lindemann, P. Nolis, A. Kiessling, M. D. Baro, M. Klose, L. Giebel, B. Rellinghaus, J. Eckert, L. Schultz and O. Gutfleisch, *Int. J. Hydrogen Energy*, 2013, **38**, 8829–8837.
- P. V. Schleyer, C. Maerker, A. Dransfeld, H. J. Jiao and N. J. R. V. Hommes, *J. Am. Chem. Soc.*, 1996, **118**, 6317–6318.
- P. V. Schleyer, H. J. Jiao, N. J. R. V. Hommes, V. G. Malkin and O. L. Malkina, *J. Am. Chem. Soc.*, 1997, **119**, 12669–12670.
- Z. F. Chen, C. S. Wannere, C. Corminboeuf, R. Puchta and P. V. Schleyer, *Chem. Rev.*, 2005, **105**, 3842–3888.
- B. Kirchner and D. Sebastiani, *J. Phys. Chem. A*, 2004, **108**, 11728–11732.
- C. Corminboeuf, T. Heine, G. Seifert, P. V. Schleyer and J. Weber, *Phys. Chem. Chem. Phys.*, 2004, **6**, 273–276.
- P. Lazzaretti, *Phys. Chem. Chem. Phys.*, 2004, **6**, 217–223.



- 40 S. Pelloni and P. Lazzeretti, *J. Phys. Chem. A*, 2011, **115**, 4553–4557.
- 41 D. Moran, F. Stahl, H. F. Bettinger, H. F. Schaefer and P. V. Schleyer, *J. Am. Chem. Soc.*, 2003, **125**, 6746–6752.
- 42 D. Sebastiani, *ChemPhysChem*, 2006, **7**, 164–175.
- 43 D. Sebastiani and K. N. Kudin, *ACS Nano*, 2008, **2**, 661–668.
- 44 A. Putrino, D. Sebastiani and M. Parrinello, *J. Chem. Phys.*, 2000, **113**, 7102–7109.
- 45 D. Sebastiani and M. Parrinello, *J. Phys. Chem. A*, 2001, **105**, 1951–1958.
- 46 A. D. Becke, *Phys. Rev. A: At., Mol., Opt. Phys.*, 1988, **38**, 3098.
- 47 C. Lee, W. Yang and R. G. Parr, *Phys. Rev. B: Condens. Matter Mater. Phys.*, 1988, **37**, 785–789.
- 48 S. Grimme, *J. Comput. Chem.*, 2006, **27**, 1787–1799.
- 49 N. Troullier and J. L. Martins, *Phys. Rev. B: Condens. Matter Mater. Phys.*, 1991, **43**, 1993.
- 50 S. Tanaka, N. Nishiyama, Y. Egashira and K. Ueyama, *Chem. Commun.*, 2005, 2125–2127.
- 51 Q. Y. Hu, J. B. Pang, N. Jiang, J. E. Hampsey and Y. F. Lu, *Microporous Mesoporous Mater.*, 2005, **81**, 149–154.
- 52 K. S. W. Sing, D. H. Everett, R. A. W. Haul, L. Moscou, R. A. Pierotti, J. Rouquerol and T. Siemieniewska, *Pure Appl. Chem.*, 1985, **57**, 603–619.
- 53 L. G. Joyner, E. P. Barrett and R. Skold, *J. Am. Chem. Soc.*, 1951, **73**, 3155–3158.
- 54 E. P. Barrett, L. G. Joyner and P. P. Halenda, *J. Am. Chem. Soc.*, 1951, **73**, 373–380.
- 55 A. S. Lekomtsev and I. V. Chernyshev, *J. Struct. Chem.*, 2003, **44**, 852–858.
- 56 H. H. Hsing and W. H. Wade, *J. Colloid Interface Sci.*, 1974, **47**, 490–498.
- 57 S. Suzuki, H. Onishi, K. Fukui and Y. Iwasawa, *Chem. Phys. Lett.*, 1999, **304**, 225–230.
- 58 K. S. W. Sing, *Pure Appl. Chem.*, 1982, **54**, 2201–2218.
- 59 M. Nakahara and C. Wakai, *Chem. Lett.*, 1992, 809–812.
- 60 S. Y. Qi, K. J. Hay and M. J. Rood, *J. Environ. Eng.*, 1998, **124**, 1130–1134.
- 61 N. J. Foley, K. M. Thomas, P. L. Forshaw, D. Stanton and P. R. Norman, *Langmuir*, 1997, **13**, 2083–2089.
- 62 H. H. Limbach, P. M. Tolstoy, N. Pérez-Hernández, J. Guo, I. G. Shenderovich and G. S. Denisov, *Isr. J. Chem.*, 2009, **49**, 199–216.
- 63 M. A. L. Marques, M. d'Avezac and F. Mauri, *Phys. Rev. B: Condens. Matter Mater. Phys.*, 2006, **73**, 125433.
- 64 H. E. Gottlieb, V. Kotlyar and A. Nudelman, *J. Org. Chem.*, 1997, **62**, 7512–7515.
- 65 H. Schubert, *Kapillarität in porösen Feststoffsystemen*, Springer-Verlag GmbH, 1982.
- 66 W. F. H. G. W. H. Höhne, H.-J. Flammersheim, *Differential Scanning Calorimetry*, Springer-Verlag, 2003.
- 67 G. Buntkowsky, H. Breitzke, A. Adamczyk, F. Roelofs, T. Emmmler, E. Gedat, B. Grünberg, Y. Xu, H. H. Limbach, I. Shenderovich, A. Vyalikh and G. H. Findenegg, *Phys. Chem. Chem. Phys.*, 2007, **9**, 4843–4853.
- 68 J. Bodurka, A. Gutsze, G. Buntkowsky and H.-H. Limbach, *Z. Phys. Chem.*, 1995, **190**, 99.
- 69 D. R. Kinney, I. S. Chuang and G. E. Maciel, *J. Am. Chem. Soc.*, 1993, **115**, 6786–6794.
- 70 M. Werner, N. Rothermel, H. Breitzke, T. Gutmann and G. Buntkowsky, *Isr. J. Chem.*, 2014, **54**, 60–73.
- 71 S. Grimme, *Angew. Chem., Int. Ed.*, 2008, **47**, 3430–3434.
- 72 J. H. Ok, R. R. Vold, R. L. Vold and M. C. Etter, *J. Phys. Chem.*, 1989, **93**, 7618.
- 73 E. Gedat, A. Schreiber, J. Albrecht, T. Emmmler, I. Shenderovich, G. H. Findenegg, H. H. Limbach and G. Buntkowsky, *J. Phys. Chem. B*, 2002, **106**, 1977–1984.
- 74 E. Gedat, A. Schreiber, G. Findenegg, I. Shenderovich, H.-H. Limbach and G. Buntkowsky, *Magn. Reson. Chem.*, 2001, **39**, S149–S157.
- 75 I. Shenderovich, G. Buntkowsky, A. Schreiber, E. Gedat, S. Sharif, J. Albrecht, N. S. Golubev, G. H. Findenegg and H. H. Limbach, *J. Phys. Chem. B*, 2003, **107**, 11924–11939.
- 76 B. Gruenberg, T. Emmmler, E. Gedat, I. Shenderovich, G. H. Findenegg, H. H. Limbach and G. Buntkowsky, *Chem. – Eur. J.*, 2004, **10**, 5689–5696.
- 77 X. Y. Guo, T. Watermann, S. Keane, C. Allolio and D. Sebastiani, *Z. Phys. Chem.*, 2012, **226**, 1415–1424.
- 78 J. C. Hindman, *J. Chem. Phys.*, 1966, **44**, 4582–4592.



Tobias Watermann and Daniel Sebastiani*

Liquid Water Confined in Cellulose with Variable Interfacial Hydrophilicity

<https://doi.org/10.1515/zpch-2017-1011>

Received July 18, 2017; accepted October 26, 2017

Abstract: We investigate liquid water confined within nanoscale cellulose slabs by means of molecular dynamics simulations. Depending on the construction of the cellulose–water interface, two different surface structures with distinct levels of hydrophilicity are exposed to the water. The different philicities are reflected in the response of the water phase to this geometric confinement, both in terms of the density profile and in the strength of the aqueous hydrogen bonding network. At the smooth surface cut along the (010) axis of the cellulose crystal, water shows typical properties of a hydrophilic confinement: the density shows fluctuations that disappear further away from the wall, the water molecules orient themselves and the coordination numbers increases at the interface. As a consequence, the water becomes “harder” at the interface, with a considerably increased local ordering. At the zigzag-shaped surface along the (111) axis, the degree of hydrophilicity is reduced, and only small effects can be seen: the density shows weak fluctuations, and the orientation of the water molecules is closer to that of bulk water than to the smooth surface. The local coordination numbers remains constant over the whole confinement. Our work shows that the nature of the exposed cellulose interface has a strong influence on how the structure of adjacent water is modified. The different ways of surface construction yield distinct degrees of hydrophilicity and spatial accessibility regarding the hydrogen bond network, resulting in a notably different interfacial water structure.

Keywords: cellulose; hydrogen bonding; hydrophilicity; molecular dynamics simulations; water.

*Corresponding author: Daniel Sebastiani, Institute of Chemistry, Martin-Luther University Halle-Wittenberg, von-Danckelmann-Platz 4, 06120 Halle, Germany,
e-mail: daniel.sebastiani@chemie.uni-halle.de

Tobias Watermann: Institute of Chemistry, Martin-Luther University Halle-Wittenberg, 06120 Halle, Germany

Bereitgestellt von | provisional account
Unangemeldet
Heruntergeladen am | 03.01.20 13:30

1 Introduction

In nature, cellulose appears abundantly in plants, where it contributes to approximately 50% of their mass, making it the most common organic material on earth. It is used in products with an extremely wide range of applications, ranging from writing paper we use every day to cotton and viscose in clothing as well as e.g. in cellophan or bank notes.

Cellulose is a homopolymeric material that consists of infinitely repeated units of cellobiose, i.e. 1-4 β -linked D-glucose monomers (see Figure 1). It can appear in different degrees of crystallinity, as well as different crystal patterns. Between the different forms, the crystal structures differ only in the hydrogen-bonding pattern between the polymer strands. Both the I α and I β structures occur naturally, the I β being the most common structure [1, 2]. Both can be transformed to another stable structure named cellulose II [3–5]. Using special procedures, further cellulose structures (III and IV) can be created [6, 7]. Numerous studies exist in literature which reflect the efforts to elucidate the structure of cellulose in its different forms and the interaction with liquid water [8–11].

In the context of biological matter, cellulose is almost always within an environment of high humidity, where it provides the mechanical stability required for plant cells [12–14]. This function as a framework for quest systems has inspired us to use cellulose as an interface system for aqueous solutions, where it acts as a “soft” confinement. Here, “soft” means that the interface may partially respond to structural forces from the quest system. We use pure liquid water as a first step to establish the fundamental structural and dynamical effects of this type of confinement [15]. Our work is in line with recent studies of water and other aqueous systems confined in hydrophilic and hydrophobic confinements [16–21]; in this context, cellulose could also be used as a confining or crowding material. Already the normal writing paper that we use every day exhibits a structure with pores of different sizes. A recent study showed an average pore diameter in high quality writing paper of 1.7 nm [22].

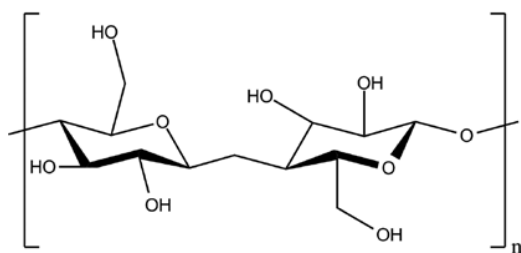


Fig. 1: Structure of the cellulose polymer.

We perform atomistic molecular dynamics simulations on two different surfaces of the cellulose. In both simulations, water is confined on two sides by the cellulose in cellulose I β structure. In this type of confined system, an interface between the two materials is created, which modifies both the cellulose crystal and water structure at the same time.

We will first investigate the induced changes in the structural and dynamic properties of the cellulose crystal, especially the outer layers, that are exposed to the water. Secondly, we will show the effects of the confinement on the water properties, ranging from local density profiles to changes in the hydrogen bonding network.

2 Computational details

We perform molecular dynamics simulations using the NAMD 2.9 program package [23], utilizing the CHARMM [24, 25] force field. Equilibration runs of the systems are performed at ambient temperature (320 K) using the NPT ensemble, while the production runs use the NVE ensemble. Visualizations have been realized in the VMD program [26].

Liquid water was confined between two different cellulose interfaces built from a cellulose crystal. By cutting along two different crystal axes, two hydrophilic surfaces with a highly different surface structure are created. The flat surface structure corresponds to a (010) surface (left), while the zigzag interface has a (111) orientation (right) (Figure 2). The cellulose crystal has first been

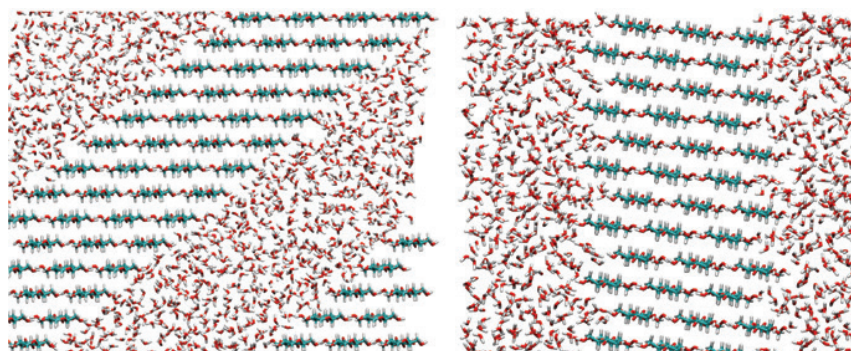


Fig. 2: Confinements built from a cellulose crystal. By cutting along two different crystal axes, two hydrophilic surfaces with a highly different surface structure are created. The flat surface structure corresponds to a (010) surface (left), while the zigzag interface has a (111) orientation (right).

created using the cellulose maker tool [27] and then cut and solvated to reach the desired confining structures. The simulation boxes contain 4758 atoms in total. The total simulation time was 30 ns for each surface type.

Angular distributions are calculated by averaging the angle θ between the surface normal vector \mathbf{v}_{norm} and the relevant molecular vector \mathbf{v}_{mol} . The distributions are normalized with the average vector population density:

$$\theta = \mathbf{v}_{\text{norm}} \cdot \mathbf{v}_{\text{mol}} \frac{1}{\sin^2 \theta}$$

We determine localized coordination numbers of the water by calculating the number of hydrogen bonding partners for each water molecule.

In our calculations, the hydrogen bond is characterized by a “soft” definition utilizing a Fermi-like function:

$$S(d) = \frac{1}{\exp \frac{d - d_{\text{HB}}}{\Delta} + 1}$$

which contains two parameters which quantify the strength of a hydrogen bond: The distance between a hydrogen donor atoms and the corresponding oxygen acceptor atom, here $d_{\text{HB}} = 2.2 \text{ \AA}$, and the width of the distance window for a “partial hydrogen bond”, here $\Delta = 0.1 \text{ \AA}$. The profile of this hydrogen bond coordination number as function of the location of the underlying water molecule and averaging over the entire trajectory, we obtain a hydrogen bond profile across the confining water slab between the cellulose interfaces. This definition has been used before [28–30] and suitably characterizes the strength of a hydrogen bond by means of a fractional number [31].

We calculate a localized hydrogen bond autocorrelation functions as the scalar product of a vector characterizing the instantaneous hydrogen bond network with itself at two different times. All hydrogen bond acceptor and donor pairs are checked: if a hydrogen bond exists at t_0 , a value of one is assigned, otherwise a zero is stored in a vector. In this context, a step function is used instead of the fermi-like $S(d)$, but using the same d_{HB} . Upon breaking, the value of the broken bond is set to zero. Reformation of the same hydrogen bond is allowed, new hydrogen bonds, however, are ignored.

The hydrogen bonding accessibility has been calculated by counting the average number of hydrogen bonding donors/acceptors in proximity of the surface hydroxyl groups. The cutoff has been set to a oxygen-oxygen distance of 3.1 \AA .

3 Results and discussion

3.1 Cellulose properties

We have started our simulations of cellulose-water slabs from the cellulose I β structure. The internal structure of the cellulose bulk remains stable, while the interfacial layer shows a characteristic response to the adjacent water slab. The overall crystal structure of the two cellulose I β crystals remain stable throughout the molecular dynamics simulations, i.e. no dissolving of cellulose crystal can be observed. The individual atom positions, however, can fluctuate strongly depending on their position in the crystal. We have computed the amplitude of the conformational fluctuation of the cellulose carbon atoms during the molecular dynamics simulations in terms of their mean displacements (MSD). The color coded MSD of the zigzag (111) structure is shown in Figure 3. We observe that cellulose sheets in the center of the crystal remain very rigid while the outer layers of cellulose that are directly exposed to water are much more mobile. Also differences in the mobility of the atoms can be seen already by visually inspecting the trajectories.

Since the cellulose crystal remains stable, the average MSD converges to a stable value as opposed to diffusion calculations in liquids. Overall, the MSD reaches up to 6 Å, with an overall average of 0.4 Å. While naturally the heavier atoms show a lower MSD than the lighter hydrogen atoms, also a strong

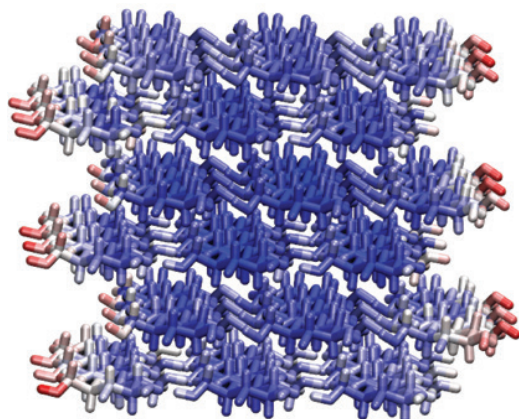


Fig. 3: Structure of the simulated cellulose crystal used to confine the liquid water slab. Average mean square displacements of the individual atoms in the cellulose wall are color coded. The central part of the wall remains rigid (blue), while the wall surface exhibits a higher mobility (white) with the surface hydrogens reaching the highest MSD (red).

dependence on the location within the cellulose crystal can be seen. The carbon atoms of the central region show only a low mobility with an average mean square displacement, the carbons of the outer layers show much higher MSD values. The effect is even stronger for the light hydrogen atoms. While the hydrogens are strongly and stably hydrogen bonded within the inner part of the crystal structure, they can move more freely between the more flexible outer layers and show an even higher MSD when exposed to the solvent.

One of the prevalent motions visible when visually inspecting the simulation data is a tilting motion of the infinite cellulose polymers. To quantify this motion, we calculate the angular distributions of the outer layers by means of a characteristic vector, namely the carbon-oxygen vector between atoms C_2 and O_1 , taken relative to the polymerization direction of the cellulose. In the bulk, this characteristic vector is oriented approximately perpendicular to the infinite cellulose polymer. In the case of the outer layer of the zigzag surface, this angle (cf. Figure 4) shows a broad distribution with a width (FWHM) of approximately 12° . The width of the distribution decreases visibly for the second outer layer and even further for the inner layers, that are not exposed to the water. This shows that the outer layers are still strongly incorporated into the cellulose crystal with a slightly increased flexibility at the water surface.

The direct contact with the water molecules takes place in form of hydrogen bonds to the cellulose. Within an infinite cellulose crystal, all of those hydrogens are stably bound to other cellulose layers. At a cellulose-water surface, however, these bonds can be broken either due to missing cellulose bond partners or more favorable hydrogen bonding to the liquid.

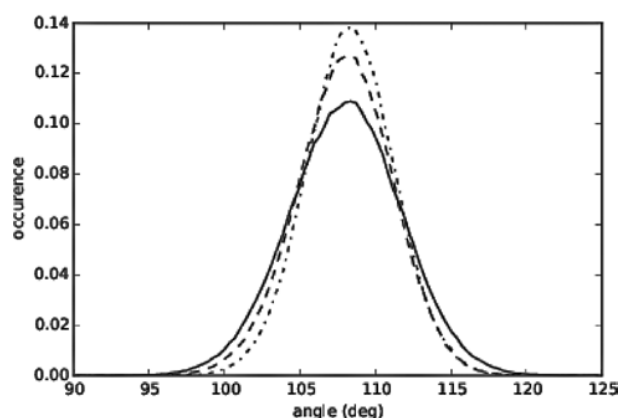


Fig. 4: Angular distribution of the C–O angles for the zigzag cellulose interface. The outer layer (solid line) shows a broader distribution than the second and inner layers (dashed line).

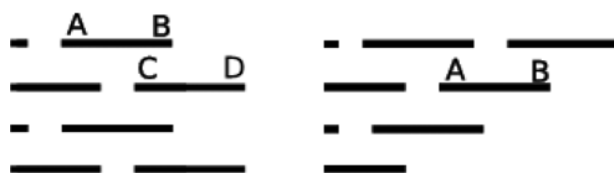


Fig. 5: Sketch of the two investigated surfaces types. The outer layer (i.e. those which are in contact with water) of the zigzag surface (left) features four distinct hydrogen bonding sites (A, B, C, D) with different accessibility to the water, while the smooth surface (right) has only a single type of cellulose monomer with two distinct hydrogen bonding sites (A and B). At all sites (A ··· D), a hydrogen-bonded OH group is located. The sites at B and D (left) as well as B (right) are in contact with water, while A and C (left) as well as A (right) are in contact with adjacent cellulose monomers.

The hydrogen bonding can be characterized by evaluating the angular distributions of the oxygen – hydrogen angles of the cellulose. We choose the bond between the O1 and H1 atoms as one characteristic vector, again taken relative to the cellulose polymerization axis. Here, we differentiate between oxygens pointing towards the surface or away from it for the outer (A and B) layer for both surfaces, and second layer (C and D) for the zigzag surface (cf. Figure 5). The hydrogen bonds pointing inwards (A and C) are strongly bound in a configuration very similar to that of the inner layers (corresponding to a quantitative overlap of the filled area and the dashed lines in Figure 6). The hydrogen bond of the outer cellulose layer pointing towards the water (D) is very flexible, giving rise to a broad angular distribution from 40° to 130° . The OH orientation of the second

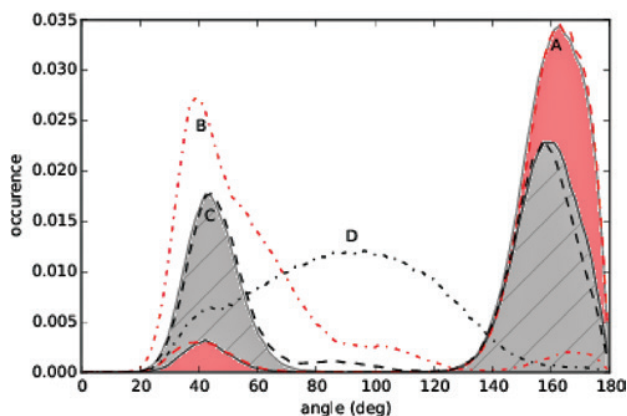


Fig. 6: Angular distributions of different OH groups of the outer cellulose layers (lines) as well as the inner layers (filled) for the zigzag cellulose–water interface. The letter codes refer to the distinct hydrogen bond sites (see Figure 5).

outer cellulose layer (B) also strongly deviates from the corresponding bulk behavior, as it is able to form hydrogen bonds to both the neighboring cellulose polymers and the adjacent liquid water.

For the smooth surface, we have only two distinct bond orientations, one pointing outwards (B), while the other points towards the water (A). We can see a broader distribution for the outer bond (B), while the inner one (A) is more tightly bound to the adjacent cellulose layers. This behavior somewhat resembles that of the cases C and D of the zigzag surface, with the difference of a slightly broader distribution for the inner hydrogen angle (data not shown).

3.2 Water properties

One of the central intentions behind the confinement strategy is that the physical and chemical properties of water as a solvent are considerably modified compared to the unconfined bulk state. In this context, both the structural aspects and the dynamical properties of water are of high relevance, as their combination determines the macroscopically visible functional behavior of water as a solvent or in liquid mixtures [32, 33]. Our main focus in this section is thus the density profile of liquid water in our soft cellulose confinements, complemented by angular distributions of the water dipoles and the hydrogen bond vectors.

The water density as function of the distance to the confining wall in the (111) cellulose surface (cf. Figure 2) is given in Figure 7. The region directly adjacent to the confinement (2–4 Å) shows an intermediate density of around half the bulk

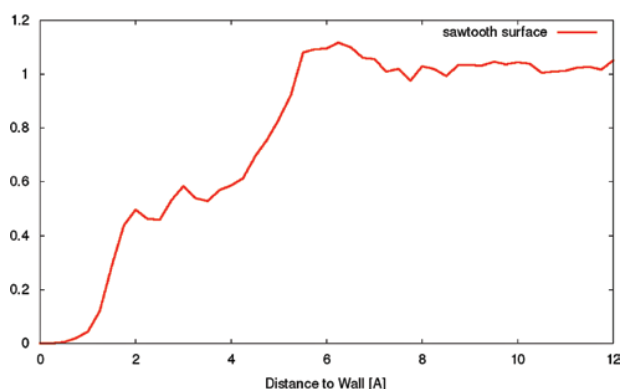


Fig. 7: Density profile of water confined by the (111) surface perpendicular to the wall direction. A region with intermediate density (about 50% of the bulk value) at a distance of about 2 Å to the cellulose is visible, while from about 6 Å on, a bulk-like is obtained.

value, and beyond 7 Å distance, the density is uniformly bulk-like. The plateau around 2–4 Å illustrates the intermediate behavior of the meander-like interface, which can accommodate a reduced amount of water. The region around 6 Å distance exhibits a significant increase of the water density beyond the bulk value, which is a common phenomenon that has already been observed for hard hydrophilic confinements [17, 18].

In comparison, water density profile confined by the smooth (010) surface is shown in Figure 8. The first high-density peak is located at about 4 Å, and a less pronounced minimum and second maximum follow at 5.5 Å and 6.5 Å, respectively. Very interestingly, the increase of the density in direct vicinity to the confinement is very smooth and resembles a quadratic function up to a distance of about 3 Å. This relatively broad transition from zero-density to bulk-density is uncommon for hard interfaces, which would normally exhibit a steeper density profile [17–19, 34, 35]. Here, it illustrates the more flexible nature of the cellulose confinement. It is interesting to notice that the initial rise is smoother for the (010) surface than for the (111) counterpart, which illustrates a somewhat higher flexibility of the (010) cellulose interface.

While the profiles of the densities at the two different surfaces show a local structure, they give no information on the source of this structuring. To elucidate the origin of this structuring and also the differences of the two surfaces, we need to find the preferred hydrogen bonding patterns and ordering motifs at the wall. To this end, we investigate the orientation of the water hydrogen bonds and dipoles. In Figure 9, the angular distributions of the water dipole relative to the surface normal vector are shown. A value of 180° corresponds to an orientation

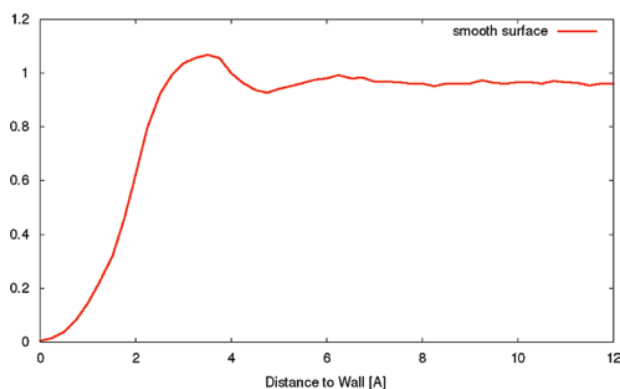


Fig. 8: Density profile of water confined by the (010) surface perpendicular to the wall direction.

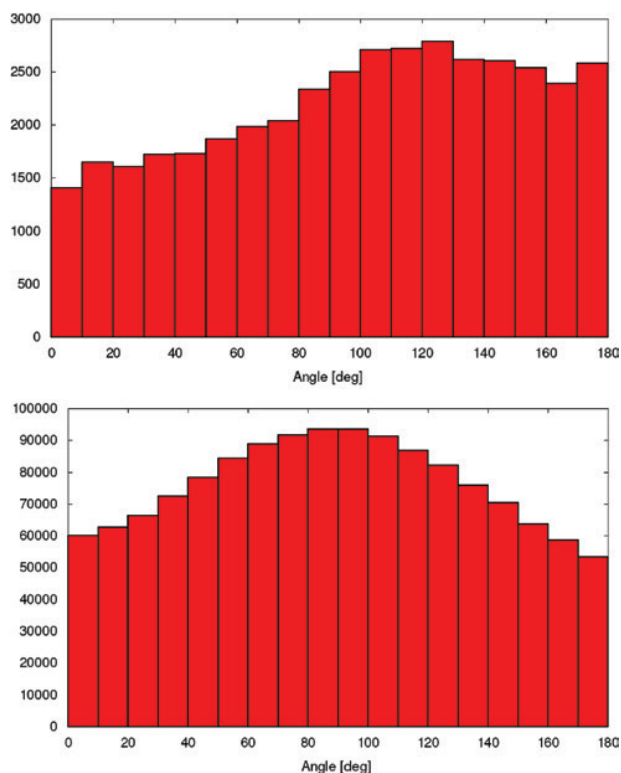


Fig. 9: Orientation of the water dipole relative to the surface normal vector for the (111) interface (top) and the (010) interface (bottom), averaged over 3 Å.

with the oxygen pointing towards the cellulose interface with both hydrogens pointing away. An angle of 90° describes a water molecule coplanar with the interface or with one hydrogen pointing up and down, respectively. The maximal value of 180° is reached when both hydrogens point towards the surface. The distribution is weighted by the angular density of states $1/\sin(\theta)$.

Both surfaces exhibit a characteristic shape in the angular distributions. In the case of the sawtooth-like (111) surface, we see a preference for angles higher than 90° , i.e. on average the water oxygen is pointing towards the surface. With increasing distance to the wall this effect is weakened. For the smoother (010) surface, the distribution shows a clear preference for an orientation of 90° . Interestingly, angles of close to 180° , in contrast to the (111) surface, are observed less frequently. This effect indicates that the (010) cellulose interface has a higher hydrogen bond donor characteristics than the (111) counterpart.

The peak at 90° for the (010) interface needs a closer analysis, as it can correspond to both a rather hydrophobic surface (water coplanar with the surface) and a strong hydrogen bond acceptor site (with one hydrogen pointing towards one away from the surface).

To this end, we investigate the orientation of the water OH vectors pointing to the wall, i.e. for each water molecule we consider only the hydrogen closest to the wall. In this case, the angular distribution can not be normalized as before, so that we show the orientation of the water molecules in the center of the confinement as reference for the unperturbed distribution (see Figure 10).

When comparing the distributions at the different surfaces with the central unordered water, we see a clear decrease in probability for low angles, i.e. hydrogens pointing directly towards the surface appear less often. The probability for high angles, on the other hand, is increased for both surfaces. This shows that the cellulose surfaces are rather hydrogen bond donors than acceptors.

A complementary aspect is contributed by the spatially resolved hydrogen bond network strength, which we characterize by hydrogen bond coordination numbers (i.e. the numbers hydrogen bonding partners of a water molecule at a certain position along the axis perpendicular to the confining surface). Bulk liquid water typically has a value of 3.5 for this quantity, the coordination of crystalline ice equals exactly 4. The spatially resolved hydrogen bond coordination profile for the water molecules confined within the smooth (010) cellulose sheets is shown in Figure 11. For the zigzag surface, we see a quite constant value with only minimal spatial fluctuations at any given position in the confinement (data not shown). In the case of the smooth surface, however, we see considerable fluctuations of the hydrogen bond number next to the confining wall. These oscillations

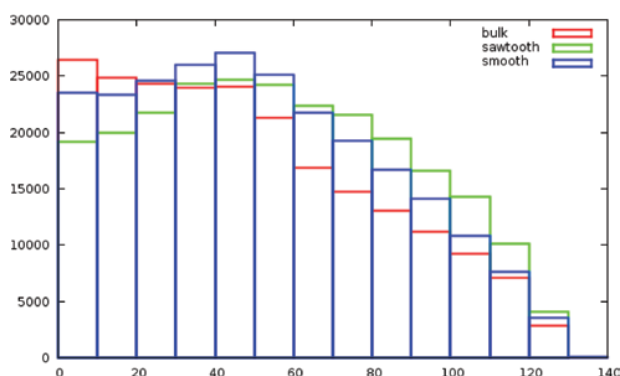


Fig. 10: Angle of the water OH (H closer to surface) vector to the surface normal vector, averaged over 2 \AA from the (111) and (010) surface. Distribution of the central waters as reference.

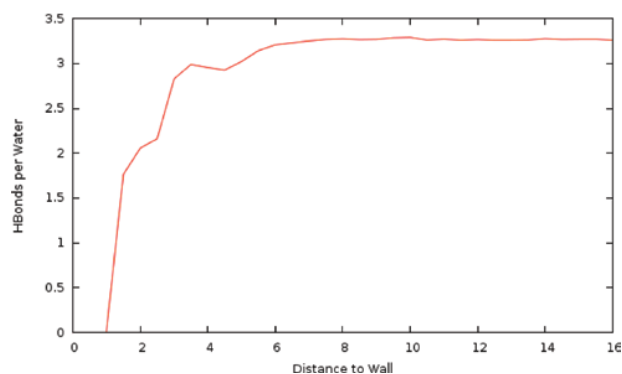


Fig. 11: Spatially resolved hydrogen bond coordination number of the water molecules in the smooth cellulose confinement.

clearly illustrate the reduced degree of hydrophilicity in the latter situation. From an alternative point of view, this effect can be interpreted as a considerably lower hydrogen bonding donor/acceptor capacity of the smooth cellulose surface compared to the corresponding capacity of bulk liquid water. Again, the effect of the confining interface reaches about 4–5 Å into the liquid water film, corresponding to a layer with a thickness of about two water molecules.

4 Conclusions

The cellulose surface is a very versatile system and can serve as a flexible hydrophilic confinement for aqueous systems. Its properties change significantly without any functionalization just by varying the exposed surface. Here, we investigated two confinement structures built from a cellulose $I\beta$ crystal with different degrees of hydrophilicity. In one case, the zigzag-shaped (111) surface is exposed to water, while in the other one the smoother (010) surface is used. We see a change in the structure of the cellulose molecules of the outer layers that are directly exposed to the water. In addition, we observe modifications of the angular distributions of the CO and OH bonds of the outer cellulose layer, as well as strong changes in the hydrogen bonding pattern of the cellulose hydrogen atoms. While the second outer layer of the zigzag surface shows almost no change, the outer layers show broad distributions for the hydrogens directly exposed to the water.

The modification of the local ordering of the interfacial water depends strongly on the nature of the surface to which the water is exposed to. Our

computed density profiles indicate an increased ordering in the water structure at the wall. The average orientation of the surface waters is changed strongly for the different surfaces: the water dipoles are oriented towards the cellulose walls for the (111) surface but parallel to the wall for the (010) surface. Complementarily, the strength of the hydrogen bonding network in the vicinity of the surfaces exhibits a characteristic fingerprint for the degree of hydrophilicity of the surfaces.

Acknowledgement: This work has been supported by the German Research Foundation (DFG) within the Forschergruppe FOR1583 (grant number Se 1008/8-2). Computing infrastructure was provided by the HLRS computing center Stuttgart (Germany).

References

1. J. F. Matthews, C. E. Skopec, P. E. Mason, P. Zuccato, R. W. Torget, J. Sugiyama, M. E. Himmel, J. W. Brady, *Carbohydr. Res.* **341** (2006) 138.
2. M. Bergensträhle, L. A. Berglund, K. Mazeau, *J. Phys. Chem. B* **111** (2007) 9138.
3. A. P. Heiner, J. Sugiyama, O. Teleman, *Carbohydr. Res.* **273** (1995) 207.
4. Y. Nishiyama, G. P. Johnson, A. D. French, V. T. Forsyth, P. Langan, *Biomacromolecules* **9** (2008) 3133.
5. R. J. Maurer, A. F. Sax, V. Ribitsch, *Cellulose* **20** (2013) 25.
6. A. C. O'Sullivan, *Cellulose* **4** (1997) 173.
7. J. A. Hadden, A. D. French, R. J. Woods, *Biopolymers* **99** (2013) 746.
8. A. P. Heiner and O. Teleman, *Langmuir* **13** (1997) 511.
9. M. Bergensträhle, J. Wohler, P. T. Larsson, K. Mazeau, L. A. Berglund, *J. Phys. Chem. B* **112** (2008) 2590.
10. K. Mazeau, L. Heux, *J. Phys. Chem. B* **107** (2003) 2394.
11. Y. Li, M. Lin, J. W. Davenport, *J. Phys. Chem. C* **115** (2011) 11533.
12. R. H. Newman, T. C. Davidson, *Cellulose* **11** (2004) 23.
13. F. Tanaka, N. Fukui, *Cellulose* **11** (2004) 33.
14. A. P. Heiner, L. Kuutti, O. Teleman, *Carbohydr. Res.* **306** (1998) 205.
15. T. Yui, S. Nishimura, S. Akiba, S. Hayashi, *Carbohydr. Res.* **341** (2006) 2521.
16. J. Geske, B. Drossel, M. Vogel, *J. Chem. Phys.* **146** (2017) 134502.
17. X. Y. Guo, T. Watermann, S. Keane, C. Allolio, D. Sebastiani, *Z. Phys. Chem.* **226** (2012) 1415.
18. C. Allolio, F. Klameth, M. Vogel, D. Sebastiani, *ChemPhysChem.* **18** (2014) 3955.
19. X. Guo, T. Watermann, D. Sebastiani, *J. Phys. Chem. B* **118** (2014) 10207.
20. Y. Xu, T. Watermann, H.-H. Limbach, T. Gutmann, D. Sebastiani, G. Buntkowsky, *Phys. Chem. Chem. Phys.* **16** (2014) 9327.
21. A. Hoffmann, D. Sebastiani, E. Sugiono, S. Yun, K. S. Kim, H. W. Spiess, I. Schnell, *Chem. Phys. Lett.* **388** (2004) 164.
22. A. Bedane, H. Xiao, M. Eic, M. Farmahini-Farahani, *Appl. Surf. Sci.* **351** (2015) 725.

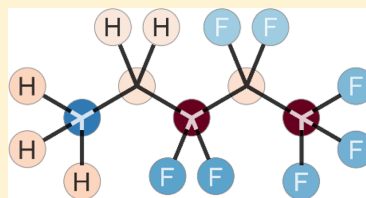
23. J. C. Phillips, R. Braun, W. Wang, J. Gumbart, E. Tajkhorshid, E. Villa, C. Chipot, R. D. Skeel, L. Kalé, K. Schulten, *J. Comput. Chem.* **26** (2005) 1781.
24. A. D. MacKerell, D. Bashford, R. L. Dunbrack, J. D. Evanseck, M. J. Field, S. Fischer, J. Gao, H. Guo, S. Ha, D. Joseph-McCarthy, L. Kuchnir, K. Kuczera, F. T. K. Lau, C. Mattos, S. Michnick, T. Ngo, D. T. Nguyen, B. Prodhom, W. E. Reiher, B. Roux, M. Schlenkrich, J. C. Smith, R. Stote, J. Straub, M. Watanabe, J. Wiórkiewicz-Kuczera, D. Yin, M. Karplus, *J. Phys. Chem. B* **102** (1998) 3586.
25. A. D. MacKerell, *J. Comput. Chem.* **25** (2004) 1584.
26. W. Humphrey, A. Dalke, K. Schulten, *J. Mol. Graph.* **14** (1996) 33.
27. T. C. F. Gomes, M. S. Skaf, *J. Comp. Chem.* **33** (2012) 1338.
28. M. Iannuzzi, M. Parrinello, *Phys. Rev. Lett.* **93** (2004) 25901.
29. M. Iannuzzi, *J. Chem. Phys.* **124** (2006) 204710.
30. G. A. Ludueña, T. D. Kühne, D. Sebastiani, *Chem. Mater.* **23** (2011) 1424.
31. D. Sebastiani, G. R. Goward, I. Schnell, H. W. Spiess, *J. Mol. Struct. Theochem.* **625** (2003) 283.
32. M. Rosenstihl, K. Kämpf, F. Klameth, M. Sattig, M. Vogel, *J. Non. Cryst. Solids* **407** (2015) 449.
33. B. Kuttich, A.-K. Grefe, H. Kröling, S. Schabel, B. Stühn, *RSC Adv.* **6** (2016) 32389.
34. J. Geske, M. Vogel, *Mol. Simul.* **43** (2017) 13.
35. M. F. Harrach, F. Klameth, B. Drossel, M. Vogel, *J. Chem. Phys.* **142** (2015).

Perfluoroalkane Force Field for Lipid Membrane Environments

Guido Falk von Rudorff,[†] Tobias Watermann,[‡] and Daniel Sebastiani^{*‡}[†]Dahlem Center for Complex Quantum Systems, Freie Universität Berlin, Arnimallee 14, 14195 Berlin, Germany[‡]Institute of Chemistry, Martin-Luther-Universität Halle-Wittenberg, von-Danckelmann-Platz 4, 06120 Halle, Germany

Supporting Information

ABSTRACT: In this work, we present atomic parameters of perfluoroalkanes for use within the CHARMM force field. Perfluorinated alkanes represent a special class of molecules. On the one hand, they are considerably more hydrophobic than lipids, but on the other hand, they are not lipophilic either. Instead, they represent an independent class of philicity, enabling a whole portfolio of applications within both materials science and biochemistry. We performed a thorough parametrization of all bonded and nonbonded parameters with a particular focus on van der Waals parameters. Here, the general framework of the CHARMM and CGenFF force fields has been followed. The van der Waals parameters have been fitted to experimental densities over a wide range of temperatures and pressures. This newly parametrized class of molecules will open the gate for a variety of simulations of biologically relevant systems within the CHARMM force field. A particular perspective for the present work is the influence of polyphilic transmembrane molecules on membrane properties, aggregation phenomena, and transmembrane channels.



INTRODUCTION

Despite their structural similarity to hydrocarbons, fluorocarbons have highly different properties and applications. They are useful for medical purposes as gas-carrier fluids,^{1,2} can aid purification or polymerization,¹ and have further applications as lubricant.³ Perfluoroalkanes are especially interesting due to their phase separation behavior in hydrocarbon environments.^{4–7} Together with hydrophilic and hydrophobic segments, fluorocarbons can help building polyphilic molecules. Some of these molecules and their behavior have been investigated by experiment recently^{8–11} and were found to exhibit a phase ordering pattern similar to liquid crystals.¹² Molecules containing (per-)fluorinated alkane chains and conjugated oligomers influence the channel formation when being added to a membrane environment^{13,14} as well as the overall stability¹⁵ and surface properties¹⁶ of a lipid membrane. Although synthesis is possible for a whole family of polyphilic compounds containing fluorinated side chains, the aggregation mechanisms are not fully understood on an atomistic scale. On the way to membrane environments, perfluoro-*n*-alkanes have to be parametrized for lipid bilayer simulations to prepare elucidating the physical processes and mechanisms that are responsible for the macroscopic behavior that has been observed so far.

Among the many force fields available, there are some that have been either specialized to treat fluorocarbons^{1,17,18} and some that include parameters for fluorocarbons among others.¹⁹ In the beginning of force field development, united-atom force fields have been extended more quickly, mainly due to the reduced computational effort necessary to actually perform simulations using these force fields. As hardware became more powerful, a tendency toward all-atom force fields

emerged due to the alleged higher accuracy of all-atom force fields. This reasoning is reflected in the history of force field development for fluorocarbons as well. The earliest force fields were based on a united-atom approach and yielded comparably poorer results.¹

We have screened the literature for an all-atom force field for perfluoroalkanes which is adequate for a phospholipid membrane environment. However, no parametrization for perfluorinated chains was found to allow a broad application to biochemical problems, which led us to developing a suitable force field ourselves. To our knowledge, there is no force field which comes with support for both perfluoroalkanes and lipids. Regarding the integration of the new set of parameters for perfluorinated chains, we chose the CHARMM force field package,^{20,21} which has been extensively benchmarked in literature to a broad range of lipids. An additional plus is the clear parametrization procedure defined for this force field type, which ensures compatibility with the other parameters within the force field. As van der Waals interactions are known to be very prominent in membrane environments, we have put particular emphasis on carefully tuning the Lennard-Jones parameters.

COMPUTATIONAL METHODS

CHARMM Force Field. Model interactions and parameter usage for the total energy function of the CHARMM force field are provided in Figure 1.

Received: April 11, 2014

Revised: October 2, 2014

Published: October 2, 2014

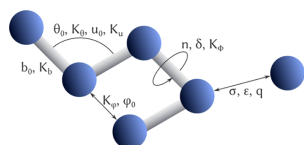


Figure 1. Model interactions and parameter usage for the total energy function of the CHARMM force field (see eq 1).

The total energy function of the CHARMM force field²⁰ and its extensions²¹ is given as

$$E = \sum_{\text{bonds}} K_b(b - b_0)^2 + \sum_{\text{angles}} K_\theta(\theta - \theta_0)^2 + \sum_{\text{dihedrals}} K_\phi(1 + \cos(n\phi - \delta)) + \sum_{\text{improper}} K_\varphi(\varphi - \varphi_0)^2 + \sum_{\text{Urey-Bradley}} K_u(u - u_0)^2 + \sum_{i < j} 4\epsilon \left[\left(\frac{\sigma_{ij}}{r_{ij}} \right)^{12} - \left(\frac{\sigma_{ij}}{r_{ij}} \right)^6 \right] + \sum_{i < j} \frac{q_i q_j}{4\pi\epsilon_0 r_{ij}} \quad (1)$$

with the terms in the first three lines being referred to as bonded parameters, leaving the last line to contain the nonbonded parameters (see Figure 1).

Besides the element of an atom, the chemical environment of every atom contributes to the partial charge, the bonded parameters, and effective van der Waals radius.²² Therefore, the CHARMM force field defines so-called atom types for atoms of a similar chemical environment in order to decrease the parametrization effort necessary to extend the force field while retaining comparable accuracy. Atom types which are not part of the force field yet have to be fully parametrized.

While most of the free parameters in this equation have to be determined for every atom type, there are two groups of parameters that are calculated individually for every simulation: the Lennard-Jones parameters ϵ and σ which are employed for modeling the van der Waals interaction in eq 1. The parameter σ relates to the minimum R_{\min} of the distance-dependent Lennard-Jones potential as given in eq 4, while the parameter ϵ scales the overall potential energy surface. For each pair (ij) of atom types, the potentially different values for the two atom types have to be combined into one. The combination rule for the distance-controlling parameter σ is given²³ by

$$\sigma_{ij} = \frac{\sigma_i + \sigma_j}{2} \quad (2)$$

and the Berthelot rule²⁴ for ϵ

$$\epsilon_{ij} = \sqrt{\epsilon_i \epsilon_j} \quad (3)$$

In the CHARMM file format, the parameters for the van der Waals interactions are defined by specifying $R_{\min}/2$ which relates to σ as follows

$$\sigma = \frac{R_{\min}}{2} \times 2^{5/6} \quad (4)$$

Due to the single on-site point charges used in its definition, the CHARMM force field (and many others) cannot properly include polarization effects, which have a high influence on the potential energy surface of the van der Waals interaction. In any

case, the van der Waals interaction is only modeled by the Lennard-Jones potential. Although a repulsive exponential and an attractive r^{-6} would be more realistic, one typically employs a repulsive r^{-12} expression for easier computation. Naturally, this model cannot be optimal for all combinations of atoms with their different interactions. It has been shown^{25,26} that for interactions of atoms of highly different van der Waals radii, the Lorentz–Berthelot combination rules may yield an effective potential energy surface which considerably deviates from the results of molecular beam experiments. While the most prominent van der Waals interaction of perfluoroalkanes with membranes will be the one between fluorine and hydrogen, we stick to the Lorentz–Berthelot definition to allow for seamless integration of the parameters presented in this work into CHARMM-based setups.

Optimization Procedure for Bonded Parameters and Charges. Although there is a procedure (see Figure 2) how to

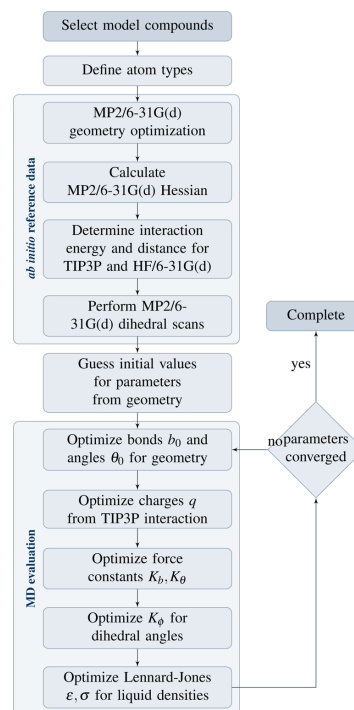


Figure 2. Parametrization schema for the CHARMM force field as applied in this work.

derive the parameters for completely new atom types in a way that is compatible with the CHARMM force field from both experimental and theoretical quantum chemical data,²⁰ it contains some vague definitions. For example, the rescaling of the vibrational frequencies when using MP2/6-31G(d) as reference values is either determined by comparison to undisclosed data or by using an arbitrary factor. There is,

however, a similar force field, CGenFF,²⁷ which employs the same energy function as the CHARMM force field²¹ but comes with a clearly defined method how to obtain new parameters while maintaining consistency with the existent parameters. The central ideas of the two force field parametrization processes are essentially the same; they only differ in the level of detail provided by the authors. Hence, we used the CGenFF parametrization procedure to obtain the necessary force field parameters for the CHARMM force field. In order to have a better manual control, we have not used recently proposed automated approaches like extrapolating parameters.²⁸

Although CGenFF contains some parameters for fluorinated compounds, they are not fully compatible to the CHARMM force field.²⁹ This is especially true for bond and angle definitions, as their reference values (b_0 or θ_0 , respectively) do not reproduce the ground state conformation by themselves but include straining effects from all the spring forces in the molecule. For van der Waals parameters, this is not an issue as they mostly depend on the combination rules, which are identical for both the CHARMM force field and CGenFF. Using CGenFF alone is no option either, as the authors themselves discourage the use of CGenFF for lipid layers which happens to be one of the most prominent-use cases of the CHARMM force field.³⁰

As target compounds for the parametrization procedure, we used *n*-alkanes, perfluoro-*n*-alkanes up to perfluoro-*n*-octane, and partially fluorinated *n*-alkanes. We use the following shorthand notation: $\text{H}_3\text{CCH}_2(\text{CF}_2)_n\text{CF}_3$ is denoted as $n_{(i+1)}$ and $\text{F}_3\text{C}(\text{CF}_2)_n\text{CF}_3$ is abbreviated as $f_{(i+2)}$.

First of all, we define atom types for all uncovered atoms in the model compound set. Then the geometrical structure of the model compounds is optimized at the MP2/6-31G(d) level. This optimized geometry yields equilibrium values for bond lengths, angles, dihedral angles together with their phases and their multiplicity. As this initial estimate neglects any spring forces on the conformations, it has to be subject to further refinement.

The second step is to estimate the partial charges on all atom types by probing the interaction energy and the interaction distance along the bond axes with a TIP3P water molecule and comparing the results to quantum chemical calculations at the HF/6-31G(d) level of theory. As the interaction energy and distances depend on the underlying geometry, which has to be a local minimum to conform to the CHARMM parametrization procedure, and the previous step changes this minimum energy conformation, the charge optimization has to be performed in every iteration cycle.

Afterward, under the assumption that the normal modes can be approximated by a harmonic potential in mass-weighted coordinates, the eigenvalues of the Hessian matrix for the conformation of the model compounds give the vibrational frequencies while the corresponding eigenvectors give the associated normal mode movement. From these frequencies, the force constants can be calculated. However, this would yield systematically shifted force constants, as even for small systems, the harmonic approximation may not reflect the critical region well enough and does not incorporate electron correlation. Therefore, empirical scaling factors have been introduced in order to account for the anharmonicity.³¹ The scaling factor depends on the level of theory and is 0.943^{27,32,33} for MP2/6-31G(d).

The method the force constants are derived from suffers from two major issues when applied to physical systems. In

general, the normal modes do not affect isolated bonds or single angles only but denote a collective movement instead. Additionally, the parameters themselves are not fully independent but form a delicate balance of interacting parameters, ensuring the stability of the molecule conformation. The force constants of angles and bonds alone play a very important role but are unable to model the whole potential energy surface of the molecule. As the normal modes denote collective movements, there is an interdependence of the resulting frequencies. Therefore, all missing force constants for a given molecule have to be optimized at once. For example, dividing the missing parameters into two sections (CF_3 group and CF_2 group) yields inferior results for the overall molecule geometry that is expected to reproduce the ab initio geometry as good as possible. Taking this mutual influence into account makes the overall optimization process harder than it may seem at first glance. Usually, the high-dimensional and nonlinear optimization problem is solved using manual iterative schemes²⁷ or by using heuristic algorithms with both energy-based and conformational sanity checks.³³ In this work, we used the latter approach together with some manual enforced sanity constraints.

In the next step, the energy profiles of the torsional angles are to be analyzed²⁷ using a relaxed surface scan. The central idea is to distort a molecular minimum energy conformation by setting a torsional angle to a specific value and constrain this internal coordinate while the rest of the molecule remains unconstrained. A consecutive energy minimization will relax all remaining internal degrees of freedom and yields a new local minimum under the constraint of the fixed dihedral angle. Afterward, the free parameters in the dihedral energy term are fitted to reproduce the MP2/6-31G(d) energy profile as good as possible.

Optimization of van der Waals Parameters. The determination of optimal parameter values for the van der Waals interaction represents a special challenge in our context. Both regular aliphatic carbon chains and perfluorinated chains are almost nonpolar but exhibit a highly subtle thermodynamic behavior in terms of mixing/demixing properties. We optimized the parameters in question to reproduce liquid densities for both perfluoro-*n*-alkanes and mixtures of perfluoro-*n*-alkanes and *n*-alkanes. The general procedure to obtain liquid densities from simulations is as follows. The geometry resulting from an initial energy minimization of a single molecule is the basis for all further steps. For each perfluoro-*n*-alkane, there is a maximum distance d_{max} between two atoms of the molecule. A cubic box with box vector lengths of $10d_{\text{max}}$ is initialized and randomly filled with copies of the molecule in question until the average density of this box is around 20% of the target value at 300 K and 1 atm. We observed that it turns out to be more efficient to compress the simulation box by pressure coupling than to try to start from a box with nearly desired density, as in the former case the equilibration phase can be distinguished clearly and the random placement for the initial box is much quicker. This geometry is subsequently minimized until the NPT simulation can be started.

Due to the interdependence of the parameters, this whole procedure is repeated until the resulting parameters converge. In each iteration, the results from the previous cycle are used as input for further refinement. In this article, we report the results from the last iteration only.

Technical Details. All quantum chemical calculations have been performed using Gaussian 09.³⁴ The classical geometry

minimization and MD simulations have been calculated with namd 2.9.³⁵ Parts of the analysis were done with the help of VMD³⁶ and its Force Field Toolkit³³ together with MDAnalysis³⁷ and its RMSD alignment code.³⁸ For simulation preparation, a few tools from the GROMACS suite³⁹ have been used, as well.

RESULTS AND DISCUSSION

The newly introduced atom types are shown in Figure 3 and are listed in Table 1 together with their (standard) atomic masses.

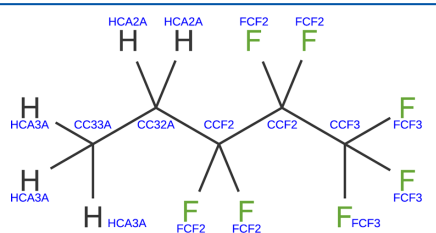


Figure 3. Atom types used for parametrization as annotation to one of the sample compounds. FCF2, FCF3, CCF2, and CCF3 are the newly introduced atom types.

Table 1. Introduced Atom Types with Both Their CHARMM-Style Label and Their Chemical Environment^a

atom type label	mass (amu)	description
CCF3	12.01	carbon in CF ₃ group
FCF3	19.00	fluorine in CF ₃ group
CCF2	12.01	carbon in CF ₂ group
FCF2	19.00	fluorine in CF ₂ group

^aSee also Figure 3.

Bonded Parameters. Starting from the MP2/6-31G(d) optimized geometries of n_1 , n_2 , and n_3 , the equilibrium values are to be determined using the atom types CC33A, CC32A, HCA3A, and HCA2A for n -alkanes from CHARMM35.⁴⁰ We chose them for compatibility, despite CGenFF defining separate atom types for linear alkyl groups.

Generally speaking, the influence in terms of variation of the values for bonded parameters of the nonfluorinated part of the n -alkanes on the fluorinated part is negligible for n_1 and, hence, neither of the conformational parameters varies with increasing chain length i . For MP2/6-31G(d) geometries, we have observed that for n_2 the carbon–carbon bond lengths and angles in the semifluorinated part do not depend on their distance from the nonfluorinated part of the molecule ($\Delta < 0.01$ Å or $\Delta < 3^\circ$, respectively). Together with hints from previous studies,¹ this gives rise to the belief that the simplification to use only four different atom types in two different chemical groups is justified for perfluoro- n -alkanes, and additional atom types at the connection between the fluorinated and nonfluorinated parts are not necessary to simulate our selection of n -alkane model compounds. This follows the typical approach for alkanes in CHARMM and CGenFF.

In this work, we used the same convergence threshold as the one used for parametrization of the CHARMM force field.²⁷ In particular, this requires calculating the rotational matrix that

minimizes the RMSD for the MP2/6-31G(d) reference structure and the force field (local) minimum. After applying this rotation, the bond lengths have to differ by less than 0.03 Å and the angles have to be reproduced with an error of three degrees at most. It is less surprising that the resulting parameters yield sufficiently good geometries for unconstrained MD optimization for each of the small compounds, n_1 – n_3 , but perfect agreement of the conformations for longer compounds f_2 – f_8 supports our approach.

The final values for the bond parameters are given in Table 2; the data for angles is listed in Table 3.

Table 2. Newly Determined Bond Lengths b_0 in Angstroms and Force Constants k_b in kcal/mol/Å²

atom types		k_b	b_0
CCF3	CC32A	222.5	1.51
FCF3	CCF3	322	1.34
FCF2	CCF2	322	1.37
CCF2	CC32A	222.5	1.51
CCF3	CCF2	222.5	1.53
CCF2	CCF2	270.134	1.5328
CCF3	CCF3	277.058	1.5308

Table 3. Newly Determined Angles θ_0 in Degrees and Force Constants k_θ in kcal/mol/rad^{2a}

atom types			k_θ	θ_0
CC33A	CC32A	CCF3	37.3227	112.397
HCA2A	CC32A	CCF3	34.600	106.820
CC32A	CCF3	FCF3	48.248	111.733
FCF3	CCF3	FCF3	35.500	107.100
CC33A	CC32A	CCF2	64	111.54
CC32A	CCF2	FCF2	52	110.66
CC32A	CCF2	CCF3	53	114.91
CC32A	CCF2	CCF2	53	114.91
CCF2	CCF3	FCF3	95	111.05
CCF3	CCF2	FCF2	55	106.36
CCF2	CC32A	HCA2A	52	107.54
FCF2	CCF2	FCF2	35	107.53
CCF2	CCF2	FCF2	21.50	107.73
CCF2	CCF2	CCF3	52.08	116.99
CCF3	CCF3	FCF3	47.149	109.724
CCF3	CCF2	CCF3	91.0318	116.620
CCF2	CCF2	CCF2	45.7428	107.626

^aAll Urey-Bradley terms are set to zero.

Charges. When optimizing the charges such that the HF/6-31(d) interaction energies and distances get reproduced by classical molecular dynamics, a conflict between two target quantities arises. For perfluoro- n -alkanes, one can either optimize for matching interaction distances or for matching interaction energies. Although the HF/6-31(d) energies are rescaled in order to reproduce bulk properties,²⁷ this rescaling is not the reason for the mismatch.

In Figure 4, one can see that there is no way to fulfill the fitting procedure's requirement to reproduce both interaction distances d_i and interaction energies E_i . In order to define a mathematical weighting W with physical justification as a single parameter fitting target, we chose the geometric mean of the relative errors.

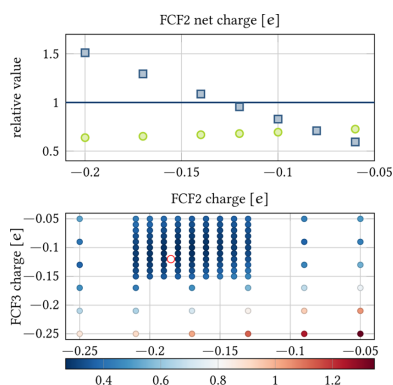


Figure 4. Top: Interaction energy (MD) normalized by the MP2/6-31G(d) results (■) and interaction distances normalized the same way (●) over the FCF2 net charge for f_2 together with the ideal target value (/). The CCF2 net charge has been set such that the overall CF_2 group is neutral. It is clearly visible that there is no optimum that fits both the interaction energies and the interaction distances. Bottom: Given the weighting in eq 5, the deviation from the target values depending on the charges of FCF2 and FCF3 has been rasterized. The optimal value is highlighted (○).

$$W^2 = \left(\frac{E_i(\text{MD}) - E_i(\text{QM})}{E_i(\text{QM})} \right)^2 + \left(\frac{d_i(\text{MD}) - d_i(\text{QM})}{d_i(\text{QM})} \right)^2 \quad (5)$$

In general, only the net charges on the fluorines were optimized, as a CF_2 or CF_3 group has to be neutral in total and, hence, the partial charge of the carbons is directly related to the charge of the fluorines. We used f_2 for charge fitting for the CF_3 group and f_8 for the CF_2 group. For example, if CF_2 would come with a net charge, the total net charge of f_2 and f_8 would be different, and, more important, nonzero. Charge fitting data as shown in the Supporting Information for MP2/6-31G(d) and in literature¹ for a higher level of theory shows that each group is approximately neutral.

The resulting charges, which are given in Table 4, are quite similar to values used in different force fields.^{1,41}

Table 4. Lennard-Jones Parameter ϵ in kcal/mol and R_{\min} in Angstroms Along with Charges in e^a

atom type	q	ϵ	R_{\min}	ϵ'	R'_{\min}
FCF3	-0.12	-0.0240	1.3400	—	—
CCF3	0.36	-0.0780	2.0400	-0.01	1.9
FCF2	-0.185	-0.1050	1.6300	—	—
CCF2	0.37	-0.0420	2.0500	—	—

^aIn one case, a correction (ϵ' and R'_{\min}) for 1,4 atoms is suggested by CGenFF.

Dihedral Angles. For perfluoro- n -alkanes, our simulations confirm the reported^{1,42} observation that the dihedral for the carbon chain does not have its minimum at zero degrees as for n -alkanes, but instead, there is a slight tilt of approximately seven degrees with MP2/6-31G(d) optimizations carried out for f_2 - f_8 , where each of which started from the all-trans n -alkane conformation. This effect is modeled accordingly by

defining a nonzero phase shift for the appropriate dihedral parameter. For the rather short chains, n_1 through n_3 , the tilted chain angle is not clearly visible. Hence, this dihedral is parametrized by using MP2/6-31G(d) geometries for f_2 through f_6 . As the overall target is to simulate comparably long perfluorinated chains, this approach is clearly justified. However, the actual conformations of short partially fluorinated compounds have to be used with care. While the overall torsional profile does not vary significantly when using a higher level of theory, the minimum conformation does: MP2/cc-pVTZ(-f)//HF/6-31G(d) calculations give a tilt angle of about ten degrees.¹

The resulting parameters are given in Table 5, while the dihedral scans are to be found in the Supporting Information.

Table 5. Newly Determined Dihedrals and Their offset δ in Degrees and Force Constants k_x in Kilocalories Per Mol Together with the Multiplicity n

atom types				k_x	n	δ
CC33A	CC32A	CCF3	FCF3	0.164	3	0.0
CCF3	CC32A	CC33A	HCA3A	0.121	3	0.0
FCF3	CCF3	CC32A	HCA2A	0.262	3	0.0
CC33A	CC32A	CCF2	CCF3	0.16	1	0.0
CC32A	CCF2	CCF3	FCF3	0.16	3	0.0
CCF3	CCF2	CC32A	HCA2A	0.16	2	0.0
CC32A	CCF2	CCF2	CCF3	1.875	1	0.0
CC32A	CCF2	CCF2	FCF2	0.530	1	0.0
CC33A	CC32A	CCF2	CCF2	1.481	1	0.0
CC33A	CC32A	CCF2	FCF2	0.510	3	0.0
CCF2	CC32A	CC33A	HCA3A	0.341	3	0.0
CCF2	CCF2	CCF3	FCF3	0.515	1	180.0
FCF2	CCF2	CCF2	CCF3	0.529	1	0.0
FCF2	CCF2	CCF2	FCF2	2.505	1	0.0
FCF3	CCF3	CCF2	FCF2	0.207	3	0.0
HCA2A	CC32A	CCF2	CCF2	0.316	1	0.0
HCA2A	CC32A	CCF2	FCF2	0.034	2	0.0
FCF3	CCF3	CCF3	FCF3	0.218	3	0.0
CCF3	CCF2	CCF3	FCF3	0.082	3	0.0
CCF3	CCF2	CCF2	CCF3	1.164	1	180.0
CCF3	CCF2	CCF2	CCF2	2.508	1	180.0
CCF2	CCF2	CCF2	FCF2	0.040	3	0.0
CCF2	CCF2	CCF2	CCF2	3.000	1	180.0

van der Waals Radii. As we are particularly interested in reproducing the intermolecular interaction, the van der Waals parameters are very important. One way to do so for nonbonded parameters is to calculate liquid densities^{26,27} and compare the results to experimental values. As interaction energies are most sensible to charges and the force constants can be derived from the Hessian matrix,²⁷ the van der Waals parameters can be considered separately from the other parameters. The separation of the bonded and nonbonded parameters is not as strict as the name suggests it to be, hence, the small remaining mutual influence can contribute significantly to torsional angles, even for fluoroalkanes.¹ However, the calculations showed that for the compounds involved, this effect can be neglected, in particular due to the iterative parametrization procedure.

Although the perfluoro- n -alkanes have been of interest to experimentalists for more than 80 years,^{43,44} there are little reference values for densities available. Some species as f_2 are difficult to use in an experiment, as both the melting and

boiling points are quite low.⁴³ In fact, many of the experimental results appear contradicting both in terms of different temperature dependencies and different densities for the same combination of pressure and temperature. This variation of experimental results may come from advances in experimental techniques and different grades of purity. Most of the older publications do not even specify the purity of the sample that has been used for the measurements which already lead⁴⁴ to wrong numbers being published, although many very old measurements^{43,44} are in excellent agreement with more recent studies.⁴⁵ We only used data points that are not contradicting other reported values from numerous studies.^{44–51}

As an initial guess, we used the van der Waals parameters for FGA2, FGA3, CG312 and CG302 from CGenFF.²⁷ Mostly independent from the pressure coupling parameters of the modified⁵² Nosé–Hoover barostat^{53,54} of namd2, the liquid densities exhibit a similar behavior in a NPT simulation. In the beginning of the simulation, the box has to be compressed as it is too large for the number of molecules defined as content. The liquid phase of f_8 ranges from 250 K⁵⁵ up to 373 K,⁵⁶ depending on the pressure. Independent simulation runs for many points in the pressure–temperature phase diagram show the same behavior during their equilibration phase of approximately 80 ps (see Supporting Information).

Due to the delayed response of pressure coupling, even the rather large system size (2394 molecules, 19152 atoms for f_2 , and 701 molecules, 18226 atoms for f_8) does not fully suppress fluctuations. Hence, averaging the density is necessary. For the further evaluation, averaging over 150 ps after a 150 ps equilibration phase seems to be safe from the data in Figure 7 of the Supporting Information. The box size as the only observable for density calculation is recorded every 0.1 ps while being averaged over this interval.

In order to check whether this equilibration phase is long enough, the autocorrelation has been monitored for the density information after equilibration has finished (see Figure 7 of the Supporting Information). The standard deviation of the fluctuations in density determines the statistical error of the resulting densities. For the described setup, the statistical error is in the order of 8 g/m³.

As shown in Figure 5, the density over temperature curve is very sensitive to the van der Waals parameters. For example, for f_8 , a mild change of the parameters used in CHARMM parameter format (R_{\min} and ϵ) of 10% has a particularly strong effect for R_{\min} and a less prominent one for ϵ . The relative impact of the two parameters matches reported results.²⁵

ϵ , which is responsible for the absolute energy of the LJ potential, mostly shifts the densities for all temperatures equally, while a change in σ affects low temperatures more severely than high ones. A larger ϵ enlargens the density, whereas the density decreases with increasing σ . This qualitative behavior matches the expectations, as the van der Waals contribution to the total energy in classical molecular dynamics simulations of f_8 is negative. Hence, increasing ϵ reduces the total energy such that the molecules can be forced to come a bit closer, resulting in increasing Coulomb repulsion until the effect of the increased ϵ is compensated. With larger values for σ , the volume a single molecule occupies is increased cubically.

Figure 6 shows the densities resulting for f_2 from the use of different parameter sets for 20 experimental data points. The initial guess consisted of CGenFF parameters for all four

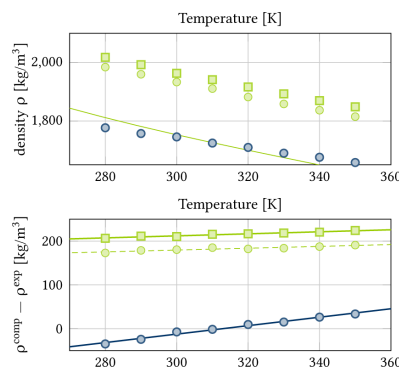


Figure 5. Influence of the van der Waals parameters (ϵ_{FCF2} , R_{\min}) on the temperature dependency of the density of f_8 . Density over temperature for f_8 with default CGenFF parameters (green ●), modified default CGenFF parameters where $R_{\min}/2(\text{FCF2})$ is scaled by 1.1 (blue ●), and modified default CGenFF parameters where $\epsilon(\text{FCF2})$ is scaled by 1.1 (green ■). The upper panel shows absolute calculated densities together with experimental densities (○), whereas the lower panel shows the relative deviation $\rho^{\text{comp}} - \rho^{\text{exp}}$ from the experimental densities.

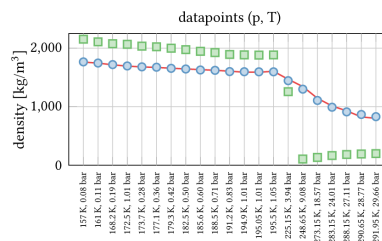


Figure 6. Computed densities for f_2 and different combinations of pressure and temperature. The optimized parameters found in this work (●) reproduce the experimental values (○) better than the original CGenFF parameters (■). The underlying data and the sources for experimental data are given in Table 6.

introduced atom types, chosen by similarity. The corresponding densities differ from the experimental reference values by 38% on average. For high pressures, the CGenFF parameters lead to gas phase simulations, although liquid phase is still expected for this regime. Adjusting only FCF3 parameters and leaving CCF3 as recommended in CGenFF yields appropriate densities with an average error of one percent.

We have also determined the force field parameters for CF_2 groups, using the same method as for CF_3 just for f_8 as target. f_8 has been chosen as there is sufficient experimental data to compare to and as it is long enough in order to diminish the influence of the CF_3 group. Figure 7 shows the resulting densities along with the data for the CGenFF parameters that have been chosen by similarity. Again, varying only the parameters of FCF2 is enough to reproduce the densities over a broad range of points in the phase diagram with an average relative error of two percent, whereas the CGenFF analogy parameters are off by five percent. In both cases, we

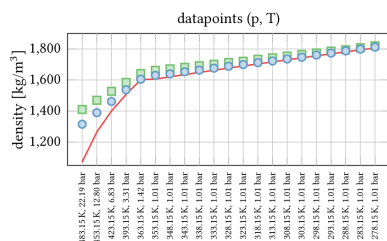


Figure 7. Computed densities for f_6 and different combinations of pressure and temperature. The optimized parameters found in this work (●) reproduce the experimental values (◻) better than the original CGenFF parameters (◼). The underlying data and the sources for experimental data are given in Table 7.

used the results for the CF_3 groups that have been found for f_2 . This is the reason why the difference in terms of the relative average error of the densities calculated from CGenFF parameters and our suggestion is not that large.

All resulting Lennard-Jones parameters are given in Table 4. For liquid perfluoroalkanes, we have excellent agreement with experimental densities, as shown in Tables 6 and 7. The mean absolute relative error for all entries is 0.6%.

Table 6. Computed (ρ^f, ρ^c) and Experimental^{43–45} Densities (ρ^e) for f_2 and Different Combinations of Pressure and Temperature^a

p (bar)	T (K)	ρ^e	ρ^f	ρ^c	$\delta\rho^f$ (%)	$\delta\rho^c$ (%)
0.08	157	1762.8 ⁴⁴	1765.9	2153.7	0.2	22.2
0.11	161	1745.3 ⁴⁴	1746.4	2108.6	0.1	20.8
0.19	168.2	1716.1 ⁴⁴	1719.7	2076.2	0.2	21.0
1.01	172.5	1693.8 ⁴⁴	1696.5	2066.7	0.2	22.0
0.28	173.7	1680.0 ⁴⁴	1681.2	2035.3	0.1	21.2
0.36	177.1	1671.0 ⁴⁴	1675.1	2024.0	0.2	21.1
0.42	179.3	1658.1 ⁴⁴	1656.0	2000.0	-0.1	20.6
0.5	182.5	1645.5 ⁴⁴	1644.4	1975.3	-0.1	20.0
0.6	185.6	1633.7 ⁴⁴	1627.7	1946.7	-0.4	19.2
0.71	188.5	1622.7 ⁴⁴	1621.6	1925.1	-0.1	18.6
0.83	191.2	1607.0 ⁴⁴	1600.4	1892.9	-0.4	17.8
1.01	194.9	1590.0 ⁴⁴	1597.9	1885.6	0.5	18.6
1.01	195.05	1589.5 ⁴⁵	1596.3	1882.6	0.4	18.4
1.05	195.5	1605.3 ⁴⁴	1596.2	1885.3	-0.6	17.4
3.94	225.15	1468.9 ^{43,44}	1444.9	1256.9	-1.6	-14.4
9.08	248.65	1344.0 ^{43,44}	1299.9	105.5	-3.3	-92.2
18.57	273.15	1143.9 ^{43,44}	1107.1	133.5	-3.2	-88.3
24.01	283.15	1012.9 ^{43,44}	991.5	165.4	-2.1	-83.7
27.11	288.15	929.7 ^{43,44}	911.8	183.5	-1.9	-80.3
28.77	290.65	824.8 ^{43,44}	867.2	192.1	5.1	-76.7
29.66	291.95	802.0 ^{43,44}	829.9	199.0	3.5	-75.2

^aFor both the densities calculated using our parameters (ρ^f) and the densities using the CGenFF parameters (ρ^c), their relative error is given as $\delta\rho$. All densities are in grams per meter cubed.

In order to provide an impression for the predictive power of molecular dynamics simulations in terms of thermodynamic quantities, we have performed miscibility simulations of perfluoroalkane f_6 with alkanes using different mole fractions for f_6 . The findings are reported in Table 8 and illustrate that our new force field parameters can give a nearly quantitative

Table 7. Computed (ρ^f, ρ^c) and Experimental^{42,49–51} Densities (ρ^e) for f_6 and Different Combinations of Pressure and Temperature^a

p (bar)	T (K)	ρ^e	ρ^f	ρ^c	$\delta\rho^f$ (%)	$\delta\rho^c$ (%)
1.01	278.15	1806.3 ⁴²	1811.7	1820.3	0.3	0.8
1.01	283.15	1793.8 ⁴²	1798.6	1807.5	0.3	0.8
1.01	288.15	1781.2 ⁴²	1787.1	1794.4	0.3	0.7
1.01	293.15	1768.5 ⁴²	1773.3	1785.7	0.3	1.0
1.01	298.15	1755.7 ⁴²	1760.9	1774.0	0.3	1.0
1.01	303.15	1742.8 ⁴²	1746.6	1764.3	0.2	1.2
1.01	308.15	1729.8 ⁴²	1735.2	1754.0	0.3	1.4
1.01	313.15	1716.7 ⁴²	1722.5	1743.0	0.3	1.5
1.01	318.15	1703.4 ⁴²	1711.6	1733.3	0.5	1.8
1.01	323.15	1690.0 ⁴²	1699.5	1720.9	0.6	1.8
1.01	328.15	1676.4 ⁴²	1688.4	1712.8	0.7	2.2
1.01	333.15	1662.7 ⁴²	1676.0	1701.9	0.8	2.4
1.01	338.15	1648.8 ⁴²	1663.6	1692.1	0.9	2.6
1.01	343.15	1634.7 ⁴²	1652.9	1681.9	1.1	2.9
1.01	348.15	1620.4 ⁴²	1639.2	1672.1	1.2	3.2
1.01	353.15	1605.9 ⁴²	1629.7	1662.5	1.5	3.5
1.42	363.15	1602. ^{49–51}	1605.1	1641.3	0.2	2.5
3.31	393.15	1507. ^{49–51}	1537.1	1584.6	2.0	5.1
6.83	423.15	1400. ^{49–51}	1461.7	1527.5	4.4	9.1
12.80	453.15	1265. ^{49–51}	1389.6	1469.5	9.8	16.2
22.19	483.15	1072. ^{49–51}	1315.1	1410.3	22.7	31.6

^aFor both the densities calculated using our parameters (ρ^f) and the densities using the CGenFF parameters (ρ^c), their relative error is given as $\delta\rho$. All densities are in grams per meters cubed.

Table 8. Experimental (exp) and Computed (comp) Miscibility of Perfluoroalkane (f_6) with Alkanes for Different Temperatures T and f_6 Mole Fractions x_1 near the Cloud Point^a

mixture	T (K)	x_1	exp	comp
perfluoroalkane–octane	300	0.9	yes ⁵⁷	yes
perfluoroalkane–octane	300	0.8	no ⁵⁷	no
perfluoroalkane–hexane	295	0.8	yes ⁵⁷	yes
perfluoroalkane–hexane	295	0.3	yes ⁵⁷	yes

^aIn all cases, the experimental observation of whether the mixture is miscible or immiscible is reproduced by our simulations.

description of the lipophilicity/lipophobicity of perfluorinated chains. This is even more remarkable as all four systems in Table 8 represent thermodynamic states close to the cloud point.

Besides the liquid densities and the miscibility with alkanes, which are of crucial importance for the interaction of perfluoroalkanes with the membrane lipids, it is reasonable to check for collective properties of pure liquid perfluoroalkanes which gain importance for higher concentrations of perfluoroalkanes in membranes. Table 9 shows thermodynamic properties which are energetics and charge-related. The heat of vaporization depends on all contributions to the total potential energy, the heat capacity is checked on the force constants as a subset thereof. The energy scaling ϵ is evaluated by checking the thermal expansion coefficient, while the charges and bond lengths are the main contributor to the static dielectric constant. The viscosity is governed by the overall dynamics of the liquid. From Table 9, one can see that some properties are overestimated and some are underestimated by the force field definition and our parameters, but none of these

Table 9. Experimental (exp) and Computed (comp) Properties of Pure Perfluorohexane (f6) along with the Relative Error δ (comp)

property	exp	comp	δ (comp) (%)
heat of vaporization at 293.15 K in cal/mol	7793. ⁵⁸	8866.	14
heat capacity (C_p) at 293 K in cal/(mol K)	61. ⁵⁹	79.	30
thermal expansion coefficient 293 K in $10^{-3}/K$	1.88 ⁵⁹	1.49	-21
static dielectric constant	1.74 ⁶⁰	1.11	-36
viscosity in mPa s	0.635 ⁶¹	0.425	-33

thermodynamic properties are highly different from the corresponding experimental result. The significant errors are no surprise, as not all physical effect relevant, for example the static dielectric constant, are incorporated in the force field energy function. As a final check, we have increased all force constants for bonded and angle terms by 10%. We got a heat capacity of 66 cal/(mol K) which is only eight percent above the experimental value (improvement), but the thermal expansion coefficient is $1.009 \times 10^{-3}/K$ which is 46% smaller than the experimental value.

CONCLUSION

We derived computational parameters for fluoroalkanes of arbitrary length for use within the CHARMM force field. Bonded parameters and charges have been calculated from quantum chemical calculations, whereas van der Waals interaction parameters have been determined in order to reproduce experimental liquid densities of perfluoroalkanes.

Having tested interaction energies with water, conformational properties (bond lengths, angles, torsional profiles) when compared to MP2/6-32G(d) calculations, pure liquid densities over a broad pressure and temperature range for perfluoroalkanes of different chain length, the miscibility with alkanes, and thermodynamic properties (heat of vaporization, heat capacity, thermal expansion coefficient, static dielectric constant, and viscosity), we believe that the parameters presented in this work adequately model the behavior of perfluoroalkanes in pure liquids and membrane environments.

Our results are in excellent agreement with experimental data. The average relative error of liquid perfluoroalkane densities over a broad range of both pressure and temperature is 0.6%. Benchmark molecular dynamics simulations using our new set of force field parameters show that the mixing behavior of different combinations of perfluoroalkanes and alkanes is reproduced.

Our extension of the CHARMM parameter set toward perfluorinated organic molecules considerably enlarges the applicability of this (already very versatile) force field to challenging applications, in particular, in view of the structural and dynamical properties of polyphilic systems embedded in lipid membranes.

ASSOCIATED CONTENT

Supporting Information

Details about Merz-Singh-Kollmann partial charges, several dihedral angle potential energy scans, and the temperature-dependent densities of the f8 system. This material is available free of charge via the Internet at <http://pubs.acs.org>.

AUTHOR INFORMATION

Corresponding Author

*E-mail: daniel.sebastiani@chemie.uni-halle.de.

Notes

The authors declare no competing financial interest.

ACKNOWLEDGMENTS

This work was supported by the Deutsche Forschungsgemeinschaft (DFG) within the Forschergruppe FOR1145 (proposal code Se1008/9-1).

REFERENCES

- (1) Pádúa, A. A. H. Torsion Energy Profiles and Force Fields Derived from Ab Initio Calculations for Simulations of Hydrocarbon-Fluorocarbon Diblocks and Perfluoroalkylbromides. *J. Phys. Chem. A* **2002**, *106*, 10116–10123.
- (2) Riess, J. G. Oxygen Carriers (“Blood Substitutes”) Raison d’Etre, Chemistry, and Some Physiology. *Chem. Rev.* **2001**, *101*, 2797–2920.
- (3) Krafft, M. P.; Riess, J. G. Chemistry, Physical Chemistry, and Uses of Molecular Fluorocarbon-Hydrocarbon Diblocks, Triblocks, and Related Compounds—Unique “Apolar” Components for Self-Assembled Colloid and Interface Engineering. *Chem. Rev.* **2009**, *109*, 1714–1792.
- (4) Elbert, R.; Folda, T.; Ringsdorf, H. Saturated and Polymerizable Amphiphiles with Fluorocarbon Chains. Investigation in Monolayers and Liposomes. *J. Am. Chem. Soc.* **1984**, *106*, 7687–7692.
- (5) Chu, Q.; Yu, M. S.; Curran, D. P. New Fluorous/Organic Biphasic Systems Achieved by Solvent Tuning. *Tetrahedron* **2007**, *63*, 9890–9895.
- (6) Cornils, B. Fluorous Biphasic Systems—The New Phase-Separation and Immobilization Technique. *Angewandte Chemie International Edition in English* **1997**, *36*, 2057–2059.
- (7) Rolland, J.-P.; Santaella, C.; Monasse, B.; Vierling, P. Miscibility of Binary Mixtures of Highly Fluorinated Double-Chain Glycerophosphocholines and 1,2-Dipalmitoylphosphatidylcholine (DPPC). *Chem. Phys. Lipids* **1997**, *85*, 135–143.
- (8) Zeng, X.; Kieffer, R.; Glettner, B.; Nürnberger, C.; Liu, F.; Pelz, K.; Prehm, M.; Baumeister, U.; Hahn, H.; Lang, H.; Gehring, G. A.; Weber, C. H. M.; Hobbs, J. K.; Tschierske, C.; Ungar, G. Complex Multicolor Tilings and Critical Phenomena in Tetraphilic Liquid Crystals. *Science* **2011**, *331*, 1302–1306.
- (9) Li, Z.; Amado, E.; Kressler, J. Self-Assembly Behavior of Fluorocarbon-End-Capped Poly(glycerol methacrylate) in Aqueous Solution. *Colloid Polym. Sci.* **2012**, *291*, 867–877.
- (10) Tan, X.; Kong, L.; Dai, H.; Cheng, X.; Liu, F.; Tschierske, C. Triblock Polyphiles Through Click Chemistry: Self-Assembled Thermotropic Cubic Phases Formed by Micellar and Monolayer Vesicular Aggregates. *Chem.—Eur. J.* **2013**, *19*, 16303–16313.
- (11) Schwieger, C.; Achilles, A.; Scholz, S.; Rüger, J.; Bacia, K.; Saalwächter, K.; Kressler, J.; Blume, A. Binding of Amphiphilic and Triphilic Block Copolymers to Lipid Model Membranes: The Role of Perfluorinated Moieties. *Soft Matter* **2014**, *10*, 6147–6160.
- (12) Tschierske, C. Development of Structural Complexity by Liquid-Crystal Self-Assembly. *Angew. Chem., Int. Ed.* **2013**, *52*, 8828–8878.
- (13) Hill, E. H.; Stratton, K.; Whitten, D. G.; Evans, D. G. Molecular Dynamics Simulation Study of the Interaction of Cationic Biocides with Lipid Bilayers: Aggregation Effects and Bilayer Damage. *Langmuir* **2012**, *28*, 14849–14854.
- (14) Raychaudhuri, P.; Li, Q.; Mason, A.; Mikhailova, E.; Heron, A. J.; Bayley, H. Fluorinated Amphiphiles Control the Insertion of α -Hemolysin Pores into Lipid Bilayers. *Biochemistry* **2011**, *50*, 1599–1606.
- (15) Krafft, M. P. Controlling Phospholipid Self-Assembly and Film Properties Using Highly Fluorinated Components—Fluorinated Monolayers, Vesicles, Emulsions and Microbubbles. *Biochimie* **2012**, *94*, 11–25.

4. PUBLICATIONS

- (16) Scholtysek, P.; Li, Z.; Kressler, J.; Blume, A. Interactions of DPPC with Semitelechelic Poly(glycerol methacrylate)s with Perfluoroalkyl End Groups. *Langmuir* **2012**, *28*, 15651–15662.
- (17) Cui, S. T.; Cochran, H. D.; Cummings, P. T. Vapor-Liquid Phase Coexistence of Alkane-Carbon Dioxide and Perfluoroalkane-Carbon Dioxide Mixtures. *J. Phys. Chem. B* **1999**, *103*, 4485–4491.
- (18) Cui, S. T.; Stepmann, J. L.; Cochran, H. D.; Cummings, P. T. Intermolecular Potentials and Vapor-Liquid Phase Equilibria of Perfluorinated Alkanes. *Fluid Phase Equilib.* **1998**, *146*, 51–61.
- (19) Borodin, O.; Smith, G. D.; Bedrov, D. A Quantum Chemistry Based Force Field for Perfluoroalkanes and Poly(tetrafluoroethylene). *J. Chem. Phys. B* **2002**, *106*, 9912–9922.
- (20) MacKerell, A. D.; et al. All-Atom Empirical Potential for Molecular Modeling and Dynamics Studies of Proteins. *J. Phys. Chem. B* **1998**, *102*, 3586–3616.
- (21) Klauda, J. B.; Venable, R. M.; Freites, J. A.; O'Connor, J. W.; Tobias, D. J.; Mondragon-Ramirez, C.; Vorobyov, I.; MacKerell, A. D.; Pastor, R. W. Update of the CHARMM All-Atom Additive Force Field for Lipids: Validation on Six Lipid Types. *J. Phys. Chem. B* **2010**, *114*, 7830–7843.
- (22) Mantina, M.; Chamberlin, A. C.; Valero, R.; Cramer, C. J.; Truhlar, D. G. Consistent van der Waals Radii for the Whole Main Group. *J. Phys. Chem. A* **2009**, *113*, 5806–5812.
- (23) Lorentz, H. A. Ueber die Anwendung des Satzes vom Virial in der kinetischen Theorie der Gase. *Ann. Phys. (Berlin)* **1881**, *248*, 127–136.
- (24) Berthelot, D. Sur le mélange des gaz. *C. R. hebdom. Acad. Sci.* **1898**, *126*, 1703–1706.
- (25) Boda, D.; Henderson, D. The Effects of Deviations from Lorentz-Berthelot Rules on the Properties of a Simple Mixture. *Mol. Phys.* **2008**, *106*, 2367–2370.
- (26) Delhomelle, J.; Millié, P. Inadequacy of the Lorentz-Berthelot Combining Rules for Accurate Predictions of Equilibrium Properties by Molecular Simulation. *Mol. Phys.* **2000**, *99*, 619–625.
- (27) Vanommeslaeghe, K.; Hatcher, E.; Acharya, C.; Kundu, S.; Zhong, S.; Shim, J.; Darian, E.; Guvench, O.; Lopes, P.; Vorobyov, I.; MacKerell, A. D. CHARMM General Force Field: A Force Field for Drug-Like Molecules Compatible with the CHARMM All-Atom Additive Biological Force Fields. *J. Comput. Chem.* **2010**, *31*, 671–690.
- (28) Yesselman, J. D.; Price, D. J.; Knight, J. L.; Brooks, C. L. MATCH: an Atom-Typing Toolset for Molecular Mechanics Force Fields. *J. Comput. Chem.* **2012**, *33*, 189–202.
- (29) Vanommeslaeghe, K.; MacKerell, A. D. Automation of the CHARMM General Force Field (CGenFF) I: Bond Perception and Atom Typing. *J. Chem. Inf. Model.* **2012**, *52*, 3144–3154.
- (30) MacKerell, A. D. Empirical Force Fields for Biological Macromolecules: Overview and Issues. *J. Comput. Chem.* **2004**, *25*, 1584–1604.
- (31) Thomas, M.; Brehm, M.; Fligg, R.; Vöhringer, P.; Kirchner, B. Computing Vibrational Spectra from ab Initio Molecular Dynamics. *Phys. Chem. Chem. Phys.* **2013**, *15*, 6608–6622.
- (32) Young, D. C. *Computational Chemistry: A Practical Guide for Applying Techniques to Real World Problems*; John Wiley & Sons, Inc., 2001.
- (33) Mayne, C. G.; Saam, J.; Schulten, K.; Tajkhorshid, E.; Gumbart, J. C. Rapid Parameterization of Small Molecules Using the Force Field Toolkit. *J. Comput. Chem.* **2013**.
- (34) Frisch, M. J. et al. Gaussian 09 Revision A.2, Gaussian Inc.: Wallingford CT, 2009.
- (35) Phillips, J. C.; Braun, R.; Wang, W.; Gumbart, J.; Tajkhorshid, E.; Villa, E.; Chipot, C.; Skeel, R. D.; Kalé, L.; Schulten, K. Scalable Molecular Dynamics with NAMD. *J. Comput. Chem.* **2005**, *26*, 1781–1802.
- (36) Humphrey, W.; Dalke, A.; Schulten, K. VMD: Visual Molecular Dynamics. *J. Mol. Graphics* **1996**, *14*, 33.
- (37) Michaud-Agrawal, N.; Denning, E. J.; Woolf, T. B.; Beckstein, O. MDAnalysis: A Toolkit for the Analysis of Molecular Dynamics Simulations. *J. Comput. Chem.* **2011**.
- (38) Theobald, D. L. Rapid Calculation of RMSDs Using a Quaternion-Based Characteristic Polynomial. *Acta Crystallogr. A* **2005**, *61*, 478–480.
- (39) Pronk, S.; Páll, S.; Schulz, R.; Larsson, P.; Bjelkmar, P.; Apostolov, R.; Shirts, M. R.; Smith, J. C.; Kasson, P. M.; van der Spoel, D.; Hess, B.; Lindahl, E. GROMACS 4.5: a High-Throughput and Highly Parallel Open Source Molecular Simulation Toolkit. *Bioinformatics* **2013**, *29*, 845–854.
- (40) Vorobyov, I.; Anisimov, V. M.; Greene, S.; Venable, R. M.; Moser, A.; Pastor, R. W.; MacKerell, A. D. Additive and Classical Drude Polarizable Force Fields for Linear and Cyclic Ethers. *J. Chem. Theory Comput.* **2007**, *3*, 1120–1133.
- (41) Song, W.; Rossky, P. J.; Maroncelli, M. Modeling Alkane+Perfluoroalkane Interactions Using All-Atom Potentials: Failure of the Usual Combining Rules. *J. Chem. Phys.* **2003**, *119*, 9145–9162.
- (42) Morgado, P.; Lewis, J. B.; Laginhas, C. M. C.; Martins, L. F. G.; McCabe, C.; Blas, F. J.; Filipe, E. J. M. Systems Involving Hydrogenated and Fluorinated Chains: Volumetric Properties of Perfluoroalkanes and Perfluoroalkylalkane Surfactants. *J. Phys. Chem. B* **2011**, *115*, 15013–15023.
- (43) Swarts, F. Sur l'hexafluoroéthane. *Bull. Soc. Chim. Belg.* **1933**, *42*, 114–118.
- (44) Ruff, O.; Bretschneider, O. Die Bildung von Hexafluoräthan und Tetrafluoräthylen aus Tetrafluorkohlenstoff. *Z. anorg. allg. Chem.* **1933**, *210*, 173–183.
- (45) Watkins, E. K.; Jorgensen, W. L. Perfluoroalkanes: Conformational Analysis and Liquid-State Properties from ab Initio and Monte Carlo Calculations. *J. Phys. Chem. A* **2001**, *105*, 4118–4125.
- (46) Simons, J. H.; Block, L. P. Fluorocarbons. The Reaction of Fluorine with Carbon. *J. Am. Chem. Soc.* **1939**, *61*, 2962–2966.
- (47) Haszeldine, R. N.; Smith, F. Organic Fluorides. Part VI. The Chemical and Physical Properties of Certain Fluorocarbons. *J. Chem. Soc.* **1951**, 603.
- (48) Morgado, P.; Laginhas, C. M. C.; Lewis, J. B.; McCabe, C.; Martins, L. F. G.; Filipe, E. J. M. Viscosity of Liquid Perfluoroalkanes and Perfluoroalkylalkane Surfactants. *J. Phys. Chem. B* **2011**, *115*, 9130–9139.
- (49) Ermakov, G. V.; Skripov, V. P. Thermodynamic Properties of Perfluorocarbons. *Russ. J. Phys. Chem.* **1969**, *13*, 726.
- (50) Skripov, V. P.; Firsov, V. V. Surface Tension of Perfluoroalkanes. *Russ. J. Phys. Chem.* **1968**, *42*, 653–656.
- (51) Chickos, J. S.; Acree, W. E. Enthalpies of Vaporization of Organic and Organometallic Compounds 1880–2002. *J. Phys. Chem. Ref. Data* **2003**, *32*, 519.
- (52) Bhandarkar, M.; Bhatle, A.; Bohm, E.; Brunner, R. NAMD User's Guide 2.9. 2012.
- (53) Hoover, W. G. Canonical Dynamics: Equilibrium Phase-Space Distributions. *Phys. Rev. A* **1985**, *31*, 1695–1697.
- (54) Nosé, S. A Unified Formulation of the Constant Temperature Molecular Dynamics Methods. *J. Chem. Phys.* **1984**, *81*, 511–519.
- (55) Campos-Vallette, M.; Rey-Lafon, M. Vibrational Spectra and Rotational Isomerism in Short Chain n-Perfluoroalkanes. *J. Mol. Struct.* **1983**, *101*, 23–45.
- (56) Dunitz, J. D. Organic Fluorine: Odd Man Out. *ChemBiochem* **2004**, *5*, 614–621.
- (57) Matsuda, H.; Kitabatake, A.; Kosuge, M.; Kurihara, K.; Tochigi, K.; Ochi, K. Liquid-Liquid Equilibrium Data for Binary Perfluoroalkane (C6 and C8)+n-Alkane Systems. *Fluid Phase Equilib.* **2010**, *297*, 187–191.
- (58) Stiles, V. E.; Cady, G. H. Physical Properties of Perfluoro-n-hexane and Perfluoro-2-methylpentane. *J. Am. Chem. Soc.* **1952**, *74*, 3771–3773.
- (59) Campos-Vallette, M.; Diaz-Fleming, G. Some Physical and Thermodynamic Properties of n-cnfn+2 Compounds with n = 4–8. *Semina: Ciências Biológicas e da Saúde* **1983**, *4*, 405.
- (60) Drummond, C. J.; Georgaklis, G.; Chan, D. Y. C. Fluorocarbons: Surface Free Energies and van der Waals Interaction. *Langmuir* **1996**, *12*, 2617–2621.

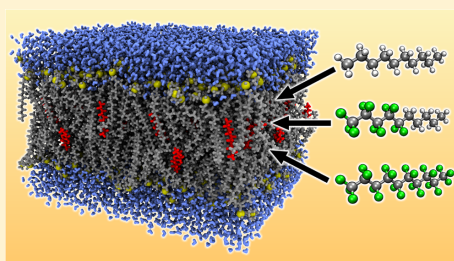
(61) Morgado, P.; Black, J.; Lewis, J. B.; Iacovella, C. R.; McCabe, C.; Martins, L. F. G.; Filipe, E. J. M. Viscosity of Liquid Systems Involving Hydrogenated and Fluorinated Substances: Liquid Mixtures of (Hexane+Perfluorohexane). *Fluid Phase Equilib.* **2013**, 358, 161–165.

Influence of Small Fluorophilic and Lipophilic Organic Molecules on Dipalmitoylphosphatidylcholine Bilayers

Martin Brehm,[✉] Ghulam Saddiq, Tobias Watermann, and Daniel Sebastiani*

Institut für Chemie—Theoretische Chemie, Martin-Luther-Universität Halle-Wittenberg, Von-Danckelmann-Platz 4, 06120 Halle (Saale), Germany

ABSTRACT: In this study, we investigate the effect of a series of additive molecules with different types of philicities on the structure and dynamics of dipalmitoylphosphatidylcholine (DPPC) bilayers. To this aim, we performed extensive force field molecular dynamics simulations of the systems, using our recently developed perfluoroalkane force field. We found that addition of perfluoro-*n*-decane and fluorotelomer alcohol at 323 K leads to a phase transition of the membrane from liquid crystalline to the gel phase, whereas the addition of *n*-decane and partially fluorinated *n*-decane leaves the liquid crystalline phase intact. The systems in the gel phase show a significantly reduced diffusivity for both DPPC and additive molecules. The addition of nonfluorinated and partially fluorinated *n*-decane even leads to an increased DPPC diffusivity. While nonfluorinated *n*-decane and partially fluorinated *n*-decane are found mainly in the middle of the bilayer, perfluoro-*n*-decane penetrates significantly deeper into the membrane leaflet. Fluorotelomer alcohol is found almost exclusively inside the leaflet, with its hydroxyl groups forming a strong hydrogen bond network to the ester oxygen atoms in the head group of DPPC. A slight increase in temperature by only 10 K is already sufficient to dynamically overcome this hydrogen bond network, such that no phase transition occurs in that case.



INTRODUCTION

Perfluorinated *n*-alkanes represent an interesting and special class of molecules due to their specific and unusual properties. As a result of the special nature of the C–F bond, they are considerably more hydrophobic than lipids, but they are not lipophilic either, which allows for interesting applications both in materials science and in biochemistry. Despite their structural similarity to hydrocarbons, these fluorocarbons have high thermal stability and chemical inactivity.¹ Although strong intramolecular forces are present due to the C–F bond, the weak polarizability of the fluorinated chains results in low intermolecular or van der Waals interactions.² Minimal intermolecular interactions, coupled with the bulkiness and rigidity of the C–F chains, lead to higher density, higher melting points, lower surface tension, low refractive indices, lower boiling points, and surface spreading of fluorocarbon compounds in comparison with hydrocarbons.³ Perfluorinated compounds (PFCs) have numerous applications for medical purposes as oxygen-carrier fluids,^{4,5} in purification or polymerization,⁴ and as lubricants.⁶ PFCs are especially interesting due to their phase separation behavior in hydrocarbon environments.⁷ The versatility of their applications can be attributed to the strength of the C–F covalent bond, which results in physicochemical properties that are distinct from those of traditional hydrocarbon-based systems.^{8,9}

Fluorinated amphiphiles are attractive due to their unique properties, such as combined hydrophobicity and lipophilicity¹⁰ and high gas-dissolving capacity, chemical and biological

inertness, and high fluidity.^{10,11} The fundamental properties and potential applications of fluorinated amphiphiles have been reviewed in the literature.^{5,6} It is generally perceived that fluorine exerts only a moderate steric influence relative to hydrogen in organic compounds,¹² but the electronegativity of fluorine can have significant electronic influences. Amphiphiles with short fluorinated chains ($n(\text{CF}_2) \leq 8$) are considered to be acceptable in clinical applications. In addition, highly fluorinated amphiphiles have multiple applications in materials science^{5,13,14} as well as in the biomedical field, often involving colloidal systems stabilized by monomolecular films of fluorinated amphiphiles. They could potentially find applications as blood substitutes^{13,15–18} and lung surfactant replacements.^{19–22}

As examples, fluorinated alcohols such as hexafluoro-2-propanol (HFIP) and trifluoroethanol (TFE) are not considered *sensu stricto* as fluorosol media.²³ However, the presence of one or more fluoroalkyl groups introduces specific properties to fluorinated alcohols compared to those that are nonfluorinated. They have high ionizing power²⁴ and an acidic character.²⁵ They are strong hydrogen bond donors²⁶ and poor nucleophiles.²⁷ The properties of fluorinated alcohols have been exploited in physical organic chemistry,²⁷ in the

Received: July 3, 2017

Revised: August 16, 2017

Published: August 16, 2017

Table 1. Systems Studied

system	composition	mixing ratio	simulation temp (K)	simulation time (ns)
pure	72 DPPC		323	69.3
	2189 H ₂ O			
H10	72 DPPC	6:1	323	311.2
	2189 H ₂ O			
	12 CH ₃ (CH ₂) ₈ CH ₃			
HSF5	72 DPPC	6:1	323	301.0
	2189 H ₂ O			
	12 CH ₃ (CH ₂) ₄ (CF ₂) ₄ CF ₃			
F10	72 DPPC	6:1	323	301.5
	2189 H ₂ O			
	12 CF ₃ (CF ₂) ₈ CF ₃			
FTOH	72 DPPC	6:1	323	268.9
	2189 H ₂ O			
	12 CF ₃ (CF ₂) ₇ (CH ₂) ₂ OH			
FTOH 333 K	72 DPPC	6:1	333	301.9
	2189 H ₂ O			
	12 CF ₃ (CF ₂) ₇ (CH ₂) ₂ OH			
FTOH 4:1	72 DPPC	4:1	323	279.4
	2189 H ₂ O			
	18 CF ₃ (CF ₂) ₇ (CH ₂) ₂ OH			

stabilization of radical cations,²⁸ and for their effect on the conformation of proteins and peptides.²⁹

Among fluorinated alcohols, fluorotelomer alcohols (FTOHs) play a significant role in studies of atmospheric chemistry. FTOHs are linear fluorinated alcohols with the formula C_nF_{2n+1}C₂H₄OH ($n = 2, 4, 6, \dots$).^{30,31}

FTOH molecules have physicochemical properties similar to those of perfluoro-*n*-alkanes. For this reason, this study investigates the fluorotelomer alcohol CF₃(CF₂)₇(CH₂)₂OH, which possesses a hydroxyl group of weak acidity in a normal aqueous environment and is not strongly affected by pH.

The choice of phospholipids as a constituent in model membranes is important in describing the partitioning in a real biological system. A prominent phospholipid is the dipalmitoylphosphatidylcholine (DPPC) bilayer, for which a phase transition at 41 °C has been reported.³² DPPC is one of the constituents of the pulmonary surfactant found in lung alveoli.³³ DPPC bilayers are well characterized,^{34,35} and are often used as models of the outer cell membrane leaflet. A characteristic feature of the DPPC is the gel–liquid crystalline phase transition, which occurs at a temperature T_m (melting temperature) that is dependent on the bilayer properties and solution conditions.³⁶ In the gel phase ($<T_m$), the lipid chains are tightly packed with strong van der Waals interactions. The chains possess restricted lateral and rotational freedom of motion, with perpendicular alignment to the head group plane (*trans* conformation) and parallel alignment to each other.^{37,38} Above T_m in the liquid crystalline phase, the bilayer is characterized by a less organized arrangement with a *trans-gauche* conformation of the hydrocarbon chains, increased lateral expansion, and rotational motion. The phase transition involves the melting of hydrocarbon tails, which is therefore dependent on the cohesion of the hydrocarbon chains.

The gel phase is rigid with high microviscosity, which decreases with increasing temperature, and a transition to the more fluid liquid crystalline state eventually occurs. Typically, for a well-ordered bilayer, the change from the gel to the fluid phase is a quick transition, occurring over a very narrow temperature range. This is due to conformational restrictions of

the ordered chains and excluded volume interactions between the terminal methyl groups in the bilayer.³⁸ As a result of these packing constraints, the chains in the bilayer become disordered by a cooperative event. Studies have demonstrated significant improvement in liposome stability with the incorporation of fluorinated chains. Vesicles formed from partially fluorinated DPPC lipids displayed a 50-fold higher stability than pure DPPC liposomes, with additional resistance to heat sterilization.³⁹

Studies have found that PFCs cause alterations in cell membrane properties.⁴⁰ Molecules containing perfluorinated alkyl chains and conjugated oligomers influence channel formation when they are added to a membrane environment,⁴¹ and also affect the overall stability⁴² and surface properties⁴³ of a lipid membrane. Due to the limited solubility of therapeutic agents in fluorocarbon fluids, the incorporation of fluorinated or partially fluorinated surfactants is often a prerequisite for effective solubilization. In the context of membrane environments, perfluoro-*n*-alkanes have been parametrized for lipid bilayer simulations to investigate the physical processes and mechanisms that are responsible for their macroscopic behavior.³ The factors affecting solute incorporation in bilayers include the solute charge and structure.⁴⁴ Temperature causes variations in the bilayer organization⁴⁵ and in the chain order at the center of the bilayer in densely packed acyl regions.⁴⁶ The incorporation of fluorinated surfactants in lipid bilayers greatly influences the chain order and permeability of liposomes.⁴⁷ Another interesting effect of the incorporation of fluorinated chains is their impact on liposome gel to fluid phase transition temperatures, T_m . Although incorporation of fluorinated chains in liposome bilayers can increase the characteristic gel to fluid phase transition temperature (T_m), this effect is highly dependent on other structural features that include the length, relative proportions, and symmetry of the fluorinated segments in the bilayer.^{48,49} The transition temperature of the lipid bilayers increases with the degree of fluorination if both lipid chains are uniformly fluorinated. However, chain asymmetry and partially fluorinated lipids where one of the two acyl chains was fully a hydrocarbon (similar to a jointed F/H chain)

resulted in fluid bilayers. Structural effects that reduced fluorinated chain interactions resulted in less cohesive packing in the bilayers.⁴⁹

■ COMPUTATIONAL DETAILS

To investigate the influence of additive molecules on DPPC bilayers, seven molecular dynamics simulations have been performed. One of them contains a pure DPPC bilayer without additive molecules as a reference; the six other simulations comprise some additive molecules within the membrane. An overview of the systems investigated within this study as well as the labels used to refer to the systems is given in Table 1. For the molecular structures of the molecules involved in this study, see Figure 1.

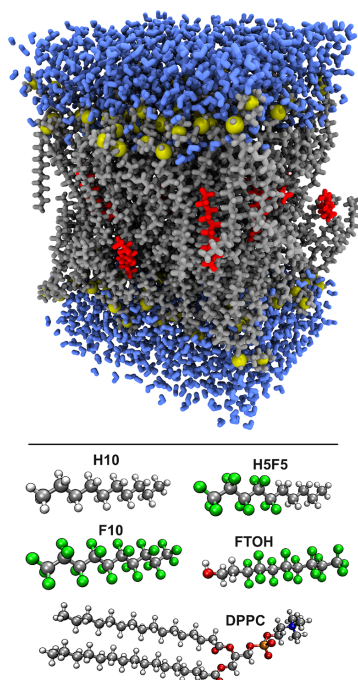


Figure 1. Upper panel: snapshot of the H10 unit cell (gray, DPPC C/H/O atoms; yellow, DPPC N/P atoms; red, *n*-decane; blue, water). Lower panel: molecular structures of the molecules involved in this study.

The simulated systems contain a bilayer of 72 DPPC molecules and 2189 water molecules in a periodic box. The lipid bilayer slabs are separated by water layers of about 4 nm diameter. Orientation was chosen such that the normal vector of the bilayer pointed in the *Z* direction. Additive molecules were inserted into the *X–Y* plane directly in the middle of the DPPC bilayer. The total system size was initially $4.742 \times 4.742 \times 6.833$ nm in all cases. The simulations have been performed with the program package NAMD 2.9,⁵⁰ within the NpT ensemble, using a Langevin thermostat with a damping

parameter of 1.0 ps to control the temperature. The pressure was kept at 1.013 bar by the Langevin piston Nosé–Hoover method (oscillating period 200 fs, damping time 100 fs), which allowed the three cell vectors to vary independently of each other. The time step was chosen to be 1.5 fs, and all rigid bond lengths were constrained by using the Shake algorithm. The cutoff distance for the nonbonded interactions was set to 1.5 nm, with a switching distance of 1.2 nm. It is known that electrostatic long-range interactions are of particular importance for this kind of system,⁵¹ so we applied the particle mesh Ewald (PME) method to handle long-range interactions. The initial atomic velocities have been randomly generated from a Maxwell–Boltzmann distribution centered at the respective simulation temperature. The production run was performed over a physical time between 250 and 300 ns in all cases.

Simulations were performed with recently developed force field parameters for organic additive molecules in DPPC membranes,¹ which are based on the CHARMM force field.^{52,53} For water, the TIP3P model^{54,55} was applied. All analyses presented within this work have been performed with our freeware program package TRAVIS.⁵⁶ The plots in this paper have been created with xmgrace⁵⁷ and Gnuplot.⁵⁸

■ RESULTS AND DISCUSSION

Area per Lipid. It has been extensively discussed in the literature that the lateral area per lipid can be a good measure of the order in DPPC bilayers, and that a significant change in the area per lipid can be an indication of phase transitions.^{59–63} Therefore, we start our analysis by investigating the temporal development of the area per lipid in our simulation trajectories. The lateral area per lipid in a DPPC double layer can simply be computed by

$$A_{\text{lipid}} := \frac{2xy}{N_{\text{DPPC}}} \quad (1)$$

where *x* and *y* are the simulation cell edge lengths in the *X* and *Y* directions (assuming that the membrane normal vector is oriented in the *Z* direction), and N_{DPPC} is the total number of DPPC molecules in the simulation. In the NpT ensemble, the cell edge lengths change over time, and therefore, the area per lipid is nonconstant over time.

The resulting temporal developments of the area per lipid are shown in Figure 2. The gray line indicates the average value from the simulation of the pure membrane without additive molecules; it has a value of 59.6 \AA^2 . It can be seen that the trajectories H10 and H5F5 remain at the area per lipid value of the pure DPPC membrane, and therefore probably do not undergo a phase transition during the simulation time. The systems F10, FTOH, and FTOH 4:1 show a significant decrease in area per lipid after 10–50 ns of simulation time, and therefore are likely to experience a phase transition in the first part of the trajectories. The decrease occurs much faster for FTOH and FTOH 4:1 than for F10. The FTOH 333 K simulation remains at the starting value, but shows some movement toward the decreased area per lipid value, which might indicate that this system is very close to a phase transition. The nature of this phase transition will be characterized in the next section.

Lipid Tail Structure. Collective Tail Tilting. As found from analyzing the area per lipid developments, some of the simulated systems are assumed to undergo a phase transition during the simulation. One might claim that this transition is

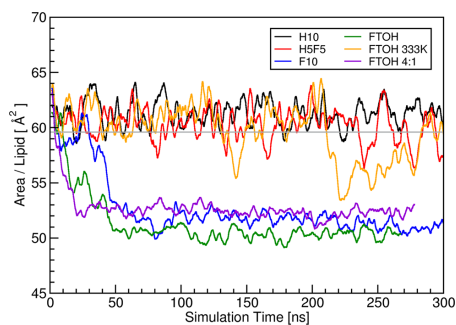


Figure 2. Temporal development of the lateral area per lipid during simulation runs. The gray line depicts the average value of the pure membrane.

from the liquid crystalline phase to a gel phase, as commonly happens when certain compounds are added to DPPC bilayers. This claim will be substantiated in the following. A DPPC gel phase is characterized by the collective tilting of the carboxylic acid tails;⁶⁴ i.e., the alkyl chains should all be significantly tilted with respect to the membrane normal vector, and the tilt vectors of the chains should all point in the same direction within each leaflet of the bilayer. To investigate this, we defined the vector from the α carbon atom to the ω carbon atom of the DPPC carboxylic acids as the tail tilt vector, and projected all these vectors into the X - Y plane. This was performed separately for each of the two leaflets of the bilayer. Only the last 5 ns of each trajectory have been considered for this analysis.

As an example, the tilting vector projections of the H10 system (left two panels) and the F10 system (right two panels) are shown in Figure 3. The upper and lower panels represent the two leaflets of the bilayer in each trajectory, respectively. It can be clearly seen that, in the H10 trajectory, the tilting vectors are distributed over a wide range and possess no preferred direction. The maximum of the distribution is found in the coordinate origin, which corresponds to no tilting of the tails on average. This behavior is characteristic for the liquid crystalline phase of DPPC. In the F10 trajectory, on the other hand, the distribution of the tilting vectors is very narrow and pronounced for both leaflets. The maximum of the distribution is far from the origin, which indicates that all tails are significantly tilted in the same direction. The distributions for both leaflets are found at opposite Y coordinates. On the basis of the definition of the tilting vector above (the vectors in both leaflets point to the inside of the membrane per definition), this means that the tilting vectors within both leaflets are almost collinear. This is another characteristic of the DPPC gel phase. Furthermore, the tilting direction does not vary significantly during 5 ns of the trajectory, which is in line with the significantly decreased chain dynamics in the gel phase.

This analysis has also been performed for the remaining trajectories. While the results from the pure membrane and the HSF5 system are very similar to those for the H10 system, the projections of the FTOH and FTOH 4:1 systems closely resemble that of the F10 system. The FTOH 333 K system yielded a result which is between these two cases, as already assumed from the area of lipid development above. On the

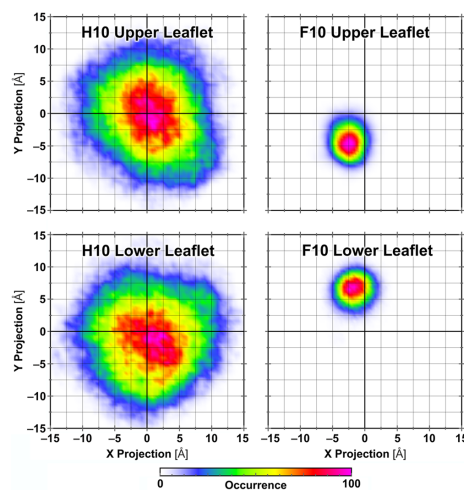


Figure 3. Projection of the DPPC chain tilting vectors (from the α to ω carbon atom of carboxylic acids) into the X - Y plane for the H10 (left) and F10 (right) systems during the last 5 ns of the trajectories. Collective tail tilting (as on the right side) indicates the gel phase.

basis of these findings, we can now clearly state that the F10, FTOH, and FTOH 4:1 systems undergo a phase transition into the gel phase during the simulations, whereas the other systems remain in the initial liquid crystalline state.

Tail Order Parameter. Another class of quantities which are commonly used in the literature to characterize lipid bilayers are order parameters. The S_{CD} order parameter is of particular interest, because it can be determined by NMR experiments.⁶⁵ It characterizes how C-H bonds are oriented with respect to the membrane normal vector. As this strongly depends on the chain position, we compute this order parameter separately for each carbon atom in the chain, as was done in studies of DPPC bilayers before.^{65–67} Again, only the last 5 ns of each trajectory have been considered. The definition of S_{CD}^k is given in eq 2,

$$S_{CD}^k = \frac{1}{NT} \sum_{i=1}^N \sum_{t=1}^T \frac{3}{2} \cos^2 \left(\angle \left(r_{ik}^{C-H}(t), \vec{n} \right) \right) - \frac{1}{2} \quad (2)$$

where k depicts the position in the alkyl chain, N is the number of DPPC molecules, T is the total number of time steps, $r_{ik}^{C-H}(t)$ is one of the C-H bond vectors of the k th carbon atom in time step t , and \vec{n} is the membrane normal vector. S_{CD} can take values between -0.5 and 1 , where 0 corresponds to statistical distribution (i.e., no ordering) and -0.5 indicates that the bond vectors are strictly within the membrane plane. Our results are shown in Figure 4. The values on the X axis describe the position of the carbon atom within the alkyl chain in IUPAC nomenclature (2 is the α carbon atom of palmitic acid, and 16 the ω carbon atom, i.e., the methyl group).

It can be seen that the values of S_{CD} start at values around -0.2 near the carboxylic group, then drop to lower values in the middle of the chains, and finally increase to around 0 when the terminal methyl group is reached. This behavior can be explained by the fact that the methyl group may rotate freely at

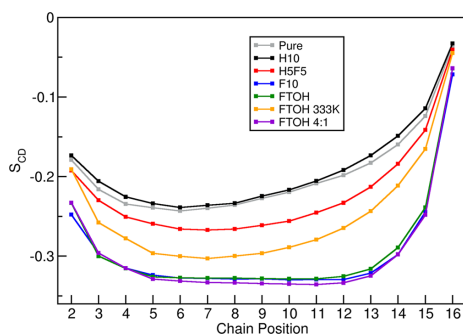


Figure 4. Order parameter S_{CD} for C–H bonds in DPPC tails at different chain positions (2 = α carbon and 16 = ω carbon of palmitic acid).

the simulation temperature, and therefore, the C–H vectors in the methyl group possess a statistical distribution of orientation. In the middle of the chains, the order parameter drops below -0.3 for the systems in the gel phase (F10, FTOH, FTOH 4:1), indicating a strict alignment of the chains. The remaining systems in the liquid crystalline phase do not possess such a strict chain alignment, as already discussed before. The systems HSF5 and FTOH 333 K are found to be still in the liquid crystalline phase, but probably very close to the phase transition, as the S_{CD} values in the middle of the chains are already significantly lower than in the pure membrane.

Tail gauche Ratio. Another useful property for the characterization of DPPC bilayers is the distribution of dihedral angles within the tails. This can be a measure for the rigidity of the chains, which could be affected by the additives. Dihedral angles within alkyl chains possess two different kinds of energy minima, which are known as the *anti* configuration (C–C–C dihedral angle around 180°) and the *gauche* configuration (C–C–C dihedral angle around 60°). As already shown in the literature before,⁶⁰ we studied the average *gauche* percentage in the tails in dependence on the position within the chain. We consider a dihedral angle as *gauche* if it is smaller than 120° , which is roughly the position of the energy barrier between *gauche* and *anti*. Only the last 5 ns of each trajectory were taken into account for this analysis. The results are presented in Figure 5. Please note that an alkyl chain with 15 carbon atoms only possesses 12 C–C–C dihedral angles, so the counting ranges from 1 to 12. We use the convention that dihedral angle 1 is close to the carboxylic group, whereas dihedral angle 12 is close to the terminal methyl group.

Similarly to the discussion of the S_{CD} order parameter, it is seen that the *gauche* percentage is relatively high at the beginning and end of the tails, and low in the middle. Again, the systems in the gel phase (F10, FTOH, FTOH 4:1) are found to possess very ordered chains with *gauche* percentages of only 10% in the middle of the chain, whereas the systems in the liquid crystalline phase are characterized by significantly larger *gauche* percentages of around 25% in the middle of the tails. As seen before, the FTOH 333 K system shows smaller percentages with respect to the other liquid crystalline systems.

To conclude this part of the study, we present the average count of *gauche* dihedral angles within each chain in Table 2. The values are given as percentages, such that 0% corresponds

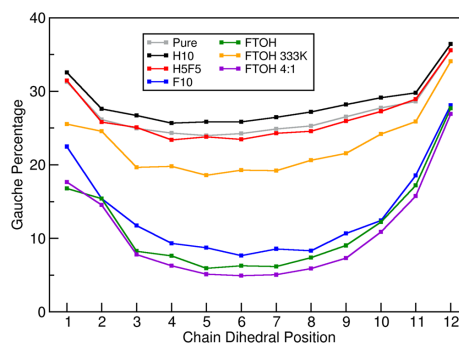


Figure 5. Average *gauche* percentage for each C–C–C dihedral angle in the DPPC tails.

Table 2. Average Percentage of *gauche* Dihedral Angles per Alkyl Chain and Standard Deviation of This Quantity

system	av <i>gauche</i> count (%)	std dev (%)
pure	26.97	13.45
H10	28.46	12.83
HSF5	26.63	13.09
F10	13.50	12.45
FTOH	11.66	11.39
FTOH 333 K	22.75	13.76
FTOH 4:1	10.67	10.80

to a tail with all dihedral angles in the *anti* position, and 100% indicates that all dihedrals are in the *gauche* position. Also, here, the difference between the systems in different phases is significant. The systems pure, H10, and HSF5 in the liquid crystalline phase possess around 27% *gauche* dihedral angles in their tails on average, whereas this number is only around 12% for the systems F10, FTOH, and FTOH 4:1. The system FTOH 333 K was found to have an average *gauche* percentage of 23%, which is between the two categories described before. The standard deviation of the *gauche* percentage is around 12% for all systems, independently of the phase. This relatively large value of the standard deviation indicates that, even in the gel phase, chains with significantly more (or less) *gauche* dihedral angles are found frequently, thus slightly attenuating the picture of a strict ordering of the chains in the gel phase.

Diffusion. Another important measure for the phase behavior of lipid bilayers is the diffusion of the molecules, which can be expressed by the diffusion constant D . If diffusion is the dominating process in a system, the diffusion constant can be put in relation with the mean square displacement (MSD) $\langle r^2(\tau) \rangle$ of the molecules:

$$\langle r^2(\tau) \rangle = 2dD\tau \quad (3)$$

where τ is the correlation depth and d depicts the number of degrees of freedom in which diffusion occurs. In a lipid bilayer, the molecules are constrained to the lipid plane, and therefore, the diffusion can only take place within two spatial directions (i.e., lateral diffusion), resulting in $d = 2$ in this case. The MSD, on the other hand, can be obtained from the trajectories by

$$\langle r^2(\tau) \rangle = \frac{1}{N(T-\tau)} \sum_{i=1}^N \sum_{t=1}^{T-\tau} (\bar{r}_i(t) - \bar{r}_i(t+\tau))^2 \quad (4)$$

where N depicts the total number of molecules, T the total number of time steps, and $\bar{r}_i(t)$ the center of mass position of molecule i at time step t . Equation 3 states that the MSD should depend linearly on the correlation depth τ in the case of normal diffusion. It is therefore a good idea to check if this linear relation holds to rule out anomalies in the diffusion behavior. Figure 6 shows the MSD plots of the simulated

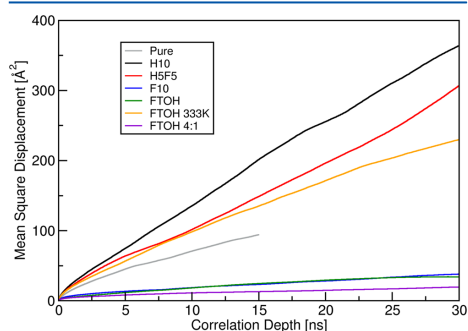


Figure 6. Mean square displacement of the DPPC center of mass, leaving out the first 75 ns in systems with additive.

systems up to a correlation depth of 30 ns. At small correlation depths, the MSD is known to possess a nonlinear behavior due to transient phenomena, such that only the range of higher correlation times should be considered for the analysis. In the range of 15–30 ns, the curves of the systems with additives obey a linear behavior in a good approximation. Deviations from perfect linear behavior are due to insufficient sampling.

Using these relations from eqs 3 and 4, the diffusion constants of DPPC and additive molecules within the simulated systems have been determined by performing a linear fit to the MSD curves, and are presented in Table 3. As mentioned before, only the range of higher correlation times of the MSD curves was considered for the fit to account for the transient behavior at low correlation times. Due to possible changes in the diffusion behavior due to phase transitions in the beginning of the simulations, the first 75 ns of simulation time have been omitted.

Table 3. Self-Diffusion Coefficients of DPPC and Additive Molecules^a

system	D_{DPPC} (pm ² /ps)	D_{additive} (pm ² /ps)
pure	5.571 ± 0.219	
H10	11.983 ± 0.553	90.718 ± 6.702
H5F5	11.374 ± 0.267	48.369 ± 2.869
F10	1.116 ± 0.035	1.428 ± 0.136
FTOH	0.758 ± 0.032	0.739 ± 0.079
FTOH 333 K	7.091 ± 0.223	10.605 ± 0.757
FTOH 4:1	0.489 ± 0.022	0.480 ± 0.046

^aAssuming 2D diffusion, all simulations performed at 323 K and a mixing ratio of 4:1 unless specified otherwise. Uncertainty given as 3σ , i.e., 99.7% confidence interval.

The numbers from Table 3 show significant differences between the systems. In the case of H10 and H5F5, the DPPC molecules possess a very high diffusivity, almost double the value from the pure membrane. The systems F10, FTOH, and FTOH 4:1 show very slow diffusion, which is around 1 order of magnitude slower than in the pure bilayer. This further substantiates the claim from the last section, suggesting that indeed a phase transition to the gel phase occurred in these three systems. The FTOH 333 K trajectory is found between these cases, with a diffusion constant close to that of the pure system. Concerning the additive molecules, we find impressively high diffusion speeds in H10 and H5F5, which are almost 1 order of magnitude larger than those of the DPPC molecules in the respective systems. This indicates that the additive molecules move almost freely between the DPPC molecules, and do not show significant interactions with them. In the remaining four systems F10, FTOH, FTOH 4:1, and FTOH 333 K, the additive molecules diffuse at approximately the same rate as the DPPC molecules, which leads to the claim that there exist significant interactions between DPPC and additive in these cases.

Particle Density Profiles. It is tempting to relate the influence of the polyphilic additives on the properties of the DPPC membrane to specific interactions with particular parts of the lipids. Therefore, it is interesting to investigate if (and how far) the additive molecules penetrate the bilayer. A suitable tool for this question is a particle density profile, which depicts the probability density of finding a certain atom in a given X – Y plane, characterized by its Z coordinate value. In the following, a value of $Z = 0$ always refers to the center of the bilayer per convention. As the bilayer slightly moves during the simulation, the center position is re-evaluated in every time step. As in the last section, the first 75 ns of simulation time have been omitted from analysis for all systems containing additives to account for phase transitions in the beginning of the simulations.

Figure 7 shows the density profiles of DPPC in the simulated systems. The dashed lines correspond to all DPPC atoms,

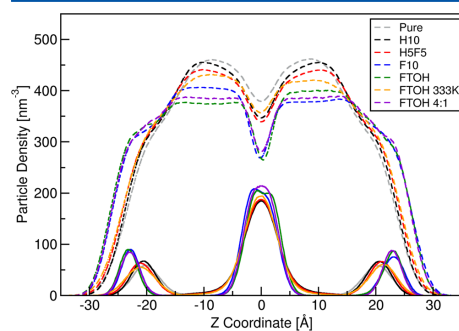


Figure 7. Density profiles of all DPPC atoms (dashed) and DPPC head/tail atoms (solid).

whereas the solid lines depict only the phosphorus atoms (at the outside) and the terminal tail carbon atoms (at the inside close to $Z = 0$). The systems H10, H5F5, and FTOH 333 K behave very similarly to the pure DPPC bilayer in this plot. In contrast, the remaining systems F10, FTOH, and FTOH 4:1 show a significantly different behavior. The DPPC head groups

are shifted further to the outside; i.e., the diameter of the bilayer is increased. This corresponds to the reduced area per lipid found for these three systems in Figure 2, indicating that the molecular volume of DPPC approximately remains constant during the phase transition. This is also supported by the decreased particle density in the bulk of the membrane, at Z values of approximately ± 10 Å.

Complementarily to the density profiles of the DPPC molecules, we have analyzed the distribution of the additive molecules. Figure 8 shows density profiles of additive molecules.

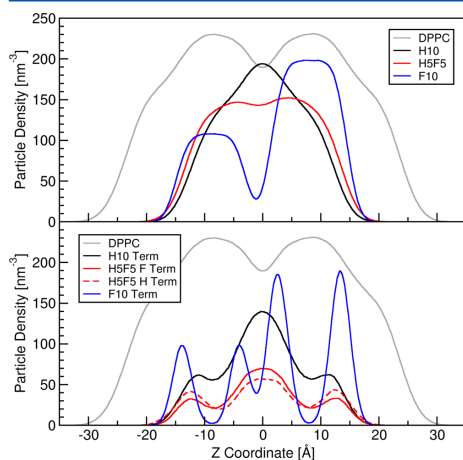


Figure 8. Density profiles of all additive atoms (upper panel) and only terminal additive atoms (lower panel) within the membrane. The gray curve depicts all atoms of DPPC from the pure system as a reference.

in the systems H10, H5F5, and F10, including both information on all atoms from the molecules (upper panel) and information on the terminal carbon atoms of the chains (lower panel). The gray curve depicts the density profile of all atoms from DPPC in the pure bilayer as a reference. First, it has to be noted that the asymmetry of the curves is a consequence of finite sampling time; for an infinite simulation time, the distribution should be symmetric to $Z = 0$. The residual asymmetry illustrates that the interleaflet transfer time of the considered additives exceeds our 300 ns simulation time.

In the H10 system, the probability of finding additive molecules has its largest value in the center of the bilayer, and monotonously decreases to the outside (black curve in the upper panel). This is nicely in line with the finding of the very high diffusivity from the last section, and the assumption of very weak interactions with the DPPC molecules. The terminal carbon atoms of the additive (solid black curve in the lower panel) show peaks both at $Z = 0$ and at around $Z = \pm 10$ Å, indicating that the additive chains penetrate the membrane for a few angstroms. A similar picture arises in the case of H5F5. Concerning all additive atoms (red line in the upper panel), the maximum at $Z = 0$ has split into a doublet at $Z = \pm 5$ Å, indicating slightly stronger interactions with DPPC. The terminal atoms of F5H5 possess their maximum at slightly larger distance from the center, therefore penetrating the membrane slightly deeper. Interestingly, the terminal carbon

atoms of the fluorinated half of the chain (solid red line in the lower panel) show a small preference for the center of the bilayer, whereas the carbon atoms at the nonfluorinated terminus (dashed red line in the lower panel) are slightly enriched at ± 13 Å. This does not support the concept of stronger interaction to DPPC due to fluorination. Finally, the additive molecules in the F10 system are mainly found within the apolar bulk of the membrane, indicated by the minimum in the bilayer center (blue curve in the upper panel) and by the position of the terminal carbon atoms at almost ± 15 Å. This corresponds to a strong interaction with the DPPC tails, which is also the reason for the reduced diffusivity of both DPPC and additive in this system.

Now the systems which contain FTOH as an additive will be considered; the corresponding curves can be found in Figure 9.

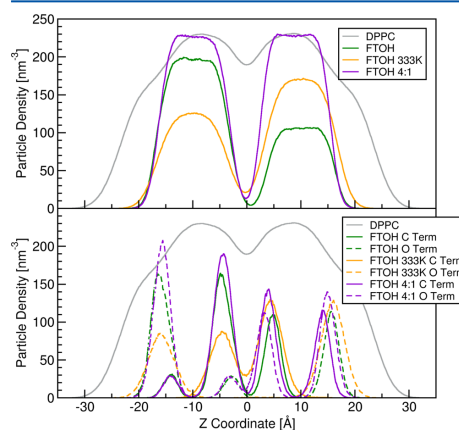


Figure 9. Density profiles of all additive atoms (upper panel) and only terminal additive atoms (lower panel) within the membrane. The gray curve depicts all atoms of DPPC from the pure system as a reference.

The gray curve, again, depicts the density profile of all atoms from DPPC in the pure membrane as a reference. We find that the systems FTOH and FTOH 4:1 show qualitatively the same behavior, which is expected, as changing the additive ratio should not influence the membrane penetration behavior significantly. The additive molecules are found almost exclusively between the DPPC chains, indicated by the distinct minimum in the center of the bilayer (green/purple curves in the upper panel). A majority of FTOH molecules are oriented in a way such that the hydroxyl group points to the outside, toward the polar head groups of the bilayer (dashed green/purple curves in the lower panel). The carbon terminus of the FTOH molecules is mainly found in the center of the bilayer, in a range of -7 to $+7$ Å, but there is also a small contribution at ± 14 Å (solid green/purple curves in the lower panel). The FTOH 333 K system shows some minor differences. The carbon terminus is now exclusively found in the middle of the bilayer; the contribution at ± 14 Å has vanished (solid orange curve in the lower panel). The hydroxyl groups, on the other hand, are now exclusively found at ± 17 Å, close to the polar head groups of DPPC.

Radial Distribution Functions. In the last section, it was found that the hydroxyl groups of the FTOH molecules are primarily (or even exclusively in the case of FTOH 333 K) located close to the polar head groups of DPPC. This leads to the assumption of a strong directed interaction behind this structural motif, most probably a hydrogen bond. To investigate this claim, radial pair distribution functions (RDFs) between the oxygen atom of the FTOH hydroxyl group and several hydrogen bond acceptors in DPPC have been computed. Again, the first 75 ns of simulation time have been omitted from analysis to account for phase transitions in the beginning of the simulations. The results are shown in Figure 10. All curves except the orange one in this figure correspond to the FTOH system, whereas the orange curve results from the FTOH 333 K system as a comparison.

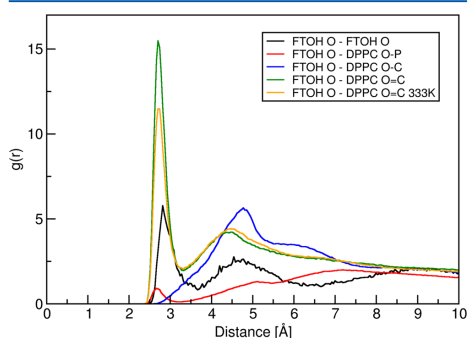


Figure 10. Radial pair distribution functions of possible hydrogen bonds in the FTOH systems. All curves except the orange one are from the system FTOH.

A first possible hydrogen bond acceptor in DPPC would be each of the four phosphate oxygen atoms. The RDF between the hydroxyl oxygen in FTOH and the phosphate oxygen atoms is given by the red curve in Figure 10. From the very weak first maximum, it can be concluded that this hydrogen bond does not play a significant role in the FTOH system. Next, the bridging oxygen atoms of the ester groups (i.e., those which originally stem from glycerol) will be considered (blue curve). This curve does not show a maximum at all at reasonably low distances, such that also this hydrogen bond is probably not present. Finally, the double-bonded oxygen atoms from the ester groups are investigated. The corresponding RDF (green curve) possesses a very distinct first maximum, which reaches a value of around 15 (relative to uniform density). This indicates a very strong hydrogen bond with a strong population. Many of the FTOH molecules are therefore tightly bound to the DPPC polar head group via their hydroxyl groups, which is in line with the previous findings of a very slow diffusion of both FTOH and additive molecules in the FTOH system. It can be assumed that the hydroxyl groups of FTOH form an extended hydrogen bond network with the DPPC ester groups, virtually chaining all of the DPPC head groups together and blocking lateral diffusion. The claim of a hydrogen bond network is substantiated by the black curve, which depicts the intermolecular RDF between different FTOH hydroxyl oxygen atoms: The distinct first maximum indicates that there exist

many hydrogen bonds between neighboring FTOH molecules. For comparison, the orange curve shows the RDF between the FTOH hydroxyl oxygen and DPPC ester double-bonded oxygen in the FTOH 333 K system. Despite having a slightly lower first maximum due to the higher thermal movement of the atoms, the picture is qualitatively the same as in the 323 K system. Interestingly, it seems that an increase in temperature of only 10 K helps to effectively overcome the hydrogen bond network (see the significantly increased diffusion constant), albeit the hydrogen-bonding patterns are similar in the RDFs.

An additional structural question is if the chains of the additive molecules are found mostly in an *all-trans* conformation, or if other conformers are significantly populated. A simple method of judging the conformation of an alkyl chain is to measure the distance between the two terminal carbon atoms within a certain molecule. All additives in this study possess a chain of 10 carbon atoms, such that these values can be directly compared. The intramolecular distance histograms between the terminal carbon atoms of the six systems which contain additives are shown in Figure 11.

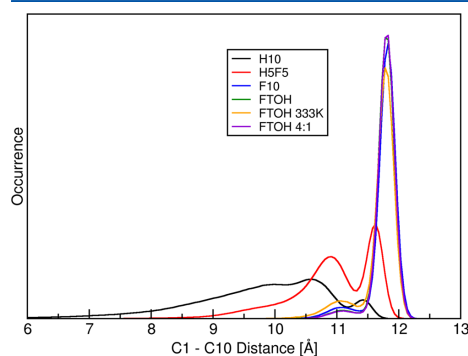


Figure 11. Intramolecular distance histograms between both terminal carbon atoms in the additive chains.

As in most other analyses discussed before, the three systems F10, FTOH, and FTOH 4:1 behave very similar in this plot, all showing a distinct maximum at around 12 Å, which corresponds to an *all-trans* conformation. There is a minor contribution at 11 Å, indicating a few twists in the chain, but this only concerns a few percent of all additive molecules over time. In the FTOH 333 K system (orange curve), the contribution at 11 Å is slightly increased, which can be easily understood due to the higher thermal energy of the atoms. A completely different picture arises for the remaining two systems. In HSF5, there is a maximum at around 11.6 Å, which corresponds to an almost untwisted chain, but the main contribution is found in the lower distance region, down to approximately 9 Å, depicting already a twisted chain. In the case of H10, the maximum at large distances has almost vanished, and the histogram shows that all possible conformers are populated, down to very small distances of around 6 Å, which would be best described as a random coil configuration. This finding nicely agrees with the results from above, where it was stated that *n*-decane possesses very weak interactions with

DPPC: A random coil configuration as found here is also predominant in liquid bulk *n*-decane (without any membrane).

■ CONCLUSION

In this study, we used our recently developed perfluoroalkane force field¹ to perform molecular dynamics simulations of a series of additive molecules with different types of philicities inside a DPPC bilayer. On the basis of these simulations, we investigate the effect of the additives on the structure and dynamics of the membrane. To elucidate the effect of the additives, we compare the simulations to a system with a pure DPPC bilayer, without additive molecules.

On the basis of the temporal development of the area per lipid values, we found that addition of perfluoro-*n*-decane and fluorotelomer alcohol at 323 K leads to a phase transition of the membrane (i.e., from liquid crystalline to the gel phase), whereas the addition of *n*-decane and partially fluorinated *n*-decane leaves the liquid crystalline phase intact. Addition of fluorotelomer alcohol at a slightly increased temperature of 333 K prevents the phase transition from happening. The same picture also emerges from analysis of the S_{CD} order parameter and the dihedral angle distribution in the tails. The gel phase is characterized by the collective tilting of the lipid tails, which we clearly observed in the tail vector projections. These results are substantiated by the diffusion constants, which we calculated from the mean square displacements: The systems in the gel phase show a significantly reduced diffusivity for both DPPC and additive molecules. The addition of nonfluorinated and partially fluorinated *n*-decane, on the other hand, even led to an increased DPPC diffusivity with respect to the pure bilayer. In these two systems, the additive molecules possess a very high diffusion constant, leading to the conclusion that they show almost no interactions with DPPC, and move freely in the center of the bilayer (*like a lubricant between the layers*).

From investigating the density profiles, we found that the phase transition of the membrane not only reduces the area per lipid, but increases the diameter of the membrane at the same time, such that the molecular volume of DPPC remains almost constant. While nonfluorinated *n*-decane and partially fluorinated *n*-decane are found mainly in the middle of the bilayer, perfluoro-*n*-decane penetrates significantly deeper into the membrane leaflet, which triggers a phase transition. Fluorotelomer alcohol is found almost exclusively inside the leaflet. The hydroxyl groups of fluorotelomer alcohol point to the outside of the bilayer in almost all cases. This is due to a very strong hydrogen bond between the hydroxyl group and the double-bonded ester oxygen atoms in the head group of DPPC. The hydroxyl groups of the alcohol form an extended hydrogen bond network with the DPPC ester groups, which chains these molecules together and significantly hinders the lateral diffusion of both DPPC and alcohol molecules. Interestingly, a slight increase in temperature by only 10 K is already sufficient to dynamically overcome this hydrogen bond network (*as shown by the increase of diffusion constants*), despite the hydrogen bonds still being strongly populated.

Concerning the conformations of the additive molecules, fluorotelomer alcohol is almost only present in *all-trans* conformation with maximal spatial chain length (with the hydroxyl groups pointing toward the polar head groups of the membrane and the alkyl chains pointing inside the membrane). Perfluoro-*n*-decane also prefers the *all-trans* configuration. This effect reduces with partially fluorinated *n*-decane, which also assumes other configurations over some time. Finally, non-

fluorinated *n*-decane has no preference for the *all-trans* configuration and assumes all possible conformations, best described as a random coil configuration. This is nicely in line with the finding of very weak interactions between *n*-decane and DPPC, because liquid bulk *n*-decane (without the influence of a membrane) also prefers a random coil configuration.

■ AUTHOR INFORMATION

Corresponding Author

*E-mail: daniel.sebastiani@chemie.uni-halle.de.

ORCID

Martin Brehm: 0000-0002-6861-459X

Notes

The authors declare no competing financial interest.

■ ACKNOWLEDGMENTS

This work was supported by the Deutsche Forschungsgemeinschaft (DFG) within the Forschergruppe FOR1145. M.B. acknowledges financial support by the DFG through Project Br 5494/1-1.

■ REFERENCES

- (1) von Rudorff, G. F.; Watermann, T.; Sebastiani, D. Perfluoroalkane Force Field for Lipid Membrane Environments. *J. Phys. Chem. B* **2014**, *118*, 12531–12540.
- (2) Simmons, J. H.; Reed, T. M. *Fluorine Chemistry*; Academic Press: New York, 1964; Vol. 5.
- (3) Ojogun, V. A. Effect of Fluorination on Partitioning Behavior and Bilayer Self Assembly. Ph.D. Thesis, University of Kentucky, Lexington, KY, 2010.
- (4) Padua, A. A. H. Torsion Energy Profiles and Force Fields Derived from ab initio Calculations for Simulations of Hydrocarbon-Fluorocarbon Diblocks and Perfluoroalkylbromides. *J. Phys. Chem. A* **2002**, *106*, 10116–10123.
- (5) Riess, J. G. Oxygen Carriers (Blood Substitutes) raison D'etre, Chemistry, and Some Physiology Blut Ist Ein Ganz Besonderer Saft. *Chem. Rev.* **2001**, *101*, 2797–2920.
- (6) Krafft, M. P.; Riess, J. G. Chemistry, Physical Chemistry, and Uses of Molecular Fluorocarbon-Hydrocarbon Diblocks, Triblocks, and Related Compounds—Unique “Apolars” Components for Self-Assembled Colloid and Interface Engineering. *Chem. Rev.* **2009**, *109*, 1714–1792.
- (7) Mukerjee, P.; Handa, T. Adsorption of Fluorocarbon and Hydrocarbon Surfactants to Air-Water, Hexane-Water and Perfluoro-hexane-Water Interfaces. Relative Affinities and Fluorocarbon-Hydrocarbon Nonideality Effects. *J. Phys. Chem.* **1981**, *85*, 2298–2303.
- (8) Goss, K. U.; Bronner, G. What is so Special about the Sorption Behavior of Highly Fluorinated Compounds? *J. Phys. Chem. A* **2006**, *110*, 9518–9522.
- (9) Shinoda, K.; Hato, M.; Hayashi, T. Physicochemical Properties of Aqueous Solutions of Fluorinated Surfactants. *J. Phys. Chem.* **1972**, *76*, 909–914.
- (10) Riess, J. G. Fluorous Micro- and Nanophases with a Biomedical Perspective. *Tetrahedron* **2002**, *58*, 4113–4131.
- (11) Baran, J. R., Jr. Fluorinated Surfactants and Repellents: Second Edition, Revised and Expanded Surfactant Science Series. Volume 97. by Erik Kissa (consultant, Wilmington, De). Marcel Dekker: New York. 2001. Xiv + 616 Pp. \$195.00. ISBN 0–8247–0472-x. *J. Am. Chem. Soc.* **2001**, *123*, 8882–8882.
- (12) Dasaradhi, L.; O'Hagan, D. The Effect of Aryl Fluorene in a Lipse Resolutions. *Bioorg. Med. Chem. Lett.* **1993**, *3*, 1655–1658.
- (13) Krafft, M. P.; Riess, J. G. Highly Fluorinated Amphiphiles and Colloidal Systems, and Their Applications in the Biomedical Field. *Biochimie* **1998**, *80*, 489–514.

- (14) Krafft, M. P. Fluorocarbons and Fluorinated Amphiphiles in Drug Delivery and Biomedical Research. *Adv. Drug Delivery Rev.* **2001**, *47*, 209–228.
- (15) Krafft, M. P.; Rolland, J. P.; Vierling, P.; Riess, J. G. New Perfluoroalkylated Phosphocholines Effect on Particle Size and Stability of Fluorocarbon Emulsions. *New J. Chem.* **1990**, *14*, 869–875.
- (16) Lowe, K. C. Fluorinated Blood Substitutes and Oxygen Carriers. *J. Fluorine Chem.* **2001**, *109*, 59–65.
- (17) Lane, T. A. Perfluorochemical-Based Artificial Oxygen Carrying Red Cell Substitutes. *Transfusion Sci.* **1995**, *16*, 19–31.
- (18) Riess, J. G.; Krafft, M. P. Fluorinated Materials for in vivo Oxygen Transport (Blood Substitutes), Diagnosis and Drug Delivery. *Biomaterials* **1998**, *19*, 1529–1539.
- (19) Gerber, F.; Krafft, M. P.; Vandamme, T. F.; Goldmann, M.; Fontaine, P. Fluidization of a Dipalmitoyl Phosphatidylcholine Monolayer by Fluorocarbon Gases: Potential Use in Lung Surfactant Therapy. *Biophys. J.* **2006**, *90*, 3184–3192.
- (20) Gerber, F.; Krafft, M. P.; Vandamme, T. F. The Detrimental Effect of Serum Albumin on the Re-spreading of a Dipalmitoylphosphatidylcholine Langmuir Monolayer Is Counteracted by a Fluorocarbon Gas. *Biochim. Biophys. Acta, Biomembr.* **2007**, *1768*, 490–494.
- (21) Gerber, F.; Krafft, M. P.; Vandamme, T. F.; Goldmann, M.; Fontaine, P. Preventing Crystallization of Phospholipids in Monolayers: A New Approach to Lung-surfactant Therapy. *Angew. Chem., Int. Ed.* **2005**, *44*, 2749–2752.
- (22) Nakahara, H.; Lee, S.; Krafft, M. P.; Shibata, O. Fluorocarbon-hybrid Pulmonary Surfactants for Replacement Therapy - A Langmuir Monolayer Study. *Langmuir* **2010**, *26*, 18256–18265.
- (23) Cuntze, J.; Owens, L.; Alcazar, V.; Seiler, P.; Diederich, F. Molecular Clefs Derived from 9,9'-Spiro[9H-Fluorene] for Enantioselective Complexation of Pyranosides and Dicarboxylic Acids. *Helv. Chim. Acta* **1995**, *78*, 367–390.
- (24) Pozzi, G.; Colombani, L.; Miglioli, M.; Montanari, F.; Quici, S. Epoxidation of Alkenes under Liquid-Liquid Biphasic Conditions: Synthesis and Catalytic Activity of Mn(III)-Tetraarylporphyrins Bearing Perfluoroalkyl Tails. *Tetrahedron* **1997**, *53*, 6145–6162.
- (25) Tian, Y.; Yang, Q. C.; Mak, T. C. W.; Chan, K. S. Asymmetric Catalytic Carbon-Carbon Bond Formations in a Fluorous Biphasic System Based on Perfluoroalkyl Binols. *Tetrahedron* **2002**, *58*, 3951–3961.
- (26) Bartlete, P. D.; Knox, L. H.; Roberts, J. D. D,L-10-Camphorsulfonyl Chloride. *Org. Synth.* **1973**, *5*, 196–198.
- (27) Curran, D. P. Fluorous Reverse Phase Silica Gel. A New Tool for Preparative Separations in Synthetic Organic and Organofluorine Chemistry. *Synlett* **2001**, *2001*, 1488–1496.
- (28) Bosanac, T.; Yang, J. M.; Wilcox, C. S. Precipitons-Functional Protecting Groups to Facilitate Product Separation: Applications in Isoxazoline Synthesis. *Angew. Chem., Int. Ed.* **2001**, *40*, 1875–1879.
- (29) Ishihara, K.; Hasegawa, A.; Yamamoto, H. A Fluorous Super Bronsted Acid Catalyst: Application to Fluorous Catalysis without Fluorous Solvents. *Synlett* **2002**, 1299–1301.
- (30) Martin, J. W.; Muir, D. C. G.; Moody, A. C.; Ellis, D. A.; Kwan, W. C.; Solomon, K. R.; Mabury, S. A. Collection of Airborne Fluorinated Organics and Analysis by Gas Chromatography/Chemical Ionization Mass Spectrometry. *Anal. Chem.* **2002**, *74*, 584–590.
- (31) Stock, N. L.; Lau, F. K.; Ellis, D. A.; Martin, J. W.; Muir, D. C. G.; Mabury, S. A. Polyfluorinated Telomer Alcohols and Sulfonamides in the North American Troposphere. *Environ. Sci. Technol.* **2004**, *38*, 991–996.
- (32) Xiang, T. X.; Anderson, B. D. Influence of Chain Ordering on the Selectivity of Dipalmitoylphosphatidylcholine Bilayer Membranes for Permeant Size and Shape. *Biophys. J.* **1998**, *75*, 2658–2671.
- (33) Xie, W.; Kania-Korwel, I.; Bummer, P. M.; Lehmler, H. J. Effect of Potassium Perfluorooctanesulfonate, Perfluorooctanoate and Octanesulfonate on the Phase Transition of Dipalmitoylphosphatidylcholine (DPPC) Bilayers. *Biochim. Biophys. Acta, Biomembr.* **2007**, *1768*, 1299–1308.
- (34) Jyoti, A.; Prokop, R. M.; Li, J.; Vollhardt, D.; Kwok, D. Y.; Miller, R.; Mohwald, H.; Neumann, A. W. An Investigation of the Compression Rate Dependence on the Surface Pressure-surface Area Isotherm for a Dipalmitoyl Phosphatidylcholine Monolayer at the Air/Water Interface. *Colloids Surf, A* **1996**, *116*, 173–180.
- (35) Klopfer, K. J.; Vanderlick, T. K. Isotherms of Dipalmitoylphosphatidylcholine (DPPC) Monolayers: Features Revealed and Features Obscured. *J. Colloid Interface Sci.* **1996**, *182*, 220–229.
- (36) Carafa, M.; Santucci, E.; Alhaque, F.; Coviello, T.; Murtas, E.; Riccieri, F. M.; Lucania, G.; Torrisi, M. R. Preparation and Properties of New Unilamellar Non-Ionic/Ionic Surfactant Vesicles. *Int. J. Pharm.* **1998**, *160*, 51–59.
- (37) Nakahara, H.; Ohmine, A.; Kai, S.; Shibata, O. Monolayer Compression Induces Fluidization in Binary System of Partially Fluorinated Alcohol (F4H11OH) with DPPC. *J. Oleo Sci.* **2013**, *62*, 271–281.
- (38) Nagle, J. F. Theory of the Main Lipid Bilayer Phase Transition. *Annu. Rev. Phys. Chem.* **1980**, *31*, 157–195.
- (39) Santaella, C.; Vierling, P.; Riess, J. G. Highly Stable Liposomes Derived from Perfluoroalkylated Glycerophosphocholines. *Angew. Chem., Int. Ed. Engl.* **1991**, *30*, 567–568.
- (40) Hu, W. Y.; Jones, P. D.; DeCoen, W.; King, L.; Fraker, P.; Newsted, J.; Giesy, J. P. Alterations in Cell Membrane Properties Caused by Perfluorinated Compounds. *Comp. Biochem. Physiol., Part C: Toxicol. Pharmacol.* **2003**, *135*, 77–88.
- (41) Hill, E. H.; Stratton, K.; Whitten, D. G.; Evans, D. G. Molecular Dynamics Simulation Study of the Interaction of Cationic Biocides with Lipid Bilayers: Aggregation Effects and Bilayer Damage. *Langmuir* **2012**, *28*, 14849–14854.
- (42) Krafft, M. P. Controlling Phospholipid Self-Assembly and Film Properties Using Highly Fluorinated Components - Fluorinated Monolayers, Vesicles, Emulsions and Microbubbles. *Biochimie* **2012**, *94*, 11–25.
- (43) Scholtysek, P.; Li, Z.; Kressler, J.; Blume, A. Interactions of DPPC with Semitechelec Poly(glycerol Methacrylate)s with Perfluoroalkyl End Groups. *Langmuir* **2012**, *28*, 15651–15662.
- (44) Austin, R. P.; Barton, P.; Davis, A. M.; Fessey, R. E.; Wenlock, M. C. The Thermodynamics of the Partitioning of Ionizing Molecules between Aqueous Buffers and Phospholipid Membranes. *Pharm. Res.* **2005**, *22*, 1649–1657.
- (45) De Young, L. R.; Dill, K. A. Solute Partitioning into Lipid Bilayer Membranes. *Biochemistry* **1988**, *27*, 5281–5289.
- (46) Tu, K.; Tobias, D. J.; Blasie, J. K.; Klein, M. L. Molecular Dynamics Investigation of the Structure of a Fully Hydrated Gel-Phase Dipalmitoylphosphatidylcholine Bilayer. *Biophys. J.* **1996**, *70*, 595–608.
- (47) Gadras, C.; Santaella, C.; Vierling, P. Improved Stability of Highly Fluorinated Phospholipid-Based Vesicles in the Presence of Bile Salts. *J. Controlled Release* **1999**, *57*, 29–34.
- (48) Guillod, F.; Greiner, J.; Riess, J. G. Vesicles Made of Glycophospholipids with Homogeneous (two Fluorocarbon or Two Hydrocarbon) or Heterogeneous (one Fluorocarbon and One Hydrocarbon) Hydrophobic Double Chains. *Biochim. Biophys. Acta, Biomembr.* **1996**, *1282*, 283–292.
- (49) Ravily, V.; Santaella, C.; Vierling, P.; Gulik, A. Phase Behavior of Fluorocarbon Di-o-alkyl-glycerophosphocholines and Glycerophosphoethanolamines and Long-term Shelf Stability of Fluorinated Liposomes. *Biochim. Biophys. Acta, Biomembr.* **1997**, *1324*, 1–17.
- (50) Phillips, J. C.; Braun, R.; Wang, W.; Gumbart, J.; Tajkhorshid, E.; Villa, E.; Chipot, C.; Skeel, R. D.; Kale, L.; Schulten, K. Scalable Molecular Dynamics with NAMD. *J. Comput. Chem.* **2005**, *26*, 1781–1802.
- (51) Anézo, C.; de Vries, A. H.; Höltje, H.-D.; Tieleman, D. P.; Marrink, S.-J. Methodological Issues in Lipid Bilayer Simulations. *J. Phys. Chem. B* **2003**, *107*, 9424–9433.
- (52) Brooks, B. R.; Brucoleri, R. E.; Olafson, B. D.; States, D. J.; Swaminathan, S.; Karplus, M. CHARMM: A Program for Macromolecular Energy, Minimization, and Dynamics Calculations. *J. Comput. Chem.* **1983**, *4*, 187–217.
- (53) Brooks, B. R.; Brooks, C. L.; Mackerell, A. D.; Nilsson, L.; Petrella, R. J.; Roux, B.; Won, Y.; Archontis, G.; Bartels, C.; Boresch,

4. PUBLICATIONS

S.; et al. CHARMM: The Biomolecular Simulation Program. *J. Comput. Chem.* **2009**, *30*, 1545–1614.

(54) Jorgensen, W. L.; Chandrasekhar, J.; Madura, J. D.; Impey, R. W.; Klein, M. L. Comparison of Simple Potential Functions for Simulating Liquid Water. *J. Chem. Phys.* **1983**, *79*, 926–935.

(55) Jorgensen, W. L.; Madura, J. D. Temperature and Size Dependence for Monte Carlo Simulations of TIP4P Water. *Mol. Phys.* **1985**, *56*, 1381–1392.

(56) Brehm, M.; Kirchner, B. TRAVIS - A Free Analyzer and Visualizer for Monte Carlo and Molecular Dynamics Trajectories. *J. Chem. Inf. Model.* **2011**, *51* (8), 2007–2023.

(57) Grace Development Team. Grace, 1996–2008. <http://plasma-gate.weizmann.ac.il/Grace/> (accessed June 2017).

(58) Williams, T.; Kelley, C.; et al. Gnuplot 4.6: An Interactive Plotting Program, 2013. <http://gnuplot.sourceforge.net/>.

(59) Hartkamp, R.; Moore, T. C.; Iacovella, C. R.; Thompson, M. A.; Bulsara, P. A.; Moore, D. J.; McCabe, C. Investigating the Structure of Multicomponent Gel-Phase Lipid Bilayers. *Biophys. J.* **2016**, *111*, 813–823.

(60) Wang, Y.; Gkeka, P.; Fuchs, J. E.; Liedl, K. R.; Cournia, Z. DPPC-Cholesterol Phase Diagram Using Coarse-Grained Molecular Dynamics Simulations. *Biochim. Biophys. Acta, Biomembr.* **2016**, *1858*, 2846–2857.

(61) Amarez, C.; Webb, A.; Rouviere, E.; Lyman, E. Hysteresis and the Cholesterol Dependent Phase Transition in Binary Lipid Mixtures with the Martini Model. *J. Phys. Chem. B* **2016**, *120*, 13086–13093.

(62) Hianik, T.; Opstad, C. L.; Sandorova, J.; Garaiova, Z.; Partali, V.; Sliwka, H.-R. Surface Properties of Polyene Glycol Phospholipid Monolayers. *Chem. Phys. Lipids* **2017**, *202*, 13–20.

(63) Gobrogge, C. A.; Blanchard, H. S.; Walker, R. A. Temperature-Dependent Partitioning of Coumarin 152 in Phosphatidylcholine Lipid Bilayers. *J. Phys. Chem. B* **2017**, *121*, 4061–4070.

(64) Uppulury, K.; Coppock, P. S.; Kindt, J. T. Molecular Simulation of the DPPE Lipid Bilayer Gel Phase: Coupling between Molecular Packing Order and Tail Tilt Angle. *J. Phys. Chem. B* **2015**, *119* (28), 8725–8733.

(65) Vermeer, L. S.; de Groot, L. B.; Réat, V.; Milon, A.; Czaplicki, J. Acyl Chain Order Parameter Profiles in Phospholipid Bilayers: Computation from Molecular Dynamics Simulations and Comparison with ²H NMR Experiments. *Eur. Biophys. J.* **2007**, *36*, 919–931.

(66) Hofsässs, C.; Lindahl, E.; Edholm, O. Molecular Dynamics Simulations of Phospholipid Bilayers with Cholesterol. *Biophys. J.* **2003**, *84* (4), 2192–2206.

(67) Leekumjorn, S.; Sum, A. K. Molecular Simulation Study of Structural and Dynamic Properties of Mixed DPPC/DPPE Bilayers. *Biophys. J.* **2006**, *90* (11), 3951–3965.

Conformational Space of a Polyphilic Molecule with a Fluorophilic Side Chain Integrated in a DPPC Bilayer

Guido F. von Rudorff,^[a,b] Tobias Watermann,^[b] Xiang-Yang Guo,^[b] and Daniel Sebastiani^{*[b]}

We investigate the conformational space of a polyphilic molecule with hydrophilic, lipophilic and fluorophilic parts inserted as a transmembrane agent into a dipalmitoylphosphatidylcholine bilayer by means of all-atom molecular dynamics simulations. Special focus is put on the competing structural driving forces arising from the hydrophilic, lipophilic and fluorophilic side chains and the aromatic backbone of the polyphile. We observe a significant difference between the lipophilic and the fluorophilic side chains regarding their intramembrane distribution. While the lipophilic groups remain membrane-centered, the fluorophilic parts tend to orient toward the

phosphate headgroups. This trend is important for understanding the influence of polyphile agents on the properties of phospholipid membranes. From a fundamental point of view, our computed distribution functions of the side chains are related to the interplay of sterical, enthalpic and entropic driving forces. Our findings illustrate the potential of rationally designed membrane additives which can be exploited to tune the properties of phospholipid membranes. © 2017 Wiley Periodicals, Inc.

DOI: 10.1002/jcc.24711

Introduction

Modifying the behavior of membranes formed from lipid bilayers is of utmost importance for the development of medical applications. These modifications can range from small changes affecting membrane flexibility to larger modifications modifying the transport through membranes up to the formation of channels in the membrane. One way of modification is the introduction of trans-membrane molecules into the lipid bilayer. In our case, we use a special type of recently synthesized polyphilic trans-membrane molecules.^[1–3]

Polyphilic molecules^[4–9] are compounds that consist of fragments of different philicity. The molecules used here feature many possibilities of functionalization to tailor the interactions with the membranes toward different goals. The molecule we use has a phenylene ring backbone which is terminated with a glycerol group at either ends (see Fig. 1). In the middle of the backbone, two side chains are attached—one of which is a perfluoro-*n*-alkane, while the other one is a regular *n*-alkane. This molecular structure ensures a transmembrane orientation of the backbone, yielding an anchor point for the alkane/perfluoroalkane chains at the center of the membrane (Fig. 2).

The use of perfluoroalkanes is particularly interesting, as they are of interest in a wide range of applications in biological systems. Studies on fluorocarbons and fluorinated amphiphiles^[10] included the use for *in vitro* protein synthesis and protein solubilization,^[11] pulmonary drug delivery,^[12] and also induced changes in vesicle properties such as permeability and interaction in biological systems.^[13,14]

Several variations of the hydrophilic end groups and side chains of the polyphile have been synthesized and inserted into phospholipid bilayers, to tune aggregation behavior and order parameters of these additives.^[1,2,5,15] In our work, we focus on a simple yet representative molecule (see Fig. 1) to

reduce the computational cost of our simulations, and in turn allow for an adequate equilibration of the system. The used molecule features small hydrophilic end groups and two side chains of similar length.

In our simulations, we want to elucidate the structural driving forces which arise from the molecular interactions between a single polyphilic molecule (see Fig. 1) and a phospholipid membrane. This includes the orientation of the polyphile within the membrane and the conformational preferences of its side chains of different philicities.

Experimentally, polyphilic molecules are known to integrate in between a lipid bilayer membrane, even though perfluoro-*n*-alkanes are not miscible with *n*-alkanes.^[16–19] As the model membrane environment is particularly well-understood, and offers a controlled separation of lipophilic and hydrophilic phases while consisting of only two simple kinds of molecules, we consider them to be an ideal candidate family for our set-up. As dipalmitoylphosphatidylcholine (DPPC) is used in our collaborating experimental groups^[3] and well-covered in force-field support, we decided to use DPPC as a first membrane system. Parameters for the fluorophilic parts of the polyphiles have been developed and tested in a previous paper^[20] and will be extended to cover the full polyphilic molecule.

[a] G. F. von Rudorff
Department of Physics and Astronomy, University College London, Gower Street, London, United Kingdom

[b] G. F. von Rudorff, T. Watermann, Xiang-Yang Guo, D. Sebastiani
Institute of Chemistry, Martin-Luther-Universität Halle-Wittenberg, von-Danckelmann-Platz 4, Halle 06120, Germany
E-mail: daniel.sebastiani@chemie.uni-halle.de

Contract grant sponsor: German Research Foundation (DFG) within the Forschergruppe FOR1145; Contract grant number: Se 1008/9-1

© 2017 Wiley Periodicals, Inc.

4. PUBLICATIONS

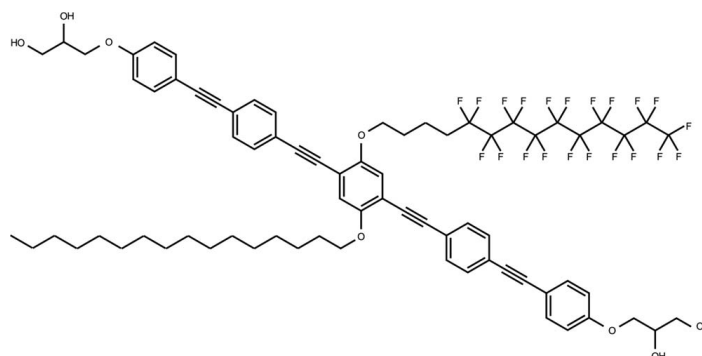


Figure 1. Chemical structure of the polyphilic molecule considered in this work.

Methodology

System

In our simulations, we use the molecule shown in Figure 1, a triphilic molecule in a DPPC bilayer environment. This molecule has been used in recent investigations within and outside of membranes. It offers a phenyl backbone with a length that allows for a transmembrane arrangement of the hydrophilic headgroups. In this transmembrane orientation, the two side

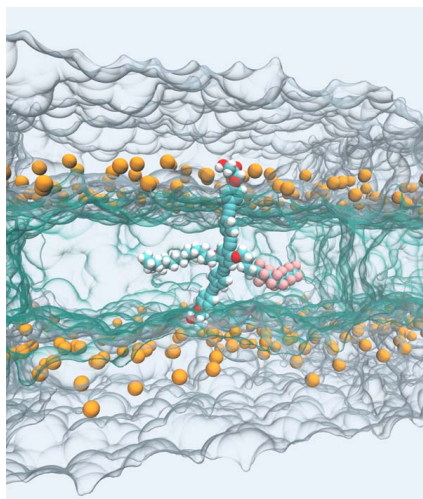


Figure 2. Single polyphile (all-atom representation) in a DPPC environment. The phosphorus atoms of the lipid head groups are denoted by orange spheres, the green layer is the volume occupied by the hydrocarbon tails of the lipids and the gray blocks show the volume occupied by the water layer. In simulations, the system was treated with periodic boundary conditions, effectively representing an infinite stack of infinite layers. [Color figure can be viewed at wileyonlinelibrary.com]

chains, one alkyl and one perfluoroalkyl are fixed in the membrane center by their connection to the central phenyl ring. We perform simulations starting from two different starting conformations in two different orientations. We chose the two low energy conformations of the side chains that offer a strong change in the overall conformation of the molecule: all-trans (x-shaped) and all-trans with the first dihedral at the central phenyl ring turned by 180 degree (cross). Additionally, we started from two different orientations of the phenyl backbone: either directly perpendicular to the membrane plane or tilted by an angle of about 15 degrees. This is a typical angle found in experiments. As the polyphilic molecule is slightly longer than the membrane thickness, this angle also allows for the hydrophilic headgroups to arrange next to the DPPC headgroups. A more detailed description of the four starting points of our simulations can be found in the Supporting Information.

Computational details

All calculations are performed at atmospheric pressure, while the temperature has been set to 330 K. This temperature is just above the transition temperature of the membrane lipids from the gel state to the liquid state,^[21,22] which is reproduced by the classical force field.^[23] Simulations below this transition temperature are expected to be less insightful, as the mobility of the lipids is highly reduced, which means that very little to no movement is to be seen on the timescales accessible with our setup. With 330 K, we have chosen a temperature that is as near to room temperature as possible, that is also still in the experimentally relevant temperature range for pattern formation of the polyphilic molecules within the membranes.

We perform NPT calculations with a timestep of 1 fs in all cases, the trajectories have been equilibrated for 5 ns and run for a total of 50 ns each or 200 ns total. Additionally, one simulation with rigid bonds and a timestep of 2 fs for 400 ns is performed to assess the diffusion. Mean square displacements show a diffusion in good agreement with experimental

values^[24] for the DPPC molecules. The diffusion constant of the polyphile slower than the DPPC molecules by roughly a factor of 2. The vdW cutoff follows the force field specifications^[23] for lipid membranes, the electrostatics are treated with PME. The simulation setup consists of a pre-equilibrated^[23] DPPC bilayer of 288 lipids enclosed by a water layer of roughly 10 Å which sums up to a simulation box of 95 × 95 × 68 Å³. For our calculations, we chose the CHARMM force field,^[25,26] which comes with both an extensively tested support^[23] for a broad range of lipids and a clear parametrization procedure. For the glycerol end groups there are parameters available.^[27,28] Recently, we have presented parameters for perfluoroalkanes.^[20] As these parameters already cover the side chains of the polyphilic molecule in Figure 1, only some additional parameters were needed for proper coverage of the molecule. For them, we strictly followed the CHARMM parametrization procedure,^[26] as discussed in the Supporting Information, where the resulting parameters as well as technical details^[29-41] are listed. For all calculations, SHAKE constraints have been used for the water molecules only. While Lennard-Jones radii of 1.47 Å^[42,43] and well above 3 Å^[44] are common in literature, we have used the Lennard-Jones radius of 1.37 Å from our previous work. This value, along with the matching dihedral and angular potentials, has been shown to reproduce the helical structure of long perfluoro-*n*-alkanes as well as liquid densities over a wide pressure and temperature range.

The quantum chemical reference data (geometries, Hessians, charges) required for parametrization has been calculated by Gaussian 09.^[45] All classical simulations were done by namd 2.9.^[46] For analysis, we used VMD^[47] and its Force Field Toolkit^[34] together with MDAnalysis^[48] and its RMSD alignment code.^[49] For simulation preparation, a few tools from the GRO-MACS suite^[50] have been used, as well.

Membrane insertion protocol

Simulating any molecules within membrane environments requires a "soft" procedure to embed the (smaller) molecules into these membrane snapshots. There are several established methods^[51,52] to achieve a smooth insertion. A frequently applied protocol consists of shrinking the molecule drastically, then put it into the membrane at the desired location and scale it back to its original size. Simultaneously, energy minimizations are performed and all those molecules are removed which overlap with the inserted molecule. It turns out that in our context, the removal of lipids eventually leads to large holes in the membrane bilayer.

Therefore, we have somewhat modified this approach. Instead of removing any lipids, we create a repulsive force between them and the atomic centers of the molecule to be inserted. The size of the area where these forces are applied is slowly increased during a thermostatted molecular dynamics simulation, until the lipids have moved apart, creating sufficient space for the new molecule with the conventional force field interactions. Finally, the membrane and the new molecule can be added together without any clashes or collisions.

Results and Discussion

Intramolecular bending

The overlap of the intramolecular conformational space of the polyphile between the four independent trajectories represents an indicator of the convergence of our conformational sampling. To this end and also to characterize the conformational behavior of the polyphile in the membrane, we analyze two representative angles which characterize the orientation of the polyphile within the DPPC membrane.

The first angle is the smallest angle between the backbone of the polyphilic molecule and the normal vector of the membrane. This means that if the backbone is perpendicular to a single membrane layer, the angle α is zero, otherwise it is the minimum angle regardless of the rotation of the polyphilic molecule around the normal vector of the membrane layer. As there are two lipid layers in the bilayer membrane, we have two angles, α_1 and α_2 which are the angle α for the top and for the bottom layer of the membrane. Technically, this angle is calculated from the vector between the center of mass of the middle phenylene ring of the backbone and the center of mass of the last one and the membrane normal vector.

The second angle β is the bending angle of the phenylene ring backbone of the polyphilic molecule. A straight polyphile corresponds to an angle of $\beta=180^\circ$. The specific angle definition is visualized in Figure 3 (top).

Figure 3 shows that the distribution of the angles α_i is quite similar for the trajectories and that the initial configurations have only little influence on the actual distribution. This means that the overlap between the conformations of the backbone is very high, hinting toward correct sampling of the system.

Figure 3 also shows that the reorganization of the lipid head groups on insertion of the polyphilic molecule into the membrane happens very fast. This can be deduced from the fact that none of the four trajectories has a hot spot around the angles the respective setup has been initialized with. As stated in the methods section, the initial conformations were perpendicular to the membrane plane ($\alpha_i = 0$) or tilted by 15 degrees ($\alpha_i = 15$). For no trajectory, there is a hot spot at that position. The highest density in the histogram is around $\alpha_1 = 35$ $\alpha_2 = 45$ which is considerably off the initial value. Figure 3 clearly shows that there is practically no probability of finding the polyphilic molecule somewhere near to the fifteen degrees. This means that the local ordering of the head group lipids should be observable within the timescale of 50 ns.

From the data in Figure 3, it is also clearly visible, that those orientations are preferred where the two angles α_i are not equal. This means that the backbone is bent most of the time. This bending can be further investigated by having a look at the angle β which is defined in Figure 3 and the distributions of which are shown in Figure 4.

Figure 4 shows the distribution functions of the backbone bending angle β of the polyphilic molecule for each of the four independent trajectories. The distribution maxima vary between 150° and 165°, the tails extend up to 130° and 145°. The variance observed for the different trajectories shows that full phase

4. PUBLICATIONS

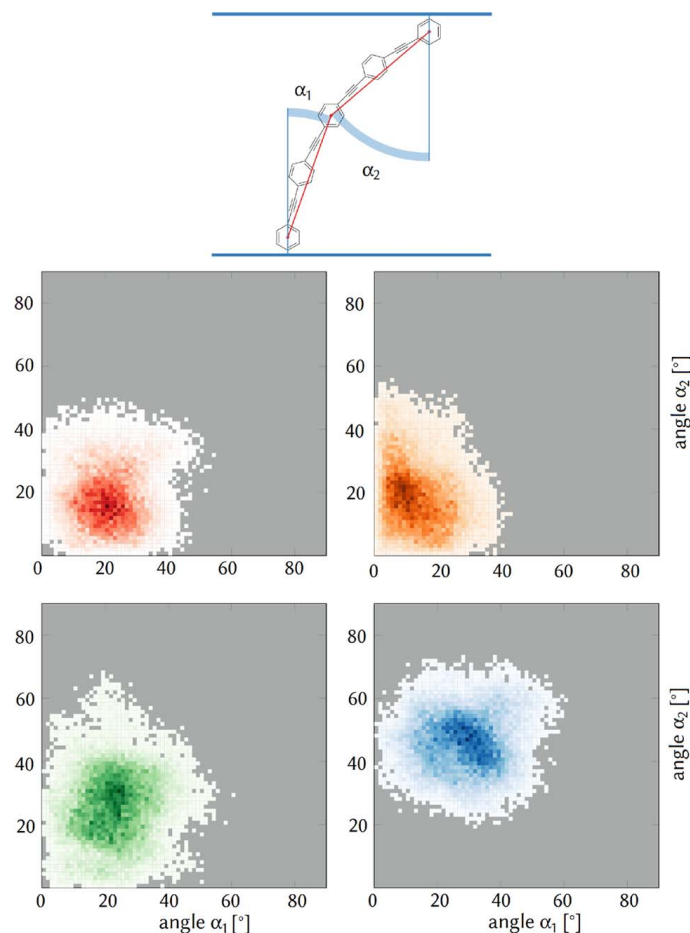


Figure 3. Top, centered: Definition of the membrane surface contact angles α_1 , α_2 of the polyphile (only the phenylene ring backbone is shown). Red dots denote the center of mass of the carbons of the respective ring. Bottom: Twodimensional histograms of (α_1, α_2) for each independent trajectory. [Color figure can be viewed at wileyonlinelibrary.com]

space convergence has not yet been reached. Nevertheless, the similarity between the distribution functions indicates that the characteristics of the distribution functions are most probably realistic. A feature common to all trajectories is the absence of conformations with angles β close to 180° (despite the normalization with $1/\sin\beta$). This indicates that the polyphiles are always bent when inserted in the lipid membrane. This bending is indicative of a slight mismatch between the length of the lipophilic core of the polyphile and the thickness of the DPPC membrane. This result might have implications on experiments where the backbone is assumed to be straight in the analysis and interpretation of measurement results.^[53]

Side chain localization within the membrane

The most important yet open question regarding the side chains of the polyphilic molecule is about their orientation within the membrane. As they are connected to the same phenylene ring in the middle of the backbone of the polyphilic molecule which happens to be in the middle of the membrane layer at all times in the simulation setup, the position of the terminal CH_3 or CF_3 groups of the side chains is a simple yet effective measure for describing the alignment of the side chains. If these terminal groups are near to the middle of the membrane, the side chains are located between the two lipid layers, making use of the low density at that part of

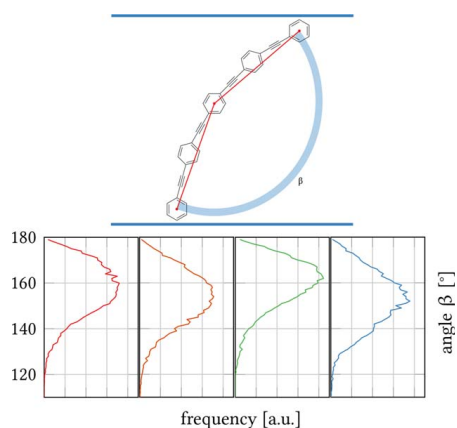


Figure 4. Top: Definition of the backbone bending angle β . Bottom: Distribution functions (histogram renormalized with $1/\sin\beta$ for each of the four trajectories. [Color figure can be viewed at wileyonlinelibrary.com])

the system. If the terminal groups are far away from the middle of the membrane, that is, near to the head group region of the lipids, then they have to be aligned parallel to the alkyl strands of the lipid molecules due to the geometric constraints. For the rest of the analysis, we have considered the middle 10 Å of the membrane layer to qualify for an orientation of the side chains in the middle of the membrane, that is the first case described above. Therefore, if the distance of the terminal group of each side chain from the middle of the lipid bilayer is more than 5 Å, then the side chain is considered to be aligned along the alkyl strands of the lipids. While we expect the alkyl side chain to be very compatible with the lipid chains of the DPPC, the prevalent interaction of the perfluorinated parts can be influenced by both, the stiffness of the side chain and the low miscibility of alkane and perfluoroalkane chains.

Using namd2, we calculated the interaction energies for the following pairs along 550 equidistant snapshots over the whole trajectory.

- DPPC lipid—all other DPPC lipids
- polyphile—all other DPPC lipids
- DPPC headgroups—non-fluorinated side chain of the polyphile
- DPPC headgroups—fluorinated side chain of the polyphile

From the calculations, it is clearly visible that the single polyphile is well-stabilized in the membrane by the interaction with the other DPPC lipids, with the largest contribution coming from the van der Waals interactions. For the two side chains, we observe a stabilizing electrostatic interaction with the lipid headgroups only for the fluorinated side chain. This is not observed for the non-fluorinated side chain.

During the molecular dynamics simulation, the instantaneous interaction energy between the DPPC lipids and the polyphile varies both for the van der Waals and for the Coulomb contribution. Insight into the flip-flop dynamics could be gained in future work by evaluating this difference in the intermediate state, but is at this time unfeasible due to the limited sampling caused by both, the rarity and speed of the flip-flop events. Histograms and further analysis of the interaction energies can be found in the Supporting Information.

However, over the course of the trajectory, a distribution of energies is sampled. This distribution has a large variance for either components. During flip-flop events, one would expect the distribution to be different, as the intermediate states are not energetically stable. In theory, knowing the difference in distribution of the interaction energies for flip-flop events as compared to the stable side-chain orientation would allow to assess the energetics of the flip-flop process. However, this process is seen very rarely in the trajectory and—due to its unstable intermediate states—completes fast, which drastically affects sampling to an extent that the distribution of interaction energies does not seem to be converged even for the length of our trajectories. Obtaining the interaction energy during such flip-flop events would require even longer trajectories or biasing methods confining the system to consecutive snapshots along a reaction coordinate.

Figure 5 shows that both cases can be observed with comparable probability. Switching between these two states is fast and typically takes less than 1 ns. This feature makes this sample system even more interesting, because the energy barrier between the three possible metastable conformations of any side chain seems to be rather small. Still, it is more likely to observe the side chains parallel to the alkyl strands than in the middle of the membrane (see Table 1).

For the case where the side chains of the polyphilic molecule are oriented along the alkyl strands of the lipids, there are two sides of the membrane the side chains can point to. This side does not necessarily stay the same in our simulations, as in total, there are some 15 changes in total. Again, this whole side chain layer switch process happens very fast (typically, between 5 ns and 10 ns for the alkyl side chain and about 15 ns for the perfluorinated side chain). This flip flop, that is, a full transition from pointing to one lipid layer to pointing to the other lipid layer without any stable intermediate third state is very fast compared to the times expected for a flip flop of a complete molecule—for model membranes, fast flip flops happen within seconds and slow ones are to be observed within minutes.^[54] Most likely, this is a result of the chemical compatibility between the fluorinated side chains and the fatty environment within the membrane. This assumption is supported by higher flip flop durations for the chemically less compatible semifluorinated side chain.

Figure 5 shows the temporal evolution and the time-averaged spatial distribution functions of the terminal CH_3/CF_3 groups of the side chains of the polyphile within the membrane. The four independent trajectories are shown separately. The characteristic shape of the temporal evolution varies considerably among the independent runs: The first and last

4. PUBLICATIONS

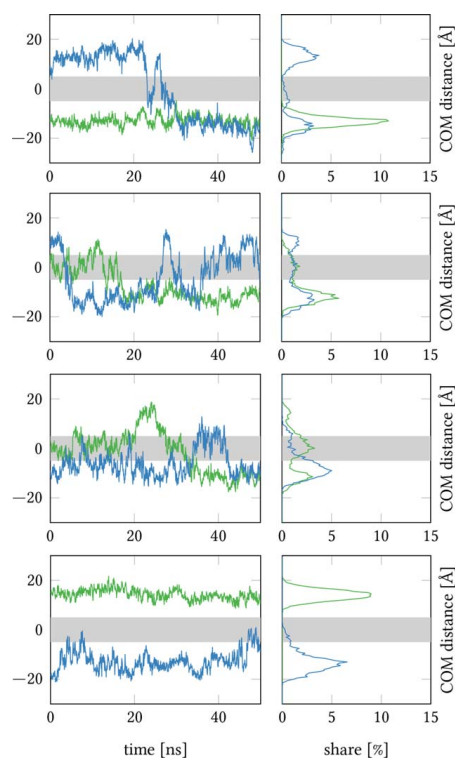


Figure 5. Trajectory (left) and distribution (right) of the terminal CF_3/CH_3 groups (green/blue) of the side chains of the side chains of the x-shaped polyphile relative to the membrane center. The shaded bar is considered as the center region. All four trajectories are shown independently. [Color figure can be viewed at wileyonlinelibrary.com]

trajectory show both CF_3 and CH_3 groups at stable localizations near the hydrophilic head groups (whose phosphorous atoms have an average coordinate of ± 20 Å), with a single crossover event from the “upper” to the “lower” head group region. In contrast to this, the second and third trajectory exhibits a less stable motional pattern of the CH_3/CF_3 endgroups, with a considerable probability in the center region of the bilayer (0 ± 5 Å, gray shaded area). This variability indicates that our phase space sampling cannot yet be considered as converged. Nevertheless, a clear trend is visible in

Table 1. Probability (%) of the side chain integration combinations where the perfluorinated side chain and the alkyl side chain are on the same side, the opposite lipid layer, or neither of these two options.

Trajectory	Same	Opposite	Undefined
Cross shaped initial geometries	38	36	27
x-shaped initial geometries	9	61	30
Overall average	23	48	28

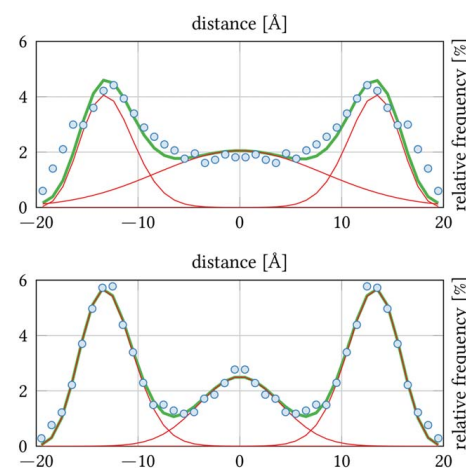


Figure 6. Histogram of the terminal group positions along the membrane normal vector and the alkyl side chain (top) and the perfluorinated side chain (bottom). The histogram from the simulation (circles) can be suitably explained by a Poisson-Gaussian fit (thick) which consists of three contributions (thin). The histogram from the simulation has been symmetrized. [Color figure can be viewed at wileyonlinelibrary.com]

the distribution functions toward a higher presence probability of the side chain endgroups in the vicinity of the lipid headgroup region, that is, around ± 15 Å. This trend is visualized even more concisely in Figure 6, where all four trajectories are shown in symmetrized and averaged form.

Figure 6 also shows that the tendency of localizing the CH_3/CF_3 endgroups toward the lipid headgroups is stronger for the perfluorinated chains than for the conventional alkane chains.

To formulate characteristic parameters for the distributions (Fig. 6) extracted from our simulations, we have fitted the distribution functions to a Poisson-type function:

$$P_{\lambda}(k) = \frac{\lambda^k}{k!} e^{-\lambda}$$

We see that this assumed probability distribution of the location of the side chains closely fits the simulation data for both side chain types. In the Supporting Information, we have shown that this Poisson-Gaussian fit works equally well for simulations at higher temperatures alongside a detailed description of the fitting process.

From the fit in Figure 6, we can obtain a relative weight for the terminal groups being at the center of the membrane (modeled by the Gaussian component of the fit) and for them being found in the outer part of which near the lipid head groups (modeled by the Poisson component). The components are shown in Figure 6, as well. According to them, the alkyl side chain is found in the center of the membrane 56% of the time, whereas the fluorinated side chain is found there 26% of the time. This clearly shows a tendency for the fluorinated side chain to avoid the center of the membrane.

Conclusions

We have determined the transmembrane orientation and intramolecular conformational distribution of a polyphilic molecule within a DPPC bilayer by means of all-atom molecular dynamics simulations of a total duration of 0.6 μ s. The polyphile was structurally designed to introduce short perfluorinated and regular alkane chains into the center of the membrane, in view of modifying the membrane properties by its partially fluorophilic character.

Our simulations show that the polyphile is indeed commensurate with the membrane, albeit a certain intramolecular bending and an inclination with respect to the membrane plane is observed, which is assigned to a slight size mismatch between the membrane and the lipophilic backbone of the molecule. We find an interesting difference in the orientational preferences between the perfluorinated side chain and the conventional alkane chain. The perfluorinated side chain orients along the lipophilic chains and toward the phosphate headgroups of the DPPC molecules, while the alkane side chain remains mostly in the center of the bilayer.

The self-diffusion for the lipids is in good agreement with experimental data. The diffusion constant of the polyphilic molecule is smaller by a factor of about 2. This illustrates that the polyphile is almost as mobile as a regular lipid, despite its twofold anchoring at both lipid-water interfaces and its additional side chains within the membrane.

Our simulations are a first step toward the understanding of intramembrane structure of polyphilic molecules with specifically designed side chains of different philicity. These molecules have the potential to enable a controlled modification of membrane properties such as water and ion permeability. In this context, the conformational space of the side chains is the key to the understanding of their structure–function relationships.

Keywords: polyphilic molecule · transmembrane · DPPC · perfluorinated side chain · molecular dynamics

How to cite this article: G. F. von Rudorff, T. Watermann, X.-Y. Guo, D. Sebastiani. *J. Comput. Chem.* **2017**, *38*, 576–583. DOI: 10.1002/jcc.24711

 Additional Supporting Information may be found in the online version of this article.

- [1] C. Schwieger, A. Achilles, S. Scholz, J. Ruger, K. Bacia, K. Saalwachter, J. Kressler, A. Blume, *Soft Matter* **2014**, *10*, 6147.
- [2] X. Zeng, R. Kieffer, B. Glettner, C. Nurnberger, F. Liu, K. Pelz, M. Prehm, U. Baumeister, H. Hahn, H. Lang, G. A. Gehring, C. H. M. Weber, J. K. Hobbs, C. Tschierske, G. Ungar, *Science* **2011**, *331*, 1302.
- [3] P. Scholtysek, A. Achilles, C.-V. Hoffmann, B.-D. Lechner, A. Meister, C. Tschierske, K. Saalwachter, K. Edwards, A. Blume, *J. Phys. Chem. B* **2012**, *116*, 4871.
- [4] E. H. Hill, K. Stratton, D. G. Whitten, D. G. Evans, *Langmuir* **2012**, *28*, 14849.
- [5] M. Schulz, A. Olubummo, W. H. Binder, *Soft Matter* **2012**, *8*, 4849.
- [6] J. Hinks, Y. Wang, W. Han Poh, B. C. Donose, A. W. Thomas, S. Wuertz, S. C. Joachim Loo, G. C. Bazan, S. Kjelleberg, Y. Mu, T. Seviour, *Langmuir* **2014**, *30*, 2429.
- [7] P. V. James, P. K. Sudeep, C. H. Suresh, K. George Thomas, *J. Phys. Chem. A* **2006**, *110*, 4329.
- [8] E. H. Hill, D. G. Whitten, D. G. Evans, *J. Phys. Chem. B* **2014**, *118*, 9722.
- [9] A. J. Crane, F. J. Martinez-Veracoechea, F. A. Escobedo, E. A. Muller, *Soft Matter* **2008**, *4*, 1820.
- [10] M. P. Krafft, *Adv. Drug Deliv. Rev.* **2001**, *47*, 209.
- [11] K. Park, C. Berrier, F. Lebaupain, B. Pucci, J. Popot, A. Ghazi, F. Zito, *Biochem. J.* **2007**, *403*, 183.
- [12] J. C. Maurizis, M. Azim, M. Rapp, B. Pucci, A. Pavia, J. C. Madelmont, A. Veyre, *Xenobiotica* **1994**, *24*, 535.
- [13] H. Permedi, B. Lundgren, K. Andersson, J. W. DePierre, *Biochem. Pharmacol.* **1992**, *44*, 1183.
- [14] J. P. Vanden Heuvel, B. I. Kuslikis, M. J. Van Rafelghem, R. E. Peterson, *J. Biochem. Toxicol.* **1991**, *6*, 83.
- [15] M. Schulz, S. Werner, K. Bacia, W. H. Binder, *Angew. Chem.* **2013**, *125*, 1877.
- [16] H. Matsuda, A. Kitabatake, M. Kosuge, K. Kurihara, K. Tochigi, K. Ochi, *Fluid Phase Equilib.* **2010**, *297*, 187.
- [17] Q. Chu, M. S. Yu, D. P. Curran, *Tetrahedron* **2007**, *63*, 9890.
- [18] B. Cornils, *Angew. Chem. Int. Ed. (English)* **1997**, *36*, 2057.
- [19] J.-P. Rolland, C. Santaella, B. Monasse, P. Vierling, *Chem. Phys. Lipids* **1997**, *85*, 135.
- [20] G. F. von Rudorff, T. Watermann, D. Sebastiani, *J. Phys. Chem. B* **2014**, *118*, 12531.
- [21] Z. V. Leonenko, E. Finot, H. Ma, T. E. S. Dahms, D. T. Cramb, *Biophys. J.* **2004**, *86*, 3783.
- [22] K. Jacobson, D. Papahadjopoulos, *Biochemistry* **1975**, *14*, 152.
- [23] J. B. Klauda, R. M. Venable, J. Alfredo Freites, J. W. O'Connor, D. J. Tobias, C. Mondragon-Ramirez, I. Vorobyov, A. D. MacKerell, R. W. Pastor, *J. Phys. Chem. B* **2010**, *114*, 7830.
- [24] G. Lindblom, G. Oradd, A. Filippov, *Chem. Phys. Lipids* **2006**, *141*, 179.
- [25] A. D. MacKerell, D. Bashford, D. Bellott, J. D. Evanseck, M. J. Field, S. Fischer, J. Gao, H. Guo, S. Ha, D. Joseph-McCarthy, L. Kuchnir, K. Kuczera, F. T. K. Lau, C. Mattos, S. Michnick, T. Ngo, D. T. Nguyen, B. Prodhom, W. E. Reiher, B. Roux, M. Schlenkerich, J. C. Smith, R. Stote, J. Straub, M. Watanabe, J. Wiorkiewicz-Kuczera, D. Yin, M. Karplus, *J. Phys. Chem. B* **1998**, *102*, 3586.
- [26] K. Vanommeslaeghe, E. Hatcher, C. Acharya, S. Kundu, S. Zhong, J. Shim, E. Darian, O. Guvench, P. Lopes, I. Vorobyov, A. D. MacKerell, *J. Comput. Chem.* **2010**, *31*, 671.
- [27] E. Hatcher, O. Guvench, A. D. MacKerell, *J. Chem. Theory Comput.* **2009**, *5*, 1315.
- [28] A. D. MacKerell, *J. Comput. Chem.* **2004**, *25*, 1584.
- [29] A. A. H. Padua, *J. Phys. Chem. A* **2002**, *106*, 10116.
- [30] W. Gordy, *J. Chem. Phys.* **1946**, *14*, 305.
- [31] G. B. M. Sutherland, D. M. Dennison, *Proc. R. Soc. Lond. Ser. A* **1935**, *148*, 250.
- [32] M. Thomas, M. Brehm, R. Fligg, P. Vohringer, B. Kirchner, *Phys. Chem. Chem. Phys.* **2013**, *15*, 6608.
- [33] P. Sinha, S. E. Boesch, C. Gu, R. A. Wheeler, A. K. Wilson, *J. Phys. Chem. A* **2004**, *108*, 9213.
- [34] C. G. Mayne, J. Saam, K. Schulten, E. Tajkhorshid, J. C. Gumbart, *J. Comput. Chem.* **2013**, *34*, 2757.
- [35] B. H. Besler, K. M. Merz, P. A. Kollman, *J. Comput. Chem.* **1990**, *11*, 431.
- [36] U. Chandra Singh, P. A. Kollman, *J. Comput. Chem.* **1984**, *5*, 129.
- [37] H. Bernhard Schlegel, *Theor. Chim. Acta* **1984**, *66*, 333.
- [38] A. Amadei, M. D. Abramo, A. D. Nola, A. Arcadi, G. Cerichelli, M. Aschi, *Chem. Phys. Lett.* **2007**, *434*, 194.
- [39] C. Moller, M. S. Plesset, *Phys. Rev.* **1934**, *46*, 618.
- [40] B. Adisa, D. A. Bruce, *J. Phys. Chem. B* **2005**, *109*, 7548.
- [41] B. Corry, D. Jayatilaka, B. Martinac, P. Rigby, *Biophys. J.* **2006**, *91*, 1032.
- [42] E. Carosati, S. Sciabola, G. Cruciani, *J. Med. Chem.* **2004**, *47*, 5114.
- [43] M. Pettersson, X. Hou, M. Kuhn, T. T. Wager, G. W. Kauffman, P. R. Verhoest, *J. Med. Chem.* **2016**, *59*, 5284.
- [44] A. K. Rappe, C. J. Casewit, K. S. Colwell, W. A. Goddard, W. M. Skiff, *J. Am. Chem. Soc.* **1992**, *114*, 10024.

4. PUBLICATIONS

- [45] M. J. Frisch, G. W. Trucks, H. B. Schlegel, G. E. Scuseria, M. A. Robb, J. R. Cheeseman, G. Scalmani, V. Barone, B. Mennucci, G. A. Petersson, H. Nakatsuji, M. Caricato, X. Li, H. P. Hratchian, A. F. Izmaylov, J. Bloino, G. Zheng, J. L. Sonnenberg, M. Hada, M. Ehara, K. Toyota, R. Fukuda, J. Hasegawa, M. Ishida, T. Nakajima, Y. Honda, O. Kitao, H. Nakai, T. Vreven, J. A. Montgomery, Jr., J. E. Peralta, F. Ogliaro, M. Bearpark, J. J. Heyd, E. Brothers, K. N. Kudin, V. N. Staroverov, R. Kobayashi, J. Normand, K. Raghavachari, A. Rendell, J. C. Burant, S. S. Iyengar, J. Tomasi, M. Cossi, N. Rega, J. M. Millam, M. Klene, J. E. Knox, J. B. Cross, V. Bakken, C. Adamo, J. Jaramillo, R. Gomperts, R. E. Stratmann, O. Yazyev, A. J. Austin, R. Cammi, C. Pomelli, J. W. Ochterski, R. L. Martin, K. Morokuma, V. G. Zakrzewski, G. A. Voth, P. Salvador, J. J. Dannenberg, S. Dapprich, A. D. Daniels, Ö. Farkas, J. B. Foresman, J. V. Ortiz, J. Cioslowski, D. J. Fox, Gaussian 09, Revision A.2; Gaussian Inc.: Wallingford, CT, **2009**.
- [46] J. C. Phillips, R. Braun, W. Wang, J. Gumbart, E. Tajkhorshid, E. Villa, C. Chipot, R. D. Skeel, L. Kalé, K. Schulten, *J. Comput. Chem.* **2005**, *26*, 1781.
- [47] W. Humphrey, A. Dalke, K. Schulten, *J. Mol. Graph.* **1996**, *14*, 33.
- [48] N. Michaud-Agrawal, E. J. Denning, T. B. Woolf, O. Beckstein, *J. Comput. Chem.* **2011**, *32*, 2319.
- [49] D. L. Theobald, *Acta Crystallogr. A* **2005**, *61*(Pt 4), 478.
- [50] S. Pronk, S. Páll, R. Schulz, P. Larsson, P. Bjelkmar, R. Apostolov, M. R. Shirts, J. C. Smith, P. M. Kasson, D. van der Spoel, B. Hess, E. Lindahl, *Bioinformatics* **2013**, *29*, 845.
- [51] A. L. Lomize, I. D. Pogozheva, M. A. Lomize, H. I. Mosberg, *Protein Sci.* **2006**, *15*, 1318.
- [52] M. G. Wolf, M. Hoefling, C. Aponte-Santamaría, H. Grubmüller, G. Groenhof, *J. Comput. Chem.* **2010**, *31*, 2169.
- [53] L. K. Tamm, S. A. Tatulian, *Q. Rev. Biophys.* **1997**, *30*, 365.
- [54] F. Kamp, J. A. Hamilton, *Proc. Natl. Acad. Sci. USA* **1992**, *89*, 11367.

Received: 11 May 2016
Revised: 20 August 2016; 17 November 2016
Accepted: 18 November 2016
Published online in Wiley Online Library

Article

Cluster Formation of Polyphilic Molecules Solvated in a DPPC Bilayer

Xiang-Yang Guo, Christopher Peschel , Tobias Watermann, Guido Falk von Rudorff and Daniel Sebastiani * 

Institute of Chemistry, MLU Halle-Wittenberg, von-Danckelmann-Platz 4, 06120 Halle, Germany; xiang.guo@chemie.uni-halle.de (X.-Y.G.); christopher.peschel@chemie.uni-halle.de (C.P.); tobias.watermann@chemie.uni-halle.de (T.W.); guido@vonrudorff.de (G.F.v.R.)

* Correspondence: daniel.sebastiani@chemie.uni-halle.de; Tel.: +49-(0)345-55-25-836

Received: 15 September 2017; Accepted: 29 September 2017; Published: 6 October 2017

Abstract: We analyse the initial stages of cluster formation of polyphilic additive molecules which are solvated in a dipalmitoylphosphatidylcholine (DPPC) lipid bilayer. Our polyphilic molecules comprise an aromatic (trans-bilayer) core domain with (out-of-bilayer) glycerol terminations, complemented with a fluorophilic and an alkyl side chain, both of which are confined within the aliphatic segment of the bilayer. Large-scale molecular dynamics simulations (1 μ s total duration) of a set of six of such polyphilic additives reveal the initial steps towards supramolecular aggregation induced by the specific philicity properties of the molecules. For our intermediate system size of six polyphiles, the transient but recurrent formation of a trimer is observed on a characteristic timescale of about 100 ns. The alkane/perfluoroalkane side chains show a very distinct conformational distribution inside the bilayer thanks to their different philicity, despite their identical anchoring in the trans-bilayer segment of the polyphile. The diffusive mobility of the polyphilic additives is about the same as that of the surrounding lipids, although it crosses both bilayer leaflets and tends to self-associate.

Keywords: lipid bilayer; DPPC; bolopolyphile; diffusion coefficient; perfluorinated; molecular dynamics (MD)

1. Introduction

Molecules which have the ability of self-assembling are of huge interest for biochemical (lipid bilayers), and nanosized materials [1]. To understand such behavior is crucial for the rational design of model and advanced systems. Many molecule types have been inserted into lipid bilayers in experiment and in simulations to understand their behavior. This ranges from early attempts by inserting alkanes into a lipid bilayer system to see where they are located inside the system [2], up to the latest investigations of fluorinated alkanes and alcohols [3]. In extend to those publications we investigated a very complex compound combining many philicities in one molecule. These so called polyphilic molecules, as the name suggests, are compounds consisting of fragments with different philicities. Special attention is paid here to polyphiles that contain a rigid rod-shaped aromatic core with opposing end groups and lateral groups with different philicities. The two end groups are typically highly polar, allowing the formation of multiple hydrogen bonds, which is only possible in the headgroup region of the bilayer and in the aqueous phase, whilst the lateral groups are alkyl, partially fluorinated or perfluorinated chains [4]. This novel class of molecules have received significant attention in recent years [5–10]. Polyphilic molecules can be used to modify the phase transitions temperature of a lipid bilayer [11] and also serve as a drug delivery agent [12,13]. Furthermore, they cause effects like compression or stretching of bilayer systems which was recently shown [11,14–18].

4. PUBLICATIONS

Polymers 2017, 9, 488

2 of 11

Fluorocarbon compounds are also studied for influencing the metabolism of rats [19,20] and for in vitro synthesis of lipid bilayer proteins [21].

To fully understand why this type of molecules influences the bilayer properties, the polyphilic molecules themselves have to be studied on a molecular scale. The molecule (B16/10) being investigated in this work possesses three philicities, namely fluorophilic, hydrophilic and lipophilic parts [6–10,22]. The rigid aromatic phenylene–ethynylene–backbone forms its frame structure, and two hydrophilic groups are terminating this backbone chain. In the middle of the backbone, two side chains are attached, one of which is a perfluoro-*n*-alkane, the other is a regular *n*-alkane (see Figure 1). The length of the side chains can be derived from the name (16 carbon atoms for the alkyl chain and 10 carbon atoms for the perfluorinated alkyl groups). This molecular structure ensures a trans-bilayer orientation of the backbone, yielding an anchor point for the alkyl/perfluoroalkyl chains at the center of the bilayer. Mobile aliphatic side chains and polar end groups offer many possibilities of functionalization to tailor the interactions with the bilayers. As the fundamental building blocks of cellular membranes, phospholipid bilayers play a decisive role in many of their biological functions. The modification of lipid bilayer functions via interactions with biomolecules such as proteins or peptides has been widely investigated [23–26]. Due to experimental investigations of the influence of purely synthetic molecules on DPPC bilayers [14,15,27], it serves perfectly as a model system for thorough investigation of the influence of our polyphilic molecules on the bilayer properties. The concept of polyphilicity was even recently used for directly modifying the lipid bilayer itself by perfluorinating the end of the lipid tails [28].

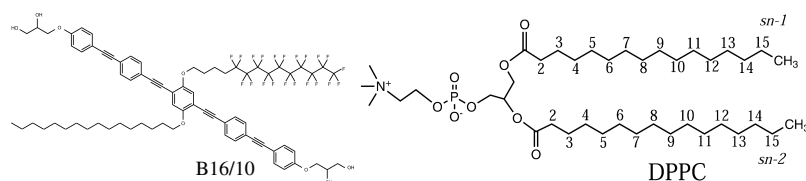


Figure 1. Molecular structure of the polyphilic molecule B16/10 and dipalmitoylphosphatidylcholine (DPPC) molecule studied in this report.

The available experimental results show that, when bolapolyphile molecules (BP) are incorporated into gel phase lipid (DPPC) bilayers, the formation of large BP domains within the bilayer and a separation into different lamellar species can be observed [16,17]. The thermal behavior of the lipid bilayers was drastically altered upon BP incorporation and several endothermic transitions above T_m of pure DPPC bilayer occurred [11]. In the liquid phase, the BPs were homogeneously distributed in the lipid bilayer plane [11,16].

Lipid bilayer simulations have reached an exciting point, where the time and length scales of simulations are approaching experimental resolutions and can be used to interpret experiments on increasingly complex model bilayers. Within molecular dynamics (MD) of hybrid-bilayer systems, one is able to get an insight into the dynamical behavior on a molecular scale. Therefore, these simulations provide complementary information to experiments [25,29–34]. Furthermore, they can yield molecular-level insight into the structure and dynamics of these systems with a spatial resolution and time-scale that may not be feasible experimentally. Summarized, they serve as rich sources of quantitative data on molecular flexibility, lipid diffusion, ordering and atomic interactions. A detailed understanding of lipid bilayer properties is necessary to fully understand their important biophysical characteristics.

Previously, we have reported a MD study of one single B16/10 molecule inserted as a trans-bilayer agent into a dipalmitoylphosphatidylcholine (DPPC) bilayer [35]. The results showed that B16/10 is commensurate with the bilayer, and at the same time, a certain intramolecular bending and an inclination with respect to the bilayer plane is observed. While the lipophilic groups remain

bilayer-centered, the fluorophilic parts tend to orient towards the phosphate headgroups, which is due to a slight size mismatch between the bilayer and the lipophilic backbone of the molecule.

In the present work, MD simulations with full atomic detail were carried out for a small trans-bilayer cluster containing six B16/10 molecules embedded into a DPPC bilayer on a large time scale. The difference of the dynamical and structural properties of the DPPC bilayer between pure bilayer system and the mixture of the lipid bilayer with B16/10 molecules is illustrated. The configurations and dynamics of incorporated B16/10 are studied. The results are compared with available experimental and literature data.

2. System Setup and Computational Details

A small cluster of six B16/10 molecules was embedded into a DPPC bilayer consisting 288 lipid molecules (144 per leaflet). The mixed molecular system was hydrated using 8756 TIP3 water molecules. The resulting periodic box has a dimension of $98 \times 98 \times 68 \text{ \AA}^3$. A snapshot of the system is shown in Figure 2.

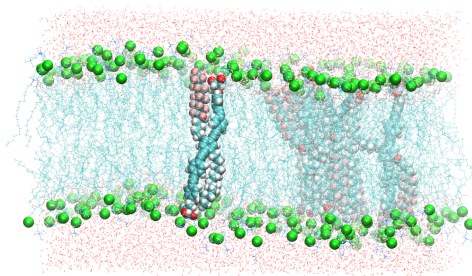


Figure 2. A snapshot of the simulated system containing six B16/10 molecules, 288 DPPC molecules and 8756 water molecules. Periodic boundary conditions were used in all directions. Atoms of B16/10 molecules and Phosphorus atoms of DPPC headgroups are represented by solid spheres. Phosphorus atoms are green, Fluorine atom of B16/10 side chains are pink, carbon atoms are cyan. All the lipid tails of DPPC are represented by cyan lines. One can see, that the backbone of the polyphile (cyan spheres) is bent and not straight.

The initial configurations of B16/10 molecules was selected based on the experimentally observed phase formation of similar structured molecules. According to the experimental results, similar structured B12 molecules spontaneously self-organize in lipid bilayers (DPPC), forming ordered snowflake like structures with 6-fold symmetry in giant unilamellar vesicles [16,17]. Furthermore, the initial structure completely vanished after an equilibration time of 20 ns. The first 20 ns have been omitted in all analyses. The structure after the equilibration is shown in Figure 3 as a top view onto the system.

All MD simulations in this work were performed by software package namd 2.9 using the CHARMM force field [32,36,37]. The detailed parameters for B16/10 are presented in a previous work of our group [38]. Three dimensional periodic boundary conditions were used. The system is kept at a constant pressure of 1 bar and a constant specified temperature (isobaric-isothermal NpT ensemble) using a modified Nose–Hoover method in which Langevin dynamics is used to control fluctuations in the barostat. The semi-isotropic pressure coupling was applied separately for the bilayer plane and bilayer normal with a coupling constant of 1 bar. Experimentally measured phase transition temperature of a DPPC bilayer is between 313 and 315 K [16,17]. It is experimentally observed that the presence of polyphile molecules increases this phase transition temperature. In order to avoid a simulation in a gel phase, we set the simulation temperature to 335 K in this work.

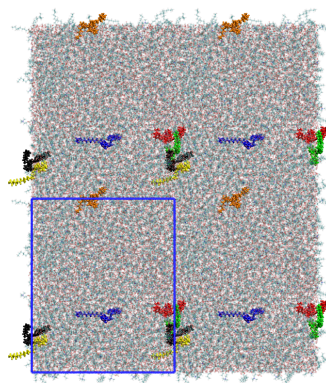


Figure 3. A snapshot of the simulated system as a top view after an equilibration time of 20 ns. The polyphiles are colored and a clustering can be observed for some of the molecules. The simulation cell dimensions are shown as blue rectangle.

The system was simulated for 1 μ s with a time step of 2 fs. The bond lengths were constrained using the SHAKE algorithm. The vdW cutoff follows the force field specifications for lipid bilayers. A particle mesh Ewald summation was used to calculate the electrostatic interactions. Cutoff radius for van der Waals interactions was set to 1.0 nm. Particle mesh Ewald (PME) summations were applied for long-range electrostatic interactions with a grid spacing of 0.12 nm and a cutoff radius of 1.0 nm was employed for real space summation. For the purpose of comparison, simulations of a pure DPPC bilayer was carried out under same conditions. The TIP3P water model was used to solvate the system. Data analysis of the trajectories were done by using VMD plugins [39], the python module MDAnalysis [40], the freeware program package TRAVIS [41] and our own codes.

3. Results and Discussion

Statistical analysis was carried out to characterize the dynamical and structural properties of B16/10 trans-bilayer molecules inside a DPPC bilayer. In particular, we (i) calculated the lateral diffusion coefficients of DPPC and B16/10 molecules and (ii) investigated the axial location and orientation of B16/10 molecules and internal structure of B16/10 cluster. The results are compared with a pure DPPC bilayer system, available experimental data and former results of our group.

3.1. Lateral Diffusion

Investigation of DPPC and B16/10 molecules lateral mobility in a planar lipid bilayer are carried out and the results are compared with the pure bilayer system. The averaged self-diffusion coefficients of B16/10 and DPPC molecules are calculated from the mean squared displacement (MSD) $\langle r^2(t) \rangle$ using the Einstein relation:

$$MSD(t) = \langle r^2(t) \rangle = \langle [r(t) - r(0)]^2 \rangle \quad (1)$$

$$D = \frac{1}{2d} \lim_{t \rightarrow \infty} \frac{d}{dt} \langle [r(t) - r(0)]^2 \rangle, \quad (2)$$

where d is the number of dimension which is 2 for our calculation. The MSD is calculated with respect to the center of mass (COM) of all lipid molecules to avoid artifacts from water layer movement. The averaged MSD for DPPC and B16/10 molecules are shown in Figure 4.

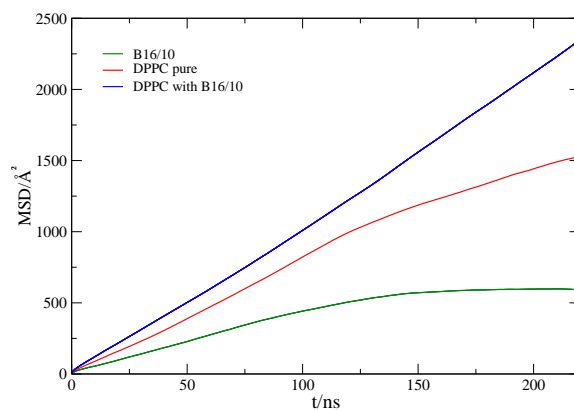


Figure 4. Mean square displacement of lipids in a pure DPPC bilayer (red), the lipids (blue) and B16/10 molecules (green) in the mixed system (lipids/B16/10).

The calculated self-diffusion coefficient of pure DPPC at 335K as presented in Table 1 is in very good agreement with the experimentally determined value of $14.2 \pm 1.2 \times 10^{-12} \text{ m}^2/\text{s}$ [42]. The diffusion coefficient of B16/10 molecules is slightly lower than the diffusion coefficient of the lipids in a pure bilayer. For the mixed system, we find high diffusivity values for the lipid molecules, which is unexpected.

Table 1. Lateral self-diffusion coefficients (D) at 335 K obtained from MD simulation (MD) and experimental data from literature (exp) [42]. Uncertainties are given as three times the standard deviation.

$D/(10^{-12} \text{ m}^2/\text{s})$	Lipids (Pure DPPC)	Lipids (mix)	B16/10 (mix)
MD	13.9 ± 0.3	24 ± 0.6	10.7 ± 0.3
exp	14.2 ± 1.2		

3.2. B16/10 Radial Distribution Functions

We calculated the pair correlation function, $g(r)$, as the probability of finding a pair of B16/10 molecules at distance r apart, relative to the probability expected for a completely random distribution at the same density [43]. The $g(r)$ of the center of mass for each central phenylene ring of a B16/10 molecule (COR-COR) and of its terminal groups (CH_3 and CF_3) is shown in Figure 5.

4. PUBLICATIONS

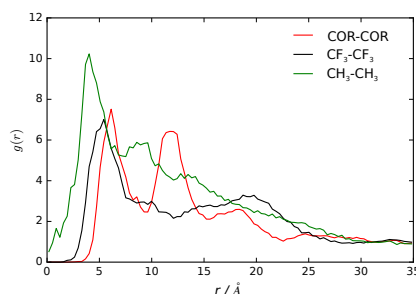


Figure 5. Radial distribution functions of the center of the central phenylene ring (COR), CF_3 and CH_3 terminal groups of B16/10 molecules within the DPPC bilayer.

We observe a clustering effect documented by the two peak nature in the radial distribution function. The first peak at 7 Å distance shows that two B16/10 molecules are directly adjacent to each other, as there is no space for interlaced molecules. Nevertheless the lipid molecules force the B16/10 molecules to tilt a little away from a coplanar orientation and causing this distance of 7 Å. Due to the tilt and high distance, pi–pi stacking does not frequently occur. Nevertheless, the radial distribution function has also non-zero values below 7 Å, which at least can be interpreted as possible pi–pi stacking. As there are only six B16/10 molecules in the system, effects of a big ensemble like in experiment [11,17] cannot be captured and therefore a strong pi–pi stacking behavior cannot be excluded even though it is unfavorable in our simulation. The second peak at 12 Å shows that a third B16/10 molecule is forming a little cluster with the other two. As the second peak is not double of the first one it can be seen that they are not completely aligned but forming a triangle. The clustering can be seen in Figure 6. Comparing Figures 3 and 6, one can see that the molecules inside the cluster are exchanging within the simulation.

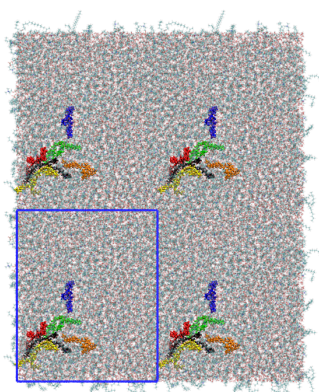


Figure 6. Snapshot of the top view onto the system showing the clustering of the B16/10 molecules. Namely the red, yellow and black colored molecules form a cluster, whereas the green and orange molecules are surrounding the cluster. Compared to Figure 3 (same coloring of the molecules), one can see that the cluster exchanges the molecules within the simulation. The simulation cell dimensions are shown as blue rectangle.

Having this in mind it is even more surprising that the diffusion coefficient discussed in the previous section of $11 \times 10^{-12} \frac{\text{m}^2}{\text{s}}$ for B16/10 (see Table 1) is rather high. This clustering behavior of x-shaped molecules like the non-perfluorinated B12 molecule was also observed experimentally [11,17]. Therefore it can be assumed that by perfluorinating one side chain, the clustering behavior is maintained. For the terminal groups CH_3 and CF_3 there is only one well defined peak at around 3 \AA for CH_3 and at 5 \AA for CF_3 . Beyond this there is a smooth decay to unity apart from residual structure but with no recognizable pattern. All in all this shows that there is a correlation of the backbones of the B16/10 molecules forming a little cluster whereas there is no correlation of the side chains aside from pairwise orientation.

3.3. B16/10 Backbone Angles Distribution

We use three angles α_1 , α_2 and β to characterize the orientation of B16/10 backbone within the bilayer as shown in Figure 7. The distributions of the three angles are displayed in Figure 8.

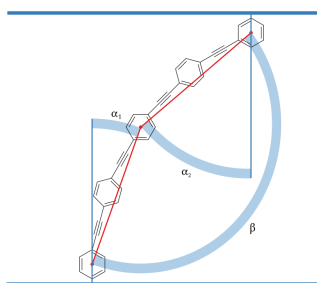


Figure 7. Angles between the bilayer normal and B16/10 backbone (α_1 and α_2) and backbone bending angle β .

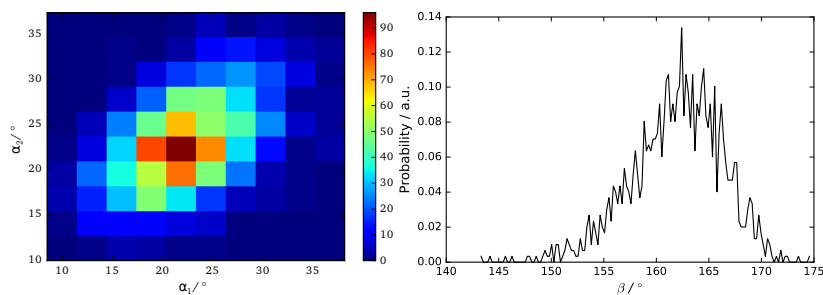


Figure 8. Probability distribution of backbone angles α_1 , α_2 and β .

The calculated angular distributions of the B16/10 backbone are in very good agreement with our former results of a single B16/10 molecule inside a DPPC bilayer [35]. The B16/10 molecules are well incorporated into the lipid bilayer, cross the whole bilayer with their well-matched hydrophobic core length and adapting into the bilayer by a slight tilt.

3.4. B16/10 Terminal Group Integration and Side Chain Orientations

In Figure 9 the averaged position distribution of CF_3 and CH_3 terminal groups of B16/10 molecules relative to the center of mass of the system is shown. For avoiding artifacts, the center of mass movement of the whole system has been subtracted. The center of the lipid bilayer is denoted

4. PUBLICATIONS

by $z = 0$ and z is the axis along the normal of the bilayer plane. The bilayer itself has a thickness of approximately $40 \pm 2.5 \text{ \AA}$. As one can see in Figure 9, both side chains approach the head group region of the bilayer. Nevertheless the CF side chain tends to stay more in the headgroup region than the CH chain. The combination of higher solubility inside the leaflets (which was recently shown by Brehm et al. [3]) and sterical issues force the CF_3 terminal group to stay in the headgroup region as in direct comparison the CF side chain is nearly inflexible whereas the CH side is more flexible and thinner which makes it easier for the CH chain to find its way through the lipid bilayer. Not surprising is, that the CH_3 terminal group has a high occurrence in the middle of the bilayer, as this the most non polar region of the bilayer which has been observed in experiment before for alkanes [2]. Of course sterical issues are more dominant because not every polyphile can arrange like this when incorporated into a cluster and therefore it also stays frequently inside the leaflets. On first sight the occurrence of the CF_3 terminal group in the middle of the bilayer seems astonishing. It is easy explained by attempts to flip the sides of the bilayer. As it is only ninth of the occurrence of the highest peak this rarely happens and is never a stationary state. By closer inspection we found that the flipping of the CF side chain happens on a nanosecond time scale.

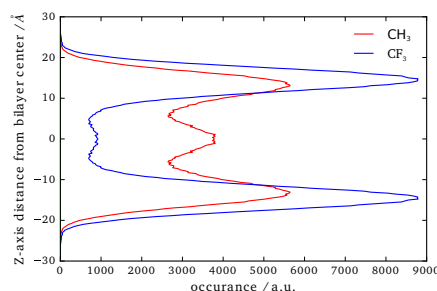


Figure 9. Position of the CF_3 and CH_3 terminal groups along the z -axis relative to the center of mass of the whole system.

The distribution of the side chain angles can be used to confirm these statements as seen in Figure 10. The angles are defined as the angle of the vector from the terminal groups to the center of the phenylene ring in the middle of the backbone and the bilayer normal. Therefore 90° denotes directly aligned between the leaflets in the bilayer plane. The prominent angles around 30° and 150° for the CF_3 terminal group confirms that it mostly stays in head group region of the bilayer. The very slight occurrence around 90° also shows the behavior to flip rather than staying between the leaflets. More or less Figure 9 and 10 resemble each other in appearance and therefore also confirm the statements for CH terminal head group mentioned above.

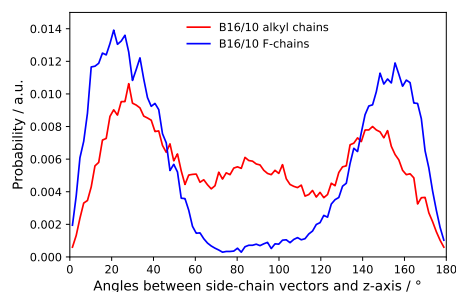


Figure 10. Probability distribution of side chains angles.

4. Conclusions

In this paper, we report a study of six polyphilic molecules embedded in a lipid bilayer/water system. Our results give insights not only into the conformational preference of the B16/10 molecules inside the DPPC bilayer, but also on the dynamics of the B16/10 molecules in the DPPC bilayer environment. Within 1 ms of simulation the stability of the bilayer maintained upon insertion of the additive B16/10 molecules. The diffusion of the lipid molecules is increased compared to the pure lipid bilayer and B16/10 molecules move only slightly slower than the lipids in the pure bilayer. For the intermolecular structure of the B16/10 molecules a clustering effect can be observed in the RDFs. The difference in the side chain orientation and configuration is also in good agreement with the simulation results we obtained before [35]. In general, the conclusions drawn from simulations are consistent with experimentally observed effects [16,17,42]. We anticipate that these findings will be important for understanding the role of polyphilic molecules in modulating and modifying bilayer properties.

Acknowledgments: This work has been supported by the German Research Foundation (DFG) within the Forschergruppe FOR1145 (grant number Se 1008/9-1). The authors thank the China Scholarship Council (CSC) for providing a scholarship.

Author Contributions: Xiang-Yang Guo, Tobias Watermann and Guido Falk von Rudorff planned and set up the simulation. Xiang-Yang Guo and Christopher Peschel analyzed the data and wrote the manuscript. Daniel Sebastiani supervised this project.

Conflicts of Interest: The authors declare no conflict of interest.

References

1. Ariga, K.; Hill, J.P.; Lee, M.V.; Vinu, A.; Charvet, R.; Acharya, S. Challenges and breakthroughs in recent research on self-assembly. *Sci. Technol. Adv. Mater.* **2008**, *9*, 014109, doi:10.1088/1468-6996/9/1/014109.
2. White, S.H.; King, G.I.; Cain, J.E. Location of hexane in lipid bilayers determined by neutron diffraction. *Nature* **1981**, *290*, 161–163, doi:10.1038/290161a0.
3. Brehm, M.; Saddiq, G.; Watermann, T.; Sebastiani, D. Influence of Small Fluorophilic and Lipophilic Organic Molecules on Dipalmitoylphosphatidylcholine Bilayers. *J. Phys. Chem. B* **2017**, *121*, 8311–8321, doi:10.1021/acs.jpcc.7b06520
4. Bates, M.; Walker, M. Dissipative particle dynamics simulation of T- and X-shaped polyphilic molecules exhibiting honeycomb columnar phases. *Soft Matter* **2009**, *5*, 346–353, doi:10.1039/b813015a.
5. Crane, A.J.; Martínez-Veracoechea, F.J.; Escobedo, F.A.; Müller, E.A. Molecular dynamics simulation of the mesophase behaviour of a model bolaamphiphilic liquid crystal with a lateral flexible chain. *Soft Matter* **2008**, *4*, 1820–1829, doi:10.1039/b802452a.
6. Hill, E.; Stratton, K.; Whitten, D.G.; Evans, D.G. Molecular Dynamics Simulation Study of the Interaction of Cationic Biocides with Lipid Bilayers: Aggregation Effects and Bilayer Damage. *Langmuir* **2012**, *28*, 14849–14854, doi:10.1021/la303158c.

4. PUBLICATIONS

Polymers **2017**, *9*, 488

10 of 11

7. Schulz, M.; Olubummo, A.; Binder, W.H. Beyond the lipid-bilayer: Interaction of polymers and nanoparticles with membranes. *Soft Matter* **2012**, *8*, 4849–4864, doi:10.1039/c2sm06999g.
8. Hinks, J.; Wang, Y.; Poh, W.H.; Donose, B.C.; Thomas, A.W.; Wuertz, S.; Loo, S.C.J.; Bazan, G.C.; Kjelleberg, S.; Mu, Y.; et al. Modeling Cell Membrane Perturbation by Molecules Designed for Transmembrane Electron Transfer. *Langmuir* **2014**, *30*, 2429–2440, doi:10.1021/la403409t.
9. James, P.V.; Sudeep, P.K.; Suresh, C.H.; Thomas, K.G. Photophysical and Theoretical Investigations of Oligo(p-phenyleneethynylene)s: Effect of Alkoxy Substitution and Alkyne–Aryl Bond Rotations. *J. Phys. Chem. A* **2006**, *110*, 4329–4337, doi:10.1021/jp055184o.
10. Hill, E.H.; Whitten, D.G.; Evans, D.G. Computational Study of Bacterial Membrane Disruption by Cationic Biocides: Structural Basis for Water Pore Formation. *J. Phys. Chem. B* **2014**, *118*, 9722–9732, doi:10.1021/jp504297s.
11. Lechner, B.-D.; Ebert, H.; Prehm, M.; Werner, S.; Meister, A.; Hause, G.; Beerlink, A.; Saalwächter, K.; Bacia, K.; Tschierske, C.; et al. Temperature-Dependent In-Plane Structure Formation of an X-Shaped Bolapolyphile within Lipid Bilayers. *Langmuir* **2015**, *31*, 2839–2850, doi:10.1021/la504903d.
12. Mukhopadhyay, S.; Maitra, U. Chemistry and biology of bile acids. *Curr. Sci.* **2004**, *87*, 1666–1683.
13. Krafft, M.P. Fluorocarbons and fluorinated amphiphiles in drug delivery and biomedical research. *Adv. Drug Deliv. Rev.* **2001**, *47*, 209–228, doi:10.1016/S0169-409X(01)00107-7.
14. Schwieger, C.; Achilles, A.; Scholz, S.; Rüger, J.; Bacia, K.; Saalwächter, K.; Kressler, J.; Blume, A. Binding of amphiphilic and triphilic block copolymers to lipid model membranes: The role of perfluorinated moieties. *Soft Matter* **2014**, *10*, 6147–6160, doi:10.1039/C4SM00830H.
15. Scholtysek, P.; Achilles, A.; Hoffmann, C.-V.; Lechner, B.-D.; Meister, A.; Tschierske, C.; Saalwächter, K.; Edwards, K.; Blume, A. A T-Shaped Amphiphilic Molecule Forms Closed Vesicles in Water and Bicelles in Mixtures with a Membrane Lipid. *J. Phys. Chem. B* **2012**, *116*, 4871–4878, doi:10.1021/jp207996r.
16. Achilles, A.; Bärenwald, R.; Lechner, B.; Werner, S.; Ebert, H.; Tschierske, C.; Blume, A.; Bacia, K.; Saalwächter, K. Self-Assembly of X-Shaped Bolapolyphiles in Lipid Membranes: Solid-State NMR Investigations. *Langmuir* **2016**, *32*, 673–682, doi:10.1021/acs.langmuir.5b03712.
17. Werner, S.; Ebert, H.; Lechner, B.-D.; Lange, F.; Achilles, A.; Bärenwald, R.; Poppe, S.; Blume, A.; Saalwächter, K.; Tschierske, C.; et al. Dendritic Domains with Hexagonal Symmetry Formed by X-Shaped Bolapolyphiles in Lipid Membranes. *Chem. Eur. J.* **2015**, *21*, 8840–8850, doi:10.1002/chem.201405994.
18. Bärenwald, R.; Achilles, A.; Lange, F.; Mendes, T.F.; Saalwächter, K. Applications of Solid-State NMR Spectroscopy for the Study of Lipid Membranes with Polyphilic Guest (Macro)Molecules. *Polymers* **2016**, *8*, 439, doi:10.3390/polym8120439.
19. Permadi, H.; Lundgren, B.; Andersson, K.; DePierre, J.W. Effects of perfluoro fatty acids on xenobiotic-metabolizing enzymes, enzymes which detoxify reactive forms of oxygen and lipid peroxidation in mouse liver. *Biochem. Pharmacol.* **1992**, *44*, 1183–1191, doi:10.1016/0006-2952(92)90383-T.
20. Heuvel, J.P.V.; Kuslikis, B.I.; Van Rafelghem, M.J.; Peterson, R.E. Tissue distribution, metabolism, and elimination of perfluorooctanoic acid in male and female rats. *J. Biochem. Toxicol.* **1991**, *6*, 83–92, doi:10.1002/jbt.2570060202.
21. Park, K.-H.; Berrier, C.; Lebaupain, F.; Pucci, B.; Popot, J.-L.; Ghazi, A.; Zito, F. Fluorinated and hemifluorinated surfactants as alternatives to detergents for membrane protein cell-free synthesis. *Biochem. J.* **2007**, *403*, 183–187, doi:10.1042/BJ20061473.
22. Brehm, M.; Weber, H.; Thomas, M.; Hollóczki, O.; Kirchner, B. Domain Analysis in Nanostructured Liquids: A Post-Molecular Dynamics Study at the Example of Ionic Liquids. *ChemPhysChem* **2015**, *16*, 3271–3277, doi:10.1002/cphc.201500471.
23. Nagle, J.F.; Tristram-Nagle, S. Structure of lipid bilayers. *Biochim. Biophys. Acta* **2000**, *1469*, 159–195, doi:10.1016/S0304-4157(00)00016-2.
24. Liu, B.; Hoopes, M.I.; Karttunen, M. Molecular Dynamics Simulations of DPPC/CTAB Monolayers at the Air/Water Interface. *J. Phys. Chem. B* **2014**, *118*, 11723–11737, doi:10.1021/jp5050892.
25. Repáková, J.; Holopainen, J.M.; Morrow, M.R.; McDonald, M.C.; Capková, P.; Vattulainen, I. Influence of DPH on the Structure and Dynamics of a DPPC Bilayer. *Biophys. J.* **2005**, *88*, 3398–3410, doi:10.1529/biophysj.104.055533.
26. Hughes, Z.E.; Mark, A.E.; Mancera, R.L. Molecular Dynamics Simulations of the Interactions of DMSO with DPPC and DOPC Phospholipid Membranes. *J. Phys. Chem. B* **2012**, *116*, 11911–11923, doi:10.1021/jp3035538.

27. Zeng, X.; Kieffer, R.; Glettner, B.; Nürnberger, C.; Liu, F.; Pelz, K.; Prehm, M.; Baumeister, U.; Hahn, H.; Lang, H.; et al. Complex Multicolor Tilings and Critical Phenomena in Tetrphilic Liquid Crystals. *Science* **2011**, *331*, 1302–1306, doi:10.1126/science.1193052.
28. Yoshino, M.; Kikukawa, T.; Takahashi, H.; Takagi, T.; Yokoyama, Y.; Amii, H.; Baba, T.; Kanamori, T.; Sonoyama, M. Physicochemical Studies of Bacteriorhodopsin Reconstituted in Partially Fluorinated Phosphatidylcholine Bilayers. *J. Phys. Chem. B* **2013**, *117*, 5422–5429, doi:10.1021/jp311665z.
29. Bennett, W.F.D.; Tieleman, D.P. Computer simulations of lipid membrane domains. *Biochim. Biophys. Acta* **2013**, *1828*, 1765–1776, doi:10.1016/j.bbamem.2013.03.004.
30. Lehmler, H.-J.; Bummer, P.M. Mixing of perfluorinated carboxylic acids with dipalmitoylphosphatidylcholine. *Biochim. Biophys. Acta* **2004**, *1664*, 141–149, doi:10.1016/j.bbamem.2004.05.002.
31. Korlach, J.; Schwille, P.; Webb, W.W.; Feigenson, G.W. Characterization of lipid bilayer phases by confocal microscopy and fluorescence correlation spectroscopy. *Proc. Natl. Acad. Sci. USA* **1999**, *96*, 8461–8466, doi:10.1073/pnas.96.15.8461.
32. Klauda, J.B.; Venable, R.M.; Freites, J.A.; O'Connor, J.W.; Tobias, D.J.; Mondragon-Ramirez, C.; Vorobyov, I.; MacKerell, A.D.; Pastor, R.W. Update of the CHARMM All-Atom Additive Force Field for Lipids: Validation on Six Lipid Types. *J. Phys. Chem. B* **2010**, *114*, 7830–7843, doi:10.1021/jp101759q.
33. Krafft, M.P. Controlling phospholipid self-assembly and film properties using highly fluorinated components—Fluorinated monolayers, vesicles, emulsions and microbubbles. *Biochimie* **2012**, *10*, 11–25, doi:10.1016/j.biochi.2011.07.027.
34. Feller, S.E.; Venable, R.M.; Pastor, R.W. Computer Simulation of a DPPC Phospholipid Bilayer: Structural Changes as a Function of Molecular Surface Area. *Langmuir* **1997**, *13*, 6555–6561, doi:10.1021/la970746j.
35. Von Rudorff, G.F.; Watermann, T.; Guo, X.Y.; Sebastiani, D. Conformational Space of a Polyphilic Molecule with a Fluorophilic Side Chain Integrated in a DPPC Bilayer. *J. Comput. Chem.* **2017**, *38*, 576–583, doi:10.1002/jcc.24711.
36. Phillips, J.C.; Braun, R.; Wang, W.; Gumbart, J.; Tajkhorshid, E.; Villa, E.; Chipot, C.; Skeel, R.D.; Kalé, L.; Schulten, K. Scalable molecular dynamics with NAMD. *J. Comput. Chem.* **2005**, *26*, 1781–1802, doi:10.1002/jcc.20289.
37. Vanommeslaeghe, K.; Hatcher, E.; Acharya, C.; Kundu, S.; Zhong, S.; Shim, J.; Darian, E.; Guvench, O.; Lopes, P.; Vorobyov, I.; et al. CHARMM General Force Field: A Force Field for Drug-Like Molecules Compatible with the CHARMM All-Atom Additive Biological Force Fields. *J. Comput. Chem.* **2010**, *31*, 671–690, doi:10.1002/jcc.21367.
38. Von Rudorff, G.F.; Watermann, T.; Sebastiani, D. Perfluoroalkane Force Field for Lipid Membrane Environments. *J. Phys. Chem. B* **2014**, *118*, 12531–12540, doi:10.1021/jp507464m.
39. Humphrey, W.; Dalke, A.; Schulten, K. VMD: Visual molecular dynamics. *J. Mol. Graph.* **1996**, *14*, 33–38, doi:10.1016/0263-7855(96)00018-5.
40. Michaud-Agrawal, N.; Denning, E.J.; Woolf, T.B.; Beckstein, O. MDAAnalysis: A toolkit for the analysis of molecular dynamics simulations. *J. Comput. Chem.* **2011**, *32*, 2319–2327, doi:10.1002/jcc.21787.
41. Brehm, M.; Kirchner, B. TRAVIS—A Free Analyzer and Visualizer for Monte Carlo and Molecular Dynamics Trajectories. *J. Chem. Inf. Model.* **2011**, *51*, 2007–2023, doi:10.1021/ci200217w.
42. Junglas, M.; Danner, B.; Bayerl, T.M. Molecular Order Parameter Profiles and Diffusion Coefficients of Cationic Lipid Bilayers on a Solid Support. *Langmuir* **2003**, *19*, 1914–1917, doi:10.1021/la026468s.
43. McQuarrie, D.A. *Statistical Mechanics*; University Science Books: Davis, CA, USA, 1976; p. 641.



© 2017 by the authors. Licensee MDPI, Basel, Switzerland. This article is an open access article distributed under the terms and conditions of the Creative Commons Attribution (CC BY) license (<http://creativecommons.org/licenses/by/4.0/>).

4. PUBLICATIONS

5

Conclusion

In this thesis, a range of hydrogen bonded systems have been investigated by means of molecular dynamics simulations at different levels of theory and ensemble averaged observables such as ab-initio NMR chemical shift calculations.

- In a solvated chromophore, we could show a solvent-induced conformational switching behavior through a combination of molecular dynamics simulations, free energy methods and ab-initio NMR spectroscopy.
- In water confined on the nanoscale in a rigid silica structure and a softer cellulose environment, we demonstrated the anomalous behavior of water in the surface region. Here the dynamics becomes subdiffusive, while the structure of the water hydrogen bond network also changes drastically as indicated by NMR chemical shifts as well as hydrogen bond orientations and coordination numbers.
- A binary ethanol-water mixture under hydrophilic silica confinement shows a similar behavior in the confinement with pure water. When examining the two solvents individually, however, additional effects can be seen. In the surface region, a partial demixing between the two solvents occurs with an increased partial density for the ethanol and a reduced one for the water molecules.
- In the last class of systems, phospholipid bilayers under addition of (semi-) perfluorinated alkanes and polyphilic transmembrane molecules, we could demonstrate an induced phase transition in the membrane in the case of perfluorinated alkanes. The large polyphilic transmembrane molecules show a surprisingly high diffusivity that is comparable to that of DPPC molecules in a pure membrane. We could also show their clustering behavior, which leads to macroscopic domain building into polyphilic rich and pure phospholipid regions in experiments.

5. CONCLUSION

In interplay with experimental results, our theoretical approaches were able to investigate the underlying microscopic origins for a wide range of phenomena.

The investigated polyphilic systems will remain of relevance in upcoming experimental and theoretical investigations. Here our insights into the domain formation process could be of importance e.g. as reference point for coarse grained simulations, while the confinement created from a cellulose crystal is currently under further investigation as a confinement of ionic liquids(83).

References

- [1] X. Y. Guo, T. Watermann, S. Keane, C. Allolio, and D. Sebastiani, "First principles calculations of nmr chemical shifts of liquid water at an amorphous silica interface," *Z. Phys. Chem.*, vol. 226, no. 11-12, pp. 1415–1424, 2012. 2
- [2] T. Watermann, H. Elgabarty, and D. Sebastiani, "Phycocyanobilin in solution—a solvent triggered molecular switch," *Phys. Chem. Chem. Phys.*, vol. 16, no. 13, pp. 6146–6152, 2014. 2
- [3] Y. Xu, T. Watermann, H.-H. Limbach, T. Gutmann, D. Sebastiani, and G. Buntkowsky, "Water and small organic molecules as probes for geometric confinement in well-ordered mesoporous carbon materials," *Phys. Chem. Chem. Phys.*, vol. 16, no. 20, pp. 9327–9336, 2014. 2
- [4] X.-Y. Guo, T. Watermann, and D. Sebastiani, "Local microphase separation of a binary liquid under nanoscale confinement," *J. Phys. Chem. B*, vol. 118, no. 34, pp. 10207–10213, 2014. 2
- [5] G. F. von Rudorff, T. Watermann, and D. Sebastiani, "Perfluoroalkane force field for lipid membrane environments," *J. Phys. Chem. B*, vol. 118, no. 43, pp. 12531–12540, 2014. 2
- [6] M. Brehm, G. Saddiq, T. Watermann, and D. Sebastiani, "Influence of small fluorophilic and lipophilic organic molecules on dipalmitoylphosphatidylcholine bilayers," *J. Phys. Chem. B*, vol. 121, no. 35, pp. 8311–8321, 2017. 2
- [7] G. F. von Rudorff, T. Watermann, X.-Y. Guo, and D. Sebastiani, "Conformational space of a polyphilic molecule with a fluorophilic side chain integrated in a dppc bilayer," *J. Comp. Chem.*, vol. 38, no. 9, pp. 576–583, 2017. 2
- [8] X.-Y. Guo, C. Peschel, T. Watermann, G. F. v. Rudorff, and D. Sebastiani, "Cluster formation of polyphilic molecules solvated in a dppc bilayer," *Polymers*, vol. 9, no. 10, 2017. 2
- [9] T. Watermann and D. Sebastiani, "Liquid water confined in cellulose with variable interfacial hydrophilicity," *Z. Phys. Chem.*, vol. 232, no. 7-8, pp. 989–1002, 2018. 2
- [10] D. Marx and J. Hutter, *Ab Initio Molecular Dynamics: Basic Theory and Advanced Methods*. Cambridge University Press, 2009. 5
- [11] M. P. Allen and D. J. Tildesley, *Computer Simulation of Liquids*. Oxford University Press, 1989. 5
- [12] U. F. Rohrig and D. Sebastiani, "Nmr chemical shifts of the rhodopsin chromophore in the dark state and in bathorhodopsin: a hybrid qm/mm molecular dynamics study," *J. Phys. Chem. B*, vol. 112, pp. 1267–1274, 2008. 5
- [13] J. Schmidt, A. Hoffmann, H. W. Spiess, and D. Sebastiani, "Bulk chemical shifts in hydrogen bonded systems from first principles calculations and solid-state-nmr," *J. Phys. Chem. B*, vol. 110, pp. 23204–23210, 2006. 5
- [14] C. Allolio and D. Sebastiani, "A simple solution? Approaches to the solvation dynamics of the molecular probe *N*-methyl-6-quinolone," *Phys. Chem. Chem. Phys.*, vol. 13, pp. 16395–16403, 2011. 5
- [15] D. Banyai, T. Murakhtina, and D. Sebastiani, "NMR chemical shifts as a tool to analyze first principles molecular dynamics simulations in condensed phases: The case of liquid water," *Magn. Reson. Chem.*, vol. 48, pp. S56–S60, 2010. 5
- [16] C. Schiffmann and D. Sebastiani, "Hydrogen bond networks: Structure and dynamics via first-principles spectroscopy," *Phys. Stat. Sol. B*, vol. 249, pp. 368–375, 2012. 5
- [17] D. Sebastiani and M. Parrinello, "Ab-initio study of NMR chemical shifts of water under normal and supercritical conditions," *ChemPhysChem*, vol. 3, p. 675, 2002. 5

REFERENCES

- [18] C. Allolio, M. Sajadi, N. P. Ernsting, and D. Sebastiani, "Deciphering the Stokes shift of methyl quinolone in water," *Angew. Chem. Int. Ed. Engl.*, vol. 52, no. 6, pp. 1813–1816, 2013. 5
- [19] L. Verlet, "Computer" experiments" on classical fluids. i. thermodynamical properties of lennard-jones molecules," *Phys. Rev.*, vol. 159, no. 1, p. 98, 1967. 6
- [20] W. C. Swope, H. C. Andersen, P. H. Berens, and K. R. Wilson, "A computer simulation method for the calculation of equilibrium constants for the formation of physical clusters of molecules: Application to small water clusters," *J. Chem. Phys.*, vol. 76, no. 1, pp. 637–649, 1982. 6
- [21] G. Bussi, D. Donadio, and M. Parrinello, "Canonical sampling through velocity rescaling," *J. Chem. Phys.*, vol. 126, no. 1, p. 014101, 2007. 7
- [22] S. Nosé *Mol. Phys.*, vol. 5, p. 255, 1984. 7
- [23] G. J. Martyna, M. L. Klein, and M. E. Tuckerman, "Nosé-hoover chains: The canonical ensemble via continuous dynamics," *J. Chem. Phys.*, vol. 97, no. 2635, 1992. 8
- [24] A. D. MacKerell, N. Banavali, and N. Fopolle, "Development and current status of the charmm force field for nucleic acids," *Biopolymers*, vol. 56, no. 4, pp. 257–265, 2001. 9
- [25] K. Vanommeslaeghe, E. Hatcher, C. Acharya, S. Kundu, S. Zhong, J. Shim, E. Darian, O. Guvench, P. Lopes, I. Vorobyov, and A. D. MacKerell, "Charmm general force field: A force field for drug-like molecules compatible with the charmm all-atom additive biological force fields," *J. Comp. Chem.*, vol. 31, no. 4, pp. 671–690, 2010. 9
- [26] W. Koch and M. C. Holthausen, *A chemist's guide to density functional theory*. John Wiley & Sons, 2015. 12
- [27] A. Szabo and N. S. Ostlund, *Modern Quantum Chemistry*. Dover Publications Inc., Mineola, New York, 1996. 12
- [28] P. Hohenberg and W. Kohn, "The inhomogeneous electron gas," *Phys. Rev.*, vol. 136, p. B864, 1964. 14
- [29] W. Kohn and L. J. Sham, "Self-consistent equations including exchange and correlation effects," *Phys. Rev.*, vol. 140, p. A1133, 1965. 14
- [30] R. Parr and W. Yang, "Density-functional theory of atoms and molecules," *Oxford University Press, New York, Capítulo*, vol. 5, pp. 87–104, 1989. 15
- [31] A. D. Becke, "Density-functional exchange-energy approximation with correct asymptotic behavior," *Phys. Rev. A*, vol. 38, p. 3098, 1988. 17, 27
- [32] C. Lee, W. Yang, and R. G. Parr, "Development of the colle-salvetti correlation-energy formula into a functional of the electron-density," *Phys. Rev. B*, vol. 37, pp. 785–789, 1988. 17, 27
- [33] J. P. Perdew in *Electronic Structure of Solids* (P. Ziesche and H. Eschrig, eds.), p. 11, Akademie Verlag, Berlin, 1991. 17
- [34] J. Perdew, K. Burke, and M. Ernzerhof *J. Phys. Chem.*, vol. 105, pp. 9982–9985, 1996. 17
- [35] P. J. Stephens, F. J. Devlin, C. F. Chabalowski, and M. J. Frisch, "Ab Initio Calculation of Vibrational Absorption and Circular Dichroism Spectra Using Density Functional Force Fields," *J. Phys. Chem.*, vol. 98, pp. 11623–11627, Nov. 1994. 17
- [36] W. Kutzelnigg, "Individual gauges for localized orbitals," *Isr. J. Chem.*, vol. 19, p. 193, 1980. 17, 23
- [37] X. Gonze, "Perturbation expansion of variational-principles at arbitrary order," *Phys. Rev. A*, vol. 52, pp. 1086–1095, 1995. 19
- [38] X. Gonze, "Adiabatic density-functional perturbation-theory," *Phys. Rev. A*, vol. 52, pp. 1096–1114, 1995. 19, 21
- [39] S. Baroni, S. de Gironcoli, A. del Corso, and P. Giannozzi, "Phonons and related crystal properties from density-functional perturbation theory," *Rev. Mod. Phys.*, vol. 73, p. 515, 2001. 19
- [40] A. Putrino, D. Sebastiani, and M. Parrinello, "Generalized variational density functional perturbation theory," *J. Chem. Phys.*, vol. 113, pp. 7102–7109, 2000. 20, 21

- [41] H.-H. Limbach, P. M. Tolstoy, N. Perez-Hernandez, J. Guo, I. G. Shenderovich, and G. S. Denisov, "OHO Hydrogen Bond Geometries and NMR Chemical Shifts: From Equilibrium Structures to Geometric H/D Isotope Effects, with Applications for Water, Protonated Water, and Compressed Ice," *Isr. J. Chem.*, vol. 49, no. 2, pp. 199–216, 2009. 22
- [42] D. Sebastiani, "Ab-initio calculation of nuclear magnetic resonance parameters in condensed phases," *Mod. Phys. Lett. B*, vol. 17, pp. 1301–1319, 2003. 22
- [43] W. Kutzelnigg, U. Fleischer, and M. Schindler, "The IGLO method," *NMR basic principles and progress*, vol. 23, p. 165, 1990. 23
- [44] R. Ditchfield, "Gauge including atomic orbitals," *J. Chem. Phys.*, vol. 56, p. 5688, 1972. 23
- [45] D. Sebastiani and M. Parrinello, "A new method to compute NMR chemical shifts in periodic systems," *J. Phys. Chem. A*, vol. 105, pp. 1951–1958, 2001. 23, 24
- [46] D. Sebastiani, G. Goward, I. Schnell, and M. Parrinello, "NMR chemical shifts in periodic systems from first principles," *Comp. Phys. Commun.*, vol. 147, p. 707, 2002. 23
- [47] F. Mauri and S. Louie, "Magnetic susceptibility of insulators from first principles," *Phys. Rev. Lett.*, vol. 76, pp. 4246–4249, 1996. 23
- [48] F. Mauri, B. Pfrommer, and S. Louie, "Ab initio theory of NMR chemical shifts in solids and liquids," *Phys. Rev. Lett.*, vol. 77, pp. 5300–5303, 1996. 23
- [49] K. Ohno, F. Mauri, and S. Louie, "Magnetic susceptibility of semiconductors by an all-electron first-principles approach," *Phys. Rev. B*, vol. 56, p. 1009, 1997. 23
- [50] T. Gregor, F. Mauri, and R. Car, "A comparison of methods for the calculation of NMR chemical shifts," *J. Chem. Phys.*, vol. 111, pp. 1815–1822, 1999. 23
- [51] C. J. Pickard and F. Mauri, "All-electron magnetic response with pseudopotentials: NMR chemical shifts," *Phys. Rev. B*, vol. 63, p. 245101, 2001. 23
- [52] J. J. V. Thor, K. L. Ronayne, and M. Towrie, "Formation of the Early Photoproduct Lumi-R of Cyanobacterial Phytochrome Cph1 Observed by Ultrafast Mid-Infrared Spectroscopy," *J. Am. Chem. Soc.*, vol. 129, no. 1, pp. 126–132, 2007. 26
- [53] K. C. Toh, E. A. Stojkovi, A. B. Rupenyan, I. H. M. V. Stokkum, M. Salumbides, M.-I. Groot, K. Moffat, and J. T. M. Kennis, "Primary Reactions of Bacteriophytochrome Observed with Ultrafast Mid-Infrared Spectroscopy," *J. Phys. Chem. A*, vol. 115, no. 16, pp. 3778–3786, 2010. 26
- [54] L. J. G. W. V. Wilderen, I. P. Clark, M. Towrie, and J. J. V. Thor, "Mid-Infrared Picosecond Pump-Dump-Probe and Pump-Repump-Probe Experiments to Resolve a Ground-State Intermediate in Cyanobacterial Phytochrome Cph1," *J. Phys. Chem. B*, vol. 113, no. 51, pp. 16354–16364, 2009. 26
- [55] J. J. V. Thor, M. Mackeen, I. Kuprov, R. A. Dwek, and M. R. Wormald, "Chromophore Structure in the Photocycle of the Cyanobacterial Phytochrome Cph1," *Biophys. J.*, vol. 91, no. 5, pp. 1811–1822, 2006. 26
- [56] S. Kaminski and M. A. Mroginiski, "Molecular dynamics of phycocyanobilin binding bacteriophytochromes: a detailed study of structural and dynamic properties," *J. Phys. Chem. B*, vol. 114, no. 50, pp. 16677–86, 2010. 26
- [57] T. Rohmer, H. Strauss, J. Hughes, H. D. Groot, W. Ga, and P. Schmieder pp. 20580–20585. 26
- [58] M. A. Mroginiski, F. Mark, W. Thiel, and P. Hildebrandt, "Quantum mechanics/molecular mechanics calculation of the raman spectra of the phycocyanobilin chromophore in [alpha]-c-phycocyanin," *Biophys. J.*, vol. 93, no. 6, pp. 1885–1894, 2007. 26
- [59] M. Röben and P. Schmieder, "Assignment of phycocyanobilin in HMPT using triple resonance experiments," *Magn. Reson. Chem.*, no. May, pp. 543–548, 2011. 26
- [60] A. Laio and M. Parrinello, "Escaping free-energy minima," *Proc. Natl. Acad. Sci. USA*, vol. 99, pp. 12562–12566, 2002. 27

REFERENCES

- [61] A. Barducci, G. Bussi, and M. Parrinello, "Well-Tempered Metadynamics: A Smoothly Converging and Tunable Free-Energy Method," *Phys. Rev. Lett.*, vol. 100, pp. 1–4, Jan. 2008. 27
- [62] J. V. Vondele, M. Krack, F. Mohamed, M. Parrinello, T. Chassaing, and J. Hutter, "Quickstep: Fast and accurate density functional calculations using a mixed gaussian and plane waves approach," *Comp. Phys. Comm.*, vol. 167, no. 167, pp. 103–128, 2005. 27
- [63] S. Grimme and M. Parac, "Substantial errors from time-dependent density functional theory for the calculation of excited states of large pi systems.," *ChemPhysChem*, vol. 3, pp. 292–295, 2003. 27
- [64] T. Laino, F. Mohamed, A. Laio, and M. Parrinello, "An Efficient Real Space Multigrid QM/MM Electrostatic Coupling," *J. Chem. Theory Comput.*, vol. 1, no. 6, pp. 1176–1184, 2005. 27
- [65] Q. Hu, J. Pang, N. Jiang, J. E. Hampsey, and Y. Lu, "Direct synthesis of palladium-containing mesoporous carbon," *Microporous and mesoporous materials*, vol. 81, no. 1-3, pp. 149–154, 2005. 31
- [66] D. Sebastiani, "Current densities and nucleus-independent chemical shift maps from reciprocal-space density functional perturbation theory calculations," *ChemPhysChem*, vol. 7, no. 1, pp. 164–175, 2006. 31
- [67] A. C. O'Sullivan, "Cellulose: the structure slowly unravels," *Cellulose*, vol. 4, no. 3, pp. 173–207, 1997. 32
- [68] A. H. Bedane, H. Xiao, M. Eić, and M. Farmahini-Farahani, "Structural and thermodynamic characterization of modified cellulose fiber-based materials and related interactions with water vapor," *Appl. Surf. Sci.*, vol. 351, pp. 725–737, 2015. 32
- [69] R. C. Weatherwax, "Collapse of cell-wall pores during drying of cellulose," *J. Colloid Interf. Sci.*, vol. 62, no. 3, pp. 432–446, 1977. 32
- [70] C. Schwieger, A. Achilles, S. Scholz, J. Rürger, K. Bacia, K. Saalwaechter, J. Kressler, and A. Blume, "Binding of amphiphilic and triphilic block copolymers to lipid model membranes: the role of perfluorinated moieties.," *Soft matter*, vol. 10, no. 33, pp. 6147–6160, 2014. 33, 35
- [71] X. Zeng, R. Kieffer, B. Glettner, C. Nürnberger, F. Liu, K. Pelz, M. Prehm, U. Baumeister, H. Hahn, H. Lang, G. A. Gehring, C. H. M. Weber, J. K. Hobbs, C. Tschierske, and G. Ungar, "Complex multicolor tilings and critical phenomena in tetraphilic liquid crystals.," *Science*, vol. 331, no. 6022, pp. 1302–1306, 2011. 33, 35
- [72] P. Scholtysek, A. Achilles, C.-V. Hoffmann, B.-D. Lechner, A. Meister, C. Tschierske, K. Saalwächter, K. Edwards, and A. Blume, "A t-shaped amphiphilic molecule forms closed vesicles in water and bicelles in mixtures with a membrane lipid.," *J. Phys. Chem. B*, vol. 116, no. 16, pp. 4871–4878, 2012. 33, 35
- [73] H. Permadi, B. Lundgren, K. Andersson, and J. W. DePierre, "Effects of perfluoro fatty acids on xenobiotic-metabolizing enzymes, enzymes which detoxify reactive forms of oxygen and lipid peroxidation in mouse liver," *Biochem. Pharmacol.*, vol. 44, no. 6, pp. 1183 – 1191, 1992. 33
- [74] J. P. V. Heuvel, B. I. Kuslikis, M. J. Van Rafelghem, and R. E. Peterson, "Tissue distribution, metabolism, and elimination of perfluorooctanoic acid in male and female rats," *J. Biochem. Toxicol.*, vol. 6, no. 2, pp. 83–92, 1991. 33
- [75] J. C. Maurizis, M. Azim, M. Rapp, B. Pucci, A. Pavia, J. C. Madelmont, and A. Veyre, "Disposition in rat of a new fluorinated, biocompatible, non-ionic telomeric carrier," *Xenobiotica*, vol. 24, no. 6, pp. 535–541, 1994. 33
- [76] E. H. Hill, K. Stratton, D. G. Whitten, and D. G. Evans, "Molecular dynamics simulation study of the interaction of cationic biocides with lipid bilayers: aggregation effects and bilayer damage.," *Langmuir*, vol. 28, no. 42, pp. 14849–14854, 2012. 33
- [77] M. Schulz, A. Olubummo, and W. H. Binder, "Beyond the lipid-bilayer: interaction of polymers and nanoparticles with membranes," *Soft Matter*, vol. 8, p. 4849, 2012. 33

REFERENCES

- [78] J. Hinks, Y. Wang, W. H. Poh, B. C. Donose, A. W. Thomas, S. Wuertz, S. C. J. Loo, G. C. Bazan, S. Kjelleberg, Y. Mu, and T. Seviour, "Modeling cell membrane perturbation by molecules designed for transmembrane electron transfer.," *Langmuir*, vol. 30, no. 9, pp. 2429–2440, 2014. 33
- [79] P. V. James, P. K. Sudeep, C. H. Suresh, and K. G. Thomas, "Photophysical and theoretical investigations of oligo(p-phenyleneethynylene)s: Effect of alkoxy substitution and alkynearyl bond rotations," *J. Phys. Chem. A*, vol. 110, no. 13, pp. 4329–4337, 2006. 33
- [80] E. H. Hill, D. G. Whitten, and D. G. Evans, "Computational study of bacterial membrane disruption by cationic biocides: Structural basis for water pore formation," *J. Phys. Chem. B*, vol. 118, no. 32, pp. 9722–9732, 2014. 33
- [81] J. B. Klauda, R. M. Venable, J. A. Freites, J. W. O'Connor, D. J. Tobias, C. Mondragon-Ramirez, I. Vorobyov, A. D. MacKerell, and R. W. Pastor, "Update of the charmm all-atom additive force field for lipids: validation on six lipid types.," *J. Phys. Chem. B*, vol. 114, no. 23, pp. 7830–7843, 2010. 34
- [82] K. Vanommeslaeghe and A. D. MacKerell, "Automation of the charmm general force field (cgenff) i: bond perception and atom typing.," *J. Chem. Chem. Inf. Model.*, vol. 52, no. 12, pp. 3144–3154, 2012. 34
- [83] M. Brehm, M. Pulst, J. Kressler, and D. Sebastiani, "Triazolium-based ionic liquids: A novel class of cellulose solvents," *J. Phys. Chem. B*, vol. 123, no. 18, pp. 3994–4003, 2019. 132

REFERENCES

6

Academic Curriculum Vitæ

Curriculum Vitæ

Personal Information

Name Tobias Watermann
E-Mail tobias.watermann@chemie.uni-halle.de
Date of Birth August 12, 1984 in Berlin
Nationality german

Education

2011 – 2016 **Doctoral Researcher**, *Martin-Luther University Halle-Wittenberg*.
Thesis title: *Complex Hydrogen Bonded Liquids with different Philicities from Molecular Dynamics Simulations*

04/2005 – 10/2010 **Dipl. Phys.**, *Technical University Berlin*.
Thesis title: *Theory of optical Properties of functionalized Carbon Nanotubes*

Publications

- E. Malic, E. Bobkin, T. Winzer, C. Köhler, T. Watermann, M. Hirtschulz, A. Knorr. Microscopic theory of ultrafast processes in carbon nanomaterials. **2011**, 79371R–79371R.
- C. Köhler, T. Watermann, A. Knorr, E. Malic. Microscopic study of temporally resolved carrier relaxation in carbon nanotubes. *Physical Review B* **2011**, *84*, 153407.
- C. Köhler, T. Watermann, E. Malic. Relaxation dynamics via acoustic phonons in carbon nanotubes. *physica status solidi (b)* **2012**, *249*, 2483–2486.
- O. A. Dyatlova, C. Köhler, E. Malic, J. Gomis-Bresco, J. Maultzsch, A. Tsagan-Mandzhiev, T. Watermann, A. Knorr, U. Woggon. Ultrafast relaxation dynamics via acoustic phonons in carbon nanotubes. *Nano letters* **2012**, *12*, 2249–2253.
- X. Y. Guo, T. Watermann, S. Keane, C. Allolio, D. Sebastiani. First Principles Calculations of NMR Chemical Shifts of Liquid Water at an Amorphous Silica Interface. *Zeitschrift für Physikalische Chemie International journal of research in physical chemistry and chemical physics* **2012**, *226*, 1415–1424.
- O. A. Dyatlova, C. Köhler, E. Malic, J. Gomis-Bresco, J. Maultzsch, A. Tsagan-Mandzhiev, T. Watermann, A. Knorr, U. Woggon. Scattering of electrons with acoustic phonons in single-walled carbon nanotubes. *Quantum Electronics and Laser Science Conference* **2012**, QTh3H–6.
- C. Köhler, T. Watermann, E. Malic. Time- and momentum-resolved phonon-induced relaxation dynamics in carbon nanotubes. *Journal of Physics: Condensed Matter* **2013**, *25*, 105301.
- T. Watermann, H. Elgabarty, D. Sebastiani. Phycocyanobilin in solution—a solvent triggered molecular switch. *Physical Chemistry Chemical Physics* **2014**, *16*, 6146–6152.

-
- Y. Xu, T. Watermann, H.-H. Limbach, T. Gutmann, D. Sebastiani, G. Buntkowsky. Water and small organic molecules as probes for geometric confinement in well-ordered mesoporous carbon materials. *Physical Chemistry Chemical Physics* **2014**, *16*, 9327–9336.
- X.-Y. Guo, T. Watermann, D. Sebastiani. Local Microphase Separation of a Binary Liquid under Nanoscale Confinement. *The Journal of Physical Chemistry B* **2014**, *118*, 10207–10213.
- G. F. von Rudorff, T. Watermann, D. Sebastiani. Perfluoroalkane Force Field for Lipid Membrane Environments. *The Journal of Physical Chemistry B* **2014**, *118*, 12531–12540.
- T. Watermann, A. Scherrer, D. Sebastiani, *Linear Response Methods in Quantum Chemistry*, Springer, **2014**.
- M. Brehm, G. Saddiq, T. Watermann, D. Sebastiani. Influence of Small Fluorophilic and Lipophilic Organic Molecules on Dipalmitoylphosphatidylcholine Bilayers. *The Journal of Physical Chemistry B* **2017**, *121*, 8311–8321, PMID: 28812889.
- G. F. von Rudorff, T. Watermann, X.-Y. Guo, D. Sebastiani. Conformational Space of a Polyphilic Molecule with a Fluorophilic Side Chain Integrated in a DPPC Bilayer. *Journal of Computational Chemistry* **2017**, *38*, 576–583.
- X.-Y. Guo, C. Peschel, T. Watermann, G. F. v. Rudorff, D. Sebastiani. Cluster Formation of Polyphilic Molecules Solvated in a DPPC Bilayer. *Polymers* **2017**, *9*.
- T. Watermann, D. Sebastiani. Liquid Water Confined in Cellulose with Variable Interfacial Hydrophilicity. *Zeitschrift für Physikalische Chemie* **2018**, *232*, 989–1002.

6. ACADEMIC CURRICULUM VITÆ

7

Eidesstattliche Erklärung / Declaration under oath

Ich erkläre an Eides statt, dass ich die Arbeit selbstständig und ohne fremde Hilfe verfasst, keine anderen als die von mir angegebenen Quellen und Hilfsmittel benutzt und die den benutzten Werken wörtlich oder inhaltlich entnommenen Stellen als solche kenntlich gemacht habe. / I declare under oath that this thesis is my own work entirely and has been written without any help from other people. I used only the sources mentioned and included all the citations correctly both in word or content.

Halle (Saale), 07.01.2020, Tobias Watermann